

Coordination-Resolved Electron Spectrometrics

Xinjuan Liu,[†] Xi Zhang,[‡] Maolin Bo,[§] Lei Li,^{||} Hongwei Tian,^{||} Yanguang Nie,[⊥] Yi Sun,[#] Shiqing Xu,^{*,†} Yan Wang,^{*,▽} Weitao Zheng,^{*,||} and Chang Q Sun^{*,○}

[†]Institute of Coordination Bond Metrology and Engineering, College of Materials Science and Engineering, China Jiliang University, Hangzhou 310018, China

[‡]Institute of Nanosurface Science and Engineering, Shenzhen University, Shenzhen 518060, China

[§]Key Laboratory of Low-Dimensional Materials and Application Technologies (Ministry of Education) and School of Materials Science and Engineering, Xiangtan University, Hunan 411105, China

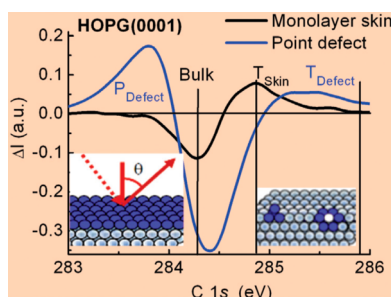
^{||}School of Materials Science, Jilin University, Changchun 130012, China

[⊥]School of Science, Jiangnan University, Wuxi 214122, China

[#]Harris School of Public Policy, University of Chicago, Chicago, Illinois 60637, United States

[▽]School of Information Technology, Hunan University of Science and Technology, Xiangtan 411201, China

[○]NOVITAS, School of Electrical and Electronic Engineering, Nanyang Technological University, Singapore 639798, Singapore



CONTENTS

1. Introduction
 - 1.1. Scope
 - 1.2. Overview
 - 1.2.1. Coordination Bonds and Energetic Electrons
 - 1.2.2. Challenges Faced by Existing Methods
 - 1.2.3. Known Mechanisms
 - 1.3. Motivation and Objectives
2. Theory: Bond–Electron–Energy Correlation
 - 2.1. Atomic Coordination Classification
 - 2.2. Core Band Energy Dispersion
 - 2.3. BOLS–NEP–LBA Notion
 - 2.3.1. Local Hamiltonian Perturbation
 - 2.3.2. Atomic Undercoordination: BOLS–NEP
 - 2.3.3. Heterocoordination: Entrapment or Polarization
 - 2.3.4. Generalization of Irregular Coordination Effect
 - 2.4. Valence Band and Nonbonding States
 - 2.4.1. Complexity of the Valence DOS
 - 2.4.2. Tetrahedral-Bonding Mediated Valence DOS
 - 2.4.3. Impact of Nonbonding States
 - 2.5. Numerical Strategies: Formulation and Quantification
 - 2.5.1. Irregular Coordination Effect
 - 2.5.2. Local Energy Density and Atomic Cohesive Energy

2.6. Summary	N
3. Probing Strategies: STM/S, PES, APECS, and ZPS	N
3.1. Energy Band Structure and Electronic Dynamics	N
3.2. STM/S: Nonbonding and Antibonding States	N
3.3. PES–AES: Valence- and Core-Band Shifts	N
3.4. APECS: Extended Wagner Plot and Dual-Band Shift	O
3.5. ZPS: CN-Resolved Bond Length and Energy Relaxation	P
3.6. Summary	P
4. Solid Skin: Quantum Entrapment Dominance	Q
4.1. XPS Spectroscopic Derivatives	Q
4.2. BOLS–TB Formulation	Q
4.3. fcc-Structured Al, Ag, Au, Ir, Rh, and Pd	R
4.4. bcc-Structured W and Mo	R
4.5. Diamond Structured Si and Ge	R
4.6. hcp-Structured Be, Re, and Ru	R
4.7. Local Energy Density and Atomic Cohesive Energy	T
4.8. Summary	U
5. Adatoms, Defects, and Kink Edges	U
5.1. Observations	V
5.2. ZPS of Pt and Rh Adatoms: Catalytic Nature	W
5.3. ZPS of Rh, W, and Re Kink Edges	X
5.3.1. Atomic Arrangement at Edges	X
5.3.2. Rh(110) and Rh(111) Vicinal Edges	X
5.3.3. W(110) Vicinal Edges	X
5.3.4. Re(0001) and (12̄31) Kink Edges	Y
5.3.5. O–Re(12̄31) Kink Edge and Chemisorbed States	Z
5.4. Summary	Z
6. Atomic Chain Ends, Clusters, and Nanocrystals	Z
6.1. Observations	Z
6.2. BOLS–TB Formulation	AA
6.3. Gold	AA
6.3.1. STM/S-DFT: End and Edge Polarization	AA

Received: November 19, 2014

6.3.2. PES: 4f and 5d Bands	AC	10. Concluding Remarks	AW
6.3.3. BOLS–TB Quantification	AC	10.1. Advantages and Attainments	AX
6.4. Silver	AC	10.2. Limitations and Precautions	AY
6.4.1. STM/S–DFT: Adatom Polarization	AC	10.3. Prospects and Perspectives	AY
6.4.2. APECS: 3d and 5s Band Cooperative Shift	AC	Author Information	AY
6.4.3. BOLS–TB Formulation and Quantification	AD	Corresponding Authors	AY
6.5. Copper	AE	Author Contributions	AZ
6.5.1. STM/S–PES–DFT: Entrapment and Polarization	AE	Notes	AZ
6.5.2. APECS: Interface 2p and 3d Energy Shift	AE	Biographies	AZ
6.5.3. BOLS–TB Formulation and Quantification	AE	Acknowledgments	BA
6.6. Nickel	AF	Nomenclature	BA
6.6.1. NEXAFS-XPS: Shell-Resolved Entrapment	AG	References	BB
6.6.2. APECS: 2p and 3d Band Cooperative Shift	AG		
6.6.3. BOLS–TB–ZPS Formulation and Derivatives	AG		
6.7. Li, Na, and K	AH		
6.7.1. Na 2p and K 3p Entrapment	AH		
6.7.2. CN Dependent Binding Energy Shift	AH		
6.7.3. Li, K, and Na Skins and Size Trends	AH		
6.8. Si and Pb	AH		
6.8.1. Si 2p and Valence Band Entrapment	AJ		
6.8.2. Pb 5d Binding Energy Shift	AJ		
6.9. Co, Fe, Pt, Rh, and Pd Nanocrystals	AJ		
6.9.1. Co Islands: Entrapment Dominance	AJ		
6.9.2. Pd, Fe, Rh, and Pt: Entrapment Dominance	AJ		
6.10. Summary	AJ		
7. Carbon Allotropes	AL		
7.1. STM/S-DFT: GNR Edge and Defect Polarization	AL		
7.2. TEM: CN-Resolved C–C Bond Energy	AN		
7.3. XPS: Core Level and Work Function Shift	AN		
7.4. BOLS–TB Formulation and Quantification	AN		
7.5. ZPS: Monolayer Skin Entrapment and Defect Polarization	AO		
7.6. Summary	AP		
8. Heterocoordinated Interfaces	AQ		
8.1. Observations	AQ		
8.2. BOLS–TB Formulation of the PES Attributes	AR		
8.3. ZPS: CuPd Entrapment, AgPd, ZnPd, BeW Polarization	AR		
8.4. Energy Density, Cohesive Energy, and Free Energy	AS		
8.5. Catalytic Nature, Toxicity, and Radiation Protectivity	AS		
8.6. Summary	AT		
9. Hetero- and Undercoordination Coupling	AT		
9.1. Ti(0001) Skin and TiO ₂ Nanocrystals	AT		
9.1.1. Photoactivity of Defected TiO ₂	AT		
9.1.2. XPS: Ti(0001) Skin 2p Band Shift	AU		
9.1.3. DFT: Oxygenation Valence States	AU		
9.1.4. ZPS: Defect Entrapment and Polarization	AU		
9.1.5. Defect Enhanced Photocatalytic Ability	AV		
9.2. ZnO Nanocrystals Passivated with H, N, and O	AV		
9.2.1. ZPS: Entrapment–Polarization Transition	AV		
9.2.2. Band Gap, Work Function, and Magnetism	AW		
9.3. Scratched SrTiO ₃ Skin: Defect States	AW		
9.4. Summary	AW		

1. INTRODUCTION

In this section, we discuss the following:

- Bond formation, relaxation, and the associated energetics, entrapment, localization, and polarization of electrons mediate the performance of a substance.
- Bonds between irregularly coordinated atoms fascinate adatoms, defects, kink edges, solid skins, impurities, interfaces, and nanocrystals in all aspects.
- Resolving the atomistic, dynamic, local, quantitative information on bond relaxation and electron binding energy shift associated with irregularly coordinated atoms remains a great challenge.
- Consistent insight into this matter with development of theoretical, experimental, and numerical strategies is necessary.

1.1. Scope

This treatise reports recent progress in resolving the atomistic, coordination-resolved, dynamic, local, and quantitative information on bond relaxation in length and energy, charge quantum entrapment and polarization, energy density, and atomic cohesive energy pertaining to the under- and heterocoordinated atoms and their joint effect.

Atomic undercoordination refers to atoms associated with grain boundaries, homogeneous adatoms, point defects, solid or liquid skins, terrace edges, and nanostructures of various shapes and dimensionalities. Atomic heterocoordination means those associated with alloys, compounds, chemisorbed skins, dopants, impurities, and interfaces.

The paper starts with section 1 providing an overview of the significance of chemical bonds and energetic electrons in discriminating the performance, for catalytic ability and Dirac fermion generation instances, of a substance at the irregularly (under- and hetero-)coordinated atomic site from that of the ideally full coordinated atoms in the bulk. Section 1 also summarizes advantages and limitations of existing electron spectroscopic techniques, and available mechanisms for the electron binding energy (BE) shift.

Section 2 describes notions of the bond order–length–strength (BOLS) correlation,¹ the nonbonding electron polarization (NEP),² and the local bond average (LBA) approach,³ as well as correlation between the valence band and the core band of electrons. Incorporation of the BOLS–NEP–LBA notion into the tight-binding (TB) approach⁴ enables the correlation, clarification, formulation, and quantification of the binding energies of the core and valence electrons pertaining to the irregularly coordinated atoms. Variation of equilibrium bond length and energy and the electron entrapment and polarization with coordination and chemical environment are the focus of this study carried out in the past 20 years.^{5,6}

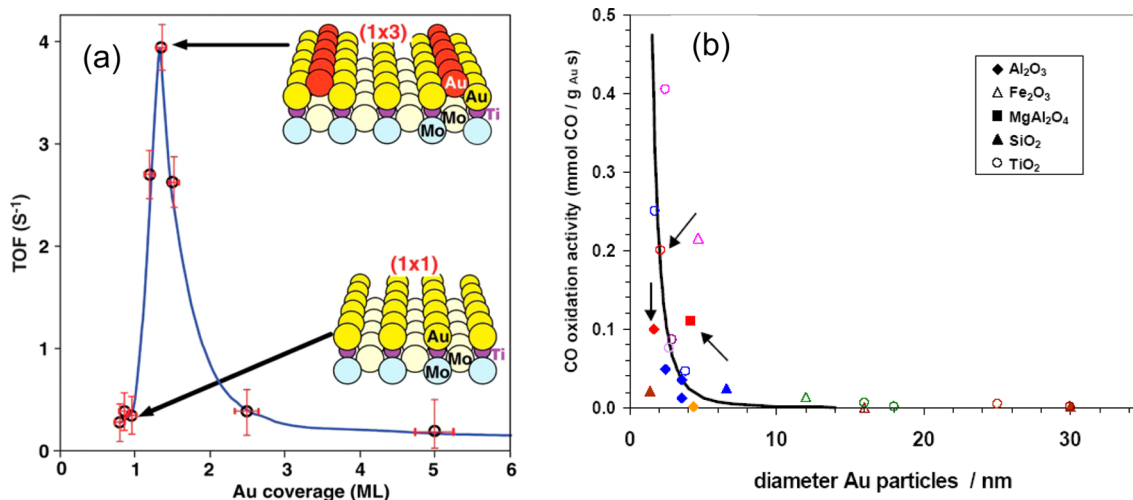


Figure 1. (a) Atomic undercoordination enhanced catalytic reactivity of Au/TiO₂ for CO room temperature oxidation. (b) Room temperature CO oxidation activity of Au nanoparticles deposited on different oxides. Reprinted with permission from ref 55. Copyright 2004 American Association for the Advancement of Science. Reprinted with permission from ref 57. Copyright 2004 Elsevier.

Section 3 presents our patented atomistic zone-resolved photoelectron spectroscopy (ZPS)⁷ for overcoming limitations faced by scanning tunneling microscopy/spectroscopy (STM/S), Auger electron spectroscopy (AES), and photoelectron emission spectroscopy (PES including UPS using UV light and XPS using X-ray source, or synchrotron radiation of various wavelengths). By differencing two spectra of the same specimen collected under different conditions, ZPS purifies the effect of conditioning on bond relaxation and the BE shift within the monolayer skin and at sites surrounding point defects. We also show Auger photoelectron coincidence spectroscopy (APECSS), which combines AES and XPS. APECSS probes simultaneously the energy shifts of two bands: one lower and one upper. We verified that the energy shift of the Auger parameter equals twice that of the upper band rather than the sum of both. Besides, APECSS provides information on interorbital screening and interatomic charge transporting during chemical conditioning of the specimen.

Sections 4–6 present case studies of adatoms, defects, solid skins, chain ends, terrace edges, atomic clusters, adsorbates, and nanocrystals with derivatives of local bond length and energy, BE density, and atomic cohesive energy associated with irregularly coordinated atoms. ZPS purification clarifies why some under-coordinated metals such as Rd adatoms are donor-like and some others such as Pt adatoms are acceptor-like catalysts. Section 7 deals with carbon allotropes including graphene nanoribbons, nanotubes, graphite, and diamond with purification of energy states for graphene edge, graphite point defect, and monolayer skin. This purification clarifies why Dirac–Fermi polaron creation prefers sites surrounding point defects and graphene zigzag edges and why the armchained edges are semiconductor-like.

Section 8 deals with heterojunction interfaces and shows that quantum entrapment dominance makes CuPd an acceptor-like catalyst while the valence polarization dominance makes AgPd and ZnPd acceptor-like. The stronger interface polarization and high energy density enable BeW to protect nuclear thermal radiation effectively. Section 9 addresses the coupling effect of under- and heterocoordination on the band gap, electroaffinity, work function, and photocatalytic ability of defected TiO₂ and ZnO nanocrystals. Defects improve the photocatalytic ability of

TiO₂ by band gap and work function reduction and by carrier life and electroaffinity elevation.

Section 10 concludes with advantages and attainments, limitations and precautions, prospects and perspectives of the present exercise. Extension of this set of strategies to *in situ* monitoring skin and molecular dynamics and to phonon and photon relaxation dynamics could contribute significantly to engineering coordination bonds and valence electrons. Here we use the term of “skin” more often than “surface”, as the former is more appealing with involvement of thickness than the latter. This set of experimental, numerical, and theoretical strategies may lead to a subject area of coordination and multifield resolved spectrometrics of bond–electron–phonon–photon relaxation dynamics. For the readers’ convenience, each section starts with key points synopsizing discussions.

1.2. Overview

1.2.1. Coordination Bonds and Energetic Electrons.

One can create a new substance with desired functionalities by breaking the old bonds and forming new bonds between atoms. Harnessing the known properties of a substance by relaxing the bond and the associated energetics and dynamics of electrons in localization, densification, polarization, and transportation becomes therefore increasingly important.⁸ For instance, materials at sites surrounding irregularly coordinated atoms perform differently from themselves in the bulk interior. Although they are traditionally unwanted, such irregularly coordinated atoms are of key importance to the advancement of condensed matter physics, solid-state chemistry, materials sciences, and device technologies, in particular, at the nanometer scale.¹

Controllable relaxation of the coordination bonds and the energetic electrons at such irregularly coordinated atomic sites provides profound impact to many areas of scientific and technological interest.^{2,3} These areas include, for instance, adhesion,⁹ adsorption,¹⁰ alloy formation,^{11,12} catalytic reaction,^{13,14} corrosion protection,¹⁵ decomposition,¹⁶ diffusion,¹⁷ doping,¹⁸ epitaxial growth,^{19,20} hydrophobic lubrication,²¹ glass formation,²² dielectric modulation,^{23,24} mechanical strength,^{25–28} thermal elasticity,^{29,30} photon and electron emission and transportation,³¹ quantum friction,³² radiation protection,³³ topological insulator conduction,³⁴ superconduc-

tivity,^{35,36} thermal stability,^{37,38} wettability,^{39,40} water and ice skin supersolidity,^{41,42} etc.

Electrons associated with point defects,^{43,44} homogeneous adatoms,⁴⁵ adsorbates,^{5,46,47} terrace edges,^{48–50} monatomic chains and their ends,^{51,52} and solid skins^{53,54} result in, for instance, new types of energy states that enhance tremendously the site-selective catalytic ability of a substance even though the bulk parent, such as gold, is chemically inert. For instance, Figure 1a shows that every third row of Au atoms added to a TiO₂ surface that has already been covered with a full layer of Au atoms could improve the CO oxidation efficiency at room temperature by about 50-fold of the otherwise fully Au-covered surface.⁵⁵ Au particle size reduction raises its CO oxidation ability (Figure 1b) and the ability of guanine binding to the particle.⁵⁶

Likewise, the activation energy for N₂ dissociation is 1.5 eV lower at terrace edges than that at the flat Ru(0001) skin, yielding at 500 K a desorption rate that is at least 9 orders of magnitude higher on edges.⁵⁸ Similar attributes hold for NO decomposition on Ru(0001) skin, H₂ dissociation on Si(100) skin,⁵⁹ and low-temperature nitridation of nanostructurally roughened Fe skins.⁶⁰

Skin roughening forms an effective means of improving the catalytic ability of a substance. The reactivity is 3 orders of magnitude higher for ammonia synthesis at the Re(11̄21) and the Re(11̄20) kink edges than at a smooth Re(0001) skin.⁶¹ An addition of a certain kind of adsorbate roughens skins of Ni(210), Ir(210),⁶² Rh(553), and Re(12̄31)⁶³ to improve their catalytic efficiencies.

Undercoordinated atoms serve as the most active sites in reaction. A few percent of adatoms in a specimen sufficiently raises the reactivity of the specimen in catalytic applications. The edged or faceted atoms account for ~70% of the total catalytic activity of the medium. The even-undercoordinated adatoms on Rh(111) skin favor the process of methane dehydrogenation more than atoms at steps or at the terrace edges.^{64,65} Adatoms deposited on oxides can activate the C–H bond scission,⁶⁶ acetylene cyclomerization,⁶⁷ and CO oxidation.⁶⁸ The catalytic efficiency of the undercoordinated atoms increases as their coordination numbers (CNs) decrease. The efficiency further increases when the undercoordinated atoms grow heterocoordinately on oxide supports.

Besides atomic undercoordination, strain generation by defect formation, by implantation, or by substrate–particle interaction can also enhance the surface catalytic ability.⁶⁹ Argon plasma implantation into the Ru(0001) subsurface stretches the lattice, which promotes adsorption of O and CO^{70,71} and enhances the NO dissociation probability in the stretched regions.⁷² Adsorption of small clusters can induce a considerable strain in the skin and improve the catalytic ability of the clusters, demonstrating the joint effect of bond strain and atomic undercoordination.⁷³

The extremely high catalytic efficiency of undercoordinated atoms is indeed fascinating, but the fundamental nature behind the efficiency elevation remains unclear. The following addresses the most advanced yet hypothetical mechanisms on the catalytic ability of gold adatoms:^{55,74}

1. Gold adatoms have fewer nearest neighbors and possibly a special yet unclear bonding geometry that creates more reactive orbits compared to the otherwise fully coordinated atoms.

2. They exhibit quantum size effects that may alter the energy band structure of nanoparticles.

3. They may undergo electronic modification by interacting with the underlying oxide that causes partial electron donation to the atomic clusters.

Therefore, comprehension of the catalytic ability due to undercoordination from the perspective of local bond relaxation and the associated electronic energetics, i.e., entrapment or polarization, is of importance.

Performance of the heterocoordinated atoms of alloys, dopants, embedded nanocrystals, impurities, and interfaces is another subject area of extensive study. Interfacial bond formation perturbs the local Hamiltonian, BE density, and atomic cohesive energy, associated with local charge entrapment or polarization, which determine the catalytic, electronic, dielectric, optic, mechanical, and thermal properties of the interface. Atomic heterocoordination makes the interface region completely different from those of the constituent parents.^{75,76}

Mixing two or more substances together forms an interface that performs differently from the respective constituent.^{77,78} One can modify bond strain and charge distribution surrounding the bonded atoms^{79,80} by varying compositions or by thermal annealing upon continuous deposition of dissimilar metals.^{81,82} For instance, Ag or Cu atoms can pair with Pd atom to form alloys with improved heterogeneous catalysts⁸³ meeting different needs.⁸⁴ CuPd is active for CO and alkene oxidation, ethanol decomposition, and CO, benzene, toluene, and 1,3-butadiene hydrogenation. Pd atom is active for CO oxidation, while Cu is active for NO dissociation. AgPd alloy is a good candidate for reduction or hydrogen reaction and permeation.⁸⁵ Both Ag and Cu grow on Pd in a layer-by-layer fashion at room temperature. Annealing at certain temperatures turns the layered structures into alloys.^{81,86} Reaction with electronegative elements such as F, O, N, C, etc., turns a metal into a semiconductor or into an insulator. Dispersion of an individual Ir atom enhances greatly the reducibility of FeO_x, leading to the single-atom Ir/FeO_x catalyst.⁸⁷

As the wall material in a fusion device, BeW alloy efficiently protects nuclear radiation in the International Thermonuclear Experimental Reactor (ITER).^{88–92} Due to the electronic structure difference between W and Be, a strong influence of alloying on both the core and the valence electrons and the interfacial energy may happen, but verification and quantification of this expectation remains unrealistic. Understanding the nature of the bond and the behavior of the energetic electrons at the alloying interface is crucial to designing such functional materials for nuclear radiation protection and catalysis application, particularly.

Therefore, experimental distillation of the atomistic, local, dynamic, and quantitative information and theoretical clarification of the physical origin regarding the bonding and electronic relaxation dynamics at the irregularly coordinated atomic site are of paramount importance to advancing heterocoordination chemistry and undercoordination physics.

1.2.2. Challenges Faced by Existing Methods. Formation of a bond between heterocoordinated atoms and relaxation of a bond between undercoordinated atoms and the associated electron entrapment and polarization mediate the performance of a substance at these irregularly coordinated atomic sites.⁸ However, resolving such atomistic, dynamic, local, and quantitative information is beyond the scope of currently available techniques though the invention of STM/S has advanced surface science enormously. STM/S maps surface electrons with energy of a few electronvolts crossing E_F.⁹³ For instance, atomic vacancies at a graphite (0001) skin⁴⁸ and at the

zigzag edge of a graphene exhibit the same topological and the same Fermi resonant attributes.⁹⁴ The resonant states, named “Dirac fermions”, serve as carriers for topological insulators.^{34,95} The Dirac fermions that are almost massless with nonzero spin and infinitely large group velocity contribute to the anomalous quantum Hall effect.

STM also probed the “checkerboard”-like protrusions from Cu(100)–O[−] surface⁹⁶ that evolve subsequently into the “dumbbell”-like protrusions when the O[−] adsorbate transits into the O^{2−} state.⁹⁷ The latter exhibits the characteristic antibonding density of states (DOS) featured at +2.0 eV above E_F and the nonbonding states at −2.1 eV below.⁹⁸ The former corresponds to polarization of Cu^p dipoles, and the latter corresponds to the electron lone pair of O^{2−}; see ref 5.

STM/S probed the volume expansion and electron polarization for Au atoms at ends of the monatomic chain,⁵² for Ag atoms added on Ag(111) skin,⁹⁹ and for Cu atoms added on Cu(111) skin.¹⁰⁰ However, using STM/S alone, one can hardly elucidate quantitatively how the local chemical bond relaxes to provide forces driving the STM/S features.

In contrast, a photoelectron spectroscopy (PES, such as UPS and XPS) collects statistic and volumetric information on electron BE in the valence band and below within a nanometer-thick skin.^{101–106} One can hardly discriminate the contribution of the skin from that of its bulk mixture. The effect of atomic undercoordination and bond nature alteration in chemisorption dominates at most the outermost four atomic layers.^{1,3,5,46,107}

Experimental conditions create artifacts in measurements. Varying the incident beam energy or the polar angle between the incident light or emission electron beam and the surface normal during a PES experiment also modulates the spectral peak energy and intensity. The intensity of the high-energy component (close to E_F) often increases with the incident beam energy or with the decrease of the polar angle (close to the surface normal).^{108–112} For instance, at the same polar angle, the intensity of the Rh 3d_{5/2} peak at 306.42 eV (bulk) increases more than that of the 307.18 eV (skin) component when the beam energy is increased slightly from 370 to 380 eV.¹¹³ At the same beam energy, the intensity of the Rh(111) skin component at 307.18 eV reduces when the polar angle reduces from 35 to 20°.¹¹⁴ Experimental artifacts also include the charging effect and the ionization, initial–final state relaxation that exist throughout the course of measurements.

XPS profiles of Nb(100),¹⁰⁸ Tb(0001),¹¹⁰ Al(100),^{115,116} Ta(100),¹¹² and Be skins^{117–120} follow the same polar angle and beam energy dependency. At higher beam energies or at smaller emission angles, the incident beam excites more electrons from deeper layers compared with otherwise.⁶ Thus, one can discriminate the contribution of the skin from that of the bulk readily by varying the beam energy or the emission angle though the derived information was qualitative.

Strikingly, the 2p energy of a Si diode shifts significantly during its operation under both forward and reverse bias^{121,122} or under high frequency charging and discharging.^{123,124} Photon illumination also enhances the Si 2p energy shift.¹²⁵ This approach traces potential variation due to concentration and location of doping as the BE shifts when the magnitude and the polarity of the applied bias changes.

Since the advent of the third generation synchrotron light sources providing soft X-rays up to 2 keV, XPS becomes a powerful tool for studying surface chemical and physical properties at an unprecedented precision level. The high resolution allows for identifying various surface species, and for small molecules, and even for the vibrational fine structures.¹²⁶

The near ambient pressure XPS mimics the ambient environment for examining the chemical effect on the core band shift of a substance such as gold.¹²⁷ The liquid microjet PES and ultrafast liquid jet UPS provide electron binding energy information for skins of liquid water and droplets.^{128,129}

However, what one can measure using a PES are the convoluted peaks of the core bands contributing from intraatomic trapping, interatomic binding, crystal orientation, defect vacancy, surface relaxation, nanosolid formation, surface passivation and adsorption, with the mixture of bulk information. An XPS spectral peak contains often multiple components of energy shift with uncertainty of their separation, direction, component height and width, and reference point from which these shifts proceed.

Based on the conventional exercises of spectral decomposition analysis, for instance, one can hardly discriminate the contribution of adatoms from that of the skin or the bulk to the PES spectrum with little information regarding the relaxation dynamics of the local bonds and the energetic electrons pertaining to adatoms. Combining the most advanced laser cooling and XPS technologies, one can only measure the energy separation between two levels of the slowly moving gaseous atoms of lower bulk melting point. Therefore, discriminating contributions of different sublayers or contributions of crystal orientations from those of the bulk and separating the contribution of the interatomic interaction from that of the intra-atomic interaction to the spectrum remains a challenge. Determination of the individual energy level of an isolated atom and its shift with coordination and chemical environment remains as a “bottleneck” in this field of study.¹³⁰

The valence DOS profile provides direct information about charge transportation during reaction from one constituent to the other (ionization), polarization, and entrapment of valence charge, which evolves the interatomic potentials from the initial form due to screening and splitting effect.⁵ Understanding valence DOS evolution requires proper models to relate the valence DOS change to the dynamics of bond formation and bond relaxation. Analyzing the valence DOS shift is much more complicated than analyzing the core-band shift as the latter simply fingerprints the BE change of a particular energy level of a specific element.⁵

Quantum computation using density function theory (DFT) can resolve the local valence DOS with optimization of crystal geometries and interatomic distances.^{131,132} However, the accuracy and reliability of the computational derivatives are often algorithm and boundary condition sensitive.¹³³ Employing the ideally periodic or the free boundary condition deviates the calculation outcome from the true situations to a certain extent. Structural distortion happens at boundaries associated with local strain, charge densification, polarization, and quantum entrapment. These happenings in turn modify the local potentials that shift the electronic BE accordingly.²

1.2.3. Known Mechanisms. Understanding the effect of ill coordination on the core level shift (CLS) and valence band evolution has been an issue of long debating from various hypothetical mechanisms through formulation and quantification of the CLS remains unrealistic in most cases:

1. The “initial–final state” relaxation, core-hole screening, and atomic covalency effect has been a long dominant mechanism for the CLS of both solid skins^{109,110,134,135} and metal particles.¹³⁶ The initial–final state notion suggests that irradiation of the incident energetic beam ionizes the initially neutral surface atom into the finally ionized one. The ionized atom becomes a “Z + 1

impurity" sitting on the substrate of Z metal atoms. The difference in cohesive energy between the Z atom and the $Z + 1$ impurity amounts to the CLS by $\text{BE} = E_{Z+1}(\text{final}) - E_Z(\text{initial})$. The CLS may be negative, positive, or their mixture depending on the Z value that is tunable in computation. However, correlation between the effective Z and the coordination and chemical environment remains yet unknown.

2. Another opinion is the skin interlayer contraction that creates the low-energy CLS component.^{6,108,112} A 12% contraction of the first layer spacing deepens the Nb(100) $3d_{3/2}$ level by 0.50 eV,¹⁰⁸ and a $(10 \pm 3)\%$ contraction of the Ta(100) first layer spacing deepens the $4f_{5/2(7/2)}$ level by 0.75 eV.¹¹² Interlayer charge densification might enhance the incident light resonance, which results in the positive CLS, according to this mechanism.

3. Electronic configuration variation (the distribution of electrons among s, p, and d orbits) mechanism^{137–140} suggests that the chemical shifts and the structural relaxations contribute to the atom–bulk CLS. The narrowing and shifting of the surface DOS is responsible for the CLS.^{135,141}

4. A metal-to-nonmetal transition mechanism explains that this transition shifts positively the CLS for nanocrystals.^{140,142,143} However, the metal–nonmetal transition takes place only in the size range of 1–2 nm diameter consisting of 300 ± 100 atoms^{144,145} but the CLS extends continually when an isolated atom grows into the bulk.¹⁴⁶

5. Mechanisms of charge transfer between dissimilar metals of an alloy,¹³⁹ size-enhanced ionicity of copper and oxygen,¹⁴⁷ and dipole formation between the substrate and the particles¹⁴⁸ explain the heterocoordination-induced CLS. The density and the momentum of dipoles might increase with reduction of particle size. Surface oxygen vacancy formation provides possible mechanism for the O-coverage-dependent CLS of Au on the MgO(100) and on the TiO₂(110) support.¹⁴⁹

6. Surface electron structure and the increase of the effective size of surface O anions¹⁵⁰ are suggested to be responsible for the 0.75 eV positive shift of the Mg 2p energy and the constant O 1s level for the MgO(100) skin.

7. Recent development^{6,7,151,152} suggests that atomic ill coordination perturbs the Hamiltonian that determines intrinsically the CLS and the amount of the CLS is proportional to the bond energy or the crystal potential at equilibrium. Bond contraction and bond energy gain deepen the CLS for undercoordinated systems such as atomic clusters, defects, and solid skins. Bond nature alteration determines the CLS for heterocoordinated systems such as alloys, interfaces, dopants, embedded nanocrystals, and impurities. Polarization of electrons splits and screens the local potentials, which shifts CLS negatively. Therefore, CLS could be positive, negative, or their mixture.

8. However, rules for the ill coordination mediated valence DOS remain unclear. The valence charge densification, localization, polarization, and transformation upon alloy and compound formation mediate the performance of the substance such as the band gap, catalytic ability, electroaffinity, work function, etc. The valence DOS evolution and the CLS are strongly correlated. Therefore, a holistic exploration of both of them with quantitative derivative is necessary.

1.3. Motivation and Objectives

Resolving the coordination-resolved, dynamic, local, and quantitative information regarding the performance of bonds and electrons of the irregularly coordinated atoms remains as a

"dead corner", though the interplay of STM/S, PES, and DFT has advanced this subject area tremendously. Bond formation and relaxation and the associated energetics, localization, entrapment, and polarization of electrons mediate the electronic binding energy and the performance of a substance accordingly.⁸ Therefore, one urgently needs to identify what the "seed" of the STM/S attributes is and how the length and strength of the nearby bonds relax, which forms the subject of the presented electron spectrometrics for the irregularly coordinated atoms, particularly.

This report aims to feature the recent progress in the development and applications of the coordination-resolved bond and electron spectrometrics with focus on the following:

- to combine the BOLS–NEP–TB notion¹³² with the enabled ZPS⁷ and APECS strategies toward comprehensive and quantitative information regarding bond and electron relaxation
- to clarify rules and factors controlling the CLS and valence DOS evolution
- to correlate the STM/S, PES, and AES attributes of a substance
- to formulate the CLS dependence on local bond relaxation, quantum entrapment, and polarization
- to quantify the local bond length, bond energy, BE density, atomic cohesive energy, and energy level of an isolated atom and its CN-resolved shift pertaining to irregularly coordinated atoms

The consistent outcome made so far is very promising. It is clear that perturbation to the Hamiltonian by bond contraction, bond nature alteration, and electron polarization dictates intrinsically and uniquely the energy shift entrapment or polarization. The extent of entrapment is proportional to the local bond energy at equilibrium. Polarization of the nonbonding states by the densely locally entrapped bonding electrons or by nonbonding lone pair screens and splits the crystal potential, which in turn offsets the entrapped states negatively.

Most strikingly, entrapment dominance entitles Pt adatom and CuPd alloy acceptor-type catalysts while polarization dominance makes Rh adatom and AgPd alloy donor-type catalysts. Isolation and polarization of the dangling σ bond electrons by the entrapped bonding electrons create Dirac–Fermi polarons surrounding graphite atomic vacancies and graphene zigzag edges.

Extension of the electron spectrometrics to the coordination-resolved phonon and photon relaxation dynamics of a substance under multifield would be even more appealing, fascinating, promising, and rewarding.

2. THEORY: BOND–ELECTRON–ENERGY CORRELATION

In this section, we discuss the following:

- Intra-atomic potential determines the energy levels of an isolated atom, from which the CLS proceeds.
- Interatomic potential governs the CLS whose extent is proportional to the bond energy at equilibrium.
- Atomic irregular CN shortens and strengthens the local bond, which densifies local charge, deepens potentials, and shifts the CLS positively.
- The densely and locally entrapped core electrons polarize nonbonding electrons, which in turn splits and screens the local potential and then offsets the entrapped CLS negatively.

Table 1. Classification, Origin, Annotation, and the Size Dependency and Size Emergency of Possible Properties of Substances at the Nanoscale, Edges, Skins, and Interfaces (with Potential Trap or Barrier Formation)^a

Tetrahedral CN (C, N, O, F)	Isolated atom	Atomic chain, sheet, tube, wire, dot, skin, nanocrystal, ...	Ideal bulk	Interface/Impurity
Interaction	0	1	1	1
Atomic CN	0	<12 (under)	12 (full)	Hetero
Notions	<ul style="list-style-type: none"> Interaction between undercoordinated atoms differs in nature nanostructures from an isolated atom or the bulk in performance. Bond between undercoordinated atoms becomes shorter and stronger. Defects, skins, adatoms, nanostructures of various shapes share the same attribute. Skin atoms/bonds dictate size dependency of nanocrystals in various properties. Interface potential barrier/trap formation results in local entrapment and/or polarization. 			
Electronic behavior	<p>Atomic ill coordination causes local bond relaxation or bond nature alteration, which results in local quantum entrapment of core electrons and polarization of nonbonding electrons.</p> <p>The energetic behaviors of bonds and electrons mediate the BE shift and the functionalities of a substance.</p>			

^aReprinted with permission from ref 8. Copyright 2014 Springer.

2.1. Atomic Coordination Classification

Table 1 classifies the atomic coordination of a substance and the possible properties. Atomic undercoordination means an atom with fewer neighbors than the bulk fcc standard of $z_b = 12$. For an isolated atom, $z = 0$, which happens only at 0 K ideally¹⁵³ or in the gaseous phase. Undercoordination ($0 < z < 12$) is ubiquitous to adatoms, defects, terrace edges, grain boundaries, solid skins, and skins of nanostructures of various shapes. Monatomic chains and monolayer atomic sheets are ideal cases of one- and two-dimensional undercoordination systems exhibiting tremendously revolutionary properties.⁸

Heterocoordination means an atom with different kinds of neighbors such as alloys, compounds, dopants, impurities, and interfaces. The A–B type exchange interaction will come into play in addition to the A–A and B–B type potentials for an AB alloy. If one specimen, such as amorphous glasses, contains n constituents, there will be $n!/(2!(n - 2!))$ types of interatomic interactions. New bond formation and bond nature alteration modify locally the Hamiltonian with the addition of such exchange interaction terms.

Tetrahedral coordination refers to sp^3 -orbital hybridization of C, N, O, and F upon interaction with atoms of a less electronegative element. This configuration creates four valence states of bonding, nonbonding lone pair, electron–hole pair, and antibonding dipole,^{5,46} which turns a metal into semiconductor or insulator and expands the band gap of a semiconductor.

2.2. Core Band Energy Dispersion

The following single-body Hamiltonian and eigen wave function describe an electron moving in the ν th orbit of an atom in the ideal bulk.⁴

$$H = H_0 + H' \quad (1)$$

with

$$H_0 = -\frac{\hbar^2 \nabla^2}{2m} + V_{\text{atom}}(r)$$

(total energy for an electron of an isolated atom)

$$H' = V_{\text{cryst}}(r) \quad (\text{interatomic interaction})$$

$$|\nu, i\rangle \cong u(r) \exp(ikr) \quad (\text{Bloch wave function})$$

H_0 is the Hamiltonian for an isolated atom, which sums the kinetic energy and the intra-atomic potential energy experienced by the specific electron. The interatomic potential $V_{\text{cryst}}(r)$ sums all interactions with neighboring atoms and electrons. The $V_{\text{atom}}(r) = V_{\text{atom}}(r + R) < 0$, the $V_{\text{cryst}}(r) = V_{\text{cryst}}(r + R) < 0$, and the wave functions are periodic in real space, where R is the lattice constant. Because of the localization nature of the core electrons, the eigen wave function $|\nu, i\rangle$ meets the following criterion, where i and j denote atomic positions:

$$\langle \nu, j | \nu, i \rangle = \delta_{ij} = \begin{cases} 1 & (i = j) \\ 0 & (i \neq j) \end{cases}$$

The energy of an electron in an ideal bulk disperses in the following way (with atomic CN or $z_b = 12$ for an fcc-structured bulk standard):

$$E_\nu(z_b) = E_\nu(0) + (\alpha_\nu + z_b\beta_\nu) + 2z_b\beta_\nu\Phi_\nu(k, R) \quad (2)$$

with

$$E_\nu(0) = -\langle \nu, iH_0|\nu, i \rangle \quad (\text{atomic core level})$$

$$\alpha_\nu = -\langle \nu, iH'|\nu, i \rangle \propto E_b \quad (\text{exchange integral})$$

$$\beta_\nu = -\langle \nu, iH'|\nu, j \rangle \propto E_b \quad (\text{overlap integral})$$

The $V_{\text{atom}}(r)$ defines the energy level of an isolated atom $E_\nu(0)$, from which the core band shifts. As intrinsic constants, $E_\nu(0)$ reduces its value with the quantum number ν from 10^3 to 10^0 eV until the vacuum level $E_0 = 0$ as the ν increases, or as one moves from the most inner orbit outwardly of an atom.

The CLS fingerprint variation of interatomic interaction changes with chemical and coordination environment. The involvement of the $V_{\text{cryst}}(r)$ upon bulk or liquid formation deepens the $E_\nu(0)$ by an amount of $\Delta E_\nu(z_b) = E_\nu(z_b) - E_\nu(0) = \alpha_\nu + z_b\beta_\nu$, and, meanwhile, turns the CL into a band of $E_{\nu W} = 2z_b\beta_\nu\Phi_\nu(k, R)$ width. Both the exchange integral α_ν and the overlap integral β_ν are proportional to the cohesive energy per bond at equilibrium, E_b , or the zeroth approximation of the crystal potential in a Taylor series. The term $\Phi_\nu(k, R) \cong \sin^2(2\pi r/R) \leq 1$, for the fcc structure instance, is a distribution function.

The exchange integral dominates the CLS. Typically

$$\begin{aligned} \Delta E_\nu(z_b) &= \alpha_\nu + z_b\beta_\nu = \alpha_\nu(1 + z_b\beta_\nu/\alpha_\nu) \\ &\propto E_b(1 + E_{\nu W}/2E_b) \\ &\approx 3.0(1 + 0.2/6.0) = 3.0(1 + 3\%) \end{aligned}$$

The 3% contribution from the overlap integral to the CLS is negligibly small. For the deeper bands, this ratio is even smaller. Thus, the bond energy E_b dominates the bulk CLS in the first order approximation. Any relaxation of the interatomic bond changes directly the $E_{\nu W}$ and the CLS accordingly.

Atomic ionization by X-ray radiation or by the charging effect modifies the crystal potential throughout the course of measurements, which serves as a removable background in calibration. In fact, the charging effect exists only for thick insulating samples in measurements because of the non-conductive character of the specimen. The charging effect for conductors or thinner insulators becomes negligible.¹⁵⁴ The charging effect can be minimized by grounding the specimen.^{8,155} The electronic multibody interaction also serves as an average background as it exists throughout the specimen in question.

The component width $E_{\nu W} = 2z_b\beta_\nu\Phi_\nu(k, R) \propto z_bE_b$ is proportional to the atomic cohesive energy. As illustrated in Figure 2a, if one moves from the valence band downward, the $\Delta E_\nu(z_b)$ will turn from 10^0 to 10^{-1} eV and the $E_{\nu W}$ approaches lines for the spin-resolved energy levels, such as the $1s$, $2p_{1/2}$, and $2p_{3/2}$ of Cu. Occupation of the core band often approximates the Gaussian or the Lorentz function in decomposing the spectrum Figure 2b.

2.3. BOLS-NEP-LBA Notion

2.3.1. Local Hamiltonian Perturbation. Atomic CN is the primary variable determining the CLS for undercoordinated systems. Any change of the CN will relax the bond in length and

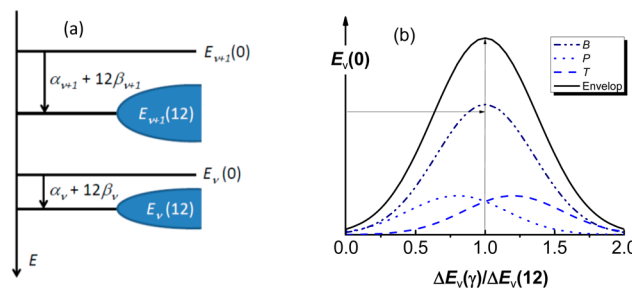


Figure 2. (a) Evolution of the ν th atomic energy level $E_\nu(0)$ to the band $E_\nu(z_b=12)$ with a shift of $\Delta E_\nu(z_b) \propto E_b$ and an expansion $E_{\nu W}(z_b) \propto z_bE_b$ of the ν th band upon bulk formation. Artifacts in measurements and charge polarization may modify the amounts of BE shift and the width of the components but not the nature of origin. (b) A typical XPS spectrum shows components of entrapment (T), polarization (P), and the bulk (B). Reprinted with permission from ref 156. Copyright 2006 American Physical Society.

energy accordingly, which perturbs the $V_{\text{cryst}}(r)$. Possible factors of perturbation include the following:

- undercoordination induced bond contraction, charge densification, localization, entrapment, and polarization
- heterocoordination induced bond nature alteration, bond relaxation, entrapment, or polarization
- radiation induced “initial–final state” relaxation during experiment
- external bias caused charge accumulation of the tested specimen
- mechanical or thermal field induced bond relaxation in length and energy

The zeroth approximation of the interatomic potential dictates the CLS. Figure 3a illustrates that bond length and energy (d, E) relax along the modulation function $f(x)$ under a certain stimulus x such as the atomic CN, mechanical, or thermal excitation. A Taylor series approximates the pairing potential $u(r)$:

$$\begin{aligned} u(r) &= \frac{\partial^n u(r)}{n! \partial r^n} \Big|_{r=d} (r-d)^n = E_b + \frac{\partial^2 u(r)}{2 \partial r^2} \Big|_{r=d} (r-d)^2 \\ &+ \frac{\partial^3 u(r)}{6 \partial r^3} \Big|_{r=d} (r-d)^3 + O((r-d)^{n \geq 4}) \end{aligned} \quad (3)$$

The zeroth differential (d, E_b) at equilibrium dominates the BE shift uniquely. The second-order differential corresponding to harmonic vibration of the atomic pair determines the shape of the $u(r)$ only. The higher-order nonlinear terms contribute to transport dynamics such as lattice expansion and heat conductivity. Bond relaxation refers to the response of the coordinates (d, E_b) at equilibrium to external stimulus such as pressure, temperature, coordination, and chemical environment.⁸

The $V_{\text{cryst}}(r)$ experienced by the electron is the sum of $u(r)$ over all nearest neighbors. For the irregularly coordinated systems, one needs to consider the local perturbation to the crystal potential from $V_{\text{cryst}}(r)$ to $V_{\text{cryst}}(r)(1 + \Delta_H) \cong E_b(1 + \Delta_H)$ without needing perturbation to the wave function or the high-order vibration terms.

The perturbation shifts the CL positively if $\Delta_H > 0$ or negatively if $\Delta_H < 0$. The former is the quantum entrapment (T) and the latter is polarization (P). A mixed shift is possible if both the T and the P contribute competitively. Perturbation turns eq 1

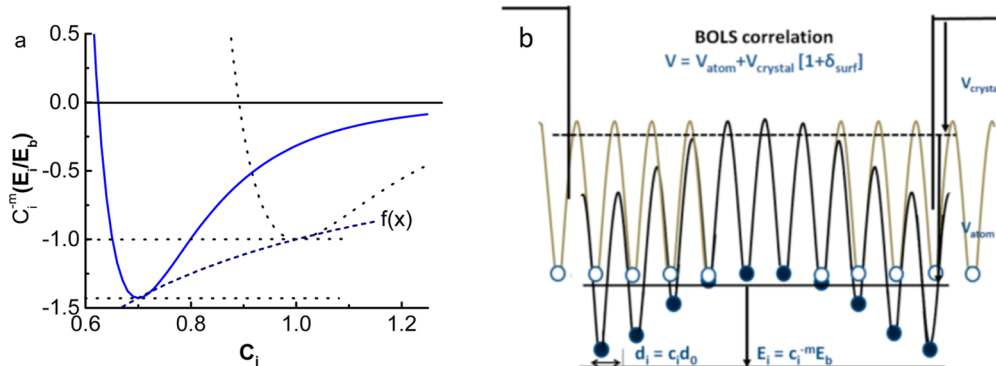


Figure 3. Potentials of a dimer bond relaxing under external stimulus. (a) Coordinate valley of the pairing potential $u(r)$ correspond to bond length and energy (d, E) that relax along the modulation function $f(x)$ under stimulus x (x can be pressure, temperature, coordination environment, etc.). (b) Bond order loss shortens and strengthens bonds between undercoordinated atoms at the bonding network terminals such as sites of defects and skins of nanocrystals, which cause local densification and entrapment of the bonding electrons, and polarization of nonbonding electrons. Reprinted with permission from ref 157. Copyright 2001 IOP Publishing Ltd.

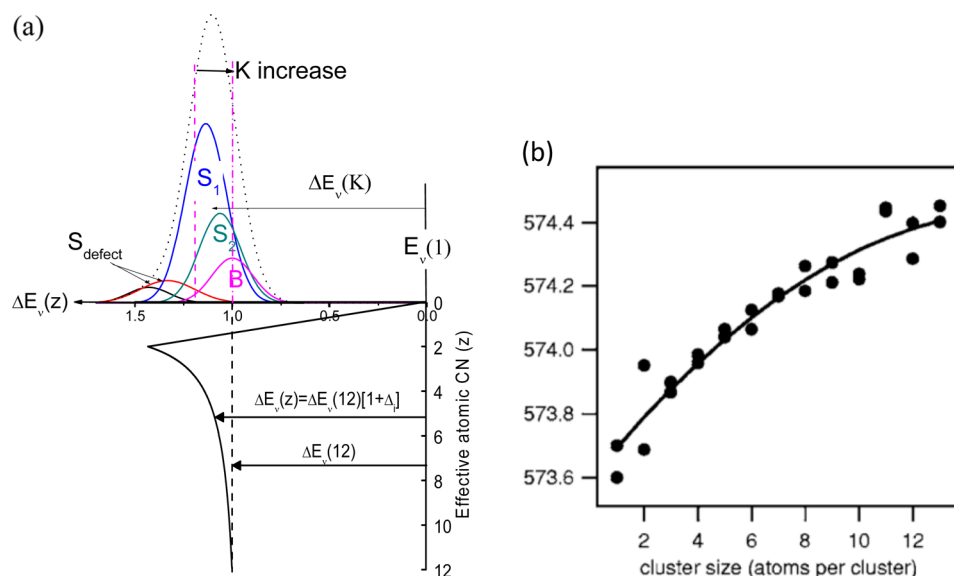


Figure 4. (a) Cluster size (K) or atomic CN resolved CLS. (b) The number-of-atom dependence of the Cr_z cluster 2p energy shift from 537.5 eV for an isolated Cr atom to E_{2p} ($n = 13$) = 574.4 eV for $z = 2$,¹⁶² follows the BOLS prediction in the $z \leq 2$ regime of (a). Reprinted with permission from ref 162. Copyright 2005 American Physical Society. Reprinted from ref 164. Copyright 2009 American Chemical Society.

into the following by replacing the z_b with x representing the effect of atomic CN(z) variation or polarization P:

$$\begin{aligned} H' &= V_{\text{cryst}}(r)(1 + \Delta_H) \\ E_\nu(x) &= E_\nu(0) + \alpha_{\nu x}(1 + x\beta_{\nu x}/\alpha_{\nu x}) + 2x\beta_{\nu x}\Phi_\nu(k, R) \end{aligned} \quad (4)$$

with

$$E_\nu(0) = -\langle \nu, iH_0|\nu, i \rangle \quad (\text{atomic core level})$$

$$\alpha_{\nu x} = -\langle \nu, iH'|\nu, i \rangle \propto E_b(1 + \Delta_H) \propto E_x \quad (\text{exchange integral})$$

$$\beta_{\nu x} = -\langle \nu, iH'|\nu, j \rangle \propto E_b(1 + \Delta_H) \propto E_x \quad (\text{overlap integral})$$

Perturbation mediates only the integrals without any influencing on the $E_\nu(0)$.

2.3.2. Atomic Undercoordination: BOLS–NEP.

2.3.2.1. BOLS Notion. According to the BOLS correlation premise,^{1,8} bond order loss shortens and strengthens bonds between undercoordinated atoms, as illustrated in Figure 3b. Bond contraction densifies the local bonding charge, binding energy, and mass; bond strength gain deepens the potential well and shifts the energy levels accordingly. The following formulates the BOLS notion:

$$\begin{aligned} C_z &= d_z/d_b = 2\{1 + \exp[(12 - z)/(8z)]\}^{-1} \\ &\quad (\text{bond length}) \\ C_z^{-m} &= E_z/E_b \quad (\text{bond energy}) \\ C_z^{-(m+\lambda)} &= (E_z/d_z^\lambda)/(E_b/d_b^\lambda) \quad (\text{energy density}) \\ z_{ib}C_z^{-m} &= zE_z/(z_bE_b) \quad (\text{atomic cohesive energy}) \end{aligned} \quad (5)$$

The bond nature index correlates the bond energy to its length of a specific substance. $\lambda = 1$ defines a monatomic chain and $\lambda = 2$ defines the monatomic sheets or single walled nanotube. $\lambda = 3$ is

the general case of a three-dimensional solid. The C_z is universal to match the CN-resolved atomic distance of carbon nanotubes, Au nanoparticles, Au, Pt, Ir, Ti, Zr, and Zn atomic chains, as well as skins of Fe, Ni, Ru, Re, W, and diamond.^{1,3}

The BOLS notion also defines the CN dependence of the reduced bond length d_z , bond energy E_z , BE density E_D , and atomic cohesive energy E_C at the irregularly coordinated atomic site in a dimensionless form. These quantities are the key to the behavior of a substance at these irregularly coordinated atomic sites as they link the local atomistic bonding identities to macroscopic properties, such as adhesion ability, diffusivity, elasticity, reactivity, strength, wettability, etc.

2.3.2.2. NEP Notion: Strong Localization. Conversely, the densely, locally entrapped bonding and core electrons in turn polarize the nonbonding electrons of the undercoordinated rim atoms.^{2,158} The polarized states (P) in turn screen and split the local potential that offsets the entrapped core bands negatively. Negative CLS may not happen if the specific CL is too deep or the extent of polarization is insufficiently high. Therefore, it is not surprising that some materials show positive and some others show negative or mixed CLS.⁶

However, the polarization is subject to the availability of nonbonding electrons.^{1,2} The nonbonding electrons refer to those composed of dipoles induced by the lone pairs of O, N, and F, the unpaired dangling bond of C and Si at defect edges, and the otherwise conduction electrons of metals at undercoordinated atomic sites. The polarization raises the nonbonding states in energy toward or cross over the E_F .² Such CN-resolved local bond strain, electron densification, entrapment, polarization, and its effect on potential screening and splitting exemplify the “strong localization and strong correlation” premise of Anderson et al.¹⁵⁹ to the irregularly coordinated systems including amorphous glasses.¹⁶⁰

Figure 4a illustrates the CLS as a function of cluster size or the effective atomic CN. If the solid grows from an isolated atom to a solid of infinitely large size, the CL peak shifts along the line in the lower part of Figure 4a. Measurements^{1,161,162} confirmed that when the solid grows from an isolated atom the BE of the ν th level deepens from the initial $E_\nu(0)$ level sharply to a maximum at $z = 2$ and then restores gradually in a K^{-1} fashion to the bulk $E_\nu(12)$,¹ as the atomic CN increases.¹⁶² The $z = 2$ corresponds to the effective CN for an atom in an fcc unit cell or in the monatomic chain. The size resolved 2p level shift of Cr_n ($n = 2 - 13$) clusters (Figure 4b) does follow the $z \leq 2$ prediction,¹⁶² and the number-of-layer resolved C 1s shift of graphene follows the $z > 2$ size trend.¹⁶³

2.3.2.3. Point Defect and Monolayer Skin. For a point defect or a solid skin, one needs only consider the relaxation of one representative bond for all under the same coordination environment. Incorporating eq 5 into eq 4 yields

$$\frac{\Delta E_\nu(z)}{\Delta E_\nu(12)} = (1 + \Delta_{Hz}) = \frac{E_z}{E_b} = C_z^{-m}$$

$$\Delta E_\nu(z \geq 2) = \Delta E_\nu(12)(1 + \Delta_{Hz}) = [E_\nu(12) - E_\nu(0)]C_z^{-m} \quad (6)$$

Figure 5a illustrates the layer-counting premise of a solid skin composed of three atomic layers with adatoms or vacancy defects. Figure 5b shows the respective CLS components in the XPS spectrum. According to the BOLS–NEP notion, adatoms (A), surface skins (S_1, S_2, \dots), bulk (B), and electron polarization (P) shift their binding energies each by an amount in the order

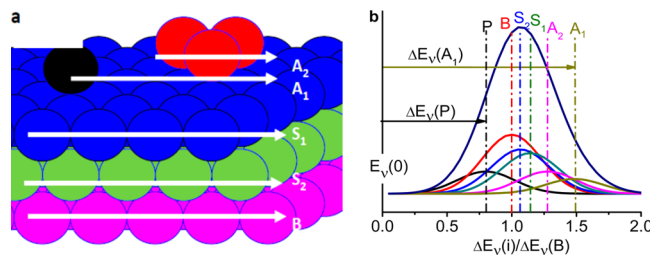


Figure 5. Atomic CN-resolved CLS. (a) Adatoms or defect vacancies, A_i , form on the bulk B crystal, which create the corresponding component in the CLS spectrum (b). In addition to the main peaks of B, S_1 , and S_2 , there are A_i and P components representing the entrapped and the polarized states of the undercoordinated atoms. The energy shift of each component is proportional to the bond energy, which follows the relationship $\Delta E_\nu(z_i)/\Delta E_\nu(12) = E_{z_i}/E_{z_b} = C_z^{-m}$ ($i = A, S_1, S_2$), if the polarization effect is insignificant; otherwise, the pC_z^{-m} replaces the C_z^{-m} with p being the polarization coefficient.

$\Delta E_\nu(A) > \Delta E_\nu(S_1) > \Delta E_\nu(S_2) > \Delta E_\nu(B) > \Delta E_\nu(P)$ with respect to the $E_\nu(0)$ reference. The component for the least coordinated adatom ($z = 2$) shifts the most.

2.3.2.4. Atomic Cluster and Nanocrystal: BOLS–LBA. For crystals of different sizes, one has to consider the sum over the outermost three atomic layers based on the LBA approach and the core–shell configuration premise.³ The Fourier transformation principle inspires the LBA, which indicates that, for a given specimen, no matter whether it is a crystal, noncrystal, with or without defects, the nature and the total number of bonds remain unchanged unless phase transition occurs. However, the length and strength of all the involved bonds will respond to the applied stimulus simultaneously. Therefore, one can focus on the length and energy response of the representative bond to the external stimulus and its effect on the CLS for the entire solid.

However, the hydrogen bond (O:H–O) in water and ice is an exception.¹⁶⁵ Because of the asymmetrical and short-range interaction, the O:H nonbond and the H–O covalent bond segment relax oppositely in length and energy. The stronger H–O bond (4.0 eV level) dictates the CL as the weaker O:H nonbond (0.1 eV level) contributes only 3% or less to the crystal binding energy.

Generally, the experimentally observed size (K), shape (τ), and bond nature (m) dependence of the $\Delta E_\nu(\tau, K, m)$, of a nanosolid follows a scaling relation based on the core–shell configuration:

$$\frac{\Delta E_\nu(K) - \Delta E_\nu(12)}{\Delta E_\nu(12)} = \begin{cases} bK^{-1} & (\text{experiment}) \\ \Delta_H & (\text{theory}) \end{cases} \quad (7)$$

with

$$\Delta_H = \sum_{i \leq 3} \gamma_i (\Delta E_{z_i}/E_{z_b}) = \sum_{i \leq 3} \gamma_i (C_{z_i}^{-m} - 1)$$

(skin resolved perturbation)

$$\gamma_i = N_i/N = V_i/V = \tau K^{-1} C_i \leq 1 \quad (\text{fraction of skin atoms})$$

As the dimensionless form of size, K is the number of atoms lined along the radius of a spherical dot ($\tau = 3$), or a cylindrical rod ($\tau = 2$), or across the thickness of a thin plate ($\tau = 1$), where τ is the shape factor. N_i is the number of atoms and V_i is the volume of the i th atomic layer, respectively. $E_\nu(K)$ is the peak energy of the ν th band for a K -sized solid. E_{z_i} is the energy of a bond in the

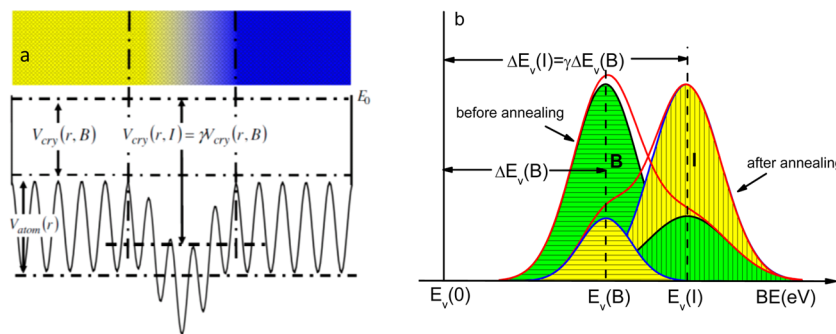


Figure 6. (a) Interface potential variation inverses (b) the spectral peak intensities from the B component dominance to the I component dominance. If $\gamma > 1$, quantum entrapment dominates and $\Delta E_\nu(I) > \Delta E_\nu(B)$; otherwise, polarization dominates and $\Delta E_\nu(I) < \Delta E_\nu(B)$, in the interface region. Reprinted with permission from ref 176. Copyright 2010 Elsevier.

ith layer between z-coordinated atoms. The weighting factor, γ_i represents the fraction of undercoordinated atoms in the i th shell of a K-sized and τ -shaped nanosolid. Subscript i counts from the outermost layer inward up to 3 as no bond order loss happens at $i > 3$.

Generally, the size dependent CN for a spherical dot follows empirically,¹

$$\begin{aligned} z_1 &= 4(1 - 0.75K^{-1}) \\ z_2 &= z_1 + 2 \\ z_3 &= z_2 + 4 \end{aligned} \quad (8)$$

$K > 0$ corresponds to a solid, and $K < 0$ corresponds to a cavity. $K = 0$ corresponds to a flat skin, and $K = \infty$ corresponds to an atom inside the ideal bulk. At $K \leq 0.75$, the solid degenerates into an isolated atom. For a spherical dot at the lower end of the size limit, $K = 1.5$ ($K_d = 0.43$ nm for an Au spherical dot example, or an fcc unit cell), $z_1 = 2$, which is equivalent to an atomic chain, the edge of a monolayer graphene, and to the primary fcc unit cell. Atoms in these sites perform identically. This LBA expression covers all possible sizes and shapes varying from a dimer, to a monatomic chain, a monolayer atomic sheet, a hollow cavity, a flat skin, and bulk solid. The BOLS–NEP notion applies to all the undercoordinated systems without exception.

2.3.3. Heterocoordination: Entrapment or Polarization. **2.3.3.1. Exchange Interaction.** The physical BOLS describes situations of atomic CN deficiency, which is different from the chemical BOLS defined for reaction dynamics in which the bond order is the number of chemical bonds between a pair of atoms.¹⁶⁶ The following correlates the bond length d , bond energy E , and bond order n for chemical BOLS:^{167,168}

$$\begin{aligned} d/d_s &= 1 - 0.26 \ln(n)/d_s \\ E/E_s &= \exp[c(d_s - d)] = n^p \end{aligned} \quad (9)$$

where subscript “s” stands for “single bond”; c and p are hypothetical parameters. This BOLS estimates^{169–174} (i) binding energies released during gas–solid reaction and (ii) activation energies for chemisorption or desorption.

2.3.3.2. Interface Potential: Entrapment or Polarization. Upon doping or alloying, diffusion of constituent atoms forms a region of graded composition (Figure 6a).³ The crystal potential for each constituent in the interface region turns from the $V_{\text{cry}}(r, B)$ to the $V_{\text{cry}}(r, I) = \gamma V_{\text{cry}}(r, B)$. The γ is the ratio of bond energy in the interface region (I) to that in the ideal constituent bulk (B). If $\gamma > 1$, quantum entrapment (T) dominates; otherwise, polarization happens. Hence, the

$V_{\text{cry}}(r, I)$ becomes deeper ($\gamma > 1$) or shallower ($\gamma < 1$ for a potential barrier formation) than the respective $V_{\text{cry}}(r, B)$ of the specific constituent standing alone. This specification is in accordance with that proposed by Popovic and Satpathy¹⁷⁵ in calculating oxide superlattices. They introduced a wedge-shaped potential well between SrTiO_3 and LaTiO_3 superlattices to mimic the monolayer sandwiched between them. Electrons in the interface form the Airy-function-localized states.

If the atomic CN changes insignificantly in the interface, the bond energy determines the interface CLS.¹⁷⁶

$$\frac{\Delta E_\nu(I)}{\Delta E_\nu(B)} = \gamma = \frac{E_I}{E_B} = 1 + \Delta_{HI} \quad (10)$$

Figure 6b shows that alloy or compound formation evolves the $E_\nu(B)$ into the $E_\nu(I)$ with an intensity inversion of the two XPS components. The peak intensity inversion happens and the total intensity conserves as the total number of electrons in the particular energy level subject to no loss.

2.3.4. Generalization of Irregular Coordination Effect.

The following formulates the irregularly coordination induced local entrapment and polarization in terms of Hamiltonian perturbation.

$$\Delta_H(x_i) = \left\{ \begin{array}{l} \frac{E_{z_i} - E_b}{E_b} = C_{z_i}^{-m} - 1 \\ \text{(defect and skin)} \\ \Delta_H(K) = \sum_{i \leq 3} \gamma_i \Delta_H(z_i) \\ = \tau K^{-1} \sum_{i \leq 3} C_{z_i} (C_{z_i}^{-m} - 1) \quad \text{(nanosolid)} \\ \Delta_H(I) = \frac{E_I - E_b}{E_b} = \gamma - 1 \quad \text{(interface)} \\ \Delta_H(P) = [E_\nu(p) - E_\nu(0)]/\Delta E_\nu(12) - 1 \\ \text{(polarization)} \end{array} \right. \quad (11)$$

The following correlates energies of components l and l' in an XPS spectrum ($l = \text{S}_1, \text{S}_2, \dots$).

$$\frac{E_\nu(x_l) - E_\nu(0)}{E_\nu(x_{l'}) - E_\nu(0)} = \frac{1 + \Delta_{Hl}}{1 + \Delta_{Hl'}} \quad (l' \neq l) \quad (12)$$

This formulation yields immediately⁶

$$\begin{aligned} E_\nu(0) &= [E_\nu(x_l)(1 + \Delta_{Hl'}) - E_\nu(x_{l'})(1 + \Delta_{Hl})] \\ &/(\Delta_{Hl'} - \Delta_{Hl}) \\ \Delta E_\nu(12) &= E_\nu(12) - E_\nu(0) \\ \Delta E_\nu(x_l) &= \Delta E_\nu(12)(1 + \Delta_{Hl}) \end{aligned} \quad (13)$$

Chemical reaction or coordination variation alters neither the $E_\nu(0)$ nor the bulk shift $\Delta E_\nu(12)$. Accuracy of determination of the $E_\nu(0)$ and the $\Delta E_\nu(12)$ is subject to calibration of the XPS and to determination in the shape and size of the nanocrystal. Nevertheless, furnished with this formulation, one could be able to elucidate, in principle, the core level positions of an isolated atom $E_\nu(0)$ and the bulk shift $\Delta E_\nu(12)$, as well as the local bond length and energy from XPS measurement, as illustrated in subsequent sections.

2.4. Valence Band and Nonbonding States

2.4.1. Complexity of the Valence DOS. Valence electrons perform quite differently from those in the core bands of a specific constituent element. Valence electrons are a mixture of all involved elements in the solid, which respond to the chemical environment directly at functioning. The behavior of valence electrons is much more complicated because of the delocalization, polarization, and charge redistribution among constituent elements in reaction. Besides the undercoordination effect featured by the BOLS–NEP notion, atomic heterocoordination due to formation of alloys, compounds, dopants, impurities, interfaces, or glasses also results in the densification, localization, entrapment, and polarization of the valence electrons because of the bond nature alteration. Both under- and heterocoordination modify the valence band substantially and irregularly.

In addition to the polarization and localization of the conduction electrons by the densely entrapped core electrons, such as the zigzag edge of graphene¹⁵⁸ and the Rh adatoms,¹⁷⁷ the presence of the nonbonding lone pair and the lone-pair-induced dipoles upon reaction with F, O, and N play a role of significance.^{2,5,46}

2.4.2. Tetrahedral-Bonding Mediated Valence DOS. Figure 7 illustrates the residual DOS of metals and semiconductors resulting from involvement of N, O, and F. The sp^3 -orbital hybridization produces four directional orbits, each capable of being occupied by two electrons, forming a quasi-tetrahedron.

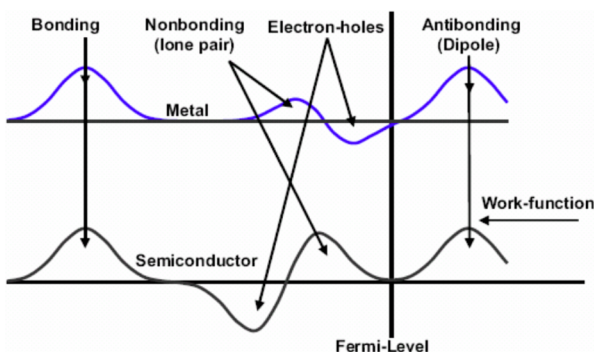


Figure 7. Differential valence DOS of metals (upper) and semiconductors (lower) mediated by N, O, and F addition with four excessive DOS features: bonding pairs ($\ll E_F$), nonbonding lone pairs ($\sim E_F$), electron–holes ($\sim E_F$), and antibonding dipoles ($\gg E_F$). The three near- E_F DOS features are crucial to the performance of a compound, yet they have received sufficient attention. Reprinted with permission from ref 46. Copyright 2006 Elsevier.

These four directional orbits can hence accommodate eight electrons. The central O atom, for example, has six $2s^2 2p^4$ electrons and requires another two to complete its valence shell. Therefore, the O forms two bonds with the nearest neighbors by sharing one electron with each of two neighbors, while its lone electron pairs occupy its remaining two orbits. Likewise, a nitrogen atom needs three electrons for sharing and generates one lone pair, and an F atom forms a tetrahedron with three lone pairs. The manner of electronic distribution, bond type, bond length, and energy surrounding the central F, O, and N atoms in the tetrahedron are anisotropic.⁸

Counting from lower to higher energy, the DOS features are the bonding states, electronic holes, electron lone pairs of F[−], O^{2−}, or N^{3−}, and the antibonding dipoles of the host. In a semiconductor compound, holes create at the top of the valence band, which further expands the semiconductor's band gap, turning a semiconductor into an insulator, such as Si₃N₄ and SiO₂. In metallic compounds, holes generate near the Fermi surface, which opens a band gap and turns the conductor into an insulator or a semiconductor, such as Al₂O₃, TiO₂, ZnO, and AlN. Nonbonding states located in the band gap form impurity states, while dipoles form antibonding states above the E_F . The production of dipoles shifts the surface potential barrier outwardly with high saturation,¹⁷⁸ opposing the effect of the positively charged ions. These dipoles also screen and split the local potentials, adding additional features to the core bands. STM probes dipoles as protrusions and the positive ions as depressions.

2.4.3. Impact of Nonbonding States. The “nonbonding” states also refer to the energetic electrons involved in the antibonding dipoles, as well as H-bond-like and C–H-bond-like. An ionic impurity in a metal also polarizes neighbors to create polarized states.^{5,179} The van der Waals bond having a maximal energy of several tenths of an electronvolt is in this category as it represents dipole–dipole interaction instead of charge sharing.

Contributing insignificantly to the Hamiltonian or to the atomic cohesive energy, the nonbonding electrons add, however, impurity states near E_F , which neither follow the regular dispersion relations nor occupy the allowed states of the valence band and below. They are located at energies right in the energy window of an STM/S. In addition to the weak interactions with energies of ~ 50 meV, as detected using Raman and electron energy loss spectroscopy,⁵ these lone pairs, however, polarize the neighboring atoms instead causing their change to dipoles.

The impact of the nonbonding lone pairs and the antibonding dipoles is ubiquitously abundant and profound. For example, the presence of the antibonding dipoles lowers the work function drastically by more than 1 eV,¹⁸⁰ which greatly aids the electron emission for imaging and display.^{181,182} Nitrogenation of diamond and carbon nanotubes, oxidation and fluorination of metals, etc., have the same effect of polarization and work function reduction. The presence of these localized nonbonding states is responsible for the size emergence of defects and nanostructures such as the Dirac fermions creation, dilute magnetism, catalytic enhancement, superhydrophobicity, etc. Such nonbonding and antibonding states play significant roles in topological insulators, thermoelectric materials, and high- T_C superconductors,² and even the skin of water and ice.^{41,165}

2.5. Numerical Strategies: Formulation and Quantification

2.5.1. Irregular Coordination Effect. With the BOLS–NEP notion and its formulation, one can decompose a skin XPS spectrum accordingly. Parameters of concern are the number of

Table 2. Definition, Formulation, Origin, and Functionality of the E_D and the E_C in the Irregular Coordinated Atomic Sites¹⁸⁴

definition	skin	interface (A_xB_{1-x} alloy)
energy density, E_D (eV/nm ³)	$E_{DS} = \int_0^{d_3} (E_{z_i}/d_{z_i})^3 dy / \int_0^{d_3} dy$	$E_{DI} = N_{cell} z_1 E_1 / V_{cell}(d_1)$ with $d_1 = xd_A + (1 - x)d_B; z_1 \cong z_b$ $E_1 = xE_A + (1 - x)E_B + x(1 - x)\sqrt{E_A E_B}$
physical origin	energy gain per unit area of ($d_1 + d_2 + d_3$) thick skin due to BOLS	energy gain due to bond nature alteration and exchange interaction
functionality	surface stress; elasticity; surface optics; dielectrics; electron and photon transport dynamics; work function, etc.	interface mechanics, joining, tunneling junction, etc.
atomic cohesive energy, E_C (eV/atom)	$E_{CS} = \int_0^3 d(z_i E_{z_i})/3$	$E_{CI} = z_1 E_1$
physical origin	energy remnant per discrete atom upon surface/interface formation	
functionality	thermal stability, wettability, diffusivity, reactivity, self-assembly, reconstruction	

components and their intensities, energies, and full width at half-maximum if one describes the peak using, but not limited to, the Gaussian distribution function. Ideally, the following provide guidelines:

$$I = \sum_i I_{z_i} \exp \left\{ - \left[\frac{E - E_\nu(z_i)}{E_{\nu W}(z_i)} \right]^2 \right\}$$

(spectral intensity)

$$\frac{E_\nu(z_i) - E_\nu(0)}{E_\nu(12) - E_\nu(0)} = \frac{E_{z_i}}{E_b} = C_{z_i}^{-m}$$

(component peak energy)

$$\frac{E_{\nu W}(z_i)}{E_{\nu W}(12)} = \frac{z_i E_{z_i}}{z_b E_b} = z_{ib} C_{z_i}^{-m}$$

(component width)

(14)

The overall intensity is a superposition of all components. The spectral components follow strictly the positive CLS according to the TB approximation unless polarization becomes dominant. The energy level of an isolated atom $E_\nu(0)$ is the unique reference from which the CLS proceeds. The bulk component width $E_{\nu W}(12)$ is to be optimized in spectral decomposition. One can determine the number of peaks and their positions, widths, and intensities in each spectrum with the known $E_\nu(0)$ and $E_{\nu W}(12)$ and the specific spectrum. The $E_\nu(0)$ and $E_{\nu W}(12)$ are available by decomposing a set of as many as possible spectra collected from different registries of the same substance, as exemplified shortly.

Equation 14 provides only guidelines for decomposition, but the actual spectral intensity and shape are subject to polarization and artifacts in measurements. Furthermore, if the bond nature index m value is sufficiently large, the width of the skin component may be broader than that of the bulk. Therefore, fine-tuning all components collectively in spectral decomposition is necessary.

Another issue is that the effective CN for the same registered sublayer of the same crystal geometry conserves regardless of the chemical composition of the material. For example, the CN of the first sublayer of the fcc(100) skin holds at 4.0 for all fcc-structured specimens such as gold, copper, and rhodium.^{1,108,112}

Proper calibration of the equipment can remove artifacts such as ionization induced core-hole relaxation and radiation induced

surface charging. Upon background correction and peak-area normalization, one can decompose a skin XPS spectrum into the B and the S_i components in a positive CLS order. A best fit to the spectral peak can estimate the number of components and the width of each for a given spectrum. One can take the effective $z_1 = 4$ for the outermost layer of the fcc(100) flat skin as the standard reference. A fine-tuning of the component energies of all involved sublayers can optimize their z values collectively. The optimized set of z values are only geometry dependent. Repeated fine-tuning optimizes the z value, intensity, energy, and width of each component. The least deviation σ justifies the accuracy and precision of the spectral analysis derivatives.

An incorporation of the BOLS–LBA–NEP notion into the TB approach and the PES measurements not only clarifies the physical origin of the CLS but also enables quantification of a number of parameters. These parameters include the energy level of an isolated atom $E_\nu(0)$ and its bulk shift $\Delta E_\nu(12)$, the CN dependent CLS $\Delta E_\nu(z)$ and component width $E_{\nu W}(z)$, local bond length d_z , bond energy E_z , energy density E_D , and atomic cohesive energy E_C , in addition to the charge distribution: entrapment or polarization. Polarization happens only to atoms with an effective CN smaller than that of an atom in the flat skin.

2.5.2. Local Energy Density and Atomic Cohesive Energy. Traditionally, the surface free energy (γ_s) is defined as the energy required for cutting a given crystal into two halves, or the energy costs in making a unit area of surface.¹⁸³ The interface energy (γ_I) is that required to form the unit area of an interface. The unit of the γ_s and the γ_I is sometimes in eV/nm² and some other times in eV/atom. The magnitude of the former is often higher than that of the latter for the same substance. Actually, the γ_s and the γ_I and their functionalities arise from nothing more than interaction between the irregularly coordinated atoms.

In fact, the energy gain per unit volume E_D or the cohesive energy remnant per atom E_C in the skin or in the interface region, instead of the energy cost for forming a surface or an interface, dominates the performance of atoms in these irregularly coordinated atomic sites. In order to describe phenomena and processes at the skin and the interface effectively, the following concepts are necessary to complement the conventional terms of surface and interface free energy. Table 2 summarizes the formulation, physical origin, and functionality of the E_D and the E_C in the irregularly coordinated atomic sites based on the BOLS notion.¹⁸⁴ The concept of skin involving thickness is much more meaningful than the surface or interface in two dimensions.⁸

2.6. Summary

Formation of a bond between heterocoordinated atoms and relaxation of a bond between undercoordinated atoms shift intrinsically the electronic BE in the core band and in the valence band of a substance. The process of charge entrapment, localization, and polarization modify the valence band and the core band consistently. The BOLS–NEP–TB describes the CLS adequately while the artifact of “initial–final state” relaxation serves as background. One could be able to determine the local bond length d , bond energy E , energy density E_D , and atomic cohesive energy E_C associated with irregularly coordinated atoms from spectral analysis based on the framework of the presented BOLS–NEP–LBA–TB notion.

3. PROBING STRATEGIES: STM/S, PES, APECS, AND ZPS

In this section, we discuss the following:

- STM/S maps electrons nearby E_F from a superficial skin.
- PES scopes BE information on the core and the valence bands from a too-thick skin.
- APECS detects two-band BE shift with quantification of potential screening and charge transportation in chemical processes.
- ZPS resolves atomistic, CN-resolved, dynamic, quantitative information on bond relaxation, valence charge evolution, BE shift, BE density, and atomic cohesive energy.

3.1. Energy Band Structure and Electronic Dynamics

Figure 8 illustrates the energy bands of a solid. When solid forms with N atoms, the discrete energy levels expand into bands that

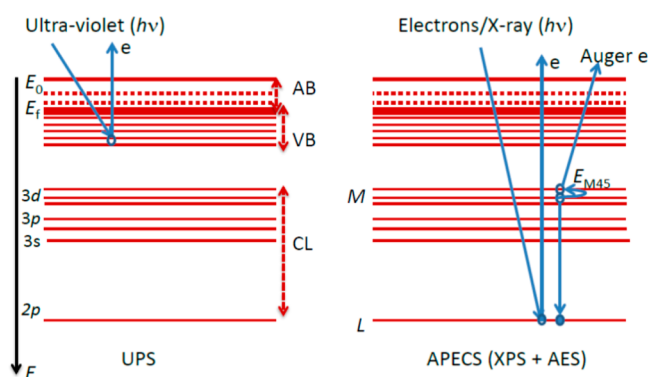


Figure 8. Schematic illustration of the energy bands of an ideal solid and principles for the PES and the APECS (XPS and AES (LMM for instance)). From top, there are the vacuum level $E_0 = 0$, unoccupied antibonding band (AB, broken lines), Fermi level E_F , valence band or conduction band (VB or CB), and core bands. The $h\nu$ is the incident beam energy of the PES or AES. The rule of energy conservation allows the PES and the AES to determine the BE and the DOS evolution in the respective bands.

contain each N sublevels because of the degeneration by interatomic interaction. $E_0 = 0$ is the vacuum level and E_F is the Fermi energy. The separation between the E_0 and the E_F is the work function ϕ , which determines the easiness of the substance to eject an electron. The separation between the E_0 and the bottom edge of the conduction band (CB) is the electroaffinity, which determines the ability of a specimen to hold electrons captured during reaction. Conversely, the electronegativity is the intrinsic attribute of an element which determines the easiness of an electron to transfer between elements of differing negativity.

The negativity difference between two elements determines the nature of the bond between them. Generally, quantum entrapment enlarges the electroaffinity and polarization reduces the work function. Electroaffinity and work function are key indicators for the catalytic behavior and the toxicity of a substance, particularly at the nanometer scale or for atoms with even fewer CNs than those at the flat skin.⁸

From E_F downward, there is the CB or the valence band (VB) and then the core bands. The center of a band shifts down by an amount that is proportional to the bond energy at equilibrium.⁶ The width of the band becomes narrower and narrower and the energy shift of the band center becomes smaller and smaller, as it moves from the valence band downward. Electrons occupy the lowest energy level and then gradually up until the VB, which follows the rule of Pauli's repulsion. Electrons in the VB or in the CB are more delocalized than those are in the core band. The energy shifts of the VB and below are fingerprints of the change of bond energy with coordination and chemical environment.

At sites nearby defects, localization and polarization of the dangling bond electrons in semiconductors such as graphene edges, or the otherwise conduction electrons of metallic adatoms or terrace edges, produce antibonding (AB) dipole states that occupy the upper edge of the VB or above the E_F .¹⁵⁹ For a solid in an amorphous phase, impurity states are present with energies close to E_F .¹⁶⁰

3.2. STM/S: Nonbonding and Antibonding States

Figure 9a illustrates the principle of STM/S that maps a surface by probing the tunneling current, I , crossing the vacuum gap between the tip and the surface of conductors or semiconductors under bias V . STS records the $dI/dV - V$ or the $d(\ln I)/d(\ln V) - V$ profile at a fixed atomic site. The energy window of STS is only a few electronvolts crossing E_F . STS features the local DOS in atomic scale in the lateral and subatomic vertical directions.⁹⁸ If the sample is negatively biased, charge will flow from the specimen to the tip; otherwise, charge flows inversely. Therefore, STS features below E_F (reference 0) represent the occupied DOS of the surface, while features above the E_F represent the allowed, yet unoccupied, DOS of the surface.

Figure 9b shows the typical STS spectra of a clean surface (spectrum A) and an O–Cu(110) surface (spectra B and C) with the tip at different locations along the “O²⁻:Cu^P:O²⁻” chain (inset), with Cu^P being protruding dipoles.⁹⁸ Upon O²⁻ chemisorption, the initially empty DOS peaking at 0.5–1.8 eV above E_F is partially occupied by the Cu^P electrons, which weakens the intensity of the unoccupied states. Meanwhile, the lone pair of O²⁻ creates additional DOS features at –2.0 eV. The presence of the lone pair and the dipole states is the same as that detected using angular-resolved PES and using the deexcitation spectroscopy of metastable atoms of the same surface.¹⁸⁵

3.3. PES–AES: Valence- and Core-Band Shifts

Using light sources of different energies, PES measures energy states at different bands. UPS monitors the change of the valence band consisting of electrons of all constituents, while XPS measures the elemental CLS as a mixture of the skin and the bulk components. PES monitors the consequence of crystal field change due to bond relaxation and bond nature alteration upon reaction.

In the PES process, the incident radiation of $h\nu$ energy excites an electron in the specific n th level. The excited electrons will overcome the bound work function ϕ and the BE of the respective CL (L level $E_{B(L,VB)}$, for example) and escape from the specimen to become free with kinetic energy $E_{K(L,VB)}$.

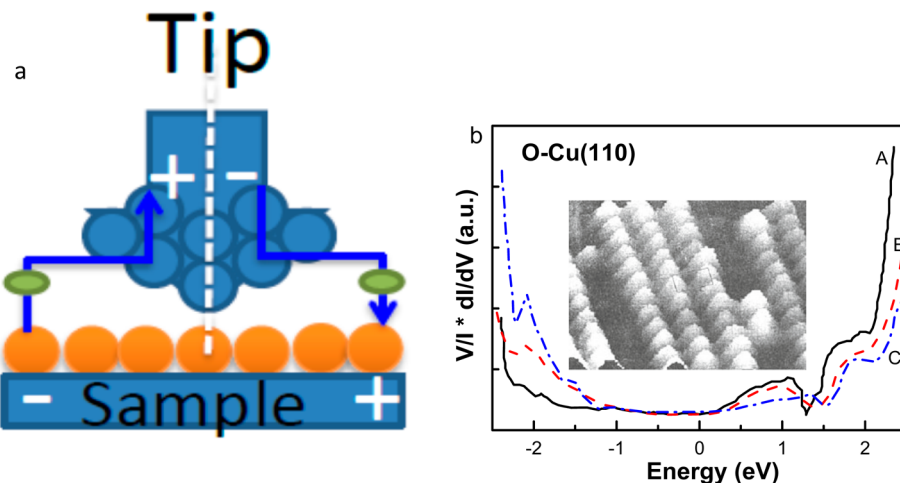


Figure 9. STM/S principle and typical profiles collected from the clean surface (a) and the Cu(110)-(2 x 1)-O²⁻ surface at sites along the “O²⁻:Cu^P:O²⁻” chain (B, bridge; C, on top; see inset STM image) (inset in b). The differential conductance dI/dV or $V dI/I dV$ versus bias V is proportional to the local DOS mapped (b). Under sample + bias, current flows from the tip to the surface and the STS peak represents the unoccupied DOS above E_F ; otherwise, it represents the occupied DOS below E_F . Reprinted with permission from ref 5. Copyright 2003 Elsevier. Reprinted with permission from ref 98. Copyright 1989 American Physical Society.

Auger electron spectroscopy (AES)^{186,187} uses an energetic electron source in place of X-rays in the XPS. The AES processes include the following:

1. The process of ionization is the same as that in the PES. The incident electron beams ionize atoms of the skin. The ejected electron flies away from the skin and leaves a hole behind the lower L(2p) level, for instance.

2. The ionization of the core electron relaxes all energy levels because of the screen weakening of both the intra-atomic potential and the interatomic potential.

3. An electron transits then from the relaxed M(3d_{5/2}) upper level to fill the hole in the initial L level. This transition releases energy that equals the separation between the two levels: $\Delta E_R = E_{BL} - E_{BM}$.

4. The ΔE_R kicks an electron off the further relaxed, degenerated M(3d_{3/2}) level to form the Auger electron that overcomes the E_{BM} and then escapes from the solid with kinetic energy E_{KM} .

The electronic energies in the PES and the AES processes conserve

$$h\nu = E_{B(L,VB)} + \phi + E_{K(L,VB)} \quad (\text{PES})$$

$$E_{BL} - E_{BM} = E_{M45} + E_{BM} + \phi + E_{KM} \quad (\text{AES}) \quad (15)$$

E_{M45} is the energy separation between the spin-resolved 3d_{3/2} and 3d_{5/2} lines of Cu, for instance.

3.4. APECS: Extended Wagner Plot and Dual-Band Shift

Differentiating eq 15 for the L and the M levels yields immediately

$$\begin{cases} \Delta E_{BL} = -\Delta E_{KL} \\ 2\Delta E_{BM} = \Delta E_{BL} - \Delta E_{KM} \end{cases} \quad \Delta\alpha' = -(\Delta E_{KL} + \Delta E_{KM}) = 2\Delta E_{BM} \quad (16)$$

The ionization and relaxation change the $\Delta\phi \cong 0$ and the $\Delta E_{M45} = \Delta(E_{3d_{5/2}} - E_{3d_{3/2}}) \cong 0$ insignificantly. Therefore, this expression correlates the energy shifts of the APECS-involved L and M levels shown in Figure 10.

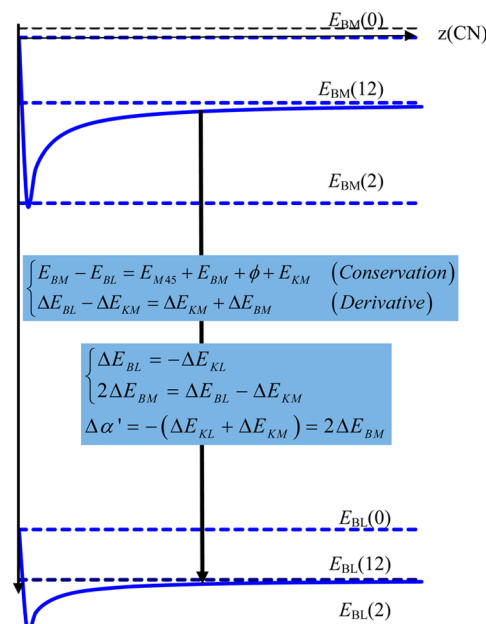


Figure 10. Energy conservation in the APECS processes for the CN-resolved energy shifts of the APECS L₃M₄₅M₄₅ lines. The energy levels $E_{BM}(z)$ and $E_{BL}(z)$, and their separation, represented by the solid lines, are measurable while $E_{BM}(0)$ and $E_{BL}(0)$ and their bulk shift (dotted lines) can be obtained with the present premise. The work function ϕ and the sublevel separation E_{45} change insignificantly in the APECS processes. Reprinted with permission from ref 193. Copyright 2006 Elsevier.

Excitingly, summing the kinetic energy shifts of the XPS and the AES electrons, conventionally called the Auger parameter $\Delta\alpha'$, equals twice the shift of the M level in magnitude. Therefore, the APECS resolves simultaneously both the L and the M levels without needing any approximation or assumption.

Traditionally, two terms describe the energy shifts of the APECS-involved levels. One is the Auger parameter and the other is the Wagner plot:^{188,189}

$$\Delta\alpha' = |\Delta E_{BL}| + |\Delta E_{KM}| \cong 2\Delta R^{\text{ex}} \quad (\text{Auger parameter})$$

$$E_{KM,x} - E_{KM,1} = \beta(E_{BL,x} - E_{BL,1}) \quad (\text{Wagner plot})$$
(17)

It is often assumed that the energy shifts of the L level and the M level contribute equally to $\Delta\alpha'$. R^{ex} is a hypothetical parameter that corresponds to extra energies of atomic relaxation or polarization coming from neighbors of the core-ionized atom. $\Delta\alpha'$ is greater than ΔE_{BL} or ΔE_{KM} alone, and therefore, $\Delta\alpha'$ is more sensitive to the chemical or coordination stimulus.

The slope β of the Wagner plot correlates the shift of the Auger kinetic energy ΔE_{KM} and the ΔE_{BL} ($= -\Delta E_{KL}$).^{190,191} Subscript x represents the concentration of the particular element in a compound. With two independent measurements of the Auger parameters, for example, $\alpha'_1 = E_B(1s) + E_K(\text{KLL})$ and $\alpha'_2 = E_B(2p) + E_K(\text{KLL})$, from compounds containing the same constituent with different x concentrations, one could estimate the separation between two levels, $E_B(1s) - E_B(2p)$, rather than either of them alone.^{188,192,193}

Actually, eq 16 proves that $\Delta\alpha'$ is exactly twice ΔE_{BM} :

$$\Delta\alpha' = |\Delta E_{BL}| + |\Delta E_{KM}| = -(\Delta E_{KL} + \Delta E_{KM}) = 2\Delta E_{BM}$$
(18)

Therefore, one can measure the energy shift of the upper M level (or the valence band) in the form of $\Delta E_{BM} = -(\Delta E_{KL} + \Delta E_{KM})/2$. The $\Delta\alpha'$ value results from the energy conservation in APECS, which is free from any assumption or approximation as the conventional $\Delta\alpha'$ was.¹⁸⁸ See Figure 10.

Although the absolute energy shift varies from level to level, the relative shift of each level across from their references should be identical if no chemical process is involved. One may extend the Wagner plot to the atomic CN (particle size) domain to correlate the relative shifts of the APECS involved levels. This extension discriminates the effect of crystal-field screening from the effect of valence recharging (initial–final state and charge transport in reaction), in the following manner:

$$\kappa_{ML} = \left\{ \frac{E_{BM}(z) - E_{BM}(0)}{E_{BM}(12) - E_{BM}(0)} \right\} \left\{ \frac{E_{BL}(z) - E_{BL}(0)}{E_{BL}(12) - E_{BL}(0)} \right\}^{-1}$$

$$= 1 \quad (\text{extended Wagner plot})$$
(19a)

$$\eta_{ML} = \frac{E_{BM}(12) - E_{BM}(0)}{E_{BL}(12) - E_{BL}(0)} > 1$$

$$(\text{screening coefficient})$$
(19b)

The slope κ_{ML} correlates the relative shift of the two levels, which represents the valence recharging effect when the coordination or chemical environment changes. Ideally, $\kappa_{ML} = 1$, if no chemical reaction occurs. Therefore, κ_{ML} can be indicative of reaction and its value relates directly to the interatomic bond. The screening coefficient, η_{ML} , represents the relative BE between these levels in the bulk of an elemental solid. Therefore, the extended Wagner plot is more convenient and revealing than its conventional form as it uses the dimension of size scale or the effective atomic CN.

3.5. ZPS: CN-Resolved Bond Length and Energy Relaxation

One can imagine what will happen to the outcome by differentiating two spectra collected under any of the following conditions from

- (i) the same defect-free surface at different emission angles

- (ii) the same surface after and before conditioning such as defect creation, atom addition, or chemisorption under the same probing conditions, or
- (iii) specimens containing the same constituent but different concentrations

Upon the standard processes of background correction and spectral peak area normalization, the ZPS in (i) distills the spectral features due to the monolayer skin by filtering out the bulk information as the XPS collects more information from the surface at larger emission angles.^{111,150} Likewise, the ZPS in (ii) purifies merely the spectral features due to conditioning. The ZPS in (iii) resolves the alloying effect on the energy shifts of the respective levels of a specific element. The ZPS also filters out all artifacts such as the surface charging and the “initial–final state” relaxation that exist throughout the course of measurements. This ZPS strategy can monitor surface and interface processes such as crystal growth, defect generation, chemical reaction, alloy formation, etc., both statically and dynamically with high sensitivity and accuracy without needing any approximation or assumption.

Generally, the integrated intensity of a spectral peak is weaker for the one collected at a larger emission angle or from a rougher skin than that of the otherwise because of the scattering effect. The mean free path of the ejected electrons is generally longer than the penetration depth of the incident beams.¹⁹⁴ Conversely, the area integral of the specific peak is proportional to the total number of electrons emitted from the specimen under the same probing conditions. In order to make all spectra quantitatively comparable, area normalization of the same peak collected under different conditions can minimize the influence of the scattering and artificial effects. Having all the spectra normalized, one can subtract the referential spectrum from the one collected from the same but conditioned specimen.

The ZPS distills the DOS gain as a component presenting above the lateral axis and features the DOS loss as valley below the lateral axis. This process removes the commonly shared spectral area that is out of concern. Ideally, the resultant ZPS components conserve as the spectral areas above and areas below the lateral axis are identical. Any improper background correction or spectral normalization may asymmetrize the spectral gain and the loss compared with the ideal situation. With these criteria, one can readily gain quantitative information on local bond length, bond energy, charge entrapment and polarization, etc.

Conventionally, one needs to correct the spectral background using the standard Tougaard method^{195–197} by employing Gaussian-, Lorentz-, or Doniach–Sunjic-type functions before decomposing the XPS profiles. However, ZPS saves such tedious procedures of background correction, component specification, and peak energy fine-tuning. ZPS gives directly the skin or conditioned component as emerging peaks and the bulk component as a valley.

3.6. Summary

Complementing STM/S and PES, ZPS resolves directly local bond relaxation and the associated CLS without involvement of trial-and-error optimization in analyzing the ill coordination effect. Extracted information includes the local binding energy density, atomic cohesive energy, charge quantum entrapment, and polarization. APECS could derive the energy shift of two energy levels simultaneously with provision of the coefficients of charge sharing and potential field screening. ZPS and APECS empower the currently available spectroscopic techniques to

resolve atomistic, local, dynamic, and quantitative information on bond relaxation and the associated energetics of bonding and nonbonding electrons pertaining to irregularly coordinated atoms. Interplay of these spectroscopic techniques would be more revealing than using any of them alone.

4. SOLID SKIN: QUANTUM ENTRAPMENT DOMINANCE

In this section, we discuss the following:

- BOLS-TB-XPS not only quantifies the $E_\nu(0)$ and $E_\nu(12)$ but also the CN-resolved d_z , E_z , E_D , and E_C .
- Atomic undercoordination not only shortens the skin bonds but also densifies and entraps core electrons, shifting the CL positively.
- Sublayer atomic CN varies only with layer order and geometrical orientation regardless of chemical composition.
- The skin of a substance is generally denser, stiffer, yet chemically and thermally active.

4.1. XPS Spectroscopic Derivatives

It has long been controversial regarding the skin CLS that may be in positive, negative, or mixed order. Rules are lacking for such order assignment despite intuitive or calculation derivative using the “final–initial state” relaxation scheme. Nb(100),^{108,109} graphite,¹¹¹ Tb(0001),¹¹⁰ Ta(100),¹¹² Ta(110),¹⁹⁸ Mg(1010),¹⁹⁹ and Ga(0001)²⁰⁰ skins follow the positive CLS order (E_F , B, ..., S_2 , S_1) with E_F as the reference point. Be(0001),¹¹⁷ Be(1010),^{199,201,202} Ru(1010),²⁰³ Mo(110),²⁰⁴ Al(100),¹¹⁵ W(110),²⁰⁵ W(320),²⁰⁶ and Pd(110), Pd(100), and Pd(111)¹¹³ skins follow the negative order (E_F , S_1 , S_2 , ..., B). However, Si(111),²⁰⁷ Si(113),²⁰⁸ Ge(100),²⁰⁹ Ge(111),²¹⁰ Ru(0001),²¹¹ and Be(1010)²¹² skins are in the mixed order (S_2 , S_1 , ..., B, E_F).

The XPS peak energies and intensities vary with the crystal orientation or with the atomic density of the skin. On one hand, a high-density skin blocks not only the incident beam from penetrating into deeper layers but also electrons from being ejected from the deeper sublayers and hence weakens the peak intensity of the bulk component; on the other hand, densely packed skin atoms shift the CL less than the loosely packed one does because of the z-resolved bond energy relaxation.²¹³ Higher skin density means higher atomic CN, which weakens the skin chemical bond, according to the BOLS notion. The skin atomic densities of the fcc(110), fcc(001), and fcc(111) skins are in the order $1/\sqrt{2}:1:2/\sqrt{3}$.

Therefore, the S_1 component of the (111) skin with slightly higher CN value will shift less from the $E_\nu(0)$ than the S_1 of the (110) skin does for the same substance with the (100) skin as reference. The S_1 peak intensity for the (111) skin is relatively higher than the same S_1 component of the loosely packed (110) skin, as observed by Andersen et al.¹¹³ Two components are present at 334.35 (B) and \sim 334.92 eV (S_1) for the Pd(110), Pd(100), and Pd(111) skins under 390 eV X-ray excitation. The intensity of the S_1 component decreases when the skin turns from (111) to (110) orientation. The (111) skin shifts the SCL indeed less than that of the (110) does. This trend agrees with derivatives of quantum computations and theoretical predictions based on the bond counting scheme.⁶ This trend holds true if the mean free path of the ejected electrons, at or around 40 nm,^{214,215} is greater than the penetration depth of nanometer scale.

The BOLS-TB formulation has enabled resolution of $E_\nu(0)$, $E_\nu(12)$, and z-resolved $E_\nu(z)$, and d_z , E_z , E_D , and E_C from the XPS

measurements. Results clarify that all skins follow the positive CLS order without any exception and that the effective CN for each sublayer depends only on the geometric orientation and the sublayer order, disregarding the chemical composition of the material.^{32,213,216} The $E_\nu(0)$ and $E_\nu(12)$ derived from skin XPS analysis provide a reference to the subsequent quantification of bonding identities for defects, nanostructures, and interfaces.

4.2. BOLS-TB Formulation

Considering a point defect or a sublayer of a solid skin, eq 12 turns out the z-resolved CL:

$$\begin{aligned} E_\nu(0) &= [C_{z'}^{-m}E_\nu(z') - C_z^{-m}E_\nu(z)]/(C_{z'}^{-m} - C_z^{-m}) \\ E_\nu(z) &= E_\nu(0) + \Delta E_\nu(12)C_z^{-m} \end{aligned} \quad (20)$$

If the polarization and entrapment couples pronouncedly, the term pC_z^{-m} will replace the C_z^{-m} in the $E_\nu(z)$ expression. Polarization will offset the originally entrapped states T back by p-fold.

In calculations, one needs to determine the $E_\nu(0)$ first. If $l > 2$ sublayer components are involved in a set of XPS spectra collected from skins of a specific substance at different registries, the $E_\nu(0)$ and the $\Delta E_\nu(12)$ take the mean value of $N = C(l,2) = l!/[l(l-2)!2!]$ possible combinations with the standard deviation σ :

$$\begin{aligned} E_\nu(x_l) &= \langle E_\nu(0) \rangle \pm \sigma + \Delta E_\nu(12)(1 + \Delta_{HI}) \\ \langle E_\nu(0) \rangle &= \sum_N E_{\nu l}(0)/N \\ \sigma &= [\sum_{C(l,2)} [E_{\nu l}(0) - \langle E_\nu(0) \rangle]^2/N(N+1)]^{1/2} \end{aligned} \quad (21)$$

One may collect a set of XPS spectra from each of the fcc(100), fcc(110), and fcc(111) skins of the same substance. There are a total of $l = 1 + 3 \times 3 = 10$ sublayers (S_1 , S_2 , and S_3 in each skin and a common B). The B component conserves in energy and exists in all spectra. There is a combination of $N = C(10,2) = 45$ possible $E_\nu(0)$ values for averaging. Higher N number means higher $\langle E_\nu(0) \rangle$ accuracy and reliability.

One needs to know the bond nature index m before analysis. A fitting to the size-dependent melting point $T_m(K)$ of the same substance with known shape (τ), for instance, gives the m value for this specimen.⁸

$$\frac{T_m(K) - T_m(\infty)}{T_m(\infty)} = \tau K^{-1} \sum_{i \leq 3} C_i(z_{ib} C_i^{-m} - 1)$$

where $T_m(K)$ and K are detectable and $T_m(\infty)$ is the known bulk reference. The $C_i(z)$ follows eq 5, and z_i follows eq 8. The relative atomic CN z_{ib} is the z_i normalized by the bulk standard 12.

With the derived m value, one can optimize the $E_\nu(0)$ toward least σ deviation ($<10^{-3}$ in general) using the following relation by tuning all $E_\nu(z)$ values collectively.

$$\frac{E_\nu(z) - E_\nu(0)}{E_\nu(z') - E_\nu(0)} = \frac{C_z^{-m}}{C_{z'}^{-m}} \quad (22)$$

The average $\langle E_\nu(0) \rangle$ with the least σ approaches the true situation. Therefore, one can resolve these skin XPS spectra simultaneously with quantification of the $E_\nu(0)$ and the geometric orientation and layer order dependent z value and the CLS, ΔE_ν ($2 \leq z \leq 12$) (see Figure 4).

4.3. fcc-Structured Al, Ag, Au, Ir, Rh, and Pd

Data sourced from the literature has been corrected by removing background information. Including the B component that counts only once, there are a total of $l = 7$ components for these fcc(100), fcc(110), and fcc(111) skins, as each peak contains the S_1 and the S_2 components.^{107,217} There will be $C(7,2) = 21$ different $E_\nu(0)$ values for averaging. The decomposition refines the effective CN of atoms in each sublayer. Figures 11–14 show

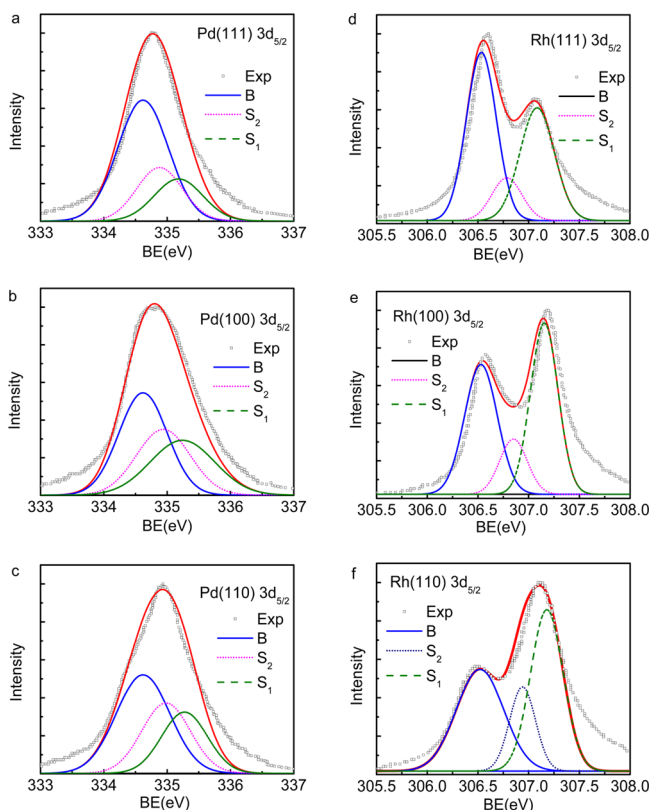


Figure 11. Decomposition of the XPS $3d_{5/2}$ spectra for the fcc(111), fcc(100), and fcc(110) skins of (a–c) Pd and (d–f) Rh^{113,114} using S_1 , S_2 , and B components. Table 1 features the derived information on strain and bond energy. The asymmetric tails at the deeper edge arise from the entrapment of vacancy defects or adatoms. Reproduced from ref 213 with permission from the PCCP Owner Societies.

the decomposed spectra for Rh, Pd, Al, Ag, Au, and Ir skins of different orientations. Table 3 summarizes the decomposition outcome. Derivatives include the effective CN, bond strain ε_z , bond energy E_z , energy density E_D , and atomic cohesive energy E_C , relative to their bulk values. These elemental quantities determine the performance of the skin. For instance, E_D determines the mechanical strength and elasticity and E_C determines the diffusivity and thermal stability such as the critical temperature for phase transition.⁸

Figure 11 displays that the Pd $3d_{5/2}$ spectra exhibit one symmetric convoluted peak but the Rh $3d_{5/2}$ spectra display two major peaks. The asymmetry at the deeper edge indicates the possible presence of defects or adatoms that induce quantum entrapment. Electronic configurations of Pd($5s^04d^{10}$), Rh-($5s^14d^8$), and Ir($5d^76s^2$) may affect their spectral patterns as they are in the same geometry and similar atomic cross-section area for scattering.²¹³

Results indicate indeed that the amount of the CLS for the (110) skin is greater than that for the (001) and (111) skins

because of its lower atomic CN. The CLS of the (111) skin shifts least because of its highest effective CN among them.¹¹³ Bonds in the outermost layer are the shortest and strongest compared with those in the subsequent sublayers, which agrees with what was discovered by Matsui et al.²¹⁸ from the Ni surface. They resolved that the Ni 2p levels of the outermost three atomic layers shift positively to deeper BE, with the outermost layer shifting the most. We will justify shortly that the CLS for the even undercoordinated vicinal skin atoms is even greater.

It is clear now that atomic undercoordination creates the local strain and stress (gradient of bond energy) that reconstructs laterally and relaxes vertically inward the skin, which is intrinsically unavoidable. The skin of the fcc-structured metals consisting of at most three atomic layers or two interatomic spacings performs differently from the bulk. Therefore, the concept of skin is more meaningful and practical than the concept of surface without thickness being involved.⁸

Figures 12 and 13 show the BOLS-TB decomposed $4f_{7/2}$ spectra for the Ir, Al, and Au (001), (111), and (110) skins.²²³ Table 3 summarizes the optimal $4f_{7/2}(0,z,12)$ component and the bulk shift $\Delta E_{4f_{7/2}}(12)$ for Au skins under the common z values for the fcc structures. One can readily derive the local strain, bond length, bond energy, atomic cohesive energy, and energy density according to practice in section 5. Figure 13d shows the ZPS $4f_{7/2}$ profiles of gold foil after 100 °C O₃ oxidation at different stages.¹²⁷ Clearly, oxidation polarizes the skin but overdosage of oxygen creates H-bond network at the surface, which annihilates the skin dipoles and prevents the skin from further oxidation.⁵

Figure 14 shows the BOLS-TB decomposed 3d spectra for the Ag(100) and Ag(111) skins using the same optimized set of CNs for the fcc skins. Table 3 summarizes the optimal $E_{3d_{5/2}}(0,z,12)$ component and the $\Delta E_{3d_{5/2}}(12)$ for Ag skins.

4.4. bcc-Structured W and Mo

The apparent atomic CN in the bcc bulk is 8 instead of 12 for the fcc standard. However, one can normalize the CN by applying $z = 12(CN_{bcc})/8$. The documented best fit using the B, S_2 , and S_1 components^{204,227–229} provides reference for fine-tuning in the present XPS spectral analysis. Figure 15 shows the decomposed XPS spectra for Mo $3d_{5/2}$ and W $4f_{7/2}$ with derivatives given in Table 4.

4.5. Diamond Structured Si and Ge

Figure 16 shows the sublayer-resolved XPS Si $2p_{3/2}$ spectra^{231,232} and the Ge $3d_{5/2}$ spectra^{210,233} for their (100) and (111) skins. Table 5 lists information derived from the best fit. Fine-tuning results in $z_1 = 5.08$ instead of 4.0 for the (100) skin because the diamond structure is an interlock of two fcc unit cells. The layer-resolved Si $2p$ ^{231,232} and Ge $3d$ ^{210,233} spectra for the (100) and (111) skins show consistently that atomic undercoordination results in local quantum entrapment.

4.6. hcp-Structured Be, Re, and Ru

Figure 18a–c shows the decomposed 1s spectra for the Be(10̄10), Be(0001), and Be(11̄20) skins.^{117,119,120,202} The Be(0001) spectrum contains four components. An S_1 addition to the deeper end of the Be(10̄10) spectrum represents the undercoordinated Be atom in the Be(10̄10) kink edge. Including the B component that was counted only once, there are a total of $n = 12$ components for the Be skins and 55 possible $E_\nu(0)$ values for averaging.

According to the decomposition criteria, the common B component must exist and keep constant in all skins of the same

Table 3. Layer Order and Crystal Orientation Resolved Atomic CN(z), Optimal $E_\nu(z)$, Atomic $E_\nu(0)$, and Its Bulk Shift $\Delta E_\nu(12)$ ^a

	z	Pd 3d _{5/2}	Rh 3d _{5/2}	Ir 4f _{7/2}	Al 2p _{3/2}	Au 4f _{7/2}	Ag 3d _{5/2}	$-\varepsilon_z$ (%)	δE_z (%)	δE_D (%)	$-\delta E_C$ (%)
m		1 ¹¹³	1 ¹¹⁴	1 ^{62,219,220,222}	1 ²²¹	1 ²²³	1 ²²⁶				
$E_\nu(0)$ (eV)	0	330.261	302.163	56.367	72.146	80.726	363.022				
σ		0.003	0.004	0.002	0.003	0.002	0.003				
$E_\nu(12)$ (eV)	B	12	334.620	306.530	60.332	72.645	83.692	367.650	0	0	0
$\Delta E_\nu(12)$ (eV)	—	—	4.359	4.367	3.965	0.499	2.866	—			
(111)	S ₂	6.31	334.88	306.79	60.571	72.675	84.057	367.93	5.63	5.97	26.08
	S ₁	4.26	335.18	307.08	60.84	72.709	83.863	368.24	11.31	12.75	61.60
	D	3.14	—	—	—	—	—	368.63	17.45	21.15	115.39
(001)	S ₂	5.73	334.94	306.85	60.624	72.682	84.099	367.99	6.83	7.33	32.70
	S ₁	4.00	335.24	307.15	60.898	72.716	83.902	368.31	12.44	14.20	70.09
(110)	S ₂	5.40	334.98	306.89	—	—	84.122	—	7.62	8.25	37.33
	S ₁	3.87	335.28	307.18	—	—	83.929	—	13.05	15.02	74.99
(210)	S ₃	5.83	—	—	60.613	—	—	—	6.60	7.07	31.43
	S ₂	4.16	—	—	60.861	—	—	—	11.72	13.28	64.68
	S ₁	2.97	—	—	61.251	—	—	—	18.78	23.12	129.77
											69.53

^aSublayers S_i of the same registry share their common z value regardless of the chemical composition. “D” denotes defect. With the optimal z and known m value, one can readily derive the bond strain $\varepsilon_z = C_z - 1$, relative increases of bond energy $\delta E_z = C_z^{-m} - 1$, binding energy density $\delta E_D = C_z^{-(m+r)} - 1$, and the atomic cohesive energy $\delta E_C = z_b C_z^{-m} - 1$ in the respective sublayer accordingly. One can obtain these quantities in the subsequent analysis.

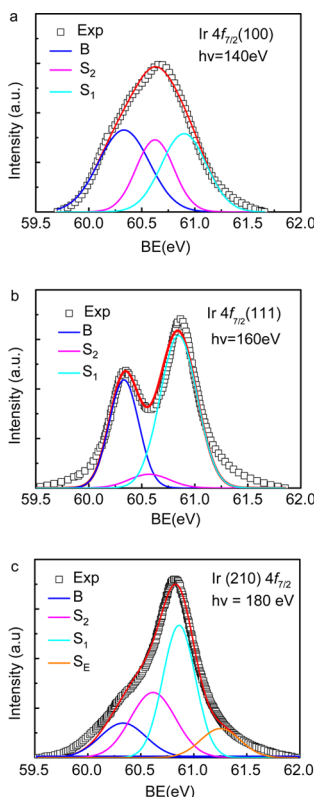


Figure 12. Decomposition of (a–c) the XPS 4f_{7/2} spectra for Ir(111), Ir(001), and Ir(210) skins^{62,219,220} and (d, e) the XPS 2p_{3/2} spectra for Al(001) and Al(111) skins²²¹ with Gaussian components representing the bulk B, S₂, and S₁ sublayers and defect D from higher to lower BE. Reprinted from ref 186. Copyright 2012 American Chemical Society. Reprinted with permission from ref 222. Copyright 2014 Elsevier.

substance regardless of geometrical orientation. However, the B component is invisible to the Be(11̄20) spectrum. This invisibility indicates that the high atomic density of the Be(11̄20) skin prevents the incident beam from penetrating into the bulk or prevents electrons from ejecting off the bulk. Deeper sublayer electrons are not energetic enough to escape

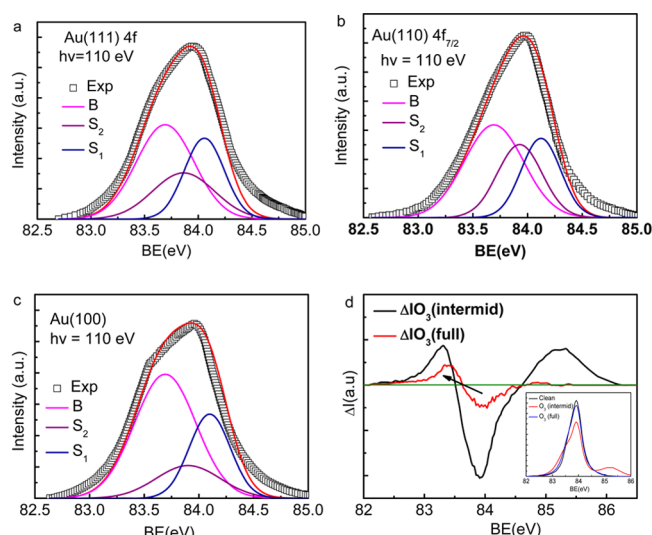


Figure 13. Decomposition of the XPS (a–c) 4f_{7/2} spectra for Au(111), Au(110), and Au(100) skins²²³ and (d) 4f_{7/2} ZPS of gold foil after O₃ treatment at 100 °C at different stages.¹²⁷ Oxidation polarizes the skin and overdosage creates an H-bond network at the surface, which annihilates the skin dipoles.⁵ Reprinted with permission from ref 224. Copyright 2015 Wiley-VCH.

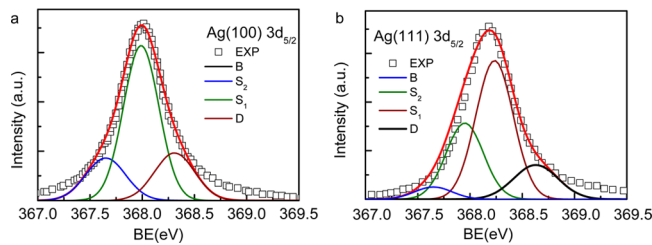


Figure 14. Decomposition of the 3d_{5/2} spectra of (a) Ag(001) and (b) Ag(111) skins^{113,225} with the bulk B, S₂, and S₁ sublayers and defect D component.²²⁶

from the crystal. This observation indicates that all the Be skins contain four atomic layers with possible addition of defects or

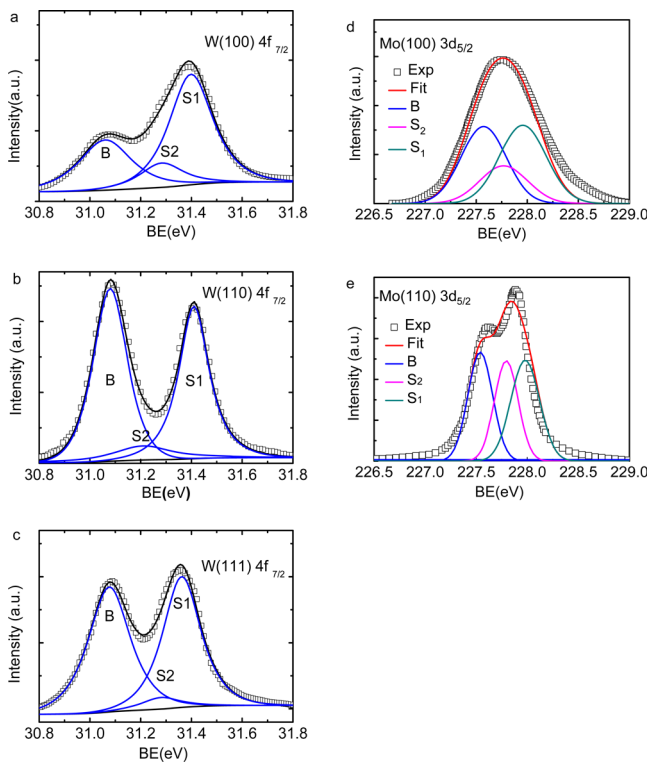


Figure 15. Decomposition of (a–c) the $4f_{7/2}$ spectra of W(100), W(110), and W(111)^{227,228} and (d, e) the $3d_{5/2}$ spectra of Mo(100) and Mo(110)^{204,229} skins using B, S_2 , and S_1 components. The baselines correspond to spectral background correction. Deconvolution also confirms the positive SCLS and leads to the quantitative information, as featured in Table 4. Reprinted with permission from ref 139. Copyright 2012 Elsevier. Reproduced from ref 230 with permission from the PCCP Owner Societies.

adatoms, rather than two in the fcc and bcc structures, because of the smaller Be atomic cross section and the high packing density. The lack of bulk information in the $\text{Be}(1\bar{1}\bar{2}0)$ spectrum also indicates the penetration depth of the 135 eV X-ray beam limited only to the outermost three atomic layers—less than 1 nm thick.

Figure 17 shows the decomposition of the Ru $3d_{5/2}$ spectra for the (0001) and $(10\bar{1}0)^{211,235}$ skins with derived information featured in Table 6.

Figure 18d–f shows the decomposed $4f$ spectra for the Re(0001) and Re(1231) skins. With respect to the data source, these skins are decomposed into three and four components, respectively, because of the $(12\bar{3}1)$ kinks. There are a total of $n =$

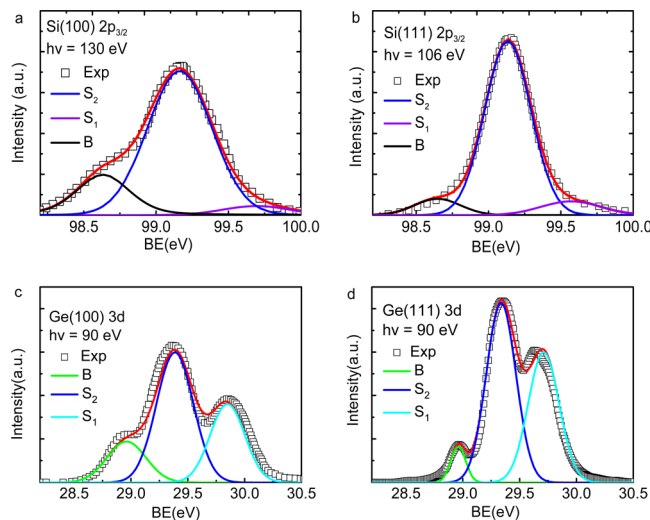


Figure 16. Sublayer-resolved (a, b) Si $2p_{3/2}^{231,232}$ and (c, d) Ge $3d_{5/2}^{210,233}$ XPS spectra for the (100) and (111) skins. Three Gaussian components represent the B, S_2 , and S_1 states. Table 4 summarizes the respectively optimized z , $E_\nu(z)$, $E_\nu(0)$, and $\Delta E_\nu(12)$. Reprinted with permission from ref 234. Copyright 2014 American Institute of Physics.

8 components and 28 possible $E_\nu(0)$ values for average. The optimized z value of 2.836 for the $(1\bar{2}\bar{3}1)$ outermost layer is lower than the value of 3.50 for the (0001) top layer. The low-energy tails in Figure 18 correspond to the quantum entrapment of the even lower coordinated defects or edge atoms.

4.7. Local Energy Density and Atomic Cohesive Energy

As the standard reference, the flat fcc(100) skin having $z_1 = 4$, $z_2 = 5.73$, and $z_{\geq 3} = 12$, the bond contracts from the bulk value to $C_1 = 0.88$, $C_2 = 0.92$, and $C_{\geq 3} = 1$, accordingly. For metals such as Au, Ag, and Cu, $m = 1$; for carbon, $m = 2.56$;¹⁵⁸ for Si, $m = 4.88$.¹ For other alloys and compounds, the m value may vary. With the given m values and the known bond energy for Cu (4.39 eV/atom), diamond (7.37 eV/atom), and Si (4.63 eV/atom),²³⁹ one can easily calculate the skin geometrical orientation and sublayer order resolved energy density E_D (in eV/nm³) and atomic cohesive energy E_C (in eV/atom), as shown in Table 7.

Results indicate that the skin E_D is always higher and that the skin E_C is lower with respect to their respective bulk values and they are in different units. Figure 19 shows the consistency between the BOLS predicted (solid curves) and the XPS derived z -dependent bond strain, $\Delta E_\nu(12)$, E_C , and E_D of solid skins.

Table 4. Sublayer-Resolved Atomic CN(z), $E_\nu(z)$, $E_\nu(0)$, Bulk Shift $\Delta E_\nu(12)$, Strain ε_z , Relative Bond Energy δE_z , Relative Atomic Cohesive Energy δE_C , and Relative Energy Density δE_D , for bcc-Structured W^{197,227,228} and Mo^{204,229}

	i	z	W $4f_{7/2}$	Mo $3d_{5/2}$	$-\varepsilon_z$ (%)	δE_z	$-\delta E_C$	δE_D
m			1^{32}	1^{230}				
$E_\nu(0)$ (eV)	–	0	28.889	224.868				
$E_\nu(12)$ (eV)	B	12	31.083	227.567	0	0	0	0
$\Delta E_\nu(12)$ (eV)		–	2.194	2.699				
σ			0.002	0.002				
(100)	S_2	5.16	31.283	227.813	8.27	9.01	53.13	41.21
	S_1	3.98	31.398	227.957	12.53	14.32	62.08	70.81
(110)	S_2	5.83	31.240	227.761	6.60	7.07	47.98	31.43
	S_1	3.95	31.402	227.962	12.67	14.51	62.31	71.92
(111)	S_2	5.27	31.275	–	7.96	8.65	52.28	39.37
	S_1	4.19	31.370	–	11.60	13.12	60.50	63.73

Table 5. Sublayer-Resolved Atomic CN(z), $E_\nu(z)$, $E_\nu(0)$, Bulk Shift $\Delta E_\nu(12)$, Strain ϵ_z , Relative Bond Energy δE_z , Relative Atomic Cohesive Energy δE_C , and Relative Energy Density δE_D , for the Diamond Structured Si^{231,232} and Ge^{210,233} Skins

	i	z	Si 2p _{3/2}	Ge 3d _{5/2}	$-\epsilon_z$ (%)	δE_z	$-\delta E_C$	δE_D
m			4.88 ¹⁶⁶	5.47				
$E_\nu(0)$ (eV)	—	0	96.089	27.579				
$E_\nu(12)$ (eV)	B	12	98.550	28.960	0	0	0	0
$\Delta E_\nu(12)$ (eV)		—	2.461	1.381				
σ			0.003	0.002				
(100)	S ₂	6.76	99.224	29.391	4.84	31.18	26.10	52.24
	S ₁	5.08	99.884	29.823	8.49	62.50	31.21	112.08
(111)	S ₂	7.08	99.143	29.339	4.34	27.47	24.79	45.62
	S ₁	5.39	99.719	29.713	7.65	54.54	30.58	96.22

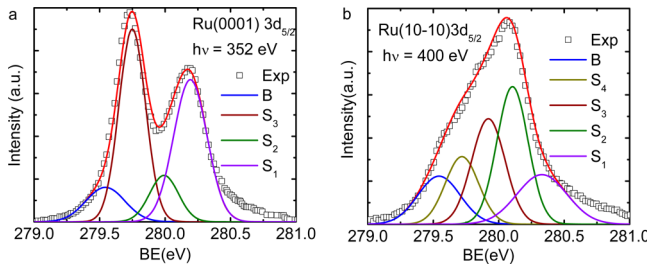


Figure 17. Decomposition of the Ru 3d_{5/2} spectra for the (0001) and (10-10)^{211,235} skins with derived information featured in Table 6. Reprinted from ref 216. Copyright 2009 American Chemical Society.

These derivatives empower the XPS in revealing such local quantitative information that is critical to devising materials.

4.8. Summary

The BOLS–TB–XPS strategy has enabled unification of the crystal-orientation and sublayer-order dependency of the CLS for skins of the fcc, bcc, hcp, and diamond structured solids with derivatives of quantitative information about the skin-resolved bond length, bond energy, BE density, and atomic cohesive energy. This strategy derives the energy levels of an isolated atom and their shift due to bulk formation and atomic under-

coordination. The orientation- and layer-order-resolved effective CN conserves for the same geometry regardless of the chemical composition.

The SCLS is always positive without any exception. Negative and mixed shifts may be possible due to the splitting and screening of the crystal potentials by skin polarization, but for the flat surface, the weak polarization is not detectable. Shorter and stronger bond between undercoordinated atoms not only raises the local energy density but also deepens the local potentials, which perturbs the Hamiltonian that determines uniquely the SCLS. However, as artifacts of measurements, the “initial–final state” relaxation and the charging effect are present throughout the course of measurements. One can correct these artifacts through background correction.

5. ADATOMS, DEFECTS, AND KINK EDGES

In this section, we discuss the following:

- Atoms with neighbors even fewer than those at the flat skin enhance the BOLS–NEP effect, which entitles nanostructures with the emerging properties that the bulk parent does not show.
- The bond between metallic adatom and its substrate is 18% shorter and 21% stronger than the bulk associated with strong entrapment and subjective polarization.

Table 6. Sublayer-Resolved Atomic CN(z), $E_\nu(z)$, $E_\nu(0)$, Bulk Shift $\Delta E_\nu(12)$, Strain ϵ_z , Relative Bond Energy δE_z , Relative Atomic Cohesive Energy δE_C , and Relative Energy Density δE_D , for the hcp-Structured Be, Re, and Ru Skins

	z	Re 4f _{5/2}	Ru 3d _{5/2}	Be 1s	$-\epsilon_z$ (%)	δE_z	$-\delta E_C$	δE_D
m		1 ³²	1 ²¹⁶	1 ²³⁸				
$E_\nu(0)$ (eV)	0	40.015	275.883	106.416				
σ		0.003	0.003	0.003				
$E_\nu(12)$ (eV)	B	42.645	279.544	111.110				
$\Delta E_\nu(12)$ (eV)		2.629	4.661	3.694				
(0001)	S ₃	6.50	42.794	279.749	111.370	5.28	5.58	42.81
	S ₂	4.39	42.965	279.992	111.680	10.79	12.10	58.99
	S ₁	3.50	43.110	280.193	111.945	15.06	17.73	65.66
(10-10)	S ₄	6.97	—	279.719	111.330	4.51	4.72	39.18
	S ₃	4.80	—	279.921	111.590	9.35	10.31	55.88
	S ₂	3.82	—	280.105	111.830	13.30	15.35	63.28
	S ₁	3.11	—	280.329	112.122	17.68	21.47	68.52
(11-20)	S ₄	6.22	—	—	111.400	5.80	6.16	44.97
	S ₃	4.53	—	—	111.650	10.27	11.45	57.93
	S ₂	3.71	—	—	111.870	13.88	16.11	64.10
	S ₁	2.98	—	—	112.190	18.70	22.99	69.46
(12-31)	S ₄	6.78	42.779	—	—	4.81	5.05	40.65
	S ₃	4.88	42.910	—	—	9.09	10.00	55.27
	S ₂	3.55	42.100	—	—	14.77	17.33	65.29
	S ₁	2.84	43.305	—	—	19.89	24.83	142.80

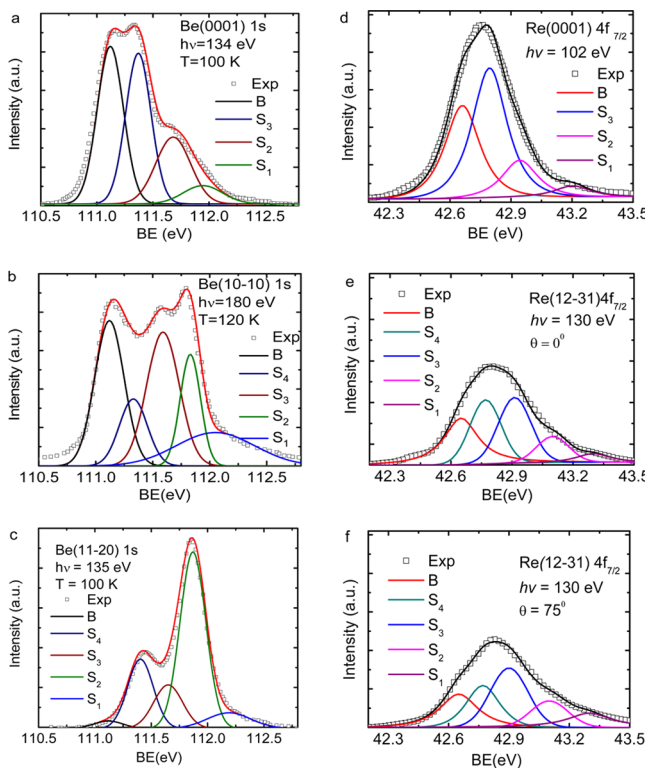


Figure 18. Decomposition of (a–c) the Be 1s spectra for the (0001), (1010), and (11-20) skins^{117,119,120,202} and (d) the Re 4f_{7/2} spectra for the (0001) and (1231) skins^{236,237} collected at (e) 0 and (f) 75° emission angles. The relative change of the S₃/B intensity with emission angle evidences the positive SCLS. Table 6 features the derived information. Reprinted from ref 32. Copyright 2011 American Chemical Society. Reproduced from ref 238 with permission from the PCCP Owner Societies.

- Shared by Re and Co edge atoms, quantum entrapment makes Pt adatom an acceptor-type catalyst.
- Shared by Au, Ag, Cu, and W adatoms, polarization entitles Rh adatom a donor-type catalyst.

5.1. Observations

Interaction between undercoordinated atoms distinguishes nanocrystals from their bulk parents in terms of size dependence of known properties and size emergence of new ones. “Size dependence” means that the quantities such as the elastic modulus and the melting point no longer remain constant but change with the shape and size of the crystal. “Size emergence” refers to properties that the parent bulk never demonstrates. For instance, nonmagnetic metals manifest magnetism at the nanoscale,^{241–243} phase transition from conductor to insulator occurs at the size of a few nanometers,²⁴⁴ nanoscale gold meets the demand of a local surface plasmon,^{245,246} and the catalytic ability of gold for CO oxidation is greatly enhanced at small

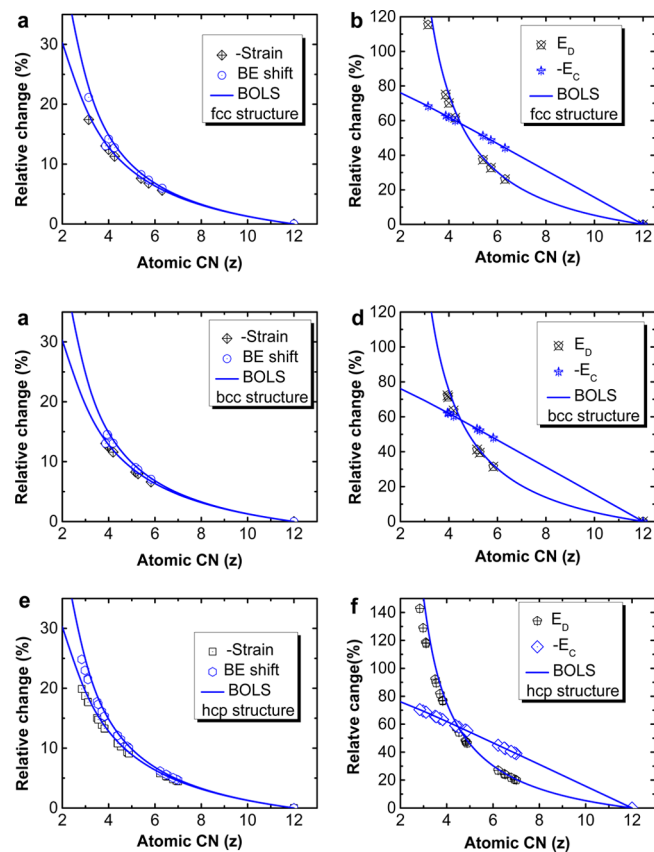


Figure 19. Consistency between the BOLS–TB predicted (solid curves) and the XPS derived *z*-dependent bond strain, $\Delta E_v(12)$, E_C , and E_D of (a, b) fcc-, (c, d) bcc-, and (e, f) hcp-structured solid skins.

sizes.^{247–249} Other intriguing properties for applications include RNA delivery, localized surface plasma resonance for Raman spectroscopy,^{250,251} laser applications in medication,²⁵² enhancement of photoluminescence,²⁵³ etc. Accompanied by the structure evolution from the fcc bulk to strained structures such as icosahedral or decahedral,^{254,255} substantial bond contraction occurs to the outermost atomic shells²¹⁷ that can be described as an elastic sheet of “skin” covering the bulk body.³

Besides the bond length contraction, potential trap depression, charge and energy density elevation, and electronic configurations occur to nanoparticles. Single-electron tunneling spectroscopy revealed the generation of an energy gap whose width is inversely proportional to the diameter of Au and Pd crystals.^{244,256} STM/S also revealed that the valence DOS of Au monomer and dimer,⁵² Au–Au chain,^{52,257} and Au nanowire²⁵⁸ moves up in energy, being an indication of local polarization. Fascinating properties demonstrated by such even undercoordinated atoms are associated with Coulomb blockade,²⁴⁴

Table 7. Bond Nature (*m*) Dependence of the Relative E_D (eV/nm³) and E_C (eV/atom) of a Skin with Respect to Their Bulk Values^a

<i>m</i>	E_D (bulk) (eV/nm ³)	E_D (skin) (eV/nm ³)	E_{Ds}/E_{Db}	E_C (bulk) (eV/atom)	E_C (skin) (eV/atom)	E_{Cs}/E_{Cb}
1 (metal, Cu)	155.04	198.60	1.468	4.39	2.00	0.455
2.56 (diamond)	1307.12	2262.63	1.713	7.37	3.86	0.524
4.88 (Si)	164.94	357.09	2.165	4.63	3.00	0.649

^aSurface free energy, E_{Ds}/E_{Db} , approximates $1 - E_{Cs}/E_{Cb}$ according to the traditional definition of the surface energy per unit area required to cut a bulk into two halves.²⁴⁰

size-dependent dynamics,²⁵⁶ and standing wave formation at edges.²⁵⁹

Atoms with even lower CNs at sites such as terrace edges, point defects, or adatoms modify the CLS significantly and irregularly. Rh adatoms modify the spectra at energies between 306.6 and 307.1 eV with features belong to neither positive nor negative CLS order.¹¹⁴ Pt adatoms enhance, however, the intensity of the 71.0 eV peak other than the 70.5 eV peak with positive shift.²⁶⁰ Terrace edges of W(110) vicinal surfaces,¹⁹⁷ Re surfaces,^{236,237} Rh(111) vicinal surfaces,²⁶¹ and Rh(110) missing-row-type reconstructed surfaces²⁶² also modify the XPS profiles irregularly. However, the signal from such lower coordinated atoms is insignificant compared to that of the skin. Direct spectral decomposition is hardly certain and less reliable.

Application of the BOLS-ZPS strategy shown in this section readily resolves this problem. The ZPS distills directly the $E_{\nu}(12)$ as a spectral valley, and the entrapment and polarization as DOS gain for the even undercoordinated adatoms, defects, kinks, chemisorbed, and reconstructed skins. The ZPS resolves a tiny change of atomic CN and trace adsorption.

5.2. ZPS of Pt and Rh Adatoms: Catalytic Nature

In order to examine the spectral features due to homogeneous epitaxy coverage of less than 1 monolayer (ML), one can appeal to the ZPS to purify bond-and-electron information due to adatoms without needing prespecification of any spectral components. The ZPS as shown in Figure 20 purifies the

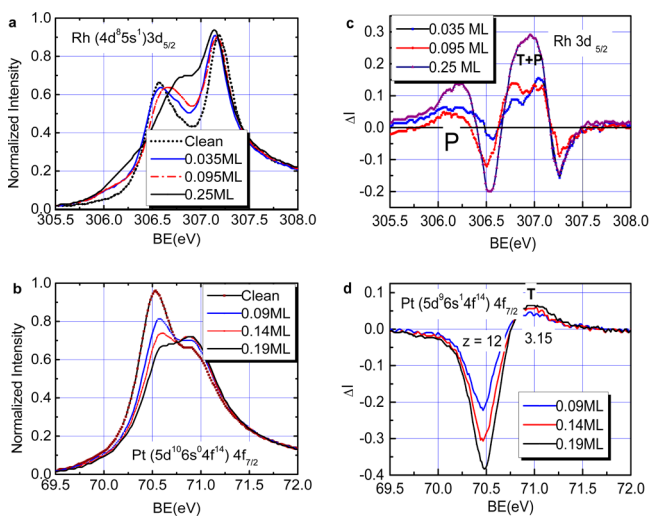


Figure 20. XPS profiles of (a) Rh 3d_{5/2}¹¹⁴ and (b) Pt 4f_{7/2}²⁶⁰ evolve with adatom coverage (ML) and the corresponding (c, d) ZPS profiles.¹⁷⁷ The ZPS valley confirms the bulk component at 70.49 for Pt and at 306.53 eV for Rh. The ZPS reveals unambiguously the atomic undercoordination-induced (c) coexistence and coupling of entrapment (T) and polarization (P) for Rh 3d_{5/2} and (d) the entrapment dominance of Pt adatoms with effective $z = 3.15$. Reprinted from ref 177. Copyright 2009 American Chemical Society.

adatom effect with additional DOS gain and the bulk/skin effect as DOS loss. The ZPS shows clearly that Pt adatoms induce only entrapment (T at 71.00 eV) at the deeper edge of the core band. The valley (70.49 eV) corresponds to the bulk component. The effective CN of the Pt adatoms is estimated to be 3.15, which is lower than the CN of 4.0 for an atom at the flat skin. The bond between the Pt adatoms and the Pt substrate is 17.5% shorter and the bond is 21% stronger compared with those in the bulk, according to the BOLS formulation.

However, the XPS profiles for Rh adatoms are much more complicated. In addition to the entrapped states at energies corresponding to $z = 4-6$, the polarized P state centered at 306.20 eV presents rendering the upward shift of the originally entrapped state that is supposed to be at $z \sim 3$. The P states are located above the bulk valley at 306.55 eV. Most strikingly, the ZPS affirms directly that the Pt bulk component is centered at 70.49 eV and that for the Rh bulk is at 306.53 eV, which is consistent with the derivative from the skin XPS analysis (Table 3 and section 4.3).

The valley at 307.25 eV for Rh arises from the screening and splitting of the crystal potential by adatom dipoles, which offset the entrapped states upwardly from effective CN = 3.15 to CN = 4–6. The conduction electrons of Rh adatoms are fully polarized, which screens the crystal potential and hence moves the core DOS up to $z = 4-6$ and creates the P + T states shifting up to pC_z^{-m} . The absence of the P states in the Pt(5d¹⁰6s⁰4f¹⁴) 4f_{7/2} spectra may indicate that the empty 6s and the fully occupied 4f¹⁴ states are hardly polarizable.

The residual 4f_{7/2} states of the hexagonally reconstructed Pt(100) surface with respect to that of the Pt(100)-(1×1) surface,²⁶³ as shown in Figure 21, manifest the same entrapment

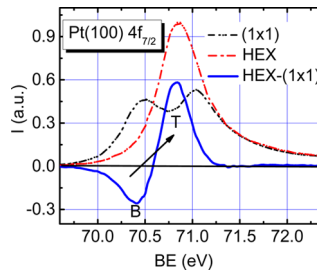


Figure 21. ZPS for the hexagonally reconstructed Pt(100) edges and the smooth Pt(100)-(1×1) surfaces²⁶³ showing the bulk valley (B) at 70.45 eV and the edge entrapment (T) at 70.80 eV. Reprinted from ref 177. Copyright 2009 American Chemical Society.

feature of adatoms. Due to the Pt–Pt distance contraction, the top layer of the reconstructed skin accommodates about 25% more edge atoms than the (100)-(1×1) layer. This fact further supports the BOLS–TB–ZPS derivatives regarding the structural relaxation and quantum entrapment by the shorter and stronger bonds between undercoordinated Pt edge atoms.

The difference in the ZPS derivatives between the Pt and the Rh adatoms confirms the BOLS–NEP expectation that the otherwise conductive half-filled s-electron Rh(4d⁸5s¹) can be polarized and locked as adatom dipoles, making less contribution to the conductivity. These locally polarized electrons are responsible for the dilute magnetism of the small clusters as well compared with their nonmagnetic parent bulk.^{1,69,264} This observation evidences that the adatom dipoles dominate the magnetism of nanocrystals.⁶⁹ However, hydrogenation annihilates the unpaired dipoles and cluster size inflation lowers the fraction of the skin dipoles of the clusters.^{2,69}

It is also clear now why the Pt and Rh adatoms perform differently in the catalytic reaction from the electronic point of view. Entrapment dominance entitles undercoordinated Pt adatoms to serve as an acceptor-type catalyst that is beneficial to oxidation but Rh adatoms to serve as a donor-type catalyst for reduction. During the reaction, Pt adatoms tend to capture electrons from the reactant while the Rh adatoms tend to donate.

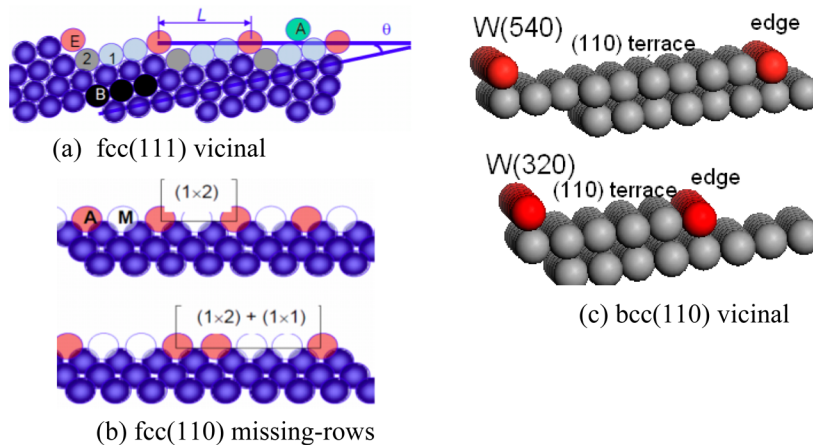


Figure 22. Schematic illustration of (a) fcc(111) vicinal (151513) and (553) skins with 0.07 and 0.26 ML edge-atom coverage ($1/L$). Denoted are adatoms (A), edge (E), surface (1, 2), and bulk (B) atoms with effective CNs in the order $z_A < z_E < z_1 < z_2 < z_B = 12$. θ is the angle between the vicinal and the ideal (111) surface. (b) The (1×2) and $(1 \times 1) + (1 \times 2)$ missing-row type reconstructed fcc(110) skins have the same 0.5 ML coverage but slightly different CNs. “M” is the vacancy. (c) The bcc(110) vicinal (320) surface with edge density of 0.28 ML and (540) skin with edge density of 0.16 ML.

Along with this guideline, it is possible to design and search for new catalysts at different needs using the ZPS spectrometrics.

5.3. ZPS of Rh, W, and Re Kink Edges

5.3.1. Atomic Arrangement at Edges. Figure 22a illustrates the vicinal fcc(111) surfaces of (151513) and (553) with an effective coverage $1/L$ (L is the edge separation) of 0.07 and 0.26 ML, respectively. The θ is the angle between the vicinal and the ideal (111) surface. There are adatom (A), edge atom (E), surface (1, 2), and bulk (B) atoms. Their effective CNs are in the order $z_A < z_E < z_1 < z_2 < z_B = 12$. Figure 22b shows the reconstructed fcc(110)-(1 \times 2) and the $(1 \times 1) + (1 \times 2)$ surfaces. Every other row of atoms is missing in the (1×2) while every other pairing row of atoms is missing in the $(1 \times 1) + (1 \times 2)$. “A” is the atom near the missing-row vacancy “M”. Although the surface coverage remains 0.5 ML, the effective CN of the E atom near the (1×2) missing-row vacancy is slightly lower than that of the other. Figure 22c is the bcc(110) vicinal surfaces with indicated red edge atoms. In contrast to the smooth hcp(0001) surface, the (1231) surface is much rougher with a higher fraction of even undercoordinated kink atoms. These even undercoordinated atoms will enhance the BOLS–NEP effect on entrapment and polarization. ZPS can resolve the effect of tiny CN difference on the CLS.

5.3.2. Rh(110) and Rh(111) Vicinal Edges. Figure 23 shows the normalized XPS profiles and the ZPS spectra for the

Rh(111) and the (110) vicinal surfaces. The ZPS reveals consistently the expected T and P features in addition to the bulk valley (“B” at 306.53 eV). For a surface with edge atoms, the peak intensity of the bulk component attenuates because of the polarization offsetting. Therefore, the ZPS reveals only one valley of B. The undercoordinated Rh atoms generally add two DOS features. One is the polarization above the B component, and the other is due to the coupling of T and P at energies corresponding to $z = 4–6$, rendering the upward shift of originally trapped states at $z \sim 3$ by pC_z^{-m} .

Despite the general features of both the quantum entrapment and the polarization of the core electrons, the (151513) (0.07 ML) in Figure 23a and the $(1 \times 2) + (1 \times 1)$ (0.5 ML) in Figure 23b exhibit weak polarization. The polarization for the former is too weak to influence the core band; the atomic CN for the latter is not low enough to induce the polarization though the overall entrapment does happen in both cases. Although the (1×2) and the $(1 \times 2) + (1 \times 1)$ in Figure 23b share the same 0.5 ML coverage, the doubly edged adatoms show a stronger polarization screening effect than the singly edged atoms (Figure 23b). Therefore, the ZPS is so far most sensitive to a tiny change of atomic CN.

5.3.3. W(110) Vicinal Edges. From the original 4f spectra in Figure 24a for the W(110), W(320), and W(540) skins collected under the same probing conditions,¹⁹⁷ one can hardly

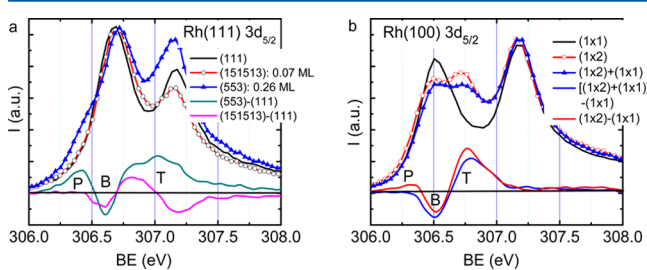


Figure 23. Comparison of XPS and ZPS for (a) Rh(111) vicinal surfaces with edges²⁶¹ and (b) Rh(110) missing-row type reconstructed surfaces.²⁶² The valley at 306.53 eV corresponds to the bulk component. Being able to resolve the tiny CN difference, ZPS spectra show the general feature of polarization screening on the core band. Reproduced from ref 265 with permission from the PCCP Owner Societies.

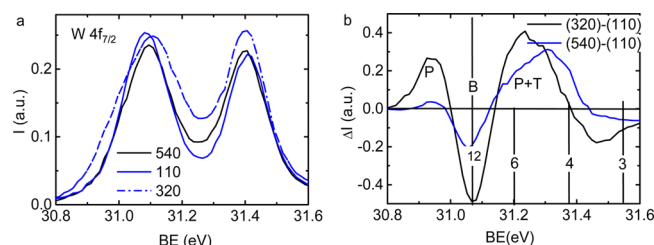


Figure 24. Normalized 4f_{7/2} spectra of the (a) W(110), W(540), and W(320) skins¹⁹⁷ hardly discriminate the vicinal edges from those of the unedged (110) surface. (b) ZPS resolves unambiguously the edge states with the P and the P + T excessive states and an additional valley at the bottom edge,²⁶⁶ which is the same as that of Rh edges and adatom: polarization dominance. Reproduced from ref 266 with permission from the PCCP Owner Societies.

discriminate one spectral feature from another. The ZPS however makes a great difference, as shown in Figure 24b, proceeding by subtracting the spectrum for the unedged W(110) spectrum from that of the edged W(540) and W(320) skins. Unexpectedly, two extra components centered at 30.95 and 31.31 eV and two valleys centered at 31.08 and 31.45 eV appear. The emergence of these spectral features indicates that the electronic structure for the edge atoms is indeed different from those at the bulk interior or at the flat surface. These spectral features are the same as that uncovered from undercoordinated Rh atoms: polarization dominance results in potential screening and splitting.

Derivatives of the CN-resolved SCLS in section 4.4 clarify the origin of the ZPS features in Figure 24. The ZPS identifies the bulk valley at 31.083 eV directly without needing any hypothetical assignment, which rectifies the bulk component that has long been mistaken at 31.45 eV.²⁰⁵ The T component below the B results from the edge quantum entrapment. ZPS confirms that the locally densely T states polarize the valence electrons of the edge atoms, which in turn screen and split the crystal potential and offsets the T states upwardly.

The polarization results in the P component at 30.95 eV. One can estimate the polarization coefficient with the known energies of the P and the B components, $p = [E_{4f_{7/2}}(p) - E_{4f_{7/2}}(0)]/[E_{4f_{7/2}}(12) - E_{4f_{7/2}}(0)] = (30.945 - 28.889)/2.194 = 93.7\%$, which means that the polarization weakens by 6.3% the crystal potential experienced by the 4f electrons in the bulk.

The otherwise T component turns out to be T + P with an additional valley at the bottom edge of the core band because of the coupling of T and P, which follows the same mechanism for the Rh adatoms and terrace edges. The screening effect also applies to the trapped states, and therefore, this valley is present and the T component becomes P + T. If C_3^{-1} is replaced with $pC_3^{-1} = C_{3.75}^{-1}$, this means that the original edge states located at $z = 3$ shift up to the energy being equivalent to $z = 3.75$. The edge bond is strengthened by $[E_{4f}(3.75) - E_{4f}(0)]/[E_{4f}(12) - E_{4f}(0)] = (31.310 - 28.889)/2.194 = 1.103$, or 10.3%, because of the joint T + P effect.

The ZPS of W edges shares the same attributes as those of Rh edges or adatoms¹⁷⁷ that have been identified as donor-type catalyst. From the electronic configuration viewpoint, one can suggest that undercoordinated W edges perform the same as Rh adatoms as donor-type catalysts, though it is subject to confirmation.

In order to verify the BOLS–NEP expectation on the skin bond contraction and valence charge polarization, DFT calculations were performed on the flat W(110) and the edged W(320) and W(540) skins focusing on the local valence DOS evolution.¹³⁹ DFT calculations also confirmed the size reduction induced 4s core band entrapment and the (4d³Ss¹) valence polarization of Mo_n clusters. Results in Figure 25 and Table 8 confirmed this expectation.

5.3.4. Re(0001) and (12̄31) Kink Edges. Figure 26a shows the ZPS of the original Re(12̄31) 4f_{5/2} and 4f_{7/2} bands^{48,127,227,228,258–261} gained by subtracting the spectrum collected at 0° from that collected at 75° emission angle after background correction and spectral area normalization.^{63,135,236,237,267–270} The obvious valleys correspond to the bulk (B) and peaks correspond to the entrapped kink edges (T). The outermost two atomic layers with the effective z values of 3.6 (S₂) and 2.8 (S₁) create the T components, as indicated in Figure

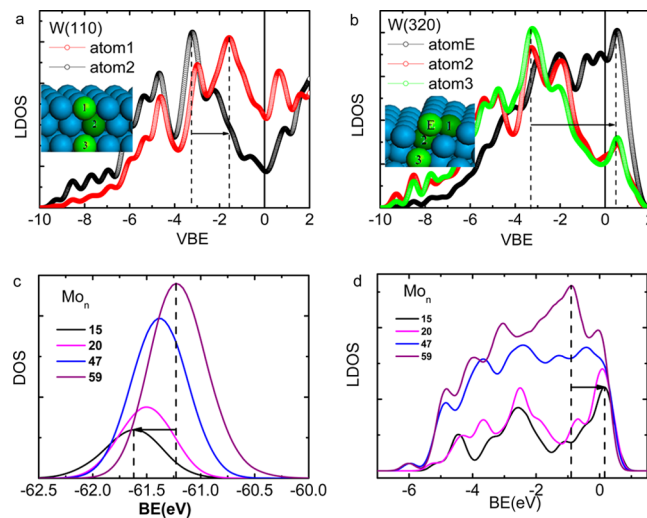


Figure 25. Coordination-resolved W(5d⁴6s²) valence DOS derived using DFT for (a) W(110) and (b) W(320) skins. Polarization of the edge atom (atom E) becomes more significant than that of the atom in the flat surface (atom 1) and those in the subsequent sublayers. Size-resolved (c) 4s core band entrapment and (d) 4d³Ss¹ valence band polarization of Mo_n clusters. Reprinted with permission from ref 139. Copyright 2012 Elsevier. Reprinted with permission from ref 230. Copyright 2015 The Royal Society of Chemistry.

Table 8. DFT Derived W Skin Bond Contraction,¹³⁹ Which Follows the Trend of BOLS Prediction though DFT Usually Underestimates the Extent of Bond Strain¹³²

	bond position	strain (%)
W(110)	1–2	-3.28
	2–3	-0.36
W(320)	E-1	-5.84
	E-2	-5.47
W(540)	2–3	-0.07
	E-1	-4.74
	E-2	-5.84
	2–3	-0.29

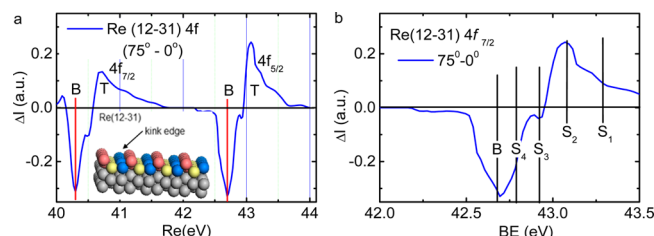


Figure 26. ZPS of (a) the kinked Re(12̄31) 4f bands.²³⁷ The B valleys correspond to bulk (B) components, and the T peaks correspond to the kink-induced quantum entrapment. (b) ZPS of the 4f_{5/2} band with the valley centered at 42.645 eV includes contribution from the B, S₄, and S₃ sublayers. The spectral gains at the bottom edge correspond to the quantum entrapment dominated by the outermost two layers of kink atoms. Reprinted from ref 32. Copyright 2011 American Chemical Society.

26b. The small feature at the upper edge of the 4f_{7/2} band arises from the Sp_{3/2} band overlap of the kinks, instead of polarization.

Figure 26b shows the ZPS of the specific 4f_{5/2} level. Two valleys centered at 42.645 and 42.910 eV correspond to the B and the S₃ components, which indicate that the B valley contains the S₄ (centered at 42.778 eV) and S₃ components. Therefore, the

ZPS reveals information on the outermost two atomic layers of the low-index ($\bar{1}2\bar{3}1$) skin. Except for the valleys, a broad peak at the bottom edge of the $4f_{5/2}$ band represents the gain of electronic energy when the S_2 and S_1 kinks are involved. The ZPS could therefore separate the kinks from their bulk mixture without needing any hypothetical assignment of the B or the skin component.

From the spectral bandwidth of the B valley, one can find that the overlap integral β is indeed negligible compared with the exchange integral α in the TB approximation. The width of a core band is $2z\beta$, and the shift of the band from that of an isolated atom is $\alpha + z\beta$. Based on the width of the B valley for both the $4f_{7/2}$ and the $4f_{5/2}$ bands of ~ 0.25 eV and the bulk shift of $\alpha + z\beta = 2.629$ eV (see Table 6), we have, $\beta/\alpha \approx 0.01/2.63 < 0.4\%$ only, in the present case.

5.3.5. O–Re($\bar{1}2\bar{3}1$) Kink Edge and Chemisorbed States.

Figure 27a,b decomposes the $4f_{7/2}$ band for the Re($\bar{1}2\bar{3}1$) surface

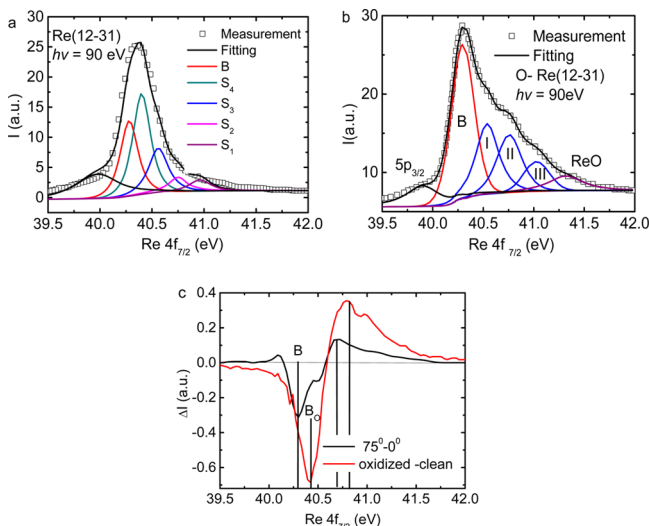


Figure 27. Decomposition of the $4f_{7/2}$ spectra collected from (a) the clean and (b) the O-adsorbed Re($\bar{1}2\bar{3}1$) skins.²³⁷ (c) ZPS for the O–Re($\bar{1}2\bar{3}1$) (red line) and for the Re($\bar{1}2\bar{3}1$) $4f_{7/2}$ kink states (black line) resolve extra gain due to the effect of oxygen chemisorption that deepens the bulk component slightly from 40.3 to 40.4 eV. The T peak corresponds to the outermost two atomic layers, which indicates that O prefers the central position of the tetrahedron.⁵ Reprinted from ref 32. Copyright 2011 American Chemical Society.

with and without oxygen chemisorption.²³⁷ A direct decomposition of the spectra for the oxygen-adsorbed Re($\bar{1}2\bar{3}1$) surface using the coordination is no longer valid because a new bond forms. The O–Re bond formation will increase the local crystal potential in the adsorbed region, which deepens the surface states, as shown in Figure 27b.^{83,268} The O-induced Re $4f_{7/2}$ shift is in line with what is detected from oxygen-chemisorbed surfaces,⁵ in which the O 2p states shift positively by an amount of ~ 0.5 eV upon oxide formation.

Figure 27c compares the ZPS for the Re($\bar{1}2\bar{3}1$) surface with and without oxygen adsorption. A B_O valley centered at 40.40 eV is different from the B (40.30 eV) and the S_4 in the referential ZPS of the unadsorbed surface. This difference indicates that the O–Re bond is much stronger and the synchrotron beam of 90 eV collects less information from the bulk or the S_4 region. The extra states extend to energy that is even lower than the energy states of the clean surface. The ZPS has thus enabled discrimination of the chemisorbed surface states from its mixture with the bulk and

thus allowed one to estimate the depth of two atomic layers involved in oxygen adsorption. Oxygen adsorbate tends to locate between the first and second sublayers preferring the central position of the tetrahedron by interacting with two metal atoms through bonding and two through nonbonding lone pairs of electrons.⁵

5.4. Summary

Table 9 summarizes BOLS–NEP–ZPS derived information in comparison with that derived from traditional practice induced by the even undercoordinated atoms. Most importantly, the effect of polarization is beyond the scope of traditional analysis.

The following summarizes the physical understandings of the even undercoordinated atoms ($z < 4$):

1. Adatoms, terrace edges, and kinks share the same attributes of global quantum entrapment and subjective polarization, of which the bulk or skin atoms do not demonstrate.

2. Bonds between such undercoordinated atoms and the substrate are even shorter and stronger than those are in the flat skin. The lower the atomic CN, the shorter the bond length and the deeper the potential well will be, and hence, the higher extent of polarization occurs to the even lower coordinated atoms.

3. The polarization dominance makes Rh adatoms or terrace edges to be donor-type catalyst. The same trend of W edges may make W a possible candidate for catalytic reduction applications.

4. The entrapment dominance makes Pt adatoms and edges acceptor-type catalysts. Re could be a possible alternative for acceptor-like catalyst because of the same DOS relaxation feature.

5. Oxygen chemisorption deepens the Re($\bar{1}2\bar{3}1$) SCL due to the stronger O–Re bond formation in the outermost two atomic layers.

6. Being sensitive to the small change of atomic CN and adsorption, ZPS gives direct information on the B valley without needing any assumptions as are usually done in spectral decomposition.

6. ATOMIC CHAIN ENDS, CLUSTERS, AND NANOCRYSTALS

In this section, we discuss the following:

- Au monatomic chain ends and Ag and Cu adatoms exhibit polarization dominance, but Co and Si nanocrystals exhibit entrapment.

- ZPS resolves the global entrapment and subjective polarization of even undercoordinated atoms.

- APECS resolves Ag, Cu, and Ni particle–substrate interaction and two-band cooperative shift.

- Curvature enhanced entrapment or polarization entitles nanocrystals to the size emergence of properties that the bulk parent never shows.

6.1. Observations

When the atomic CN increases from 0 to the fcc bulk standard 12, the CL shifts from the $E_v(0)$ to a maximum at $z = 2$ and then recovers in a K^{-1} fashion to the bulk value of $E_v(12)$. The amount of the CLS depends not only on the specific $E_v(0)$ value but also on the shape and size of the crystal. Au, Ag, Ni, Cu, Pd, Si, C, and their compounds^{6,105,131,162,271–278} follow this size CLS trend. Calculations revealed that bonds in Ag, Cu, Ni, and Fe atomic chains contracted by 12.5–18.5% with 0.5–2.0 eV gain of bond energy.^{279,280} The 2p levels of Cu_{18} and Ni_{18} clusters undergo positive shifts from their bulk values by 0.7–0.8 eV while the average strain of the clusters increases from 0 to $\sim -6\%$.⁷³ These

Table 9. BOLS–NEP–ZPS Analysis of the Electron BE Shift of the Even Undercoordinated Atoms That Leads to Quantitative Information about the Energy Level of an Isolated Atom and the Associated Entrapment and Polarization^a

energy levels	site	<i>z</i>	<i>C_z</i>	<i>d_z</i> (Å)	<i>E_z</i> (eV)	<i>E_v(z)</i> (eV)
Rh(100) 3d _{3/2} ¹¹⁴	atom	0				302.16
	bulk	12.0	1.00	2.68	0.48	306.53
	(100) S ₁	4.0	0.88	2.36	0.54	307.15
	adatom	3.0	0.82	2.20	0.58	307.51
	polaron					306.20
W(110) 4f _{7/2} ¹⁹⁷	atom	0				31.083
	bulk	12	1.00	2.79	1.11	33.256
	(110) S _{1(p)}	6	0.94	2.61	1.19	33.401
	kink(<i>p</i>)	4	0.88	2.44	1.29	33.565
	polaron					28.910
Pt(111) 4f _{7/2} ²⁶⁰	atom	0				68.10
	bulk	12.00	1.00	2.77	0.4867	70.49
	S ₁	4.25	0.89	2.47	0.5468	70.91
	adatom	3.15	0.83	2.20	0.5935	71.18
Re(12̄31) 4f _{5/2} ²³⁷	atom	0				40.014
	bulk	12	1.00	2.75	0.67	42.643
	S ₁	3.6	0.86	2.35	0.78	43.088
	kink	2.8	0.80	2.19	0.84	43.310
Re(12̄31) 4f _{7/2} ²³⁷	S ₁	3.6	0.86	2.35	0.78	40.30
	O-(12̄31)S ₁ ^b					40.65

^aWith the derived *z*, *d_z*, and *E_z*, one is able to find *E_D* and *E_C* (the skin and adatom components and their effective CNs are subject to offset by polarization *pC_z^{-m}*). ^bO sits between the outermost two layers.

observations evidence the shortening and strengthening of bonds between undercoordinated atoms.

The S 2s and S 2p bands of ZnS and CdS nanosolids each exhibit three components.^{281,282} These components correspond to the outermost capping layer, the surface layer, and the core of the nanosolid. The capping layer and the surface layer are each 0.2–0.3 nm thick. Particle size reduction enhances the intensities of the capping layer and the surface components rendering the intensity of the core component, which follows the size dependence of the surface-to-volume ratio of a nanosolid. These observations evidence that cluster size reduction enhances globally the CLS for nanostructures, regardless of composition or structure phase.⁶

This section shows that incorporation of the BOLS–NEP scheme to STM/S, PES, APECS, and ZPS as well as DFT calculations leads to consistent understanding of the performance of atomic clusters and nanocrystals from the perspective of local bond contraction, quantum entrapment, and nonbonding (valence) electron polarization.

6.2. BOLS–TB Formulation

The size dependent CLS of a nanocluster follows the core–shell configuration:^{186,187}

$$\frac{E_v(K) - E_v(12)}{E_v(12) - E_v(0)} = \begin{cases} \Delta_H(\tau, m, K) & (\text{BOLS}) \\ B_v/K & (\text{measurement}) \end{cases} \quad (23\text{a})$$

$$\Delta_H(\tau, m, K) = \sum_{i \leq 3} \gamma_i(C_i^{-m} - 1) \quad (\text{perturbation}) \quad (23\text{b})$$

$$\gamma_i = \tau C_i K^{-1} \quad (\text{surface to volume}) \quad (23\text{b})$$

The perturbation Δ_H is bond nature *m*, cluster size *K*, and geometrical shape τ dependent. B_v is the slope of the linearization of the measured size dependent CLS for nanocrystals. The perturbation counts the weighted contribution of the outermost three atomic layers. The $C_i^{-m} - 1$ term is exactly what is used for

defects and solid skins with different *z* values. Therefore, nanostructure is an extension of the point defects and solid skins of varied curvatures and core–shell configuration.

The following illustrates how to resolve the cluster size dependent CLS when the τ , *m*, $E_v(12)$, and $E_v(0)$ are yet to be known. First, one can obtain the $E_v(12)$ by linearizing the measurements $E_v(K) = b + B'/K$. The intercept at the vertical axis is the $E_v(12)$. Equaling the BOLS prediction to the measurement yields $\Delta_H = (B_v/K)$ and $B_v = \tau \sum_{i \leq 3} C_i(C_i^{-m} - 1)$. One can determine the *m*, τ , and $E_v(0)$ from measurements using this relationship with the known $C_i(z)$ given in eq 5 and the known *z_i* in eq 8. The accuracy of quantities estimated from analyzing the XPS data for nanostructures is often 1 order of magnitude lower with respect to that derived from skin XPS analysis as the former is subject to the accuracy and uniformity of particle sizes.

6.3. Gold

6.3.1. STM/S-DFT: End and Edge Polarization. STM/S profiles in Figure 28a,b reveal that the chain-end Au atoms on Si(553) substrate are topologically higher than those in the chain interior associated with a new DOS feature at −0.5 eV below E_F .⁵² This observation indicates the presence of edge atom polarization by the densely entrapped electrons of bond between the edge atom and its nearest neighbor. The polarization increases the atomic volume and raises the energy of the local valence states. The dI/dV profiles for wires of different thicknesses in Figure 28c,d further evidence the size trends of polarization. The wire of narrower (red) cross section exhibits stronger polarization.²⁵⁸

Using electron cohesive diffraction, Huang et al.¹⁰⁷ uncovered that the Au–Au bond contracts only in the outermost two atomic layers of a gold nanosolid in a radial way, which is further supported by molecular dynamics (MD) simulations.²¹⁷ The Au–Au bond of a 3.5 nm size Au crystal contracting by 7% (Figure 28b)¹⁰⁷ is below BOLS expectation. The equilibrium Au–Au bond in the monatomic chain contracts by 30% from the

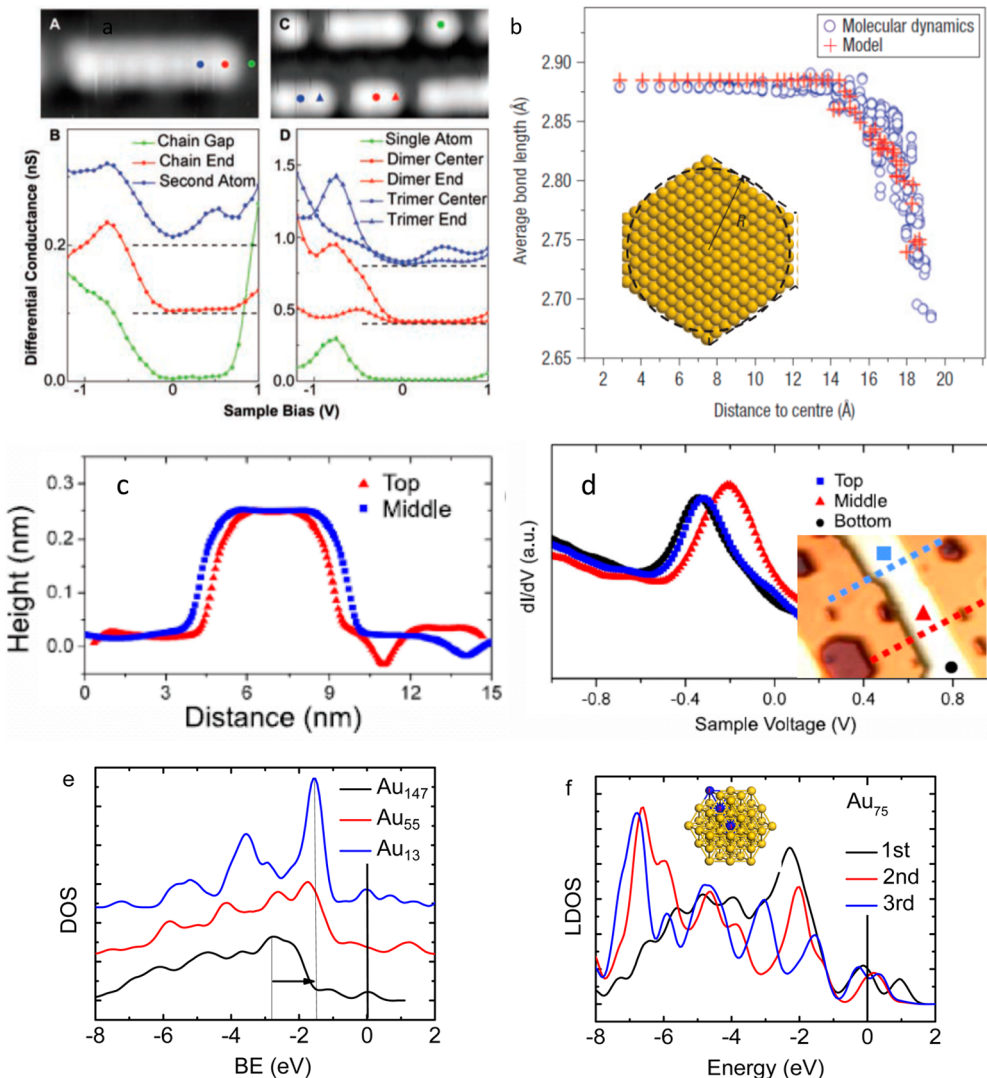


Figure 28. (a) STM/S discriminates morphology and energy states of Au atoms at the ends from that in the interior of the chain. Reprinted from ref 52. Copyright 2005 American Association for the Advancement of Science. (b) Coherent electron diffraction and MD derived Au skin bond contraction in a 3.5 nm crystal (inset). Reprinted with permission from ref 107. Copyright 2008 Nature Publishing Group. STM/S (c) line scans (inset in d) of an Au nanowire of different thickness and (d) the respective dI/dV spectrum. Results show the width effect on the polarization of the valence DOS. Reprinted with permission from ref 258. Copyright 2009 IOP Publishing Ltd. Polarization of the (e) size-resolved valence DOS and (f) shell-resolved LDOS of an Au_{75} cluster (inset denotes the layer number). Reprinted with permission from ref 131. Copyright 2010 The Royal Society of Chemistry.

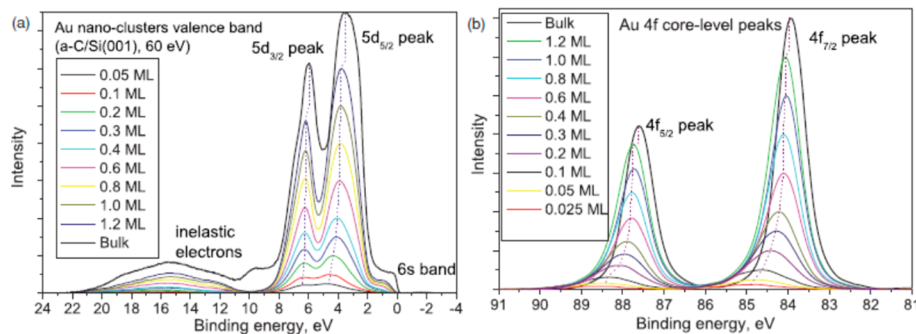


Figure 29. Size induced positive BE shift of the spin-degenerated (a) $5\text{d}_{3/2}$, $5\text{d}_{5/2}$ valence band (60 eV beam energy) and (b) $4\text{f}_{7/2}$, $4\text{f}_{5/2}$ core band (140 eV) of Au clusters grown on amorphous carbon. Reprinted with permission from ref 284. Copyright 2011 American Physical Society.

bulk value of 0.29 to 0.20 nm at 4 K, according to the thermally resolved strain limits of the chain.¹⁶¹ The Au–Au bond contracts by 12% in the fcc(100) skin. The CN-resolved bond contraction is insensitive to the types of substrate support²⁸³ or to the

structural phase or particular elements or the nature of the bond.^{1,3}

DFT calculations of Au clusters with 13–147 atoms have confirmed the BOLS–NEP predictions (Figure 28e, f).¹³¹

- The Au–Au bond contracts by up to 30%.
- The valence charge transfers from the inner to the outer atomic shells of the crystal.
- The valence charge transits from lower to higher binding energies and the extent of polarization is more significant for smaller clusters than for larger ones.
- Such polarization should be responsible for the enhanced catalytic ability of Au adatoms.

Further DFT calculations for the binding mechanism between gold nanoparticles and DNA bases confirmed that⁵⁶ negative charges transfer from the inner area to the skin of Au nanoparticle as a result of the local quantum entrapment and the valence states shift up toward the Fermi level due to polarization. Thereby Au dipoles participate more actively in the binding to guanine. These effects are more prominent in a smaller nanoparticle. Fragment orbital analysis revealed that electron donation from the lone-pair orbital of N to the unoccupied orbital of the Au cluster occurs in all complexes.

6.3.2. PES: 4f and 5d Bands. Visikovskiy and co-workers²⁸⁴ measured the size dependence of the 5d valence band and the 4f core band of Au nanoclusters deposited on amorphous carbon. They examined the d-bandwidth $W(d)$, d-band center position $E(d)$, and the apparent $5d_{3/2}, 5d_{5/2}$ spin-orbit splitting $E(SO)$, as a function of the number of Au atoms per cluster, Au_n , and an average atomic CN in the size range of $11 < n < 1600$. Figure 29 shows that both the 5d valence band and the 4f core band shift positively when the cluster size is reduced without apparent polarization.

Figure 30 shows the size-induced positive shift of the 4f band for the thiol-capped Au²⁸⁵ and Au clusters deposited on Octan (octanedithiol),²⁷⁸ TiO₂,²⁸⁶ and Pt²⁸⁷ substrates, which agrees with those obtained from Au deposited on CNT,^{271,288} highly oriented pyrolytic graphite (HOPG),^{289,290} SiO₂,^{291–294} GaN,^{295,296} and Re²⁸⁷ substrates. However, the 4f of Au on

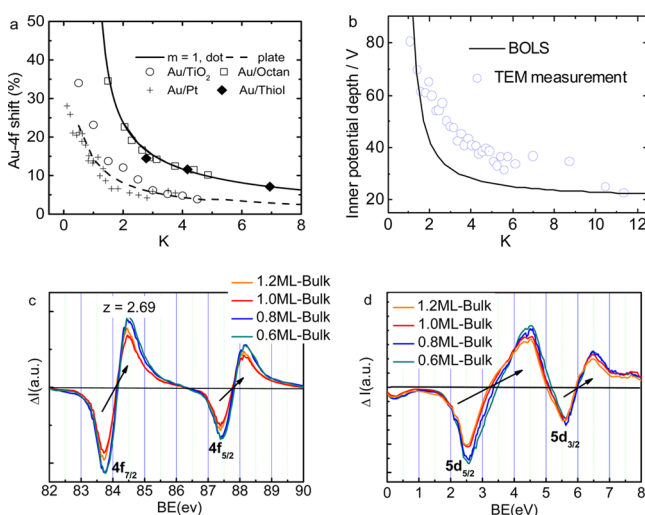


Figure 30. BOLS (solid line) reproduction of the measured (scattered) size dependence of (a) the relative shift³⁰⁰ $\Delta E_{4f}(K)/\Delta E_{4f}(\infty) - 1$ and (b) the muffin-tin inner potential of gold clusters.^{131,299} The thiol-capped Au²⁸⁵ and Au on Octan²⁷⁸ show three-dimensional features, while Au on TiO₂²⁸⁶ and Pt²⁸⁷ show two-dimensional patterns of formation. (c, d) ZPS distilled BE shift of the spin-degenerated 5d and 4f band of Au grown on amorphous carbon (raw data in Figure 29). Reprinted with permission from ref 6. Copyright 2004 American Physical Society. Reprinted from ref 300. Copyright 2004 American Chemical Society.

Pt²⁸⁷ shifts oppositely and the 4f of Au on NiO(100) remains unchanged²⁹⁷ because of the involvement of interface alloying effect.

6.3.3. BOLS–TB Quantification. With the known size dependent CN, $z_1 = 4(1 - 0.75/K)$, $z_2 = z_1 + 2$, and $m = 1$,²⁹⁸ BOLS formulation of the measured $\Delta E_{4f}(K)$ of Au on Octan gives $E_{4f}(0) = 81.50$ eV and $\Delta E_{4f}(\infty) = 2.86$ eV, agreeing with that derived from skin XPS analysis (section 4.3). Formulation (see Figure 30a) revealed that Au growth on TiO₂ and on Pt(100) substrates proceeds in a layer-by-layer fashion.^{286,287} The size-induced deepening of the inner muffin-tin potential of gold NPs in Figure 30b²⁹⁹ follows the same size trend.

The ZPS profiles of the 5d and 4f spectra, in Figure 30c,d, of selected coverages show that both the 5d and the 4f bands undergo quantum entrapment but by different amounts. As expected, the upper 5d band shifts more than the inner 4f band does. The ZPS resolves the relative shift of the spin-degenerated 4f band as $[E_{4f_{5/2}}(K) - E_{4f_{7/2}}(K)]/[E_{4f_{5/2}}(\infty) - E_{4f_{7/2}}(\infty)] \approx (88.2 - 84.5)/(87.4 - 83.7) = 1$ and the 5d band as $(6.5 - 4.4)/(5.6 - 2.5) = 2.1/3.1 \approx 2/3$, respectively. The valence 5d band is more sensitive to the chemical and coordination environment than the inner bands. Table 10 summarizes information gained from duplicating the 4f size tends of Au deposited on various substrates.

Table 10. $E_{4f}(0)$ of an Isolated Au Atom and its Bulk Shift $\Delta E_{4f}(12)$ Obtained from Decoding the Size-Dependent $E_{4f}(K)$ of Au Nanosolids⁶ in Comparison to That Derived from Skin XPS Analysis (Table 3)^a

	Au/Octan	Au/TiO ₂	Au/Pt	Au skins
m^6	1	1	1	1
τ	3	1	1	1
$E_{4f}(0)$	81.504	81.506	81.504	80.726
$E_{4f}(12)$	84.370	84.370	84.370	83.692
$\Delta E_{4f}(12)$	2.866	2.864	2.866	2.866

^aThe charging effect of nanocrystals offset the $E_{4f}(0)$ but not the $\Delta E_{4f}(12)$.³⁰⁰

6.4. Silver

6.4.1. STM/S–DFT: Adatom Polarization. STM/S profiles in Figure 31a show the polarization (bias positive) of Ag atoms added onto Ag(111) surface.^{99,301} The extent of polarization increases with the reduction of cluster size. The shell-resolved LDOS and the size-resolved DOS in Figure 31b,c follow the same trend of BOLS–NEP prediction of polarization. The outermost shell of a cluster and the smallest dot polarize the valence electrons most.²⁷⁷ The size-enhanced polarization may explain why Ag particles could enhance the Raman signal or plasmonics with respect to their bulk parent³⁰² and why the size and shape influence its biocide property³⁰³ from the perspective of core electron local quantum entrapment and valence charge polarization.

6.4.2. APECS: 3d and 5s Band Cooperative Shift. Figure 32 shows the APECS profiles for Ag particles deposited on CeO₂ surface,^{304–307} which is the same as that of Ag clusters on Al₂O₃ surface.^{188,308–310} Results show consistently that the $\Delta E_{3d_{5/2}}$ increases and the Auger parameter ($E_{3d} + E_K$) drops in magnitude when the crystal size is reduced. Ag particle size reduction polarizes the valence charge slightly. The 3d states of Ag particles on HOPG³¹¹ and on TiO₂³¹² follow the same size

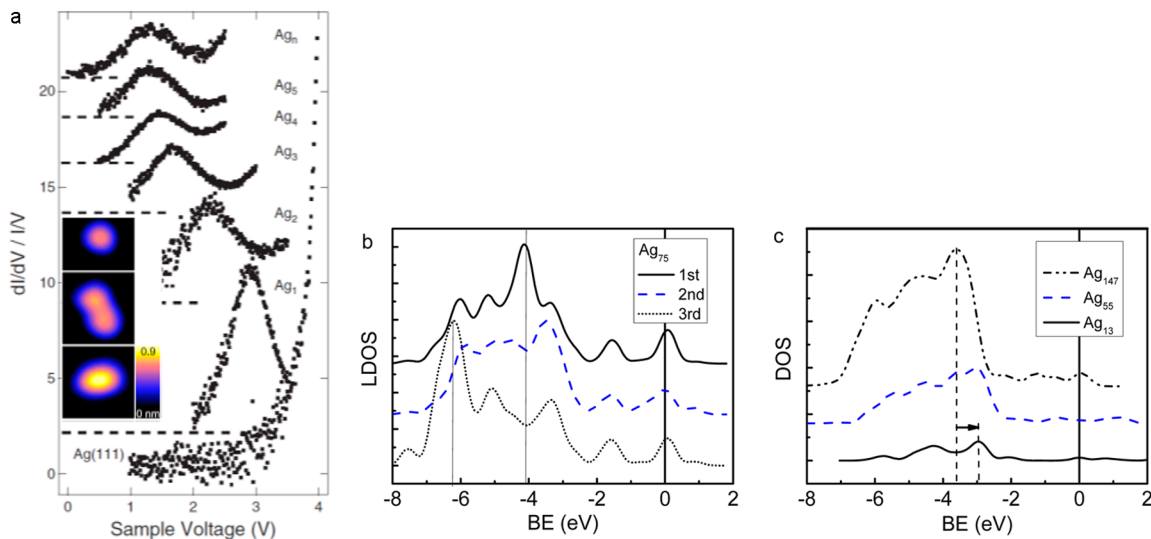


Figure 31. (a) STS spectra of Ag clusters deposited on Ag(111) surface with inset showing STM images of Ag₁, Ag₂, and a quasi-dimer (middle). Reprinted with permission from ref 99. Copyright 2009 IOP Publishing Ltd. Reprinted with permission from ref 301. Copyright 2008 American Physical Society. DFT derived shell-resolved (b) Ag₇₅ LDOS and (c) size-resolved DOS polarization for Ag_n clusters. Reproduced from ref 277 with permission from the PCCP Owner Societies.

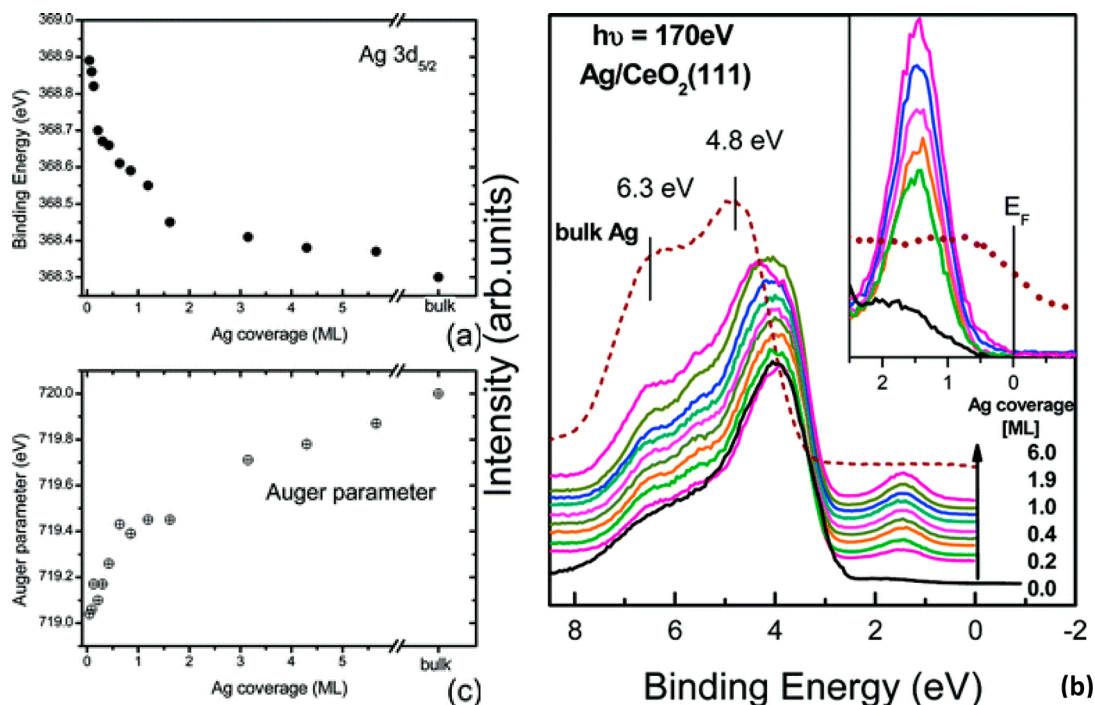


Figure 32. Size dependence of the (a) 3d_{5/2} BE entrapment, (b) valence band polarization, and (c) Auger parameter reduction of Ag particles (coverage) on CeO₂(111) surface at 300 K. Reprinted from ref 307. Copyright 2011 American Chemical Society.

trend of quantum entrapment. Conversely, the CL shifts more at lower measuring temperature.³¹¹

6.4.3. BOLS-TB Formulation and Quantification. To formulate the size trends of the APECS involved energies for Ag particles, we need to obtain the dimensionality τ and the bond nature index m of Ag clusters on different substrates. Because there is no charge transfer between the CeO₂ substrate and the Ag nanoclusters,³⁰⁷ $m = 1$ holds for Ag/CeO₂ clusters.¹ Linearization of the measured size trend $E_{3d_{5/2}} - K$ turns out the slope $B_\nu = 5.567$ and the intersection $E_{3d}(\infty) = 368.25$ eV. The slope gives the dimensionality $\tau = 1.45$ (see eq 23a), based on the known $z_i(K)$ relationship, $z_1 = 4(1 - 1.5/K)$. Because Ag

particles have the same shape when grown on CeO₂ and Al₂O₃ substrates,³⁰⁸ the value τ holds for both.¹ However, the bond nature of Ag derived from the experiment is different because of charge transfer between Ag and Al₂O₃ substrate.³¹⁰ Similarly, linearization of the measurement results in the B_ν and $E_{3d}(\infty)$ gives $m = 3.82$ for Ag/Al₂O₃ clusters. The higher m value indicates that the Ag bonds strongly to the Al₂O₃ substrate, as revealed by DFT calculations.³¹⁰

With the derived m and τ values, BOLS formulation resolves the size dependence of the 3d_{5/2}, the valence 5s band, and the Auger E_K of Ag particles. Figure 33a,b show the BOLS reproduction of the measurements, and Table 11 features the

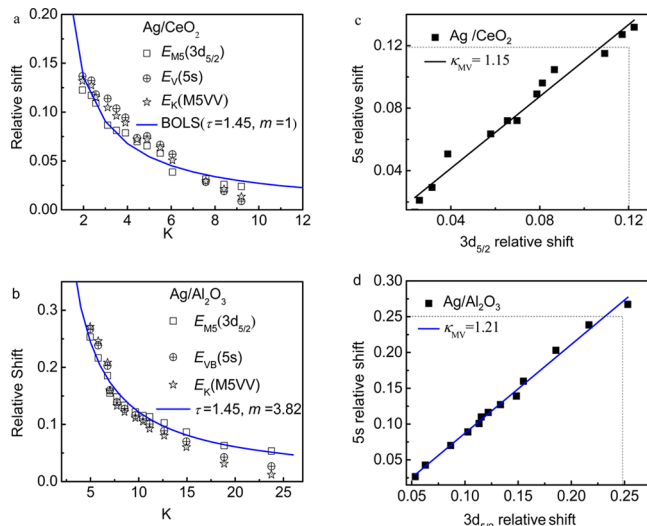


Figure 33. BOLS reproduction (solid line) of the size trend of E_{3d} , E_{Ss} , and E_K (scattered data) for Ag particles deposited on (a) CeO₂³⁰⁷ and (b) Al₂O₃³⁰⁸ substrates. The extended Wagner plots (c, d) correlate the relative shift of the $[\Delta E_{Ss}(K)/\Delta E_{Ss}(12) - 1] = \kappa_{MV} [\Delta E_{3d}(K)/\Delta E_{3d}(K) - 1]$ for Ag clusters. Reprinted from ref 186. Copyright 2012 American Chemical Society.

Table 11. BOLS–APECs Derived $E_{3d}(z)$, $E_{Ss}(z)$, and $E_K(z)$ for Ag Clusters¹⁸⁶ and BOLS–XPS Resolved CN(z), $E_{3d_{5/2}}(0)$, and $\Delta E_{3d_{5/2}}(\infty)$ for Ag(100) and (111) Skins,^{113,225} (Reprinted from ref 186. Copyright 2012 American Chemical Society.)^a

APECs	Ag/Al ₂ O ₃	Ag/CeO ₂	Ag skin
m^{186}	3.82	1	1
τ	1.45 (dome)	1.45 (dome)	1
$E_{3d}(\infty)$	367.59	368.25	367.650
$E_{3d}(0)$	363.02	363.02	363.022
$\Delta E_{3d}(\infty)$	4.57	5.23	4.628
$E_{Ss}(\infty)$	7.56	8.32	
$E_{Ss}(0)$	0.36	0.36	
$\Delta E_{Ss}(\infty)$	7.20	7.96	
$E_K(\infty)$	352.45	351.61	
$E_K(0)$	362.30	362.30	
$\Delta E_K(\infty)$	-9.85	-10.69	
η_{MV}	1.55	1.52	
κ_{MV}	1.21	1.15	

^a $K = \infty$ is equivalent to $z = 12$ for the ideal bulk. The screening coefficient η_{MV} shows the relative BE in the deeper 3d and the upper 5s levels. The recharging coefficient κ_{MV} describes the chemical process. One can also derive ε_z , E_ν , E_C , and E_D for the skins and the nanoparticles with the known relationship $\Delta E_\nu(K) = [\Delta E_\nu(\infty)](1 + \Delta_H)$, where $\Delta_H(\tau, m, K) = \tau K^{-1} \sum_{i \leq 3} C_i (C_i^{-m} - 1)$.

derivatives. Figure 33c,d shows the extended Wagner plots of Ag nanostructures on CeO₂ and Al₂O₃ substrates. The $E_{3d}(0)$ and $E_{3d}(\infty)$ derived from the XPS of clean Ag skin (see Table 11) and from the APECs are consistent, evidencing that the BOLS governs the energy shift as probed using both XPS and APECs.

Parameters m , κ_{MV} , and η_{MV} characterize the interface reaction or skin chemical conditioning. A higher m value means that a stronger chemical bond forms between the cluster and the substrate. The κ_{MV} describes the effect of valence recharging during processing. The κ_{MV} in Table 11 is almost independent of the shape and size of the particle, but it is sensitive to the chemical

treatment. If charge transfers from one constituent to another, κ will increase; otherwise it remains unity. The $\eta_{MV} \approx 1.21/1.15$ means that the strength of crystal binding to the VB(5s) level is η_{MV} times stronger than that to the deeper M5(3d) level. Polarization happens only to the antibonding vacant states or to the upper edge of the valence band in this case. The polarization of Ag is not strong enough to split and screen the local potential as the valence electrons of Rh and W specimens do.

6.5. Copper

6.5.1. STM/S–PES–DFT: Entrapment and Polarization.

Figure 34 shows the low-temperature STM/S profiles for Cu atoms added on Cu(111) surface¹⁰⁰ and the size-resolved DOS of Cu_n clusters and the shell-resolved LDOS of a Cu₇₅ cluster. Both STM/S and DFT confirm consistently that the densely locally entrapped bonding electrons polarize the valence and the conduction states. PES measurements, in Figure 35, further confirm (Figure 35a) the valence DOS polarization³¹³ and (Figure 35b) the 2p band entrapment,³¹⁴ which is the same as that of Au and Ag clusters.

6.5.2. APECs: Interface 2p and 3d Energy Shift.

Yang and Sacher^{315–317} systematically studied the 2p shift of Cu nanoparticles deposited on HOPG and Cyclotene 3022 (CYCL, a polymer of microelectronic industry interest) under various conditions using APECs. They also examined the effect of Ar⁺ and N⁺ bombardment on the 2p energy shift of Cu nanocrystals. Figure 36a,b shows that both the 2p_{3/2} and the Auger parameter shift following the K^{-1} scaling relation, eq23a: $\Delta E_\nu(K) = K^{-1} [\tau E_\nu(\infty) \sum_{i \leq 3} C_i (C_i^{-m})] = B_\nu K^{-1} \pm (0.01–0.02)$, where B_ν is the slope and σ is the standard deviation of linearization.

Wu et al.³¹⁸ examined the 2p shift for Cu films deposited on Al₂O₃ substrate at 80 and 300 K substrate temperatures. They found that both the 2p_{3/2} and the Auger parameter shift not only with the film thickness but also with the substrate temperature; see Figure 36c,d. Heating weakens interatomic interaction, which reduces the 2p_{3/2} shift but increases the Auger energy E_{KM} .

6.5.3. BOLS–TB Formulation and Quantification.

The BOLS–TB formulation extracts bonding and electronic information from these nice sets of data. The linearization of the size dependent APECs peaks of Cu/HOPG gives the slope B_ν and the interception that corresponds to the $E_{2p}(\infty) = 932.7$ eV.³¹⁹ The slope corresponds to $m = 1$ for the Cu spherical dot ($\tau = 3$). Fitting to the $E_L(K)$, the $\alpha'(K)$, the $E_M(K)$, and the $E_K(K)$ curves, one can obtain the responsive $E_\nu(0)$ and $E_\nu(\infty)$ values for the Cu/HOPG clusters. Figure 37 presents the fitting to the size dependent APECs lines.

Table 12 presents information derived from the formulation of observations. The atomic 2p level energy $E_{2p}(0) = 931.0$ eV and its bulk shift $\Delta E_{2p}(\infty) = 1.70$ eV. Likewise, the $E_{3d}(0) = 5.11$ and the $\Delta E_{3d}(\infty) = 2.12$ eV. The $E_{3d}(0)$ corresponds to E_F and $E_{3d}(\infty) = E_{3d}(0) + \Delta E_{3d}(\infty) = 7.23$ eV is the upper edge of the Cu 3d band.^{3,8,320}

Further formulating the size-induced $\Delta E_{2p}(K)$ for Cu/CYCL clusters by taking $\Delta E_{2p}(\infty) = 1.70$ eV reference turns out $m = 1.82$, which indicates that the Cu/CYCL interface interaction is stronger than that of Cu/HOPG. Repeating the iteration using the same values of $\Delta E_{2p}(\infty) = 1.70$ and $\Delta E_{3d}(\infty) = 2.12$ eV to the APECs lines of other chemically treated Cu samples results in m values that vary with the processing conditions, as shown in Figure 38.

As compared in Figure 38 and Table 12, BOLS–TB duplication of the measured APECs lines of the as-grown and

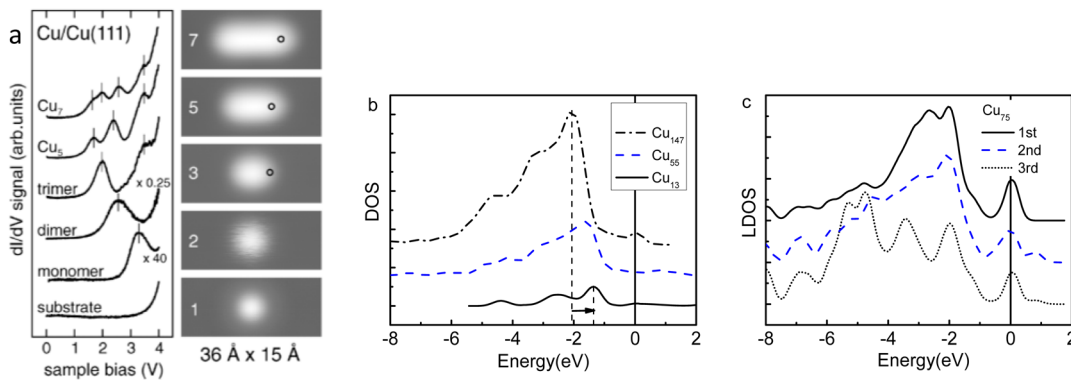


Figure 34. STM/S profiles of (a) Cu adatoms on Cu(111) surface, (b) Cu_n cluster size-resolved valence DOS, and (c) Au₇₅ shell-resolved LDOS with respect to $E_F = 0$ reference. Reprinted with permission from ref 100. Copyright 2004 American Physical Society. Reproduced from ref 277 with permission from the PCCP Owner Societies.

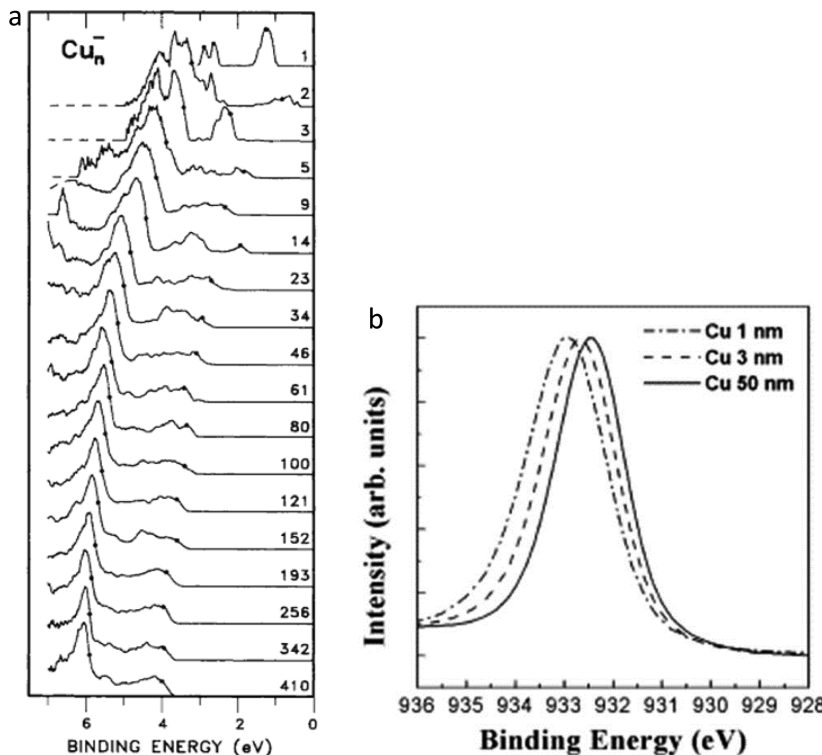


Figure 35. PES profiles of size-resolved (a) valence DOS polarization and (b) 2p DOS entrapment of Cu clusters. Reprinted with permission from ref 313. Copyright 1990 American Physical Society. Reprinted with permission from ref 314. Copyright 2006 Elsevier.

the chemically conditioned Cu nanocrystals on different substrates revealed the following:

1. The m value increases from unity for Cu/HOPG/Ar⁺ to 1.30 for Cu/CYCL and to 1.82 for Cu/CYCL/Ar⁺, which indicates that the Cu is more reactive with CYCL than with HOPG. Cu atoms hardly react with carbon at room temperature,³²¹ but they react easily with polymers.^{322,323} Although the Ar⁺ does not react with Cu, Ar⁺ bombardment promotes the Cu/CYCL reaction by heating.

2. The m value increases from 1.3 for Cu/CYCL to 1.96 for Cu/CYCL/N⁺. N⁺ bombardment alters the surface bond from metallic to ionic, that enhances the crystal potential.³²⁴

3. The layer-by-layer growth fashion ($\tau = 1$) of Cu films on Al₂O₃ could fit the results better, though a dispute remains on the growth mode of metal on oxide surfaces (ref 147 and refs therein). The m increase from 1.27 at 80 K to 1.94 at 300 K for

Cu/Al₂O₃ indicates that Cu bonds to oxygen atom more easily at room temperature than at lower temperatures.³¹⁵

4. The $\eta_{ML} \cong 1.25$ means that the strength of crystal binding to the M(3d) level is 25% stronger than that to the deeper L(2p) level.

5. The κ_{ML} in Figure 38d–f is independent of the shape and size of the particle, but it is sensitive to the chemical treatment. If charge transfers from one constituent to another, the κ_{ML} will change; otherwise it is unity, as compared in Table 12 for the conditioned Cu crystals.

6.6. Nickel

6.6.1. NEXAFS-XPS: Shell-Resolved Entrapment. Figure 39 shows the near-edge X-ray absorption fine structure (NEXAFS) spectra, which revealed the sublayer-resolved Ni 2p shift.²¹⁸ The 2p shifts positively and the outermost layer shifts the most. Low-energy electron diffraction (LEED) measurement

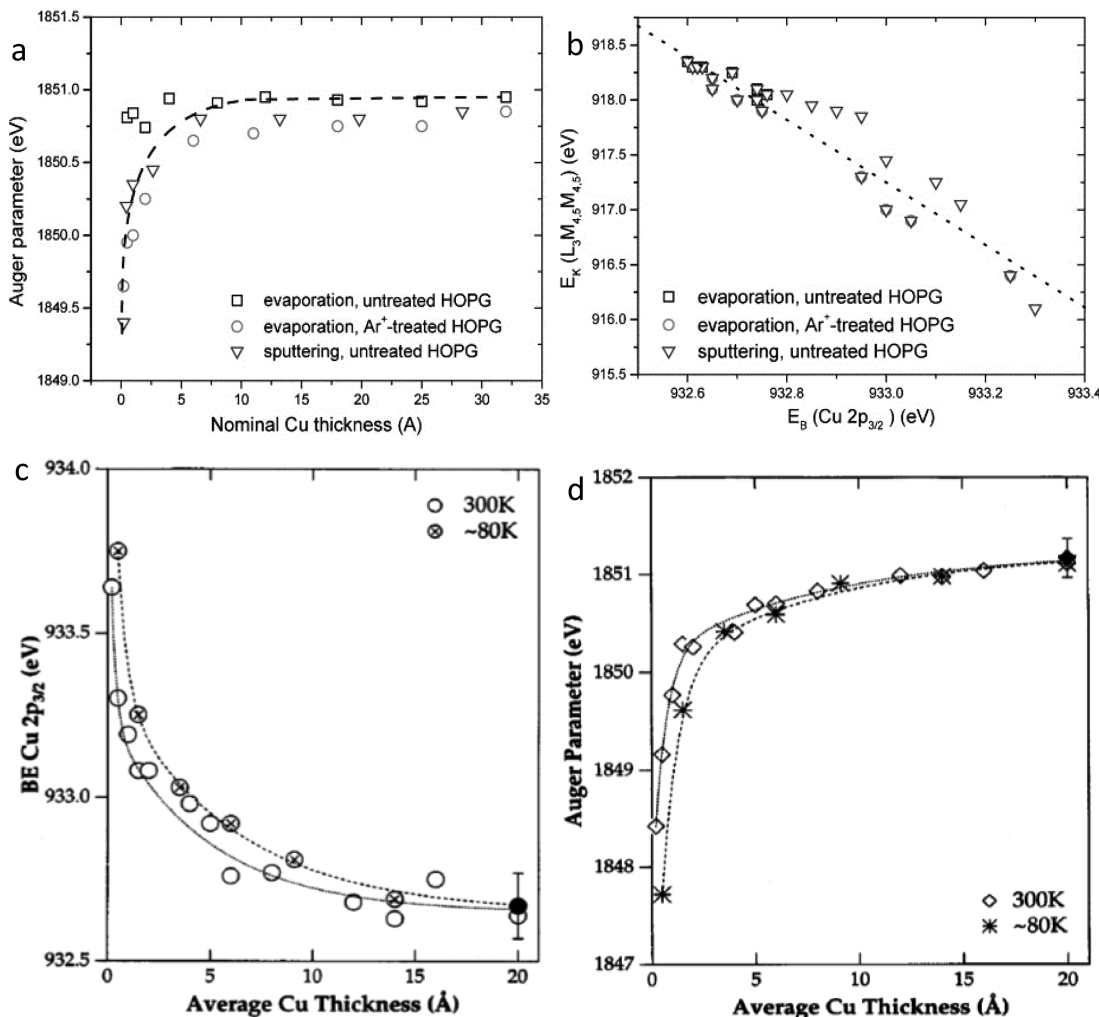


Figure 36. Size dependence of the (a) Auger parameter $\alpha'(K)$ and (b) Wagner plot for Cu/HOPG clusters. Size and temperature induced shift of the (c) $2p_{3/2}$ and (d) $\alpha'(K)$ for Cu on Al_2O_3 substrate. Reprinted with permission from ref 315. Copyright 2002 Elsevier. Reprinted with permission from ref 318. Copyright 1996 American Institute of Physics.

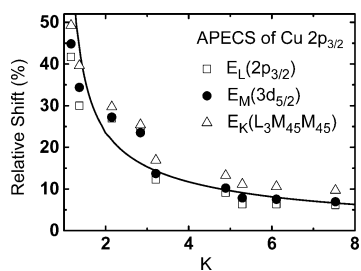


Figure 37. BOLS reproduction (solid line) of the measured (scattered) $E_L(K)$, $E_M(K)$, and $E_K(K)$ of Cu nanostructures deposited on HOPG³¹⁵ results in the atomic $E_L(0)$, $E_M(0)$, and $E_K(0)$ and their bulk shifts. Reproduction also results in the screening $\eta_{ML} = 1.25$ and the valence recharging $\kappa_{ML} = 1.05$ coefficients, as featured in Table 12. Reprinted with permission from ref 193. Copyright 2006 Elsevier.

also revealed that the first Ni(110) layer spacing contracts by $9.8 \pm 1.8\%$ with respect to the bulk lattice constant.³²⁵ These observations evidence the BOLS prediction on the skin bond contraction and the associated local quantum entrapment.

6.6.2. APECS: 2p and 3d Band Cooperative Shift. Figure 40a shows the XPS $2p_{3/2}$ spectra and Figure 40b shows the TEM images of Ni crystals deposited on SiO_2 substrates. Results indicate that the 2p peak undergoes quantum entrapment due to

particle size reduction.³²⁶ The thickness dependent APECS spectra in Figure 41 demonstrate that the (a) $E_{2p1/2}$, (b) $E_{2p3/2}$, (c) $E_K(\text{LMM})$, and (d) $E_{3d_{5/2}}$ shift positively but the E_K negatively when the Ni/TiO₂ film becomes thinner.³²⁷ The broad $3d_{5/2}$ band contains the 4s band contribution. NEXAFS, XPS, and APECS measurements verified consistently the BOLS expectation of Ni skin quantum entrapment.

6.6.3. BOLS–TB–ZPS Formulation and Derivatives.

Subtracting the XPS 2p spectrum collected from Ni film deposited for 3 min by that for 60 min resulted in the ZPS shown in Figure 42a. The valley at 853 eV corresponds to the bulk component and the peak at 854 eV corresponds to the size-induced quantum entrapment. Figure 42b shows the BOLS reproduced APECS lines (scattered data), and Figure 42c shows the extended Wagner plot with a slope $\kappa_{L3MS} \sim 1$. The linear fitting to the $E_\nu(K)$ curves of the $2p_{1/2}$, $2p_{3/2}$, $E_K(\text{LMM})$, and $3d_{5/2}$ peaks gives the respective slope and intercept, which allows determination of the $E_\nu(0)$ and $\Delta E_\nu(\infty)$ in BOLS convention. Figure 42d shows the BOLS duplication of the size-resolved mean lattice strain of Ni²⁷⁹ in comparison to that of Al³²⁸ and Pd³²⁹ films. Table 13 summarizes the BOLS–APECS derivatives.

Table 12. M($3d_{5/2}$) and the L($2p_{3/2}$) Energies of an Isolated Cu Atom and Their Bulk Shifts Derived from BOLS Formulation of the Size Dependent APECS ($E_K(L_3M_{45}M_{45})$) Lines^a

substrate	HOPG	CYCL	CYCL	CYCL	Al_2O_3	Al_2O_3
conditions	Ar ⁺	—	Ar ⁺	N ⁺	80 K	300 K
m	1	1.30	1.82	1.96	1.27	1.94
τ	3	3	3	3	3	1
$B_v/E_v(\infty)$	2.08	2.78	4.03	4.39	1.01	1.61
$E_{MS}(\infty)$ (eV)					7.23	
$E_{MS}(0)$					5.11	
$\Delta E_{MS}(\infty)$					2.12	
$E_L(\infty)$					932.70 ¹⁹³	
$E_L(0)$					931.00	
$\Delta E_L(\infty)$					1.70	
η_{ML}					1.25	
K_{ML}	1.05	1.42	1.15	2.05	1.04	1.23

size dependent energy shift for both levels:

$$E_\nu(z) = \langle E_\nu(0) \rangle \pm \sigma + \Delta E_\nu(12)(1 + \Delta_H)$$

$$= \begin{cases} 931.00 \pm 0.01 + 1.70(1 + \Delta_H) & (2p) \\ 5.11 \pm 0.02 + 2.12(1 + \Delta_H) & (5s) \end{cases}$$

^aLinearization of the XPS data³¹⁸ using $\Delta E_{2p}(K) = b/K \pm \sigma$ (0.01–0.02) for the chemically treated Cu/HOPG, Cu/CYCL, and Cu/ Al_2O_3 ³¹⁵ derives the given quantities.¹⁸⁷

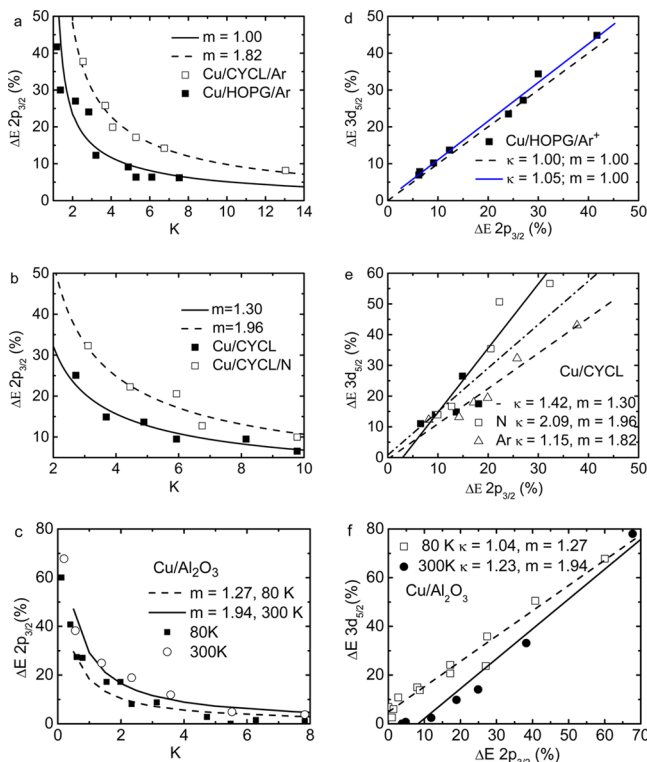


Figure 38. Size dependence of the $2p_{3/2}$ shift with involvement of the (a) Cu/HOPG and Cu/CYCL interface contribution and (b) N⁺ plasma passivation,³¹⁵ and (c) substrate temperature effect on Cu/ Al_2O_3 clusters.³¹⁸ Cu prefers a layer-by-layer growth mode on Al_2O_3 ($\tau = 1$ and K is the average thickness of Cu film). The extended Wagner plots (d–f) correlate the energy shifts of the APECS involved M(3d) and L(2p) lines and their slopes κ_{ML} as the valence recharging coefficient. Reprinted with permission from ref 187. Copyright 2003 Elsevier.

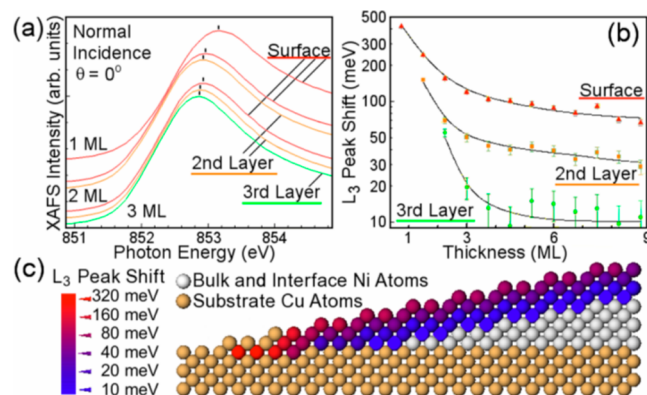


Figure 39. Sublayer-resolved Ni(110) (a) NEXAFS L3($2p_{3/2}$) spectra and (b) L3-edge peak shift with respect to the bulk component. Panel c illustrates the respective Ni(110) sublayers. Reprinted with permission from ref 218. Copyright 2008 American Physical Society.

6.7. Li, Na, and K

6.7.1. Na 2p and K 3p Entrapment. Figure 43 and Table 14 feature the decomposition of the XPS 2p profiles for Na_N^{331} and the 3p profiles for K_N^{332} atomic clusters. Table 15 lists the DFT derived charge transportation and bond strain for atoms located at different positions of I_h -13 and I_h -55 structures. Results indicate that skin of lower coordinated atoms gain charge from the inner atoms because of the skin quantum entrapment. Bonds between lower coordinated corner or edge atoms contract more than those in the cluster interior.³³³

6.7.2. CN Dependent Binding Energy Shift. Figure 44 shows the DFT derivatives of atomic-site-resolved 2p shift for Na_{13} and Na_{55} clusters. Clearly, the fewer the neighbors there are, the more the CLS there will be. The size trend of the K 3p CLS is the same, and it is unnecessary to repeat. This observation elaborates sufficiently the size trends for the Na 2p and the K 3p CLS. Table 15 features the local strain, charge gain, and the CLS for atoms at different sites in the Na_{13} and Na_{55} clusters. Consistency between measurements and DFT calculations confirms the BOLS prediction.

6.7.3. Li, K, and Na Skins and Size Trends. Figure 45 shows the decomposition of the Li_{1s}^{335} Na 2p,³³⁶ and K 3p³³⁷ energy shifts of the (110) surfaces and the size-selected free Li_N , Na_N (Exp³³¹), and K_N (Exp³³⁸) clusters based on measurements and DFT calculations. Table 16 features the energy shift derived from XPS analysis. Results show consistently that atomic undercoordination deepens the core levels without any discrimination. The solid skin and atomic clusters share the same nature of undercoordination effect. One can obtain the local bond length, bond energy, energy density, and atomic cohesive energy by repeating the previous iteration.

6.8. Si and Pb

6.8.1. Si 2p and Valence Band Entrapment. The valence band of the Si_N^+ clusters³⁴⁰ and Si(210) edge atoms show the quantum entrapment dominance. Figure 46a,b plots the size-resolved 2p and valence band entrapment of Si_N^+ ($N = 5$ –92) obtained by Vogel et al.³⁴⁰ using the soft X-ray photoionization method. Figure 46c is the size dependent 2p CLS for porous Si with effective clusters sizes of 1.4–2.1 nm.³⁴¹ Results show consistently that molecular undercoordination induces local quantum entrapment, agreeing with the skin-XPS derivatives (section 4.5).

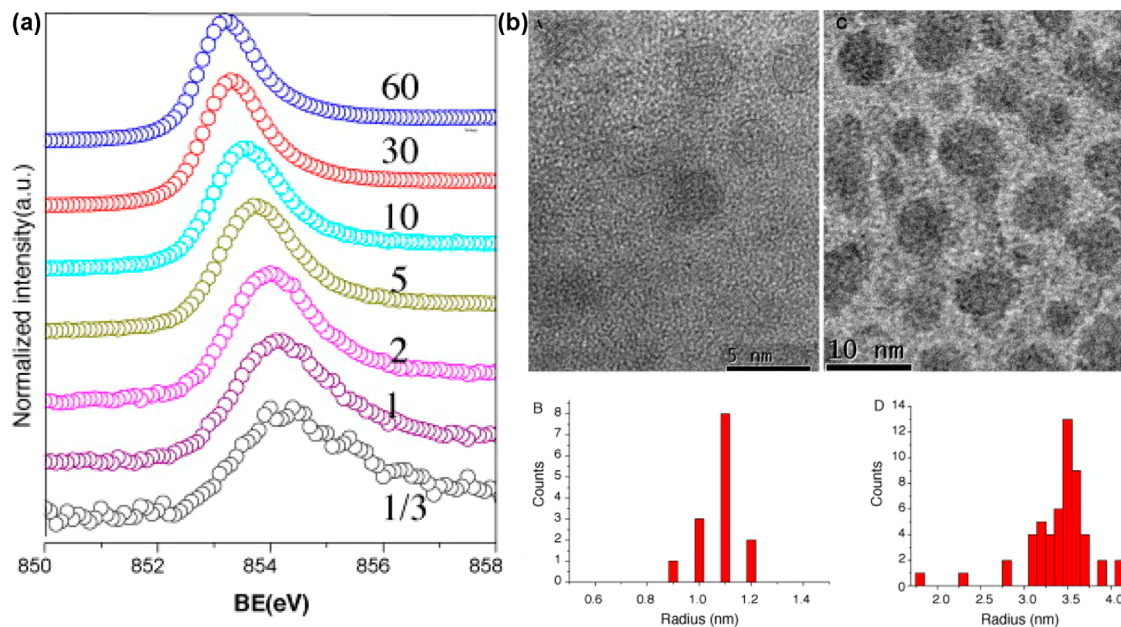


Figure 40. (a) Deposition time (min) dependent Ni 2p_{3/2} CLS and (b) typical TEM images and the histogram for Ni/SiO₂ growing 2 and 30 min. Reprinted with permission from ref 326. Copyright 2010 Elsevier.

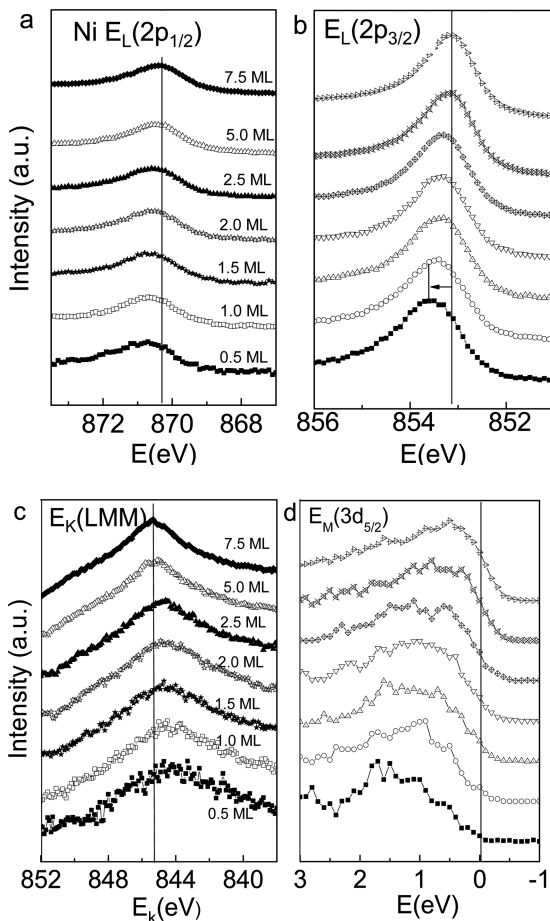


Figure 41. Thickness dependent APECS (a) $E_{2p_{1/2}}$, (b) $E_{2p_{3/2}}$, (c) E_K (LMM), and (d) $E_{3d_{5/2}}$ spectra for Ni films deposited on TiO₂ substrate. Reprinted from ref 327. Copyright 2009 American Chemical Society.

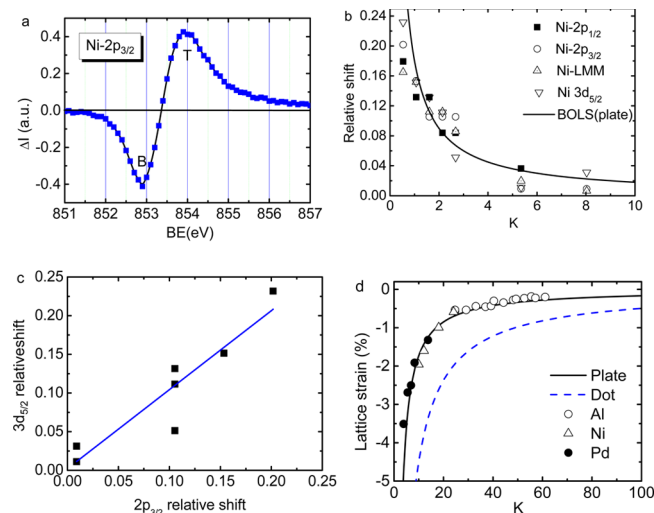


Figure 42. (a) The Ni 2p_{3/2} ZPS (spectral difference between films deposited for 3 min and that for 60 min on TiO₂) shows the bulk valley ($B \approx 853$ eV) and the size-induced quantum entrapment ($T \approx 854$ eV). (b) BOLS reproduction of (b) the APECS involved relative energy shifts ($\Delta_H = \Delta E_v(K)/\Delta E_v(\infty)$) with derived information featured in Table 13. (c) The unity $\Delta E_M - \Delta E_L$ slope indicates that interaction between the Ni crystals and TiO₂ substrate is negligible. Reprinted from ref 327. Copyright 2009 American Chemical Society. (d) BOLS reproduction of the size-resolved mean lattice strain of Ni^{2+₉} in comparison to those of Al,³²⁸ Pt,³³⁰ and Pd³²⁹ films.

The entrapment of both the 2p and the valence bands follows the same $N^{-1/3}$ fashion. The cluster size $N = 4\pi K^3/3$ is converted to $K^{-1} = (3N/4\pi)^{-1/3} = 1.61^{-1/3}$. With respect to the known bulk $E_{2p}(12)$ value at -99.2 eV, a 0.14 eV (=99.2 - 99.06) and a -3.4 (=99.2 - 102.6) eV offset correction is necessary, which arises from the surface charging during experiment. The missing of one electron in the Si⁺_N cluster weakens the screening on the crystal potential, which enhances the shift. BOLS reproduction of the measurements turns out the $E_{2p}(0)$ of 96.74 eV for an isolated Si atom and its bulk shift $\Delta E_{2p}(12)$ of 2.46 eV.

Table 13. BOLS–TB–APECs Derived Information of E_M , E_L , and E_K Energy Shifts for Ni/TiO₂ Films^{327 a}

Ni ($m = 1$, $\tau = 1$)	$E_\nu(0)$ (eV)	$E_\nu(\infty)$ (eV)	$\Delta E_\nu(\infty)$ (eV)
2p _{1/2}	868.23	870.33	2.10
2p _{3/2}	851.10	853.18	2.08
3d _{5/2}	0.51	5.49	4.99
E_K (LMM)	853.02	845.45	-7.57

CN dependent L1, L3, and M5 shift:

$$E_\nu(z) \text{ (eV)} = \langle E_\nu(0) \rangle + \Delta E_\nu(12) C_z^{-1}$$

$$= \begin{cases} 868.23 + 2.10 C_z^{-1} & (2p_{1/2}) \\ 851.10 + 2.08 C_z^{-1} & (2p_{3/2}) \\ 0.51 + 4.99 C_z^{-1} & (3d_{5/2}) \end{cases}$$

^a $\eta_{L3M5} = 4.99/2.08 = 2.40$ indicates that the crystal field experienced by the 3d electrons is 2.4 times that of the 2p electrons. The $\kappa_{L3M5} \sim 1$ (Figure 42c) indicates that the Ni/TiO₂ interface effect is negligible.

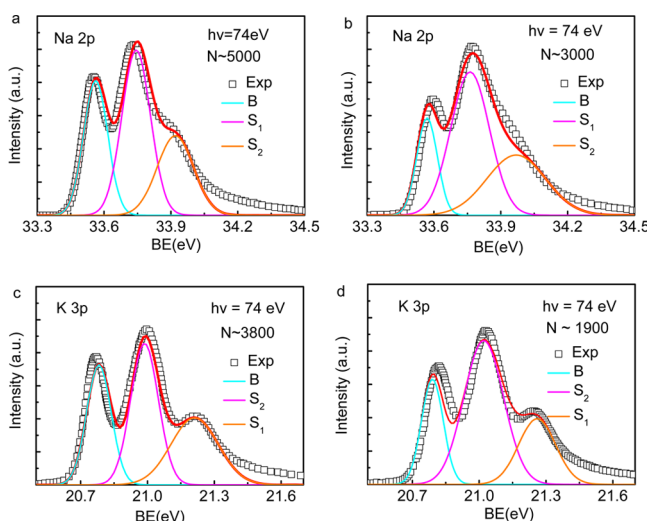


Figure 43. BOLS–TB decomposition of the XPS profiles for (a, b) Na 2p and (c, d) K 3p atomic clusters with the bulk B, S₂, and S₁. Table 14 features the derived information. Reprinted with permission from ref 333. Copyright 2015 Elsevier. Reprinted with permission from ref 334. Copyright 2015 Elsevier.

A fitting to the size trends for porous Si¹⁶⁶ and Si⁺_N clusters³⁴⁰ results in the K dependent Si 2p energy shift of both atomic clusters and nanostructured Si:

$$E_{2p}(K) = E_{2p}(\infty) + b/K = 99.06 + 9.68/K \quad (\text{p-Si})$$

$$E_{2p}(K) = 102.60 + 13.8/N^{1/3} = 102.60 + 10.69/K \quad (\text{Si}^+_{N})$$

$$E_{\nu b}(K) = 4.20 + 10.89/K \quad (\text{Si}^+_{N})$$

Figure 46d compares the DFT optimized valence DOS for the (100) and the stepped (210) skins. Bond contraction of the undercoordinated (210) edge bond entraps the valence DOS by about 1.0 eV without polarization. Results show consistently that Si atoms have undercoordination in the skin of clusters and the terrace-edge entrapped electrons and deepen both the 2p and the valence bands of Si simultaneously. These observations are consistent with that derived from skin XPS analysis, as shown in section 4.5.

6.8.2. Pb 5d Binding Energy Shift. Figure 47a–d shows the BOLS–TB decomposed Pb 5d_{3/2} spectra collected from the

Table 14. Effective Atomic CN(z) and the Respective Component Energy of Na_N³³¹ and K_N³³² Clusters ($m = 1$)^a

	z	E_{2p}
Na		
$E_{2p}(0)$ (eV)	0	31.167
$E_{2p}(12)$ (eV)	12	33.568
$\Delta E_{2p}(12)$ (eV)		2.401
3000	S ₂	5.46
	S ₁	3.63
5000	S ₂	5.71
	S ₁	3.91
K		
$E_{3p}(0)$ (eV)	0	18.034
$E_{3p}(12)$ (eV)	12	20.788
$E_{3p}(12)$ (eV)		2.754
1900	S ₂	5.32
	S ₁	3.58
3800	S ₂	5.74
	S ₁	3.80
		21.212

^aOne can obtain the local bond strain ε_z , bond energy, relative E_C , and E_D in sublayers accordingly.³³³ As shown in Figure 45, Li_N follows the same size trend but with a different slope of core level shift.

(111) skin and Pd film deposited on Si(100) substrate as well as Pb₃₀₀₀ and Pb₁₀₀₀ clusters. Figure 47e is the BOLS linearization of the measured and the DFT calculated size dependence of the 5d CLS with respect to E_F (offset).

Table 17 summarizes the optimal z and $E_\nu(z)$ components, and the energy levels $E_\nu(0)$ and their bulk shift $\Delta E_\nu(12)$, for Pb and Si skins and clusters. One electron short of the Si⁺_N offsets the $E_\nu(0)$ from that derived from skin by 4.87 eV without changing the $\Delta E_\nu(12)$ value of 2.46 eV. This observation exemplifies how to correct the charging effect in calibrating and analyzing the XPS spectra.

6.9. Co, Fe, Pt, Rh, and Pd Nanocrystals

6.9.1. Co Islands: Entrapment Dominance. A combination of STM/S measurements and DFT–MD calculations revealed that the mean lattice constant of Co islands contracts by 6% from the bulk value of 0.251 to 0.236 nm if one moves from the center to the edge of Co islands deposited on copper substrates.³⁴⁶ Figure 48 shows that island size reduction from 22.5 to 4.8 nm entraps the valence DOS by ~0.2 eV.³⁴⁷ However, the unoccupied states at 0.3 eV remain unchanged, which indicates that atomic undercoordination induces only the entrapment without polarization, which is the same as Pt adatoms²⁶⁰ and Si terrace edges.

6.9.2. Pd, Fe, Rh, and Pt: Entrapment Dominance. Figure 49 shows the BOLS–TB reproduction of the size dependent CLS of Pd, Pt, Fe, and Rh nanocrystals using the same BOLS iteration. The inset in Figure 49d shows the size-induced lattice strain of Pt and Rh crystals. XRD measurements further confirmed the size dependence of Pt lattice contraction.³⁴⁹ Table 18 summarizes the estimated information from the size trend of XPS. Outcomes show consistently the size induced quantum entrapment to the electron BE without any exception albeit the accuracy of derivatives, as further confirmed with DFT calculations for the Rh and Pt clusters³⁵⁰ and Cu and Ag clusters.³⁵¹

6.10. Summary

Consistency in the BOLS–NEP predictions, DFT calculations, STM/S, TEM, XPS, and APECs measurements of CN

Table 15. DFT Derived Local Bond Strain $C_z - 1$, CLS and Charge Gain of Na and K Atoms at Different Sites^a

	$C_z - 1$ (%) (1–2)	$C_z - 1$ (%) (2–3)	e (1–2)	e (1)	e (2)	e (3)	CLS (1–2)	CLS (1–3)
Na ₁₃	-8.32	—	-0.072	-0.006	0.075	—	0.198	—
Na ₅₅	-10.04	-6.65	-0.510	-0.052	-0.011	0.051	0.196	0.393
K ₁₃	-7.814	—	-0.324	-0.027	0.323	—	0.324	—
K ₅₅	-8.335	-5.188	-1.186	-0.059	-0.009	0.097	0.188	0.338

^aNegative sign means charge gain; otherwise there is a charge loss.³³³

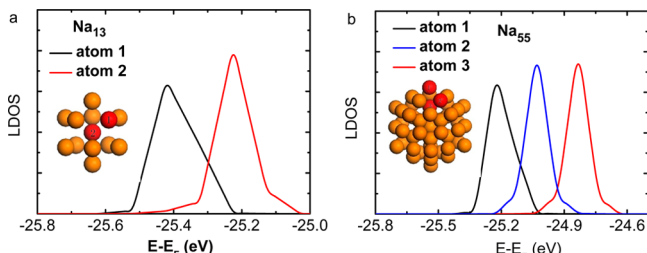


Figure 44. DFT-derived atomic site-resolved BE of the 2p level for (a) Na₁₃ and (b) Na₅₅ clusters ($z_1 < z_2 < z_3$). The atom with the lowest CN shifts positively the most. The BE shift for K atoms is in the same trend. Reprinted with permission from ref 333. Copyright 2015 Elsevier.

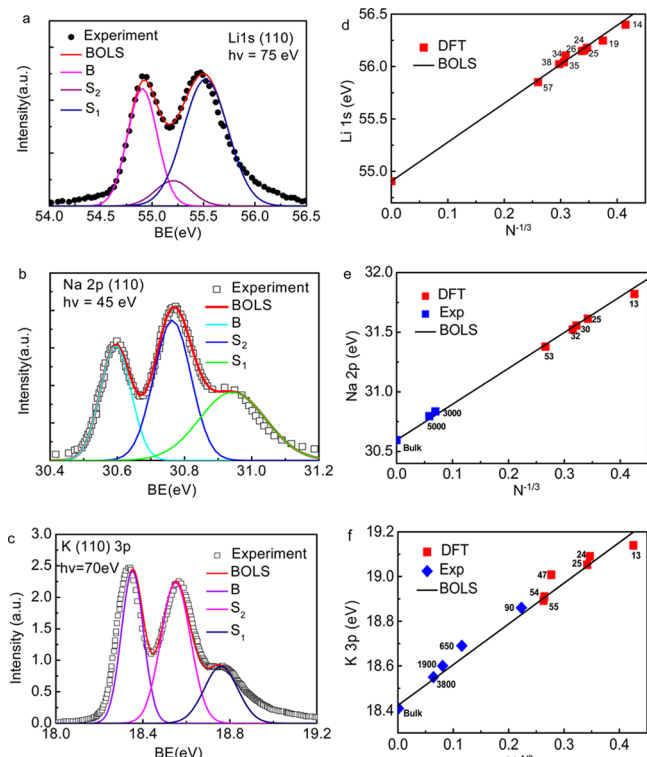


Figure 45. Layer-resolved (110) skin energy shift of (a) Li 1s,³³⁵ (b) Na 2p,³³⁶ (c) K 3p,³³⁷ and the size-selected free (d) Li_N, (e) Na_N (Exp³³¹), and (f) K_N (Exp³³⁸) clusters. Reprinted with permission from ref 333. Copyright 2015 Elsevier. Reprinted with permission from ref 334. Copyright 2015 Elsevier. Reprinted with permission from ref 339. Copyright 2015 The Royal Society of Chemistry.

dependence of the lattice strain, muffin-tin inner potential depression, core level shift, and the chain end and island charge polarization of a number of metallic nanostructures confirmed the BOLS–NEP predictions. Atomic undercoordination is so important that it results in the local strain, quantum entrapment, charge densification, and subjective valence charge polarization, which is responsible for the size dependence of known bulk

Table 16. Binding Energy Information of the bcc(110) Skins of Li, Na, and K^{333,334,339}

$m = 1$	i	z	Li ³³⁵ $E_{1s}(z)$	Na ³³⁶ $E_{2p}(z)$	K ³³⁷ $E_{3p}(z)$
bcc(110)	atom	0	50.673	28.194	15.595
	B	12	54.906	30.595	18.354
	S ₂	5.83	55.205	30.764	18.551
	S ₁	3.95	55.520	30.943	18.757
	$\Delta E_{1s}(12)$	—	4.233	2.401	2.758

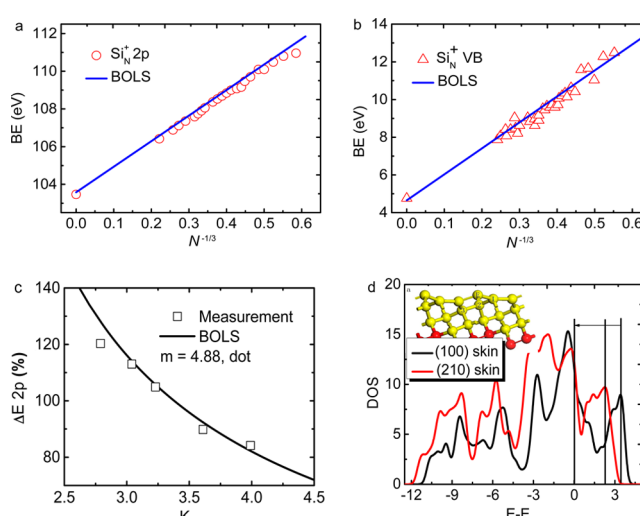


Figure 46. Size trends of (a, b) the 2p and the valence band for Si_N⁺ clusters³⁴⁰ and (c) the 2p band for porous Si.³⁴¹ The p-Si increases its size from $K = 2.7$ (A, 1.4 nm) to 4.0 (2.1 nm, E) in radius. DFT optimized (d) edge entrapment of valence DOS for Si(210) (inset) with respect to that of the Si(100) surface. DFT revealed distances between atom E and its neighbors denoted 1, 2, and 3 are 0.2577, 0.3572, and 0.3394 nm with respect to the bulk distance of 0.3840, 0.4503, and 0.3840 nm. Reprinted with permission from ref 234. Copyright 2014 American Institute of Physics.

properties and size emergence of anomalies that the bulk never shows. These emerging properties include the catalytic enhancement, toxicity, dilute magnetism, and Dirac–Fermi polarons in topological insulators, as well as the conductor–insulator transition, etc. Entrapment enlarges the electroaffinity and the band gap. Polarization lowers the work function. These elemental quantities mediate intrinsically the performance of a substance.

The localized polarization of the nonbonding s-electrons for Au(6s¹), Ag(5s¹), Rh(5s¹), and Cu(4s¹) adatoms makes the conducting metal be an insulator at the nanoscale. However, Pt(6s⁰) adatoms, reconstructed Pt surface, Co(4s²) islands, and Co, Si, and Ni nanocrystals show entrapment dominance, instead, because of the lack of the unpaired s¹ charge, according to the BOLS expectation and the present observations. In contrast, W(5d⁴6s²) and Mo(5s¹4d⁵) exhibit valence strong polarization dominance.

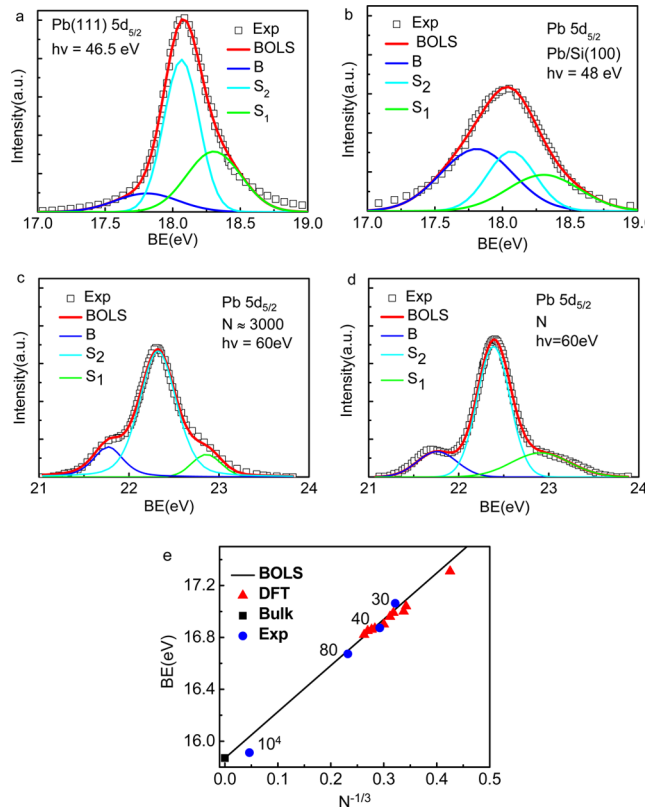


Figure 47. BOLS–TB decomposition of Pb 5d_{5/2} spectra for (a) the (111) skin,³⁴² (b) Pb film on Si(100) substrate,³⁴³ and (c, d) atomic clusters.³⁴⁴ (e) Linearization of the size-resolved BE shift. Reprinted with permission from ref 345. Copyright 2014 The Royal Society of Chemistry.

Table 17. BOLS–TB Derived Effective z , $E_\nu(z)$ Component, $E_\nu(0)$, and $E_\nu(12)$ for Pb Skins and Si Atomic Clusters^{340,342–344}

	z	Pb 5d _{3/2}	Si 2p _{3/2} (Si^+_N)	Si 2p _{3/2} (skins)
m		1 ⁶	4.88 ²³⁴	4.88 ²³⁴
$E_\nu(0)$ (eV)	0	14.334	100.96	96.089
σ		0.005	0.003	0.003
$E_\nu(12)$ (eV)	B	12	17.809	98.550
$\Delta E_\nu(12)$ (eV)	—	—	3.475	2.461
fcc(111)	S ₂	6.31	18.016	—
	S ₁	4.26	18.304	—
fcc(100)	S ₂	5.73	18.020	—
	S ₁	4.00	18.254	—
$N = 3000$	S ₂	3.69	22.325	—
	S ₁	2.45	22.855	—
$N = 1000$	S ₂	3.47	22.387	—
	S ₁	2.37	22.910	—

^aDerivatives for Si clusters are the same as the Si skin XPS (section 4.5).³⁴⁵

7. CARBON ALLOTROPIES

In this section, we discuss the following:

- Three-coordination shortens the C–C bond by 19% with 68% strength gain and entrapment dominance.
- Two-coordination shortens the C–C bond by 30% with 150% strength gain and both entrapment and polarization.

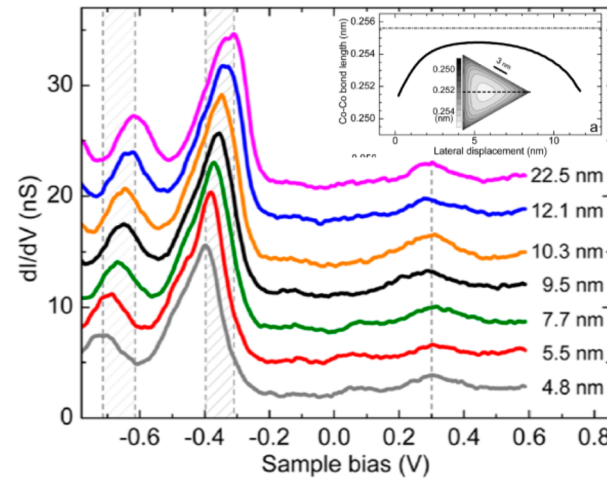


Figure 48. STS spectroscopy of Co islands on Cu(111) surface with inset showing the variation of Co–Co bond length across the island. Reprinted with permission from ref 348. Copyright 2007 American Physical Society.

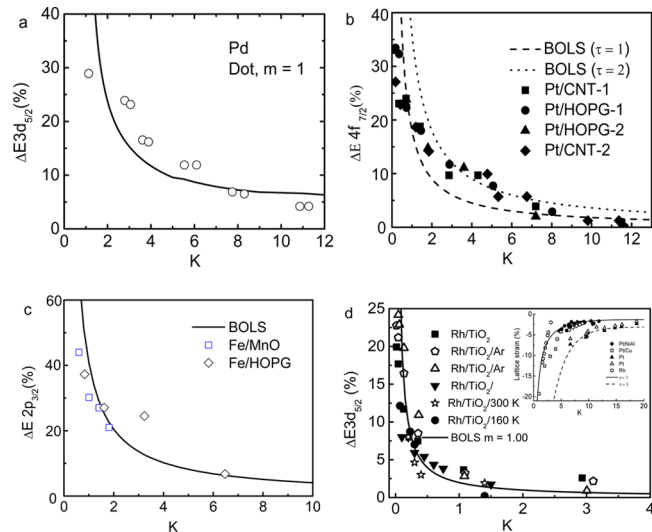


Figure 49. BOLS reproduction of the size dependent energy shift of (a) Pd 3d,¹⁴⁴ (b) Pt 4f,^{146,352–354} (c) Fe 2p,^{355,356} and (d) Rh 3d^{357–359} on various substrates with derived information featured in Table 18. Inset in (d) shows BOLS reproduced size dependence of the lattice strains of Pt and Rh nanocrystals. Reprinted from ref 164. Copyright 2009 American Chemical Society. Reprinted with permission from ref 360. Copyright 2009 Elsevier. Reprinted with permission from ref 361. Copyright 2003 World Scientific Publishing Co. Pte. Ltd.

• DFPs form with C atoms of $\sqrt{3}d$ distance along the z -edge by dangling-bond electron polarization, making the z -edged graphene metallic-like and topologically conducting.

• Quasi-triple-bond formation between C atoms of d separation prevents DFP formation along the armchair or the reconstructed z -edge of graphene, which entitles their semiconducting attributes.

7.1. STM/S-DFT: GNR Edge and Defect Polarization

Bond-order variation and the versatility of the sp-orbital hybridization have enabled carbon allotropes, a group of amazing materials varying from diamond, to graphite, fullerene C₆₀, nanotube (CNT), nanobud (CNB), graphene, and graphene nanoribbons (GNRs) with different topological edges. Graphite is a good electronic conductor, yet opaque, but diamond is an

Table 18. Estimation of the Energy Levels of an Isolated Atom and Their Bulk Shift of Pd,³⁶¹ Pt,¹⁶⁴ Fe,^{355,356} and Rh^{357–359} Nanocrystals Deposited on Different Substrates in Comparison with the $\Delta E_{\nu}(12)$ (Denoted with References) Derived from XPS Analysis

	Pd 3d	Pt/C 4f	Fe/MgO 2p	Fe/HOPG 2p	Rh/TiO ₂ 3d
m	1	1	1	1	1
τ	3	3	1	1	3
$E_{\nu}(12)$ (eV)	330.34	71.10	706.37	707.02	307.50
$E_{\nu}(0)$ (eV)	334.35	68.10	704.38	704.65	302.16
$\Delta E_{\nu}(12)$ (eV)	3.98	2.99	1.99	2.37	5.34
$\Delta E_{\nu}(12)$ (eV)	4.359 ²¹³	3.28 ¹⁷⁷	—	—	4.367 ²¹³

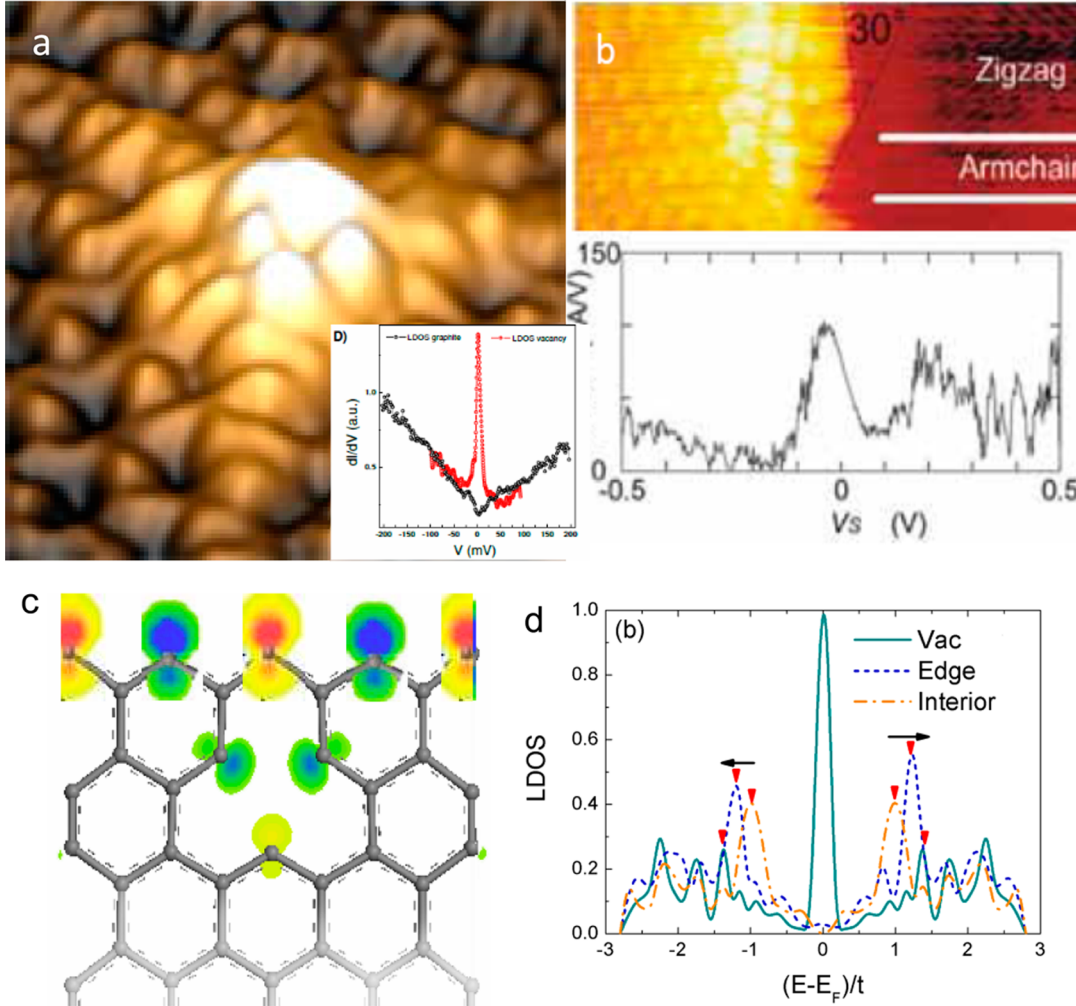


Figure 50. STM protrusions and STS resonant current probed from (a) graphite surface atomic vacancies and from (b) GNR z-edge. (c, d) DFT derived edge states of asymmetric-dumbbell shaped, unpaired, and polarized electrons with spin up and spin down (color difference). The locally densely entrapped bonding and core electrons polarize and pin the dangling bond electrons.¹³² Reprinted with permission from ref 43. Copyright 2010 American Physical Society. Reprinted with permission from ref 383. Copyright 2005 American Physical Society.

insulator, yet transparent to light of almost all wavelengths; the former shares nonbonding unpaired (or π -bond) electrons due to sp^2 -orbital hybridization compared with the latter of an ideal sp^3 -hybridization. GNR performs quite differently from CNT or from an infinitely large sheet of graphene because of the involvement of the two-coordinated edge atoms.^{132,158,362–368}

Graphite point defects and GNRs with different types of edges demonstrate many fascinating properties that neither the large graphene sheet nor the bulk graphite displays. One such property is the edge-selective generation of the Dirac fermions (DFs) with unexpectedly low effective mass, extremely high mobility, and³⁶⁹

nonzero spin,^{370–373} demonstrating the spin quantum Hall effect.^{94,374} The DFs perform abnormally beyond the description of the Schrödinger equation, but they follow the Dirac equation of motion with a nearly linear dispersion crossing E_F .^{375,376} Because of the polarization and localization nature,¹³² it would be comprehensive to name DFs as Dirac–Fermi polarons (DFPs) that are associated with atoms at the zigzag GNR edges or surrounding point defects. Performing differently from those unpaired nonbonding electrons in the GNR interior, the DFPs determine the catalytic, electric, magnetic, optic, and transport properties of the edged graphenes.^{94,377,378} Zigzag-edged GNR

performs metallic-like while the armchair-edged GNR is semiconductor-like.

STM/S probed the graphitic DFPs as bright protrusions with resonant peak at E_F from sites surrounding atomic vacancies (Figure 50a),^{43,379–381} from edges of monolayer graphite terraces, and from graphene nanoribbons (Figure 50b).^{94,364,382} Resonant current flows between the STM tip and the GNR edge under zero bias across them. However, such resonant states are absent from the flat skin, from the graphene interior, or from graphene armchained edges. The sharpness of the STM images and the resonant peaks are tip condition and probing temperature sensitive. These observations suggest that the skin point defects and the GNR z-edge are naturally the same in terms of bond relaxation, core electron entrapment, and nonbonding electron polarization.¹³²

DFT calculations¹³² revealed that the DFPs with a high spin density create preferably at z-edge or at an atomic vacancy of a GNR. The densely entrapped core electrons polarize the dangling σ -bond electrons of atoms of identical $\sqrt{3}d$ distance along the edge; see Figure 50c. BOLS-TB and DFT derived edge LDOS for atomic vacancy and GNR edge manifest a sharp resonant peak at E_F , which is the same as that probed using STS from an atomic vacancy of graphite skin.⁴³ The locally and densely entrapped bonding electrons pin the DFPs through polarization. However, along the armchair-GNR edge and the reconstructed-zigzag-GNR edge, the quasi-triple-bond formation between the nearest edge atoms of d distance or less prevents the DFP formation.

7.2. TEM: CN-Resolved C–C Bond Energy

Figure 51 shows the transmission electron microscopy (TEM) of a GNR with three types of chirality or shape of edges: the zigzag

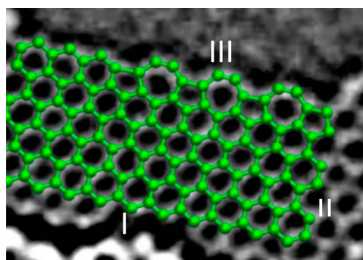


Figure 51. TEM image of a GNR with three types of edges: I, ZGNR edge with identical ($\sqrt{3}d$) atomic distance; II, AGNR edge with alternative d and $2d$ atomic distances; III, rec-ZGNR with atomic distances being similar to those of the AGNR.^{364,390} The ZGNR edge generates Dirac fermions with magnetic and metallic nature while the AGNR and rec-ZGNR edges generate otherwise. Reprinted with permission from ref 364. Copyright 2009 American Association for the Advancement of Science.

(I, ZGNR), the armchair (II, AGNR), and the reconstructed (III, rec-ZGNR) edges. Compared with large graphene sheet or single-walled CNT, the ZGNR and vacancies share the hexagonal sublattice possessing strongly localized edge states⁴⁹ with magnetic and metallic nature, whereas the AGNRs have a larger band gap (E_G) with semiconducting nature. The E_G of the AGNR is found roughly proportional to the inverse width of the GNRs.^{384–389} The rec-ZGNR shares considerable similarity with the AGNR. The difference between these edges is only the distances between atoms along the outermost edge. The atomic distance at the ZGNR edge is periodic with $\sqrt{3}d$, but at the AGNR the distance is d and $2d$ alternatively. A single-walled

CNT is equivalent to a sheet infinitely large without edges, though the rolling of the GNR may introduce some slight strains.¹⁵⁸

The TEM measurements revealed a 14.7% mean lattice contraction from 0.246 nm for graphite to 0.21 nm for the suspended GNR. For an 80-keV incident electron, the maximum energy that can be transferred to a carbon atom is 15.8 eV. The knock-on energy threshold for ejecting an in-lattice carbon atom with three bonds is 17 eV, corresponding to a beam energy of 86 keV, and hence those atoms are not ejected. However, this threshold drops below the maximum transfer energy to 15 eV for sites with a neighboring vacancy and may be even less, where atoms at the edge may have several vacant next-nearest-neighbor sites. The observation means that the minimal energy ($15/2 = 7.50$ eV/bond) required for breaking a bond between two-coordinated carbon atoms is 32% times higher than that ($17/3 = 5.67$ eV/bond) required for breaking a bond between three-coordinated carbon atoms in the suspended graphene.³⁶⁴

7.3. XPS: Core Level and Work Function Shift

Figure 52a shows the C 1s spectra measured using 635 eV photon energy from graphene flakes deposited on a SiO₂ substrate.³⁹¹ The well-resolved components at 285.97, 284.80, and 284.20 eV and their change of intensity with the number of layers confirmed the CN effect on the C 1s shift. These peaks counted from deeper to higher binding energy correspond to the GNR edge (E), monolayer GNR or skin (S), and the bulk graphite (B) in the layered graphene, respectively. The S and B components dominate the C 1s spectrum of the multilayered graphene, while the E and S dominate the triple-layered and monolayered graphene.

Figure 52b,c shows the number-of-layer resolved shift of the C 1s and the work function for the few-layer GNR grown on 6H-SiC(0001) substrate.^{392–395} The C 1s shifts positively from 284.42 to 284.83 eV associated with a work function reduction from 4.6 to 4.3 eV when the number of layers is decreased from 10 to 1, which is consistent with the reported thickness dependent shift of the DFP energy.³⁹² This observation follows the same trend demonstrated by C₆₀ deposited on CuPc substrate as detected using UPS, XPS, and synchrotron radiation spectroscopy.³⁹⁶ Lin et al.¹⁵⁵ examined systematically the suspended and grounded graphene of different numbers of layers and confirmed the same trend of C 1s and work function change. The C 1s shifts of other allotropes also show the same atomic CN dependent trend.³ Variation of the emission and azimuth angles³⁹⁷ and surface termination affect the C 1s spectral features.³⁹⁸ The cooperative relaxation of the C 1s and the work function indicates that quantum entrapment and polarization take place simultaneously and their extents increase as the atomic CN is reduced.

7.4. BOLS-TB Formulation and Quantification

The measured stiffness that is the product of Young's modulus Y and the wall (bond) thickness t , $Yt = 0.3685 \text{ TPa}\cdot\text{nm}$, and the known melting point of 1593 K for the terminal edge of the single-walled CNT³⁹⁹ have enabled determination of the C–C bonding identities as summarized in Table 19.⁴⁰⁰ The C–C bond contracts by 18.5% and strengthens by 69% with respect to the C–C bond in a diamond (0.154 nm, 1.84 eV). The C–C bond at the open edge of the CNT is 30% shorter and 152% stronger with the bond nature index of $m = 2.56$. The elastic modulus of CNT reaches 2.6 TPa compared with the value of 1.0 TPa for diamond.⁴⁰⁰ The effective atomic CN of diamond is 12 instead of 4 as it is an interlock of two fcc-structured unit cells. The known

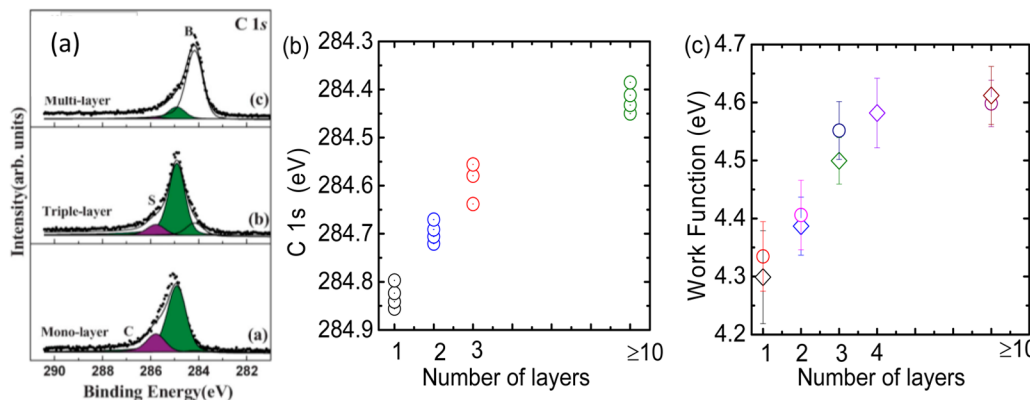


Figure 52. Number-of-layer resolved (a) C 1s spectra³⁹¹ and the cooperative BE shift of the (b) C 1s and (c) work function³⁹² of GNR flakes indicate the coexistence of entrapment and polarization pertaining to undercoordinated C atoms. Reprinted with permission from ref 391. Copyright 2008 Wiley-VCH. Reprinted with permission from ref 392. Copyright 2009 American Physical Society.

Table 19. BOLS Resolution of the C–C Bond Length, Bond Thickness, Bond Energy, Bond Nature Index *m*, Elastic Modulus, and Wall Interior Melting Point with the Measured (*Yt*)_{*z*=3} and *T*_m(2) Data as Input^{158,400}

(<i>Yt</i>) _{<i>z</i>=3}	0.3685 TPa·nm
tip-end melting point, <i>T</i> _m (2)	1593 K
bond nature index, <i>m</i>	2.5585
tube wall melting point, <i>T</i> _m (3)	1605 K
elastic modulus, <i>Y</i>	2.595 TPa
effective wall thickness, <i>t</i> (3)	0.142 nm
bond length, <i>d</i> (2) (<i>c</i> (2) = 0.6973)	0.107 nm
bond length, <i>d</i> (3) (<i>c</i> (3) = 0.8147)	0.126 nm
relative bond energy, <i>E</i> (2)/ <i>E</i> (12)	2.52
relative bond energy, <i>E</i> (3)/ <i>E</i> (12)	1.69

C–C bond lengths of 0.154 nm for diamond and 0.142 nm for graphite result in the effective CN of 5.335 for graphite using the *C*_{*z*} expression.¹⁵⁸

According to the BOLS–TB notion, the XPS spectral components for carbon allotropes follow the relationship¹⁶³

$$\frac{E_{1s}(z) - E_{1s}(0)}{E_{1s}(z') - E_{1s}(0)} = \frac{E_z}{E_{z'}} = \frac{C_z^{-2.56}}{C_{z'}^{-2.56}} \quad (z' \neq z) \quad (24)$$

With the given C 1s values (for *z* = 2, 3, 5.335) of 285.97, 284.87, and 284.27 eV,³⁹¹ one can easily calculate the values of *E*_{1s}(0) and $\Delta E_{1s}(12)$. The mean value of $\langle E_{1s}(0) \rangle$ is 282.57 ± 0.01 eV for an isolated C atom and the bulk shift $\Delta E_{1s}(12) = 1.321 \pm 0.001$ eV. Therefore, the following formulates the CN-resolved C 1s shift (*z* > 2):

$$E_{1s}(z) = E_{1s}(0) + \Delta E_{1s}(12) C_z^{-2.56} \\ = 282.57 \pm 0.01 + 1.32 C_z^{-2.56} \quad (\text{eV}) \quad (25)$$

Figure 53 shows the BOLS–TB formulated C 1s shift of carbon allotropes. One can determine the effective CN of a graphene with the given number of layers. Conversely, the work function reduction arises from the elevation of *E*_F that is proportional to the density of charge centered at a specific energy, *E*, in the form of $[n(E)]^{2/\tau}$ ¹⁸⁰ with τ being the dimensionality. Polarization of the dangling bond electrons^{2,50} will raise the DOS energies.¹ Hence, the observed work function reduction and the C 1s shift of the few-layer graphenes and the graphene flakes evidence the BOLS–NEP prediction.

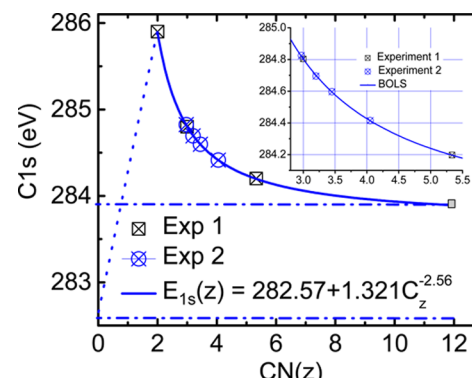


Figure 53. Atomic CN dependence of the C 1s of carbon allotropes with scattered symbols representing measurements (Exp 1³⁹¹ and Exp 2³⁹²). Correlating the layer-resolved C 1s to theory prediction results in the effective CN for 1 (*z* = 2.97), 2 (3.20), 3 (3.45), and 10 (4.05) layer GNRs. Reprinted from ref 163. Copyright 2009 American Chemical Society.

7.5. ZPS: Monolayer Skin Entrapment and Defect Polarization

Figure 54 shows the well-resolved XPS spectra collected from (Figure 54a) the defect-free HOPG(0001) surface at different emission angles and (Figure 54b) the surface of different defect densities at the emission angle of 50°.¹⁵¹ The Ar⁺ doses represent defect densities. One can control the density of the atomic vacancies by spraying the graphite surface using 0.5 keV Ar⁺ ions along the surface normal with programmed time and current intensity. Ar⁺ bombardment creates only vacancy defects without any chemical reaction or phase transition taking place in high vacuum.⁴⁰¹

The angle-resolved spectra show a slight positive shift, while defected spectra exhibit tails at both spectral ends. The spectra collected at larger emission angles or from higher defect densities weaken their overall intensities due to scattering loss.⁴⁰²

The spectrum collected from the defect-free surface at the least emission angle (25°) serves as the reference for the ZPS processing upon all spectral peak area normalization and background correction. The skin ZPS is the difference between spectra collected at the highest and lowest emission angles. The latter is the reference. The defect ZPS is the difference between a defected spectrum and this reference as well, as compared in Figure 54c,d.

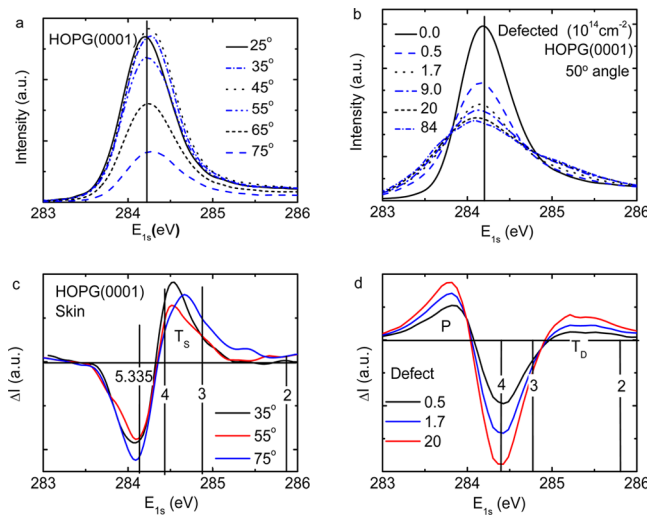


Figure 54. XPS raw spectra collected from (a) the defect-free HOPG(0001) skin at different emission angles and from (b) the defected skin at 50° angle of different Ar^+ ion doses. The ZPS distills (c) the entrapped monolayer skin states (T_S) that evolves from $z \sim 4$ to $z \sim 3$ and the bulk valley at $z = 5.335$. (d) ZPS distilled entrapped (T_D , $z \sim 2.2\text{--}2.4$) and polarized (P) defect states. The valley of the defected ZPS corresponds to a mixture of skin and bulk (centered at $z = 4$) states. Reprinted with permission from ref 151. Copyright 2012 The Royal Society of Chemistry.

The ZPS spectra in Figure 54c,d purify the energy states of the (Figure 54a) defect-free monolayer skin and (Figure 54b) the vacancy defects at graphite skin. The peaks above the x -axis are the DOS gain due to defects or the skin, while the DOS loss under the axis is the bulk/skin components. According to the BOLS–TB notion, the separation between the spectral features and the $E_{1s}(0) = 282.57$ eV is proportional to the cohesive energy of the C–C bond at the specific sites.

The valley at 284.20 eV in Figure 54c corresponds to graphite bulk ($z = 5.335$). The valley at 284.40 eV in Figure 54d is a mixture of the bulk and the skin ($z = 4$). In addition to the spectral valleys, one entrapped peak (T_S) presents at the bottom edge of the C 1s band corresponding to the skin with $z \sim 3.1$. The T_S moves to an energy even deeper and evolves into the T_D component with effective CN of 2.2–2.4, as defects generate. The shift from T_S to T_D is accompanied by the surprising emergence of both the P component at the upper edge of the C 1s band and the DFPs at the E_F as probed using STM/S.^{43,94,364,379–382} The T_D is deeper than T_S , indicating the defect bonds are indeed shorter and stronger than that of the monolayer skin, according to the relation

$$\begin{aligned} & [E_{1s}(z) - E_{1s}(12)]/[E_{1s}(5.335) - E_{1s}(12)] \\ &= (C_z/C_{5.335})^{-2.56} \end{aligned}$$

As the defect density is increased, the intensity of the T_D component grows but retains its energy. In contrast, the P component moves up in both energy and intensity. These results indicate that the atomic CN has reached and stabilized at the lowest value (2.2 for the nearest neighbor and 2.4 for the next nearest neighbors) and that the extent of polarization increases with defect density. The T_S energy depends only on the atomic CN but polarization depends on both the density and the CN of undercoordinated atoms.

Figure 55 summarizes the ZPS spectra of graphite monolayer skin and vacancy defect. The skin ZPS differentiates two spectra

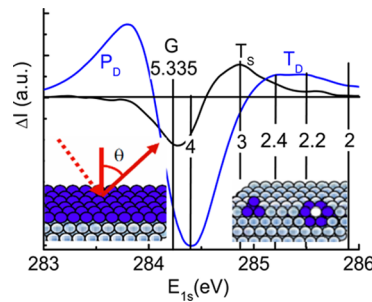


Figure 55. ZPS purified C 1s spectra for the defected ($9 \times 10^{14} \text{ cm}^{-2}$ dosed Ar^+ ion) and undefected HOPG(0001) monolayer skin of graphite. The valley G centered at 284.20 eV ($z = 5.335$) corresponds to the bulk component, and the 284.40 eV valley corresponds to a mixture of the bulk and the skin. The extra component T_S ($z \sim 3.1$) is the skin entrapment, and T_D ($z \sim 2.2\text{--}2.4$) is the defect entrapment. The P component at the upper edge arises from the screening and splitting of the crystal potential by the DFPs. Insets illustrate the emission angle and blue-colored zones dominating the extra components in each situation. Reprinted with permission from ref 151. Copyright 2012 The Royal Society of Chemistry.

collected at 75° and at 25°. The defect ZPS differentiates two spectra collected at 75° from the surface after and before high density defect generation. Insets illustrate color zones contributing the excessive states in each case. The atomic CN for the skin is about 3.1, which is close to the ideal case of 3.0 of graphene interior. The atomic CN for the vacancy extends from 2.2 to 2.4, which indicates that the next nearest neighbors contribute to the ZPS identity of the vacancy.

Strikingly, the CNs of atoms annexed the vacancy defects are compatible to that of the GNR edge of 2.0. Based on eq 25, one can evaluate the length and strength of the C–C bonds and the C 1s shift associated with the undercoordinated atoms, as featured in Table 20. Consistency in the expected effective CN and the specific energy between the present results and previous observations evidences sufficiently the accuracy and reliability of the BOLS–TB–ZPS derivatives.

The ratio of the energy shift between the two- and three-coordinated atoms ($252/169 = 149\%$) and the bond contraction of monolayer graphene (18.5%) agrees exceedingly well with that observed from monolayer graphene.³⁶⁴ The C–C bond contracts by 14.7% from 0.246 to 0.21 nm and the minimal energy (7.50 eV/bond) required for breaking a bond between two-coordinated carbon atoms is 32% times higher than that (5.67 eV/bond) required for breaking a bond between three-coordinated carbon atoms in a suspended graphene. Information in Table 20 further confirms BOLS–NEP derivatives on the CN dependence of the Raman shift.^{403,404} With the known bond length, bond energy, and effective CN, one is able to derive the local energy density E_D and atomic cohesive energy E_C at different sites of carbon allotropes.

Most strikingly, only one neighbor loss makes a great difference between C atoms at edges and C atoms in the monolayer skin. The defected P states of C are the same as those of Rh, Au, Ag, Cu, and W adatoms or terrace edges and the skin entrapment is the same as that of Pt, Re, and Co adatoms or nanocrystals.

7.6. Summary

BOLS–NEP incorporation into the STM/S, TEM, and ZPS has enabled comprehensive information on the local bond length, bond energy, energy density, and cohesive energy at GNR edges,

Table 20. BOLS–TB–ZPS Resolved *z*-Dependent C–C Bond Length d_z , Bond Energy E_z , and C 1s BE of Carbon Allotropes in Comparison to the Documented C 1s Shifts (Reprinted with permission from ref 151. Copyright 2012 The Royal Society of Chemistry.)

	<i>z</i>	C_z	d_z (nm)	E_z (eV)	C 1s (eV)	ref	<i>P</i> (eV)
atom	0	—	—	—	282.57	—	
GNR edge	2.00	0.70	0.107	1.548	285.89	285.97 ³⁹¹	
graphite vacancy	2.20	0.73	0.112	1.383	285.54		283.85
	2.40	0.76	0.116	1.262	285.28	—	
GNR interior	3.00	0.81	0.125	1.039	284.80	284.80, ³⁹¹ 284.42, ¹¹¹ 284.90; ⁴⁰⁵ 284.53–284.74 ⁴⁰⁶	
graphite skin	3.10	0.82	0.127	1.014	284.75	—	
graphite	5.335	0.92	0.142	0.757	284.20	284.20, ³⁹¹ 284.30, ^{111,405} 284.35; ⁴⁰⁷ 284.45 ⁴⁰⁸	
diamond	12.00	1.00	0.154	0.615	283.89	283.50–289.30 ^{409–411}	

point defects, and monolayer skin of graphite. As compared in Figure 50, STM protrusions and STS resonant peaks of vacancy defects at graphite surface are naturally the same as those of the graphene zigzag edge. One can therefore focus on the graphite surface vacancy more conveniently to mimic the GNR edge, as the latter is hardly accurately detectable in measurements. One neighbor loss differentiates greatly the edge carbon atom from the skin atom in the entrapment or the polarization dominance. Importantly, the practice clarifies the mechanism and dynamics of DFP creation. Polarization of the dangling-bond electrons by the locally densely entrapped bonding electrons dictates the unusual performance of GNRs.

8. HETEROCOORDINATED INTERFACES

In this section, we discuss the following:

- Heterocoordination alters bond nature, which shifts the CL accordingly.
- Dominance of quantum entrapment makes CuPd and ZnPd acceptor-like catalysts.
- Dominance of polarization entitles AgPd a donor-like catalyst.
- Interface polarization and energy density gain make BeW a medium protecting fusion radiation.

8.1. Observations

As the key components in alloys, compounds, dopants, impurities, glasses, and superlattices, heterocoordination is ubiquitously important.⁸ Bonds at the interface are completely different from those of the constituent parents^{75,76} because of the involvement of the A–B type exchange interactions. Formation of the interfacial bonds perturbs the Hamiltonian, BE density, atomic cohesive energy, and consequently the catalytic, electronic, dielectric, optic, mechanical, and thermal properties. The interface alloys have many industrial applications, such as in searching for new catalysts,^{77,78} thermal barrier coatings,⁴¹² wear resistance,^{25,413} optoelectronics,⁴¹⁴ CMOS devices,⁴¹⁵ and irradiation protection.^{416,417}

Varying composition or thermal annealing upon continuous deposition of dissimilar metals^{81,82} has formed effective methods to modify interatomic strain and redistribute charge around the bonded atoms at the interface.⁷⁹ Controlling the performance of bonds, energies, and electrons is a key concern in mediating the macroscopic properties of a substance.

As the first wall material in a nuclear fusion device, BeW alloying easily occurs in the processes of plasma interaction within the wall for radiation protection.^{416,417} However, understanding the energetics and electronics of the interface alloy is crucial to engineering such functional materials. Due to the electronic structures of W ($6s^25d^4$, delocalized d electrons

dominate) and Be ($2s^2$ states dominate), a strong influence of the alloying on both the core and the valence electrons is apparent, but so far it remains poorly understood.

Another example is the catalytic nature of alloys. Ag and Cu often form alloys with Pd because their interactions typically result in improved heterogeneous catalysts^{83,418,419} that behave quite differently in reactions—reduction or oxidation.^{84,420} CuPd is more active for the CO and alkene oxidation, CO, NO, benzene, toluene, and 1,3-butadiene hydrogenation, and ethanol decomposition.⁴²¹ AgPd is a good candidate for hydrogenation and permeation.^{85,422}

In the process of catalytic reaction, the direction and the ability of charge flow between the catalyst and the gaseous adsorbate are the key concern. The reactivity depends on the filling degree of the empty antibonding states of the catalyst by the reactant electrons. The reactivity also depends on the ability of the catalyst donating its valence electrons to the specimen. The catalyst and the adsorbate having orbits of similar energies should overlap for charge transportation during reaction.^{69,74} Although the catalytic behaviors of CuPd and AgPd alloys have been intensively investigated,^{81,84,423–427} laws governing the energetic behavior of the core and the valence electrons and their catalytic nature are yet to be established.

Upon reacting with electronegative elements such as oxygen with lone pair production, metals demonstrate CLS accordingly. For instance, oxygen adsorption deepens the bulk and the skin $3d_{5/2}$ components of a clean Ru(0001) surface simultaneously by up to 1.0 eV.²⁰⁷ Oxidation also deepens the Rh $3d_{5/2}$ level and its satellite by 0.40 eV further.⁴²⁸ These observations confirm that both surface bond relaxation and new bond formation could shift the core level positively in a superposition way by an amount that varies not only with the original $E_\nu(0)$ but also with the extent of reaction.⁴²⁹ However, the polarization due to lone pair production is unapparent in the energy shift of deeper levels, but the lone pairs create new energy states in the upper conduction and valence bands.²

Heterojunction bond formation shifts the XPS features positively or negatively, depending on the local potentials. For instance, AgPd,⁴³³ ZnPd,⁴³⁴ and BeW^{430,435} alloy formation shift the core and the valence bands upwardly but CuPd^{176,433} alloy formation deepens all bands simultaneously, as summarized in Table 21. For alloy containing *N* constituent elements, there will be $C(N,2)$ terms of interactions such as the A–A, B–B, and A–B interactions for an AB alloy instance. The additional A–B type exchange interactions contribute to the overall potentials of an amorphous state. Understanding the fundamental nature of the interface bond formation and its consequence on the electronic BE shifting as well as determination of the relevant energetics is a great challenge.

Table 21. Summary of Component XPS Peak Energies and Their Intensity Conversion upon CuPd, ZnPd, AgPd, and BeW Alloy Formation by Annealing^{430–432}

T (K)	bulk	interface	I_B/I_A	bulk	interface	I_B/I_A
CuPd						
	Pd 3d _{5/2} (eV)			Cu 2p _{3/2} (eV)		
340	335.67	337.10	15.30	931.65	933.20	11.50
540	335.66	337.17	5.06	931.57	933.21	2.93
940	335.58	337.26	0.18	931.65	933.19	0.28
mean	335.63	337.18	—	931.62	933.20	—
ZnPd						
	Pd 3d _{5/2} (eV)			Zn 3d _{5/2} (eV)		
540	335.43	334.75	4.0	9.6	8.8	4.0
940			0.2			0.2
AgPd						
	Pd 3d _{5/2} (eV)			Ag 3d _{5/2} (eV)		
300	335.62		14.17	368.32	367.18	12.00
473	335.52	334.33	1.83	368.28	367.16	0.79
573	335.52		0.32	368.38	367.10	0.12
mean	335.55	334.33	—	368.33	367.15	—
BeW						
	Be 1s (eV)			W 4f _{7/2} (eV)		
300	111.11	110.48	8.47	31.07	30.66	9.19
970			0.19			1.02

In order to verify the proposed mechanism of the interface quantum entrapment or polarization and to clarify their catalysis mechanism, Cu (2 nm) and Ag (2 nm) thin films were deposited, separately, onto Pd (10 nm) substrate using the physical vapor deposition method.⁸² Both Ag and Cu grow on Pd in a layer-by-layer fashion at room temperature without alloy formation.^{81,86,436} Heating up to 940 K for the CuPd and up to 573 K for the AgPd, alloys form completely, which result in transition of the XPS and UPS spectral peaks from the elemental bulk (B) dominance to the alloy interface (I) dominance.⁴³¹

8.2. BOLS-TB Formulation of the PES Attributes

One can drive the interface bond energy E_I and elucidate whether the entrapment or the polarization dictates the interface performance by ZPS analysis of the PES spectra. One can also calculate the interface BE density, atomic cohesive energy, and free energy with the known $E_\nu(12) - E_\nu(0)$ reference derived from skin XPS analysis,

$$\gamma_I = \frac{E_\nu(x) - E_\nu(0)}{E_\nu(12) - E_\nu(0)} = E_I/E_b = \begin{cases} >1 & (\text{T}) \\ <1 & (\text{P}) \end{cases}$$

Figure 56a compares the normalized valence DOS of pure Ag (in the range 4–7 eV), Cu (2–6 eV), and Pd (0–6 eV) with respect to E_F .^{423–425,431} The VB spectra clarify why Pd and Ag are so special for catalysis. The Pd valence DOS extends to energy across the E_F that is readily donating electrons to the reactant-donor-like. However, the valence DOS of Ag is far from the E_F , which may allow Ag to capture electrons readily—acceptor-like. Therefore, Ag and Pd should perform differently in catalytic reaction.

Subtracting the composed UPS spectrum, $I_{\text{composed}} = [xI_A + (1-x)I_B]$, for instance, from the alloying UPS spectrum I_{alloy} upon spectral peak normalization results in the valence ZPS. The x is the concentration of A constituent in the AB alloy. The ZPS, $\Delta I = I_{\text{alloy}} - I_{\text{composed}}$, purifies the valence DOS due to alloy formation. The valence ZPS profiles in Figure 56 reveal that (Figure 56b) AgPd alloy formation migrates the valence DOS upwardly and that (Figure 56c) CuPd alloy shifts the DOS downwardly. The opposite directions of valence DOS polarization distinguish the CuPd (acceptor-like) from the AgPd (donor-like) in their catalytic performance.

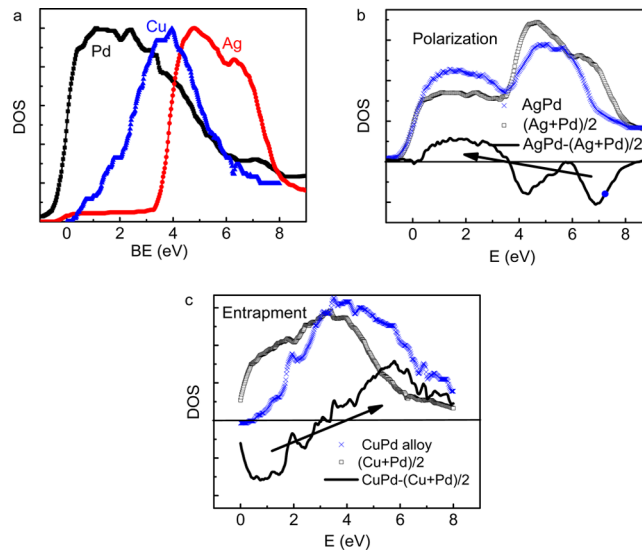


Figure 56. (a) Normalized valence DOS of Cu, Pd, and Ag skins probed using UPS.⁴³³ $E = 0$ is the E_F reference. ZPS reveals that (b) AgPd alloying shifts the valence DOS upwardly (polarization) and that (c) CuPd alloying lowers the valence DOS (entrapment). The opposite directions (indicated by arrows) of polarization distinguish the CuPd from the AgPd in the catalytic nature. AgPd readily donates electrons to benefit reduction, and CuPd tends to capture electrons for oxidation. Reproduced from ref 431 with permission from the PCCP Owner Societies.

8.3. ZPS: CuPd Entrapment, AgPd, ZnPd, BeW Polarization

XPS spectra in Figures S7 and S8 show the evolution of the Cu 2p_{3/2}, Ag 3d_{5/2}, Pd 3d_{5/2}, Zn 3d_{5/2}, Be 1s, and W 4f_{7/2} bands upon

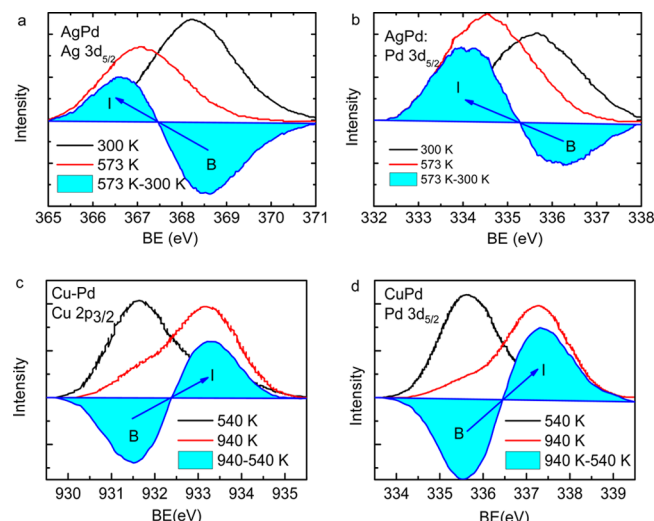


Figure 57. Thermally driven core band XPS-intensity evolution in (a, b) AgPd and (c, d) CuPd alloy interfaces.⁴³³ The ZPS reveals polarization dominance in the AgPd interface and entrapment dominance in the CuPd alloying interface. Reproduced from ref 431 with permission from the PCCP Owner Societies.

annealing at transition temperatures.^{430,431} The intensity inversion of the I component and the B component indicates the completeness of interface alloying as summarized in Table 21.

The ZPS features allow one to calibrate the potential depth, $\gamma = \Delta E_\nu(I)/\Delta E_\nu(B)$, for the respective alloys, as summarized in

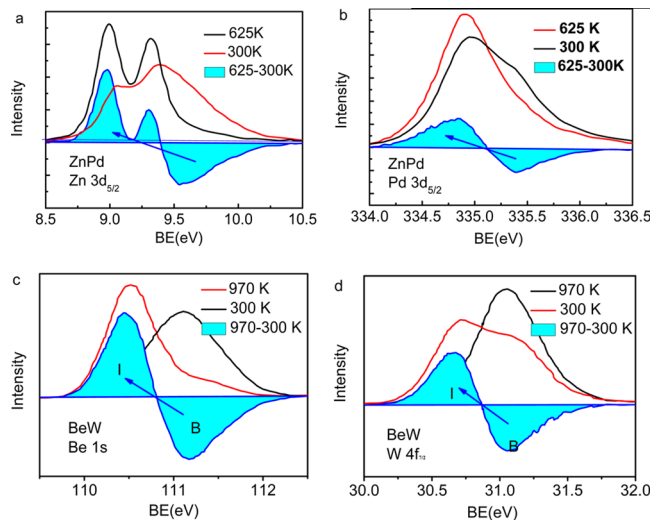


Figure 58. Thermally driven XPS-intensity evolution in (a, b) ZnPd⁴³⁴ and (c, d) BeW⁴³⁰ alloying interfaces. The ZPS reveals polarization dominance in both ZnPd and BeW interfaces. Reprinted with permission from ref 33. Copyright 2011 Elsevier.

Table 22. ZPS profiles in Figures 57 and 58 reveal the following information:

- Both the Cu 2p and the Pd 3d bands shift positively from B to I component upon CuPd alloy formation, which is consistent with the valence band shift. CuPd alloy formation strengthens the interface Cu–Cu and Pd–Pd bonds, causing quantum entrapment.
- Both the Ag 3d and Pd 3d bands at the AgPd interface shift upwardly from B to I, which also agrees with the valence band evolution. AgPd alloy formation weakens the interface Ag–Ag and Pd–Pd bonds, resulting in polarization.
- The Zn 3d, Pd 3d, Be 1s, and W 4f bands shift up at the ZnPd and BeW interfaces, following the same polarization trend at the AgPd interface.
- The core and valence bands evolve consistently in the same direction of the same alloy. One can infer that the BeW and ZnPd valence bands follow the same polarization trend of their core bands, though it is subject to experimental verification.

8.4. Energy Density, Cohesive Energy, and Free Energy

One can estimate the energy density, atomic cohesive energy, and the free energy in the interface region based on the ZPS derived interface potential depth γ . The energy density is the sum of BEs per unit cell. The cohesive energy is the sum of BEs over all coordinates of an interface atom. Instead of the conventionally defined excessive energy required for creating the unit area of interface, the interface free energy equals the energy per unit cell divided by the cross-section area of the unit cell.

Table 22. Relative BE Shift $\gamma = \Delta E_\nu(I)/\Delta E_\nu(B)$ for the CuPd, AgPd, and BeW Alloy Interfaces (in eV)^a (Reprinted with permission from ref 152. Copyright 2014 Elsevier. Reprinted with permission from ref 432. Copyright 2013 Elsevier.)

alloy	band	$E_\nu(0)$	$\Delta E_\nu(B)$	$\Delta E_\nu(I) - \Delta E_\nu(B)$	γ	
CuPd	Cu 2p _{3/2} (eV) ³¹⁵	931.00	1.70	1.58	1.94	T
	Pd 3d _{5/2} (eV) ¹⁴³	330.26	4.36	1.55	1.36	T
AgPd	Pd 3d _{5/2} (eV) ¹⁴³	330.26	4.36	-1.22	0.72	P
	Ag 3d _{5/2} (eV) ¹⁸⁶	363.02	4.63	-1.18	0.75	P
BeW	Be 1s (eV) ²³⁸	106.42	4.69	-0.63	0.86	P
	W 4f _{7/2} (eV) ²⁶⁶	28.91	2.17	-0.41	0.81	P

^aThe γ values for Pd and Zn will be available provided with $E_{3d}(0)$ of Zn.

For simplicity, the interface is assumed to be an fcc structure with four atoms ($N = 4$) in a unit cell. Atoms in the interface region are fully coordinated with $z_I = 12$. The following determines the mean interface bond energy $\langle E_I \rangle$:

$$\frac{\langle E_I \rangle}{\langle E_b \rangle} = \frac{\Delta E_\nu(I)}{\Delta E_\nu(B)} = \gamma \quad (26)$$

Vegard's notion expresses the mean interface bond energy $\langle E_{IS} \rangle$ and bond length $\langle d_{IS} \rangle$ with the involvement of the A–A, B–B, and A–B type interactions:⁴³⁷

$$\begin{aligned} \langle d_{IS} \rangle &= xd_{IA} + (1-x)d_{IB} \\ \langle E_{IS} \rangle &= xE_{IA} + (1-x)E_{IB} + x(1-x)\sqrt{E_{IA}E_{IB}} \end{aligned} \quad (27)$$

The last term in the $\langle E_{IS} \rangle$ denotes the A–B exchange interaction and x is the concentration of A. Table 23 summarizes the elucidated information regarding the interface energetics.

With the derived $\langle d_{IS} \rangle$ and $\langle E_{IS} \rangle$, we are able to determine the energy density E_{ID} , atomic cohesive energy E_{ID} , and the free energy γ_I at the interface:

$$\begin{aligned} E_{IC} &= z_I \langle E_{IS} \rangle \quad (\text{atomic cohesive energy}) \\ E_{ID} &= \frac{E_{\text{sum_cell}}}{V_{\text{cell}}} = \frac{Nz_I \langle E_{IS} \rangle}{2d_{IS}^3} \\ &\quad (\text{binding energy density}) \\ \gamma_I &= \frac{E_{\text{sum_cell}}}{A_{\text{sectional}}} = E_{ID}d_{IS} = \frac{Nz_I \langle E_{IS} \rangle}{2d_{IS}^2} \\ &\quad (\text{interface free energy}) \end{aligned} \quad (28)$$

These quantities are different from those of the corresponding bulk constituent because of the involvement of interface exchange coupling. As given in Table 23, the E_{ID} of the BeW interface is the highest among the three, which justifies the BeW becoming an important medium for radiation protection due to its higher energy density and interface polarization.

8.5. Catalytic Nature, Toxicity, and Radiation Protectivity

ZPS revealed the quantum entrapment dominance in CuPd alloy and polarization dominance in AgPd, ZnPd, and BeW alloys. The entrapment generates holes at the upper edge of the valence band; thus CuPd, acting the same as Pt adatoms,¹⁷⁷ serves as a charge acceptor in the process of catalytic reaction. The entrapment enlarges the electroaffinity that is responsible for the toxicity of undercoordinated adatoms and heterocoordinated impurities.

Comparatively, the polarization of AgPd, ZnPd, and BeW generates excessive electrons at the upper conduction band edge, which makes AgPd and ZnPd alloys, acting the same as Rh adatoms,¹⁷⁷ serve as charge donors in the process of catalytic

Table 23. Interface Mean Bond Energy ($\langle E_{IS} \rangle$), Mean Lattice Constant ($\langle d_{IS} \rangle$), Cohesive Energy E_{IC} , Energy Density E_{ID} , and Free Energy γ_I ^a

alloy	atom	E_b (eV)	$E_I(A-A)$ (eV)	$E_I(A-B)$ (eV)	$\langle E_{IS} \rangle$ (eV)	d_b (nm)	$\langle d_{IS} \rangle$ (nm)	E_{IC} (eV)	E_{ID} (10^{10} J/m ³)	γ_I (J/m ²)
BeW	Be	0.28	0.24	0.38	0.52	0.229	0.273	6.24	9.85	26.85
	W	0.74	0.60			0.316				
CuPd	Cu	0.29	0.56	0.50	0.63	0.360	0.375	7.56	4.59	17.20
	Pd	0.32	0.45			0.389				
AgPd	Pd	0.32	0.22	0.20	0.26	0.389	0.399	2.76	1.57	6.28
	Ag	0.25	0.19			0.409				

^a E_b and d_b are the bond energy and bond length of the bulk constituent, respectively. $E_I(A-A$ or $B-B)$ is the bond energy of A or B in the interface; $E_I(A-B)$ is the A–B exchange interaction energy.^{152,431,432}

reaction. The polarization of the valence electrons and the high interface energy density explain why BeW can protect nuclear radiation. ZnPd is an alternative for the donor-type catalyst despite its efficiency.⁴³⁸

The CuPd alloying entrapment seems to disobey the rule of electronegativity difference between the Cu (1.9) and the Pd (2.2). The valence charge should flow partially from Cu to Pd, but results show that both tend to gain electrons from outside. This paradox suggests that interface quantum entrapment does occur due to the lattice strain and alloy bond formation; the initial electronegativity rule losses its effect in forming alloy.

Low-energy electron and photoelectron diffraction studies have revealed that the Cu–Pd distance contracts by up to 7 ± 2.5% at the interface^{426,439,440} and the Ag–Pd bond contracts by 2.5%.⁴²⁷ This fact explains that the heterocoordinated Cu atom, having a half-occupied 4s¹ valence band, accepts charge from the Pd 4d¹⁰ valence band that is fully occupied, though the electronegativity of Cu (1.9) is lower than that of Pd (2.2).^{75,81} However, the electronegativity of Ag (1.9) is the same as that of Cu, but AgPd shows charge polarization, instead. The possible reason for the polarity could be the number of electron shells or the radius of the atom. Electrons in the half-filled s-orbital of Ag(5s¹) tend to be polarized more readily compared with those in Cu(4s¹) because of different radii of the s-orbitals. The charge polarization also happens to Au(6s¹) and Rh(5s¹) but not to Pt (6s⁰) and Co (3d⁷4s²) at sites with localized strain.¹⁷⁷ Nevertheless, discrepancy in the charge transferring direction of Cu and Ag upon alloy formation with Pd is an interesting issue for further investigation.

8.6. Summary

An extension of the BOLS–NEP–ZPS spectrometrics has correlated the interface energetics with the interatomic bonding from the perspective of bond–energy–electron correlation and Hamiltonian perturbation. ZPS identifies readily quantum entrapment or polarization in the alloying interfaces. Interface entrapment makes the CuPd a p-type catalyst, while polarization makes AgPd and ZnPd n-type catalysts. The high energy density and the polarization entitle the BeW to protect nuclear irradiation. The following summarizes ZPS enabled findings of interfaces:

1. The concepts of energy-density-gain per unit volume and cohesive-energy-remnant per atom are essential to classify the interface energetics and their responsibilities.
2. Bond nature alteration and charge sharing determine the interfacial energetics, which follows unessentially the general rule of electronegativity difference.
3. BOLS–NEP–ZPS allows determination of the interface bond energy, energy density, cohesive energy, and free energy, at the atomic scale, which is beyond the scope of existing approaches.

4. The interface potential modulation due to bond order distortion and bond nature alteration perturbs essentially the Hamiltonian and hence leads to the BE shifts and the associated functionalities.

The accuracy of estimation is strictly subject to the measurement. Other factors such as materials purity, defect concentration, and testing techniques may render the accuracy of the derived $E_v(0)$ and $E_v(I)$ values. The concepts of interface quantum entrapment and polarization are essential for understanding the bonding and electronic behavior of heterocoordinated atoms at the interface region or nearby impurities.

9. HETERO- AND UNDERCOORDINATION COUPLING

In this section, we discuss the following:

- Hetero- and undercoordination enhance each other on the local entrapment and polarization.
- The enhanced polarization in turn screens and splits the interatomic potential, which offsets the CLS negatively.
- The joint effect mediates the band gap, electroaffinity, carrier life, and work function with addition of impurity midgap states, in a controllable and predictable way.
- Coordination mediation modulates the ability of a substance in catalysis, DFP creation, electron emission, magnetization, photocatalysis, photoemission, toxicity, superhydrophobicity, etc.

9.1. Ti(0001) Skin and TiO₂ Nanocrystals

9.1.1. Photoactivity of Defected TiO₂. The photoactivity of the nanoscaled or the highly defected TiO₂ has received much attention owing to its tunable band gap and work function.^{441–446} The heterocoordinated bulk TiO₂ is only active under UV irradiation exciting electrons to overcome the band gap of 3.2 eV for the anatase phase and 3.0 eV for the rutile phase.^{447,448} Although the defected or undercoordinated TiO₂ that contains the Ti³⁺ ions or oxygen vacancies absorbs visible light,^{449,450} the mechanism for the defect modulation of the band gap, affinity, carrier life, and work function remains inconclusive.

It has been proposed that the oxygen-derived Ti 3d states located ~0.85 eV below the E_F narrow the band gap.^{447,451} Such Ti 3d states arise from oxygen (O_{br}) vacancies that bridge two Ti³⁺ ions across.^{452–454} Two excessive electrons per O_{br} vacancy transfer to the neighboring Ti atoms in an ionic route. However, based on their UPS, STM, and DFT investigations of TiO₂(110) surfaces, Martinez et al.⁴⁴¹ suggested that the Ti 3d defect states were primarily due to Ti³⁺ interstitials in the near-surface region rather than the surface O_{br} vacancies. The defected black TiO₂ exhibits substantial activity in photocatalytic production of hydrogen from water under sunlight radiation.⁴⁵⁵ Both the valence and conduction bands of the black TiO₂ shift upward because of the defect induced band bending.⁴⁵⁶

9.1.2. XPS: Ti(0001) Skin 2p Band Shift. Figure 59 shows the BOLS-TB decomposition of the Ti $2p_{3/2}$ XPS spectra

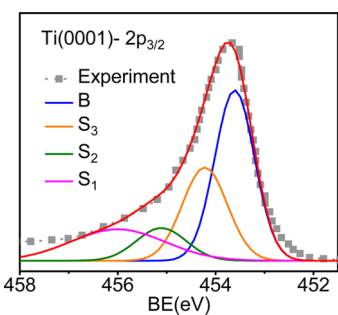


Figure 59. BOLS-TB decomposition of the Ti(0001) $2p_{3/2}$ spectrum⁴⁵⁸ with derived information featured in Table 24. The optimized atomic CN ($z_1 = 3.50$, $z_2 = 4.36$, $z_3 = 6.48$, and $z_b = 12$) is identical to those derived from the same hcp skins.²¹⁶ The refinement leads to the bond nature index $m = 4.6$ for Ti. Reprinted with permission from ref 457. Copyright 2014 Elsevier.

collected from a well-faceted Ti(0001) surface.⁴⁵⁷ The decomposition results in the $E_{2p_{3/2}}(0)$, $\Delta E_{2p_{3/2}}(12)$, and the CN-resolved $E_{2p_{3/2}}(z)$ for calibrating the BE shift of the Ti $2p_{3/2}$ upon oxidation and defect formation: $E_{2p_{3/2}}(z) = 451.47 \pm 0.003 + 2.14C_z^{-4}$ (eV).

9.1.3. DFT: Oxygenation Valence States. Figure 60 shows the optimal configuration of oxygen and the heterocoordination effect on the valence DOS of Ti(0001) surface. Oxygen chemisorption results in four additional DOS features that are the same as those that appeared in the N–Ru(0001)⁴⁵⁹ and the O–Ru($10\bar{1}0$)⁴⁶⁰ skins. These features correspond to the O–Ti bonding, O lone pairs, Ti⁺ electron holes, and Ti dipole antibonding states.^{8,457}

9.1.4. ZPS: Defect Entrapment and Polarization. The ZPS in Figure 61 resolves the Ti $2p_{3/2}$ and the O 1s defect states. Ar⁺ bombardment creates defects at controllable concentrations.⁴⁶² Subtracting the spectrum collected from an undefected $\text{TiO}_2(110)$ surface from that of the defected- $\text{TiO}_2(110)$ surface reveals the following:

1. The B valley at 458.41 eV in Figure 61a corresponds to the $2p_{3/2}$ bulk component, and that at 529.83 eV in Figure 61b corresponds to the O 1s in the bulk TiO_2 . Ti–O interaction

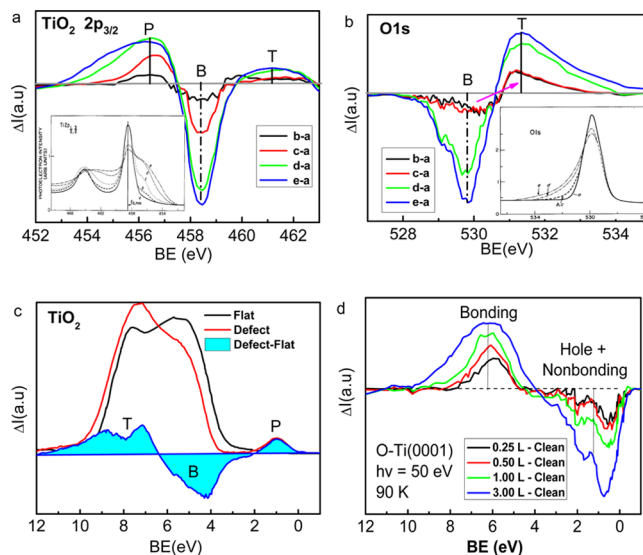


Figure 61. ZPS of (a) Ti $2p_{3/2}$, (b) O 1s, and (c) the valence band of the defected TiO_2 at different defect concentrations with respect to the undefected TiO_2 . Insets are the raw data sourced from a, flat surface; b, thermally and Ar⁺ bombardment produced defects; for c, 10 min; d, 30 min; and e, 50 min.⁴⁶² (d) Oxygen coverage (in langmuir) dependence⁴⁶³ of the valence ZPS of TiO_2 with respect to that of clean Ti(0001) surface. Both the core and the valence bands show coexistence of the entrapment and polarization due to the combination of hetero- and undercoordination. The deeper O 1s BE prevents this level from being polarized. Reprinted with permission from ref 457. Copyright 2014 Elsevier.

substantially magnifies the crystal potential, which shifts the Ti $2p_{3/2}$ states positively by 4.8 eV with respect to that of bulk Ti metal.

2. Defects create both entrapment ($T = 461.14$ eV) and polarization states ($P = 456.41$ eV) to the TiO_2 in addition to the B valley at 458.41 eV. However, the O 1s shows only entrapment ($T = 531.33$ eV) without polarization. The O 1s orbit, $528.83 - 458.41 = 71.42$ eV deeper than that of the TiO_2 , seems insensitive to the polarization.

3. The peak intensities of the entrapment and the polarization increase with defect concentration. The effective CN of the defected TiO_2 should be lower than the ideal surface of 3.5 for the Ti(0001) skin. The ZPS gives the polarization coefficient:

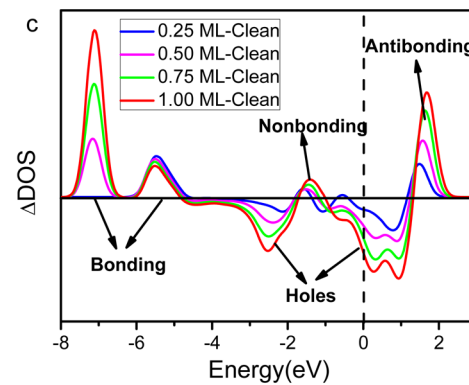
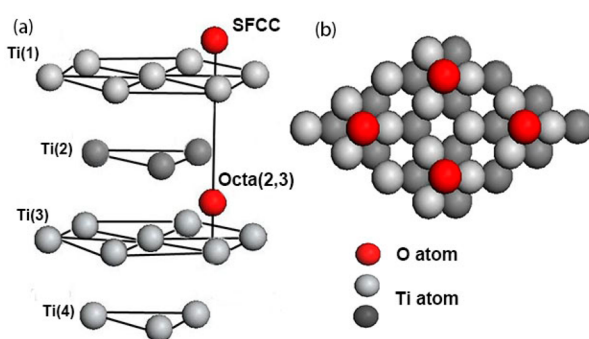


Figure 60. (a) Side and (b) top views of O–Ti(0001)-p(2×2) skin and (c) the residual energy states, $n(\text{Ti}+\text{O})-n(\text{Ti})$. Oxygen atoms occupy the surface fcc sites at 0.25 ML and then occupy both the fcc and the octahedral sites between the second and the third Ti layers (Octa(2,3)) sites at 0.50 ML. Four DOS features correspond to the antibonding dipoles (+1.6 eV), nonbonding lone pairs (-1.6 ± 0.5 eV), holes (-1.5 ± 1.5), and bonding pair (-6.0 ± 1 eV) states. Reproduced from ref 461 with permission from the PCCP Owner Societies.

$$p = [E_{2p_{3/2}}(p) - E_{2p_{3/2}}(0)]/[E_{2p_{3/2}}(12(\text{TiO}_2)) - E_{2p_{3/2}}(0)] \\ = 0.71$$

4. Because the CLS is proportional to the equilibrium bond energy, one can obtain the TiO_2 bulk bond energy $\langle E_b(\text{TiO}_2) \rangle = 1.51 \text{ eV/bond}$ and defected bond energy $\langle E_b(\text{defect}) \rangle = 2.11 \text{ eV/bond}$ in comparison to that of Ti bulk bond energy $\langle E_b(\text{Ti}) \rangle = 0.41 \text{ eV/bond}$.²³⁹

The valence ZPS in Figure 61c shows noticeably the coexistence of entrapment and polarization. Therefore, the valence band and the core band shift simultaneously in the same direction because of the screening effect on the core charge, which are the same as for AgPd alloy and Rh adatoms. The ZPS in Figure 61d for different oxygen coverages matches DFT derivatives in energy below E_F . Table 24 summarizes the oxidation and defect effects on the E_{2p} and the VB attributes of Ti and TiO_2 .

Table 24. Layer-Order Resolved $E_{2p_{3/2}}$ for Ti(0001), VB for O–Ti(0001), and Defect-Induced Entrapment and Polarization of the Core and VB for TiO_2

	z	Ti(0001) $E_{2p_{3/2}}$	defected TiO_2	O-adsorbed Ti(0001) ⁴⁶³
m		4.6 ⁴⁵⁷	5.34 ^{464,465}	
atom	0	451.47	—	—
bulk	12.00	453.61	458.41 (B)	—
S_3	6.48	454.22	—	—
S_2	4.36	455.11	—	—
S_1	3.50	456.00	—	—
$E_{2p_{3/2}}$		461.14 (T)	—	
		456.41 (P)	—	
O 1s		529.8 (B)	—	
		531.3 (T)	—	
VB		1.0 (P)	−1.6 (antibond)	
		4.5 (B)	1.6 ± 0.5 (nonbond)	
			1.5 ± 1.5 (hole)	
		8 ± 1 (T)	6.0 ± 1 (bond)	

9.1.5. Defect Enhanced Photocatalytic Ability. Figure 62 illustrates the principle for TiO_2 photocatalytic reaction. When a

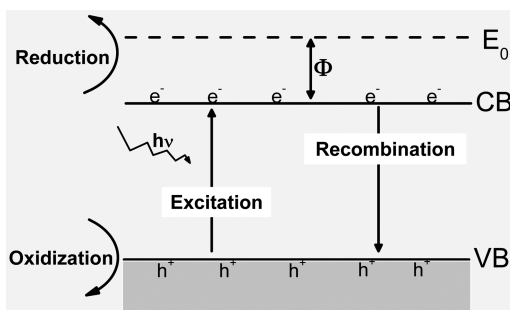


Figure 62. Schematic illustration of electron transferring in the process of photocatalytic reaction. The incident light produces e^-h^+ pairs with electrons surpassing the band gap. The excited electrons reserved for catalytic activity undergo thermalization and then recombination. Therefore, mediating the band gap, work function (Φ), electroaffinity, and carrier lifetime are key measures for improving the photocatalytic ability of TiO_2 . Atomic under- and heterocoordination could be an efficient way. Reprinted with permission from ref 457. Copyright 2014 Elsevier.

TiO_2 surface is illuminated by light with energy equaling that of the band gap, the radiation excites electrons in the ground valence band (VB) to the upper conduction band (CB, e^-), leaving a hole (h^+) behind in the VB. The excited carriers are highly reactive to radicals with robust reducing and oxidizing capacity. The carriers may recombine or be trapped by metastable surface states, or react with suitable electron acceptors/donors preadsorbed on the catalyst surface.

Major concerns in improving the photocatalytic ability of TiO_2 include (i) reducing the band gap to match the wavelength of visible light for electron excitation, (ii) lowering the work function to ease migration of the excited electrons, and (iii) prolonging the lifetime of the carriers for slowing electron–hole recombination. Currently, the band gap matches only the UV range that accounts only 4% of solar light. During photocatalytic reaction, when the reduction and oxidation do not proceed simultaneously, there is an electron accumulation in the CB, thereby causing a fast recombination of the e^-h^+ pairs. Therefore, improving the utilization rate of sunlight by modulating the band gap and the work function and by raising the carrier lifetime and affinity via locally pinning the polarized electrons is essential.

Atomic undercoordination and heterocoordination are useful in this situation. At first, the entrapment of the valence electrons deepens the energy states and enlarges the electroaffinity, which polarizes the conduction electrons shifting up in energy to lower the work function. Meanwhile, the polarization screens and splits the local potential to create the polarized states to raise the upper edge of the VB. This process narrows the band gap. The strong localization of the defect dipoles by pinning prolongs the carrier life effectively. Therefore, undercoordinated defects modulate the band gap, carrier life, and work function and are clearly a promising means.

It is also clear now why metal atoms added to a defected TiO_2 and graphene surface could improve the efficiency of CO oxidation at room temperature compared with the otherwise fully covered surface, like Au.⁵⁵ TiO_2 defect dipoles polarize the undercoordinated metal adatoms further to lower the work function and hence improve the reactivity of the supported metallic adatom dipoles.⁵⁶

9.2. ZnO Nanocrystals Passivated with H, N, and O

9.2.1. ZPS: Entrapment–Polarization Transition. Figure 63a shows the joint under- and heterocoordination effects on the Zn 2p energy. XPS revealed that a transition from the positive to the negative CLS happens at 8.5 nm.⁴⁶⁶ When the ZnO crystal reduces its size from 200 to 8.5 nm, entrapment dominates. The extent of entrapment is proportional to the size reduction. Further size reduction from 8.5 to 3.0 nm reverses the CLS direction, which evidences that further CN reduction enhances the polarization.

Figure 63b demonstrates the heterocoordination effect on the CLS of 200 nm sized ZnO. Both oxidation and nitrogenation enhance the polarization through lone pair interaction. However, hydrogenation attenuates the polarization by annihilating skin dipoles, which deepens the CLS. Hydrogen annihilation of skin dipoles attenuates the magnetism of Pt clusters.² Photoluminescence (PL) spectra show the same size trend of the (Figure 63a) transition from blue shift (T) to red shift (P) at the critical size 8.5 nm for ZnO.⁴⁶⁶ The photoluminescence energy shift involves the processes of intrinsic band gap relaxation, electron–phonon coupling, and bond relaxation, which is proportional to the bond energy as well.^{166,469}

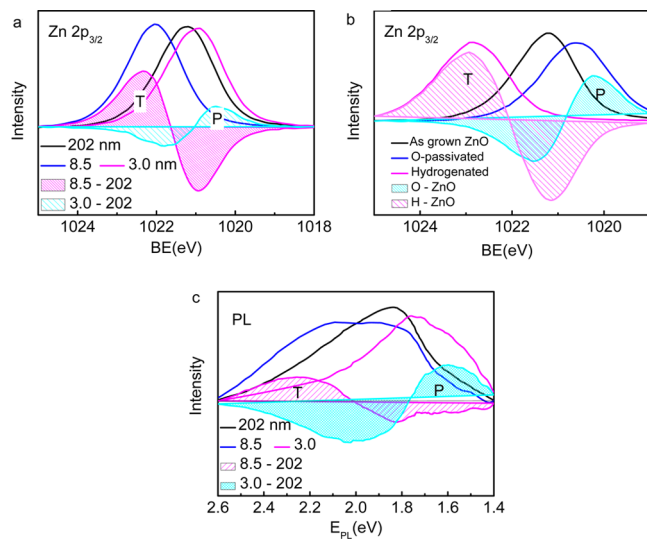


Figure 63. ZPS spectra of Zn 2p_{3/2} reveal (a) transition from entrapment (T) to polarization (P) at 8.5 nm size⁴⁶⁶ and (b) annealing under 0.21O₂ + 0.79N₂ ambient enhances polarization and annealing under 0.03H₂ + 0.97Ar ambient enhances entrapment.^{467,468} H-passivation annihilates the surface dipoles and weakens the screening effect on the crystal potential.² (c) Photoluminescence spectra show the same size trend of (a) transition from blue shift (T) to red shift (P) at 8.5 nm.⁴⁶⁶

9.2.2. Band Gap, Work Function, and Magnetism. Annealing the specimen up to 900 °C under the ambient pressure of 0.03H₂ + 0.97Ar (I) and 0.21O₂ + 0.79N₂ (II) for 24 h creates two kinds of defected ZnO.⁴⁶⁸ Type I (H-induced) shows the PL energy at 2.46 eV and type II (O and N induced) at 2.26 eV (Figure 63c). Annealing under pure O₂ at ambient pressure lowers the PL peak to 2.15 eV.⁴⁶⁸ O-passivation reduces the band gap of ZnO rather than enlarges it because of the potential weakening by polarization. The band gap, and the CLS as well, is proportional to the bond energy. However, dipole formation can narrow the band gap by screening the crystal potential. For both I and II types, the valence band maximum moves down and the valence band expands slightly as the relative intensity of the green emission to that of UV emission increases.

The skin dipoles are critical to the dilute magnetism, electron emission, and hydrophobicity of ZnO. The effects of under- and heterocoordination do enhance each other in modulating the band gap, work function, electroaffinity, and density of surface dipoles that determines surface hydrophobicity. These attributes make the sharp edge of ZnO structures hydrophobic, magnetic, easy to emit electrons, and sensitive in photocatalysis.

9.3. Scratched SrTiO₃ Skin: Defect States

An *in situ* XPS measurement confirmed the defect-enhanced entrapment and polarization at the SrTiO₃ skin shown in Figure 64.²¹ The ZPS of two VB spectra collected from the SrTiO₃ skin before and after 3 keV Ar⁺ bombarding for 20 min creates the additional polarization at 1 eV and entrapment at 12 eV. The O 1s band exhibits a 0.6 eV entrapment without the presence of polarization because of its low sensitivity. These observations confirm the BOLS–NEP expectation that defect creation by surface roughening enhances the entrapment and polarization. The valence ZPS shows clearly the features of polarization, electron–hole pair production, and the entrapment, which is the same as the defected TiO₂ (see Figure 62b).

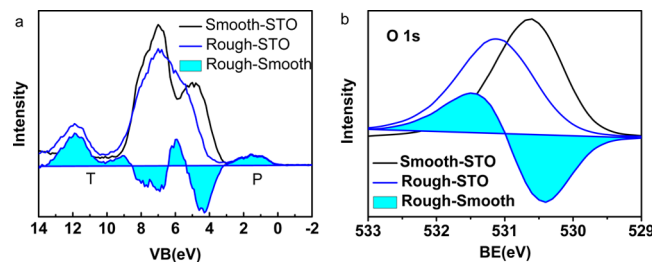


Figure 64. ZPS of the (a) valence and (b) O 1s bands for SrTiO₃ with and without defect creation by 3 keV Ar⁺ beam bombardment.²¹ The DOS shows polarization at 1 eV and entrapment at 12 eV. The O 1s band shows 0.6 eV entrapment without the presence of polarization.

Table 25 summarizes the irregular coordination coupling effect on the electronic structures of ZnO and SrTiO₃.

Table 25. Hetero- and Undercoordination Coupling Effect on the Energy States of ZnO and SrTiO₃^a

ZnO	polarization (P)	entrapment (T)	bulk valley (B)
8.5–200 nm	Zn 2p _{3/2} (eV) PL (eV)	— 2.3	1022.5 1.8
3.5–200 nm	Zn 2p _{3/2} (eV) PL (eV)	1020.7 1.6	— 1021.8 2.0
O-passivated 200 nm	Zn 2p _{3/2} (eV)	1020.3	— 1021.4
H-passivated 200 nm	Zn 2p _{3/2} (eV)	—	1023.0 1021.2
SrTiO ₃	VB (eV) O 1s (eV)	1 —	12 531.5 4–8 530.4

^aThe bulk valley for ZnO should remain constant with reference to large bulk. Energy is in electronvolts. O 1s is insensitive to the polarization effect.

nanocrystals. The photoluminescence energy correlates to the CLS. Atomic CN reduction by creating defect enhances the BOLS–NEP effect. The chemical passivation and undercoordination modulate each other.

Mechanical scratching of the SiO₂ surface⁴⁷⁰ and O-plasma etching of the HOPG⁴⁷¹ also induce the local charge entrapment for the same reason for under- and heterocoordination combination. Using the ZPS technique, one can readily identify the effect of metal skin nanometerization followed by passivation to clarify the origin for metal skin functionalization such as Fe.⁶⁰

9.4. Summary

A combination of the BOLS–NEP notion and the ZPS distillation has enabled us to identify the coupling effect of hetero- and undercoordination on the electron binding energy shift of TiO₂, ZnO, and SrTiO₃. Coupling of the irregular coordination effect may form an efficient means to tune the band gap, carrier life, electroaffinity, and work function, which determine the catalytic ability, electron and photon emissivity, hydrophobicity, magnetic property, and toxicity of the under-coordinated compounds. Narrowing band gap allows for extension of light adsorption to the visible, and lower work function promotes electronic consumption and prevents the recombination of photogenerated carriers.

10. CONCLUDING REMARKS

The BOLS–NEP–LBA scheme has enabled ZPS to resolve atomistic, dynamic, local, and quantitative information regarding

Table 26. BOLS–NEP Enhanced Capabilities of Spectroscopies

method	spatial resolution	quantitative information	physical origin
STM/S	subatomic layer	localized nonbonding states: antibonding dipole ($>E_F$); nonbonding lone pair ($<E_F$); nonbonding unpaired electron ($\sim E_F$)	oxygen, nitrogen, fluorine lone pair induced polarization; undercoordination induced polarization; Dirac–Fermi polarons; etc.
UPS	multiple layer	valence DOS evolution: electronic hole ($<E_F$); nonbond states ($<E_F$); regular bonding ($\ll E_F$)	heterocoordination: chemisorption, interface formation, etc.; undercoordination: Defect, skin, edge, cluster formation, etc.
APECS	multiple layer	two-level cooperative shift; potential screening; charge transporting in reaction; interface interaction	crystal potential mediation; bond formation and relaxation; quantum entrapment, localization, polarization, etc.
XPS/AES	multiple layer		
ZPS	atomic site monolayer	CLS and bond relaxation: effective z , bond strain ϵ_z , bond energy E_z , energy density E_z , atomic cohesive energy E_z , energy levels of an isolated atom $E_z(0)$, z -resolved $E_z(z)$ shift; entrapped and polarized states	

the bond relaxation and BE shift pertaining to irregularly coordinated atoms. Understanding has unified the unusual performance of adatoms, defects, monolayer skins, nanocrystals, and heterocoordinated interfaces and alloys to the electronic quantum entrapment, localization, polarization, and potential screening. Coordination-resolved spectrometrics of the local bond length, bond energy, energy density, atomic cohesive energy, energy levels of an isolated atom, and their shifts now becomes easily possible. Such knowledge is essential for one to engineer the coordination bonds and electrons as wished in functional material devices. The scheme also has enhanced the capabilities of APECS, STM/S, UPS, XPS, and AES to gain complementary information regarding the performance of local bonds and electrons in various energy levels.

10.1. Advantages and Attainments

The following summarizes major progress reported in this work:

1. Bond formation and relaxation and the associated energetics, localization, densification, entrapment, and polarization mediate the structure and property of a substance.

2. Perturbation to the Hamiltonian by undercoordination-induced bond contraction and by heterocoordination-induced bond nature alteration and the associate subjective polarization of the nonbonding electrons shift intrinsically all energy levels of a substance cooperatively in the same direction but at different extents. The highest energy level shifts the most.

3. The BOLS–NEP notion formulates adequately the bond–energy–electron attribute of the irregularly coordinated systems based on the conventional TB approach. One needs only to care about the $V_{\text{cryst}}(r)$ at equilibrium without bothering the Bloch wave function or the shape of the potential $V_{\text{cryst}}(r)$ in examination.

4. The energy level of an isolated $E_\nu(0)$ is the reference for the CLS shift. Local densification and quantum entrapment shifts globally positively energy levels, while polarization of the nonbonding electrons by the densely entrapped bonding electrons screens and splits the crystal potential and hence offsets the entrapped states negatively.

5. The conventional “initial–final state” relaxation and “surface charging” exist throughout the course of probing, which could be minimized in numerical calibration and particularly in ZPS processing.

6. Table 26 features the BOLS–NEP enhanced capabilities of APECS, ZPS, STS/M, UPS, XPS, and AES and quantitative information that one can obtain using the present strategies.

Most strikingly, extremely sensitive to a tiny change of atomic CN or chemical condition, ZPS resolves directly the atomistic,

dynamic, local, and quantitative information regarding local bond relaxation, entrapment, and polarization, without needing any approximation or assumption, which is beyond the scope of available approaches. ZPS discriminates the DOS gain from DOS loss due to interface and skin conditioning with high sensitivity. ZPS is particularly of use in purifying energy states in the following situations:

(1) surface reconstruction exhibiting slight CN difference between different patterns such as the Rh(110)-(1×2) and the (1 × 1) + (1 × 2) skins, where the former corresponds to the situation of every other row missing and the latter corresponds to every other pairing row missing

(2) surface contamination, chemisorption, and catalytic reaction (O on Re skins in section 5.3.5, O, N, H contamination and cluster size variation of ZnO in section 9.2)

(3) surface roughening (such as SrTiO₃ skin, HOPG plasma etching, and SiO₂ mechanical etching in section 9.3)

(4) joint effect of under- and heterocoordination (section 9.1 for TiO₂ and section 9.2 for ZnO)

(5) spin-degenerated sublevel relative shift and correction of the charging effect (sections 6.3 and 6.8)

(6) monolayer skin, point defects, and graphene edges

The ZPS requires no critical background correction or spectral area normalization. Inaccurate background correction results in only slight quantitative deviation without rendering the nature and trend behind observations. As demonstrated in section 6.3.2 for Au 4f_{5/2} and 4f_{7/2} states, background correction is not critical to distilling the spin-orbit doublets for data obtained under the same probing conditions. Spectral area normalization may compensate for the anisotropy of photoemission caused by photoelectron diffraction as the anisotropy affects only the peak intensity instead of the peak energy.

APECS resolves simultaneously the energy shifts of two energy levels. One is the upper valence band, and the other is a core band. The energy shift of the Auger parameter equals twice that of the upper band instead of the average of both, as conventionally thought. An extended Wagner plot reveals information on the screening effect on the two levels and the chemical effect on the respective shift.

We also understood the following:

1. The skin of a solid consisting of at most three atomic layers forms such a phase that the interatomic bonds are shorter and stronger and the charge and energy are denser while the atomic cohesive energy is generally lower compared to the bulk interior. The energy density and BE shift determine the performance of the undercoordinated and the heterocoordinated systems.

2. Defects, terrace edges, grain boundaries, and nanostructures share the common origin of atomic undercoordination. One atomic neighbor shortage makes a great difference in performance for the even undercoordinated atoms—polarization dominance at sites with fewer nearest neighbors than that in the flat skin—which is of use in modulating band gap, work function, electroaffinity, and the emissibility of electrons and photons.

3. Pt adatom and CuPd alloy serve as acceptor-type catalysts because of the dominance of entrapment while Rh adatoms and AgPd alloy serve as donor-type catalysts due to the dominance of polarization. Undercoordinated Co, Ni, and Re atoms exhibit entrapment dominance, while W, Au, Ag, and Cu manifest polarization dominance. Dominance of entrapment or polarization may provide guidelines for catalyst design and diagnosis.

4. Graphitic Dirac–Fermi polarons result from the isolation and polarization of the dangling σ bond electrons by the densely locally entrapped bonding electrons surrounding the defects and at the zigzag edges of graphene, which may extend to other topological insulators, thermal electronic materials, and superconductors with the dominance of strong local polarization.

5. The high interface energy density and charge polarization entitles BeW to fusion radiation protection, which may help in searching and fabricating such devices for nuclear industry.

6. Defect formation improves the photocatalytic ability of TiO_2 by band gap and work function reduction and carrier life extension through the undercoordination-induced quantum entrapment and polarization-pinning dipoles.

The findings demonstrate not only the power of the BOLS–NEP–ZPS and the APECS strategies in complementing STM/S and PES but also the essentiality of the perspective of bond relaxation and BE shift that follows the BOLS–NEP notion. Controlling the process of bond and nonbond formation, dissociation, vibration, and relaxation and the associated dynamics and energetics of charge repopulation, polarization, densification, and localization forms the effective means of engineering bonds and electrons toward devising functional materials.

10.2. Limitations and Precautions

In using this set of BOLS–NEP notion and the APECS and ZPS strategies, the following precautions are necessary to ensure the accuracy and reliability in determining the local bond relaxation and electronic BE shift:

1. The CLS is proportional to the sum of the exchange and the overlap integrals in the TB approach. The contribution of the overlap integral is 3% or less than that of the exchange integral, particularly for the deeper core levels. Involving such an overlap integral may improve the numerical accuracy of determination.

2. Unlike the core band of a particular element, the valence band includes the convoluted features of the alloy or compound showing states of bonding, nonbonding, holes, and antibonding dipoles.

3. BOLS–TB derivatives from the skin PES analysis are more reliable than those from analyzing the size PES of nanocrystals as the uniformity of crystal size and shape can hardly be certain. The reliability and accuracy also depend on the volume of the skin PES database. The larger the database is, the more reliable and higher the accuracy of the analysis will be. For example, PES profiles collected from the layered and oriented (hkl) skins determine the energy levels of an isolated atom and its z -dependent shift with a standard deviation that is inversely proportional to the square root of the number of data sets.

4. In analyzing the APECS profiles, the relative shift of the spin–orbit degenerated levels is negligible particularly for the deeper energy levels.

5. ZPS applies to monitoring the coordination and chemical effect on the performance of bonds and electrons in conductors and semiconductors. Meanwhile, one may appeal to electron and photon spectrometrics for detecting the bonding energetic behavior of insulators and liquids particularly under mechanical and thermal stimuli without needing a high-vacuum environment.

10.3. Prospects and Perspectives

The high sensitivity of the ZPS to a tiny change of the chemical and coordination environment makes it of particular use in monitoring *in situ* trace element adsorption both statically and dynamically. The ZPS process keeps the meaningfully intrinsic information by removing the general background. For instance, in purifying the adatom or defect states, the ZPS keeps features due to the least atomic CN as new peaks and the features due to the highest atomic CN in the bulk as a valley. The ZPS removes the energy states belonging to those of intermediate atomic CNs. The ZPS should be able to resolve a bimetallic system with surface enrichment by one component, change of surface composition of alloys caused by adsorption or catalytic reaction, etc. The energy and intensity of the peak may change with the richness of the excessive skin element.

Besides the chemical and coordination modulation, the ZPS should be sensitive to any change of electric, magnetic, mechanical, or thermal fields applied to the substance examined. With the establishment of the BOLS–NEP–LBA notion and ZPS strategy, one is able to gain quantitative information on the local bond length and energy, charge distribution in various bands, BE density, and atomic cohesive energy, which form the key to mediating the macroscopic properties of a substance at the atomic scale in a way of bond-by-bond, and electron-by-electron engineering.

This atomistic, CN-resolved electron spectrometrics, or the BOLS–NEP–ZPS strategy, may extend to spectrometrics more generally such as to phonons and photons to resolve the multiple-field effect on the collective performance of bond, electron, phonon, and photon at a specific atomic site. One can imagine what will happen if we turn our current focusing point from the bond energy at equilibrium to the phonon frequency or to the photoemission wavelength. Bond energy is the zeroth derivative and the phonon vibration energy is the second derivative of the interatomic potential in a Taylor series. Energies of photon emission and photon absorption depend on the band gap and electron–phonon coupling. The band gap is proportional to the bond energy at equilibrium. Therefore, atomistic spectrometrics for bond, electron, phonon, and photon is useful. This extension could be extremely appealing, fascinating, promising, and rewarding, which will advance surely profoundly the undercoordination physics and the heterocoordination chemistry.

AUTHOR INFORMATION

Corresponding Authors

*E-mail: Shiqingxu@cjlu.edu.cn (S.X.).

*E-mail: Ywang8@hnust.edu.cn (Y.W.).

*E-mail: wtzheng@jlu.edu.cn (W.Z.).

*E-mail: ecqsun@ntu.edu.sg (C.Q.S.).

Author Contributions

All authors contributed equally.

Notes

The authors declare no competing financial interest.

Biographies

Xinjuan Liu received her Ph.D. degree from East China Normal University with a research focus on nanocomposite catalysts and the size dependence of nanostructures.



Xi Zhang received her Ph.D. degree from Nanyang Technological University with a research focus on the development of ZPS-TB algorithm and DFT-TB computation of graphene edges, metallic nanocrystals, and water ice.



Maolin Bo is conducting his Ph.D. at Xiangtan University toward DFT-ZPS probing bond–electron–energy relaxation of adsorbed skins and atomic clusters.



Hongwei Tian received his Ph.D. degree at Jilin University with a research focus on material synthesis and phonon and electron spectrometrics.



Yi Sun received her B.Sc. degree in physics at the University of Illinois at Urbana–Champaign and Ph.D. in economics at the University of Chicago. She was working on the cluster size dependence of XPS for graphene, Ni/TiO₂, Pt/CNT interfaces, and the superhydrophobicity, superfluidity, superlubricity, and supersolidity at contacting interfaces. She coauthored *The Soul of Water* (Springer, 2016).



Lei Li is conducting her Ph.D. at Jilin University toward DFT-ZPS probing Ti chemisorption and catalytic ability of defected TiO₂.



Yanguang Nie completed his Ph.D. degree at Nanyang Technological University with a research focus on photoelectron spectroscopy of graphite defects and Ni nanocrystals.



Weitao Zheng received his Ph.D. degree in condensed matter physics at Jilin University with a research interest in the electronic structures and physical properties of C, N, and O based materials.



Shiqing Xu received his Ph.D. at the Shanghai Institute of Optics and Fine Mechanics with a research interest in optic–dielectric spectrometrics of glass, glass fibers, glass–ceramics, and ceramics, and related nanomaterials such as graphene, nanodiamonds, and their modifications.



Chang Q. Sun received his Ph.D. degree at Murdoch University, Australia, with a research focus on *Relaxation of the Chemical Bond* (Springer, 2014), *The Soul of Water* (Springer, 2016), and *Atomistic Spectrometrics* of bond–electron–phonon–photon relaxation dynamics associated with skin chemisorption, quantum size matter, multifield solid mechanics, and hydrogen bond cooperativity.

ACKNOWLEDGMENTS

Inspiring discussions with John Colligon, Sefik Suzer, and Philip Jennings, and financial support from NSF (Nos. 11172254(CQ), 51472106(HW), 11402086(WY), 21401180(XJ)) China, are gratefully acknowledged.



Yan Wang received her Ph.D. degree from Hunan and Nanyang Technological University with a research focus on the BOLS–TB–ZPS analysis of the bond–electron relaxation dynamics of adatoms, solid skins, kink edges, and interfaces.

NOMENCLATURE

AB	antibonding band between E_F and vacuum level
AES	Auger electron spectroscopy
APECS	Auger photoelectron coincidence spectroscopy
BOLS	bond order–length–strength
CB/VB	conduction band/valence band
CN(z)	coordination number
CNT	carbon nanotube
DFP	Dirac–Fermi polaron
DFT	density function theory
E_F	Fermi energy
GNR	graphene nanoribbon
LBA	local bond average
LDOS	local density of states
NEP	nonbonding electron polarization
NP	nanoparticles
PES	photoelectron spectroscopy

SCLS	surface core level shift
STM/S	scanning tunneling microscopy/spectroscopy
TB	tight-binding
UPS	ultraviolet photoelectron spectroscopy
XPS	X-ray photoelectron spectroscopy
ZPS	zone-resolved photoelectron spectroscopy

REFERENCES

- (1) Sun, C. Q. Size dependence of nanostructures: Impact of bond order deficiency. *Prog. Solid State Chem.* **2007**, *35*, 1–159.
- (2) Sun, C. Q. Dominance of broken bonds and nonbonding electrons at the nanoscale. *Nanoscale* **2010**, *2*, 1930–1961.
- (3) Sun, C. Q. Thermo-mechanical behavior of low-dimensional systems: The local bond average approach. *Prog. Mater. Sci.* **2009**, *54*, 179–307.
- (4) Omar, M. A. *Elementary Solid State Physics: Principles and Applications*; Addison-Wesley: New York, 1993.
- (5) Sun, C. Q. Oxidation electronics: bond-band-barrier correlation and its applications. *Prog. Mater. Sci.* **2003**, *48*, 521–685.
- (6) Sun, C. Q. Surface and nanosolid core-level shift: Impact of atomic coordination-number imperfection. *Phys. Rev. B* **2004**, *69*, 045105.
- (7) Sun, C. Q. Atomic-scaled electronic spectrum information purification. U.S. Patent US 20130090865 A1, April 11, 2013.
- (8) Sun, C. Q. *Relaxation of the Chemical Bond*; Springer: Heidelberg, Germany, 2014.
- (9) Sun, C. Q.; Fu, Y. Q.; Yan, B. B.; Hsieh, J. H.; Lau, S. P.; Sun, X. W.; Tay, B. K. Improving diamond-metal adhesion with graded TiCN interlayers. *J. Appl. Phys.* **2002**, *91*, 2051–2054.
- (10) Koch, N.; Gerlach, A.; Duhm, S.; Glowatzki, H.; Heimel, G.; Vollmer, A.; Sakamoto, Y.; Suzuki, T.; Zegenhagen, J.; Rabe, J. P.; Schreiber, F. Adsorption-induced intramolecular dipole: Correlating molecular conformation and interface electronic structure. *J. Am. Chem. Soc.* **2008**, *130*, 7300–7304.
- (11) Blackstock, J. J.; Donley, C. L.; Stickle, W. F.; Ohlberg, D. A. A.; Yang, J. J.; Stewart, D. R.; Williams, R. S. Oxide and carbide formation at titanium/organic monolayer interfaces. *J. Am. Chem. Soc.* **2008**, *130*, 4041–4047.
- (12) He, T.; Ding, H. J.; Peor, N.; Lu, M.; Corley, D. A.; Chen, B.; Ofir, Y.; Gao, Y. L.; Yitzchaik, S.; Tour, J. M. Silicon/molecule interfacial electronic modifications. *J. Am. Chem. Soc.* **2008**, *130*, 1699–1710.
- (13) Long, C. G.; Gilbertson, J. D.; Vijayaraghavan, G.; Stevenson, K. J.; Pursell, C. J.; Chandler, B. D. Kinetic evaluation of highly active supported gold catalysts prepared from monolayer-protected clusters: An experimental Michaelis-Menten approach for determining the oxygen binding constant during CO oxidation catalysis. *J. Am. Chem. Soc.* **2008**, *130*, 10103–10115.
- (14) Lee, S. W.; Chen, S.; Suntivich, J.; Sasaki, K.; Adzic, R. R.; Shao-Horn, Y. Role of Surface Steps of Pt Nanoparticles on the Electrochemical Activity for Oxygen Reduction. *J. Phys. Chem. Lett.* **2010**, *1*, 1316–1320.
- (15) Hope, G. A.; Schweinsberg, D. P.; Fredericks, P. M. Application of FT-Raman spectroscopy to the study of the benzotriazole inhibition of acid copper corrosion. *Spectrochim. Acta, Part A* **1994**, *50*, 2019–2026.
- (16) Kravchuk, T.; Vattuone, L.; Burkholder, L.; Tysoe, W. T.; Rocca, M. Ethylene decomposition at undercoordinated sites on Cu(410). *J. Am. Chem. Soc.* **2008**, *130*, 12552–12553.
- (17) Foster, A. S.; Trevethan, T.; Shluger, A. L. Structure and diffusion of intrinsic defects, adsorbed hydrogen, and water molecules at the surface of alkali-earth fluorides calculated using density functional theory. *Phys. Rev. B* **2009**, *80*, 115421.
- (18) Seitz, O.; Vilan, A.; Cohen, H.; Chan, C.; Hwang, J.; Kahn, A.; Cahen, D. Effect of doping on electronic transport through molecular monolayer junctions. *J. Am. Chem. Soc.* **2007**, *129*, 7494–7495.
- (19) Wei, Q. S.; Tajima, K.; Tong, Y. J.; Ye, S.; Hashimoto, K. Surface-Segregated Monolayers: A New Type of Ordered Monolayer for Surface Modification of Organic Semiconductors. *J. Am. Chem. Soc.* **2009**, *131*, 17597–17604.
- (20) Lee, J.; Lee, J.; Tanaka, T.; Mori, H. In situ atomic-scale observation of melting point suppression in nanometer-sized gold particles. *Nanotechnology* **2009**, *20*, 475706.
- (21) Sun, C. Q.; Sun, Y.; Ni, Y. G.; Zhang, X.; Pan, J. S.; Wang, X. H.; Zhou, J.; Li, L. T.; Zheng, W. T.; Yu, S. S.; Pan, L. K.; Sun, Z. Coulomb Repulsion at the Nanometer-Sized Contact: A Force Driving Superhydrophobicity, Superfluidity, Superlubricity, and Supersolidity. *J. Phys. Chem. C* **2009**, *113*, 20009–20019.
- (22) Wang, L.-M.; Tian, Y.; Liu, R.; Wang, W. A “universal” criterion for metallic glass formation. *Appl. Phys. Lett.* **2012**, *100*, 261913.
- (23) Wang, L. M.; Zhao, Y.; Sun, M. D.; Liu, R. P.; Tian, Y. J. Dielectric relaxation dynamics in glass-forming mixtures of propanediol isomers. *Phys. Rev. E* **2010**, *82*, 062502.
- (24) Pan, L. K.; Sun, C. Q.; Chen, T. P.; Li, S.; Li, C. M.; Tay, B. K. Dielectric suppression of nanosolid silicon. *Nanotechnology* **2004**, *15*, 1802–1806.
- (25) Veprek, S.; Veprek-Heijman, M. G. J. The formation and role of interfaces in superhard nc-MnN/a-Si3N4 nanocomposites. *Surf. Coat. Technol.* **2007**, *201*, 6064–6070.
- (26) Chen, C. R.; Mai, Y. W. Comparison of cohesive zone model and linear elastic fracture mechanics for a mode I crack near a compliant/stiff interface. *Eng. Fract. Mech.* **2010**, *77*, 3408–3417.
- (27) Lu, C.; Mai, Y. W.; Tam, P. L.; Shen, Y. G. Nanoindentation-induced elastic-plastic transition and size effect in alpha-Al2O3(0001). *Philos. Mag. Lett.* **2007**, *87*, 409–415.
- (28) Zhao, Z.; Xu, B.; Zhou, X.-F.; Wang, L.-M.; Wen, B.; He, J.; Liu, Z.; Wang, H.-T.; Tian, Y. Novel Superhard Carbon: C-Centered Orthorhombic C8. *Phys. Rev. Lett.* **2011**, *107*, 215502.
- (29) Bian, K.; Bassett, W.; Wang, Z.; Hanrath, T. The Strongest Particle: Size-Dependent Elastic Strength and Debye Temperature of PbS Nanocrystals. *J. Phys. Chem. Lett.* **2014**, *5*, 3688–3693.
- (30) Ma, Z. S.; Zhou, Z. F.; Huang, Y. L.; Zhou, Y. C.; Sun, C. Q. Mesoscopic superelasticity, superplasticity, and superrigidity. *Sci. China: Phys., Mech. Astron.* **2012**, *55*, 963–979.
- (31) Zhang, Y. B.; Tang, T. T.; Girit, C.; Hao, Z.; Martin, M. C.; Zettl, A.; Crommie, M. F.; Shen, Y. R.; Wang, F. Direct observation of a widely tunable bandgap in bilayer graphene. *Nature* **2009**, *459*, 820–823.
- (32) Nie, Y.; Pan, J.; Zheng, W.; Zhou, J.; Sun, C. Q. Atomic Scale Purification of Re Surface Kink States with and without Oxygen Chemisorption. *J. Phys. Chem. C* **2011**, *115*, 7450–7455.
- (33) Wang, Y.; Nie, Y. G.; Pan, L. K.; Sun, Z.; Sun, C. Q. Potential barrier generation at the BeW interface blocking thermonuclear radiation. *Appl. Surf. Sci.* **2011**, *257*, 3603–3606.
- (34) Hsieh, D.; Qian, D.; Wray, L.; Xia, Y.; Hor, Y. S.; Cava, R. J.; Hasan, M. Z. A topological Dirac insulator in a quantum spin Hall phase. *Nature* **2008**, *452*, 970–U975.
- (35) Li, S.; Prabhakar, O.; Tan, T. T.; Sun, C. Q.; Wang, X. L.; Soltanian, S.; Horvat, J.; Dou, S. X. Intrinsic nanostructural domains: Possible origin of weaklinkless superconductivity in the quenched reaction product of Mg and amorphous B. *Appl. Phys. Lett.* **2002**, *81*, 874–876.
- (36) Li, S.; White, T.; Laursen, K.; Tan, T. T.; Sun, C. Q.; Dong, Z. L.; Li, Y.; Zho, S. H.; Horvat, J.; Dou, S. X. Intense vortex pinning enhanced by semicrystalline defect traps in self-aligned nanostructured MgB2. *Appl. Phys. Lett.* **2003**, *83*, 314–316.
- (37) Ricci, D. A.; Miller, T.; Chiang, T. C. Controlling the thermal stability of thin films by interfacial engineering. *Phys. Rev. Lett.* **2005**, *95*, 266101.
- (38) Jiang, Q.; Lu, H. M. Size dependent interface energy and its applications. *Surf. Sci. Rep.* **2008**, *63*, 427–464.
- (39) Paneru, M.; Priest, C.; Sedev, R.; Ralston, J. Static and Dynamic Electrowetting of an Ionic Liquid in a Solid/Liquid/Liquid System. *J. Am. Chem. Soc.* **2010**, *132*, 8301–8308.
- (40) Hodgson, A.; Haq, S. Water adsorption and the wetting of metal surfaces. *Surf. Sci. Rep.* **2009**, *64*, 381–451.
- (41) Zhang, X.; Huang, Y.; Ma, Z.; Zhou, Y.; Zheng, W.; Zhou, J.; Sun, C. Q. A common supersolid skin covering both water and ice. *Phys. Chem. Chem. Phys.* **2014**, *16*, 22987–22994.

- (42) Zhang, X.; Huang, Y.; Ma, Z.; Zhou, Y.; Zhou, J.; Zheng, W.; Jiang, Q.; Sun, C. Q. Hydrogen-bond memory and water-skin supersolidity resolving the Mpemba paradox. *Phys. Chem. Chem. Phys.* **2014**, *16*, 22995–23002.
- (43) Ugeda, M. M.; Brihuega, I.; Guinea, F.; Gómez-Rodríguez, J. M. Missing Atom as a Source of Carbon Magnetism. *Phys. Rev. Lett.* **2010**, *104*, 096804.
- (44) Niimi, Y.; Matsui, T.; Kambara, H.; Fukuyama, H. STM/STS measurements of two-dimensional electronic states trapped around surface defects in magnetic fields. *Physica E* **2006**, *34*, 100–103.
- (45) Cox, A. J.; Louderback, J. G.; Bloomfield, L. A. Experimental observation of magnetism in Rhodium clusters. *Phys. Rev. Lett.* **1993**, *71*, 923–926.
- (46) Zheng, W. T.; Sun, C. Q. Electronic process of nitriding: Mechanism and applications. *Prog. Solid State Chem.* **2006**, *34*, 1–20.
- (47) Sun, C. Q. The sp hybrid bonding of C, N and O to the fcc(001) surface of nickel and rhodium. *Surf. Rev. Lett.* **2000**, *7*, 347–363.
- (48) He, Z.; Zhou, J.; Lu, X.; Corry, B. Ice-like Water Structure in Carbon Nanotube (8,8) Induces Cationic Hydration Enhancement. *J. Phys. Chem. C* **2013**, *117*, 11412–11420.
- (49) Nakada, K.; Fujita, M.; Dresselhaus, G.; Dresselhaus, M. S. Edge state in graphene ribbons: Nanometer size effect and edge shape dependence. *Phys. Rev. B* **1996**, *54*, 17954–17961.
- (50) Sun, C. Q.; Fu, S. Y.; Nie, Y. G. Dominance of Broken Bonds and Unpaired Nonbonding pi-Electrons in the Band Gap Expansion and Edge States Generation in Graphene Nanoribbons. *J. Phys. Chem. C* **2008**, *112*, 18927–18934.
- (51) Stepanyuk, V. S.; Klavsyuk, A. N.; Niebergall, L.; Bruno, P. End electronic states in Cu chains on Cu(111): Ab initio calculations. *Phys. Rev. B* **2005**, *72*, 153407.
- (52) Crain, J. N.; Pierce, D. T. End states in one-dimensional atom chains. *Science* **2005**, *307*, 703–706.
- (53) Fauster, T.; Reuss, C.; Shumay, I. L.; Weinelt, M.; Theilmann, F.; Goldmann, A. Influence of surface morphology on surface states for Cu on Cu(111). *Phys. Rev. B* **2000**, *61*, 16168–16173.
- (54) Eguchi, T.; Kamoshida, A.; Ono, M.; Hamada, M.; Shoda, R.; Nishio, T.; Harasawa, A.; Okuda, T.; Kinoshita, T.; Hasegawa, Y. Surface states of a Pd monolayer formed on a Au(111) surface studied by angle-resolved photoemission spectroscopy. *Phys. Rev. B* **2006**, *74*, 073406.
- (55) Chen, M. S.; Goodman, D. W. The structure of catalytically active gold on titania. *Science* **2004**, *306*, 252–255.
- (56) Zhang, X.; Sun, C. Q.; Hirao, H. Guanine binding to gold nanoparticles through nonbonding interactions. *Phys. Chem. Chem. Phys.* **2013**, *15*, 19284–19292.
- (57) Lopez, N.; Janssens, T.; Clausen, B.; Xu, Y.; Mavrikakis, M.; Bligaard, T.; Nørskov, J. K. On the origin of the catalytic activity of gold nanoparticles for low-temperature CO oxidation. *J. Catal.* **2004**, *223*, 232–235.
- (58) Dahl, S.; Logadottir, A.; Egeberg, R. C.; Larsen, J. H.; Chorkendorff, I.; Tornqvist, E.; Nørskov, J. K. Role of steps in N₂ activation on Ru(0001). *Phys. Rev. Lett.* **1999**, *83*, 1814–1817.
- (59) Woisetschlager, J.; Gatterer, K.; Fuchs, E. C. Experiments in a floating water bridge. *Exp. Fluids* **2010**, *48*, 121–131.
- (60) Tong, W. P.; Tao, N. R.; Wang, Z. B.; Lu, J.; Lu, K. Nitriding iron at lower temperatures. *Science* **2003**, *299*, 686–688.
- (61) Asscher, M.; Somorjai, G. A. The remarkable surface structure sensitivity of the ammonia synthesis over rhenium single crystals. *Surf. Sci. Lett.* **1984**, *143*, L389–L392.
- (62) Gladys, M. J.; Ermanoski, I.; Jackson, G.; Quinton, J. S.; Rowe, J. E.; Madey, T. E. A high resolution photoemission study of surface core-level shifts in clean and oxygen-covered Ir(2 1 0) surfaces. *J. Electron Spectrosc. Relat. Phenom.* **2004**, *135*, 105–112.
- (63) Wang, H.; Chan, A. S. Y.; Chen, W.; Kaghazchi, P.; Jacob, T.; Madey, T. E. Facet Stability in Oxygen-Induced Nanofaceting of Re(1231). *ACS Nano* **2007**, *1*, 449–455.
- (64) Kokalj, A.; Bonini, N.; Sbraccia, C.; de Gironcoli, S.; Baroni, S. Engineering the reactivity of metal catalysts: A model study of methane dehydrogenation on Rh(111). *J. Am. Chem. Soc.* **2004**, *126*, 16732–16733.
- (65) Fratesi, G.; de Gironcoli, S. Analysis of methane-to-methanol conversion on clean and defective Rh surfaces. *J. Chem. Phys.* **2006**, *125*, 044701.
- (66) Abbet, S.; Sanchez, A.; Heiz, U.; Schneider, W. D.; Ferrari, A. M.; Pacchioni, G.; Rosch, N. Acetylene cyclotrimerization on supported size-selected Pd_n clusters ($1 \leq n \leq 30$): one atom is enough! *J. Am. Chem. Soc.* **2000**, *122*, 3453–3457.
- (67) Abbet, S.; Heiz, U.; Hakkinen, H.; Landman, U. CO oxidation on a single Pd atom supported on magnesia. *Phys. Rev. Lett.* **2001**, *86*, 5950–5953.
- (68) Zhang, C. J.; Hu, P. The possibility of single C-H bond activation in CH₄ on a MoO₃-supported Pt catalyst: A density functional theory study. *J. Chem. Phys.* **2002**, *116*, 4281–4285.
- (69) Roduner, E. Size matters: why nanomaterials are different. *Chem. Soc. Rev.* **2006**, *35*, 583–592.
- (70) Jakob, P.; Gsell, M.; Menzel, D. Interactions of adsorbates with locally strained substrate lattices. *J. Chem. Phys.* **2001**, *114*, 10075–10085.
- (71) Gsell, M.; Jakob, P.; Menzel, D. Effect of Substrate Strain on Adsorption. *Science* **1998**, *280*, 717–720.
- (72) Wintterlin, J.; Zambelli, T.; Trost, J.; Greeley, J.; Mavrikakis, M. Atomic-Scale Evidence for an Enhanced Catalytic Reactivity of Stretched Surfaces. *Angew. Chem., Int. Ed.* **2003**, *42*, 2850–2853.
- (73) Richter, B.; Kuhlenbeck, H.; Freund, H. J.; Bagus, P. S. Cluster core-level binding-energy shifts: The role of lattice strain. *Phys. Rev. Lett.* **2004**, *93*, 026805.
- (74) Hammer, B.; Nørskov, J. K. Why gold is the noblest of all the metals. *Nature* **1995**, *376*, 238–240.
- (75) Rodriguez, J. A.; Goodman, D. W. The nature of the metal metal bond in bimetallic surfaces. *Science* **1992**, *257*, 897–903.
- (76) Kamakoti, P.; Morreale, B. D.; Ciocco, M. V.; Howard, B. H.; Killmeyer, R. P.; Cugini, A. V.; Sholl, D. S. Prediction of hydrogen flux through sulfur-tolerant binary alloy membranes. *Science* **2005**, *307*, 569–573.
- (77) Fox, E. B.; Velu, S.; Engelhard, M. H.; Chin, Y. H.; Miller, J. T.; Kropf, J.; Song, C. S. Characterization of CeO₂-supported Cu-Pd bimetallic catalyst for the oxygen-assisted water-gas shift reaction. *J. Catal.* **2008**, *260*, 358–370.
- (78) Bloxham, L. H.; Haq, S.; Yugnet, Y.; Bertolini, J. C.; Raval, R. trans-1,2-dichloroethene on Cu50Pd50(110) alloy surface: dynamical changes in the adsorption, reaction, and surface segregation. *J. Catal.* **2004**, *227*, 33–43.
- (79) Zhang, D. H.; Shi, W. Dark current and infrared absorption of p-doped InGaAs/AlGaAs strained quantum wells. *Appl. Phys. Lett.* **1998**, *73*, 1095–1097.
- (80) Dang, Y. X.; Fan, W. J.; Ng, S. T.; Yoon, S. F.; Zhang, D. H. Study of interdiffusion in GaInNAs/GaAs quantum well structure emitting at 1.3 μm by eight-band k center dot p method. *J. Appl. Phys.* **2005**, *97*, 103718.
- (81) Liu, G.; St. Clair, T. P.; Goodman, D. W. An XPS study of the interaction of ultrathin Cu films with Pd(111). *J. Phys. Chem. B* **1999**, *103*, 8578–8582.
- (82) Khanuja, M.; Mehta, B. R.; Shivaprasad, S. M. Geometric and electronic changes during interface alloy formation in Cu/Pd bimetal layers. *Thin Solid Films* **2008**, *516*, 5435–5439.
- (83) Newton, M. A. The oxidative dehydrogenation of methanol at the CuPd[85:15]{110} p(2 × 1) and Cu{110} surfaces: Effects of alloying on reactivity and reaction pathways. *J. Catal.* **1999**, *182*, 357–366.
- (84) Venezia, A. M.; Liotta, L. F.; Deganello, G.; Schay, Z.; Guczi, L. Characterization of pumice-supported Ag-Pd and Cu-Pd bimetallic catalysts by X-ray photoelectron spectroscopy and X-ray diffraction. *J. Catal.* **1999**, *182*, 449–455.
- (85) Amandusson, H.; Ekedahl, L. G.; Dannetun, H. Hydrogen permeation through surface modified Pd and PdAg membranes. *J. Membr. Sci.* **2001**, *193*, 35–47.
- (86) Lee, C. L.; Huang, Y. C.; Kuo, L. C. High catalytic potential of Ag/Pd nanoparticles from self-regulated reduction method on electroless Ni deposition. *Electrochim. Commun.* **2006**, *8*, 1021–1026.

- (87) Lin, J.; Wang, A.; Qiao, B.; Liu, X.; Yang, X.; Wang, X.; Liang, J.; Li, J.; Liu, J.; Zhang, T. Remarkable Performance of Ir₁/FeO_x Single-Atom Catalyst in Water Gas Shift Reaction. *J. Am. Chem. Soc.* **2013**, *135*, 15314–15317.
- (88) Parker, R. R. ITER in-vessel system design and performance. *Nucl. Fusion* **2000**, *40*, 473–484.
- (89) Doerner, R.; Baldwin, M.; Hanna, J.; Linsmeier, C.; Nishijima, D.; Pugno, R.; Roth, J.; Schmid, K.; Wiltner, A. Interaction of beryllium containing plasma with ITER materials. *Phys. Scr.* **2007**, *2007*, 115.
- (90) Garai, J.; Laugier, A. The temperature dependence of the isothermal bulk modulus at 1 bar pressure. *J. Appl. Phys.* **2007**, *101*, 2424535.
- (91) Halsall, M. P.; Harmer, P.; Parbrook, P. J.; Henley, S. J. Raman scattering and absorption study of the high-pressure wurtzite to rocksalt phase transition of GaN. *Phys. Rev. B* **2004**, *69*, 235207.
- (92) Li, X.-C.; Gao, F.; Lu, G.-H. Molecular dynamics simulation of interaction of H with vacancy in W. *Nucl. Instrum. Methods Phys. Res., Sect. B* **2009**, *267*, 3197–3199.
- (93) Reiter, G. F.; Deb, A.; Sakurai, Y.; Itou, M.; Krishnan, V. G.; Paddison, S. J. Anomalous Ground State of the Electrons in Nanoconfined Water. *Phys. Rev. Lett.* **2013**, *111*, 036803.
- (94) Enoki, T.; Kobayashi, Y.; Fukui, K. I. Electronic structures of graphene edges and nanographene. *Int. Rev. Phys. Chem.* **2007**, *26*, 609–645.
- (95) Wang, Y.; Huang, Y.; Song, Y.; Zhang, X. Y.; Ma, Y. F.; Liang, J. J.; Chen, Y. S. Room-Temperature Ferromagnetism of Graphene. *Nano Lett.* **2009**, *9*, 220–224.
- (96) Fujita, T.; Okawa, Y.; Matsumoto, Y.; Tanaka, K. Phase boundaries of nanometer scale c(2 × 2)-O domains on the Cu(100) surface. *Phys. Rev. B* **1996**, *54*, 2167–2174.
- (97) Jensen, F.; Besenbacher, F.; Laegsgaard, E.; Stensgaard, I. Dynamics of oxygen-induced reconstruction on Cu(100) studied by scanning tunneling microscopy. *Phys. Rev. B* **1990**, *42*, 9206–9209.
- (98) Chua, F. M.; Kuk, Y.; Silverman, P. J. Oxygen chemisorption on Cu(110): An atomic view by scanning tunneling microscopy. *Phys. Rev. Lett.* **1989**, *63*, 386–389.
- (99) Sperl, A.; Kroger, J.; Berndt, R.; Franke, A.; Pehlke, E. Evolution of unoccupied resonance during the synthesis of a silver dimer on Ag(111). *New J. Phys.* **2009**, *11*, 063020.
- (100) Folsch, S.; Hyldgaard, P.; Koch, R.; Ploog, K. H. Quantum Confinement in Monatomic Cu Chains on Cu(111). *Phys. Rev. Lett.* **2004**, *92*, 056803.
- (101) Fister, T. T.; Fong, D. D.; Eastman, J. A.; Iddir, H.; Zapol, P.; Fuoss, P. H.; Balasubramanian, M.; Gordon, R. A.; Balasubramanian, K. R.; Salvador, P. A. Total-Reflection Inelastic X-Ray Scattering from a 10-nm Thick La_{0.6}Sr_{0.4}CoO₃ Thin Film. *Phys. Rev. Lett.* **2011**, *106*, 037401.
- (102) Hebboul, S. X-raying the Skin. <http://physics.aps.org/synopsis-for/10.1103/PhysRevLett.106.037401>. Feb 3, 2011.
- (103) Speranza, G.; Minati, L. The surface and bulk core line's in crystalline and disordered polycrystalline graphite. *Surf. Sci.* **2006**, *600*, 4438–4444.
- (104) Yang, D. Q.; Sacher, E. Carbon 1s X-ray photoemission line shape analysis of highly oriented pyrolytic graphite: The influence of structural damage on peak asymmetry. *Langmuir* **2006**, *22*, 860–862.
- (105) Aruna, I.; Mehta, B. R.; Malhotra, L. K.; Shivaprasad, S. M. Size dependence of core and valence binding energies in Pd nanoparticles: Interplay of quantum confinement and coordination reduction. *J. Appl. Phys.* **2008**, *104*, 064308.
- (106) Chambers, S. A. Elastic-scattering and interface of backscattered primary, Auger and X-ray photoelectrons at high kinetic-energy—principles and applications. *Surf. Sci. Rep.* **1992**, *16*, 261–331.
- (107) Huang, W. J.; Sun, R.; Tao, J.; Menard, L. D.; Nuzzo, R. G.; Zuo, J. M. Coordination-dependent surface atomic contraction in nanocrystals revealed by coherent diffraction. *Nat. Mater.* **2008**, *7*, 308–313.
- (108) Fang, B. S.; Lo, W. S.; Chien, T. S.; Leung, T. C.; Lue, C. Y.; Chan, C. T.; Ho, K. M. Surface band structures on Nb(001). *Phys. Rev. B* **1994**, *50*, 11093–11101.
- (109) Alden, M.; Skriver, H. L.; Johansson, B. Ab-initio surface core-level shifts and surface segregation energies. *Phys. Rev. Lett.* **1993**, *71*, 2449–2452.
- (110) Navas, E.; Starke, K.; Laubschat, C.; Weschke, E.; Kaindl, G. Surface core-level shift of 4f states for Tb(0001). *Phys. Rev. B* **1993**, *48*, 14753.
- (111) Balasubramanian, T.; Andersen, J. N.; Wallden, L. Surface-bulk core-level splitting in graphite. *Phys. Rev. B* **2001**, *64*, 205420.
- (112) Bartynski, R. A.; Heskett, D.; Garrison, K.; Watson, G.; Zehner, D. M.; Mei, W. N.; Tong, S. Y.; Pan, X. The 1st interlayer spacing of Ta(100) determined by photoelectron diffraction. *J. Vac. Sci. Technol., A* **1989**, *7*, 1931–1936.
- (113) Andersen, J. N.; Hennig, D.; Lundgren, E.; Methfessel, M.; Nyholm, R.; Scheffler, M. Surface core-level shifts of some 4d-metal single-crystal surfaces: Experiments and ab initio calculations. *Phys. Rev. B* **1994**, *50*, 17525–17533.
- (114) Baraldi, A.; Bianchettin, L.; Vesselli, E.; de Gironcoli, S.; Lizzit, S.; Petaccia, L.; Zampieri, G.; Comelli, G.; Rosei, R. Highly under-coordinated atoms at Rh surfaces: interplay of strain and coordination effects on core level shift. *New J. Phys.* **2007**, *9*, 143.
- (115) Nyholm, R.; Andersen, J. N.; Vanacker, J. F.; Qvarford, M. Surface core-level shifts of the Al(100) and Al(111) surfaces. *Phys. Rev. B* **1991**, *44*, 10987–10990.
- (116) Benito, N.; Galindo, R. E.; Rubio-Zuazo, J.; Castro, G. R.; Palacio, C. High- and low-energy x-ray photoelectron techniques for compositional depth profiles: destructive versus non-destructive methods. *J. Phys. D* **2013**, *46*, 065310.
- (117) Johansson, L. I.; Johansson, H. I. P.; Andersen, J. N.; Lundgren, E.; Nyholm, R. Surface-shifted core levels on Be(0001). *Phys. Rev. Lett.* **1993**, *71*, 2453–2456.
- (118) Johansson, L. I.; Johansson, H. I. P.; Lundgren, E.; Andersen, J. N.; Nyholm, R. Surface Core-level shift on Be(11–20). *Surf. Sci.* **1994**, *321*, L219–L224.
- (119) Johansson, L. I.; Johansson, H. I. P. Unusual behavior of surface shifted core levels on Be(0001) and Be(10–10). *Nucl. Instrum. Methods Phys. Res., Sect. B* **1995**, *97*, 430–435.
- (120) Johansson, L. I.; Glans, P. A.; Balasubramanian, T. Fourth-layer surface core-level shift on Be(0001). *Phys. Rev. B* **1998**, *58*, 3621–3624.
- (121) Suzer, S. XPS investigation of a Si-diode in operation. *Anal. Methods* **2012**, *4*, 3527–3530.
- (122) Suzer, S.; Sezen, H.; Dana, A. Two-dimensional X-ray photoelectron spectroscopy for composite surface analysis. *Anal. Chem.* **2008**, *80*, 3931–3936.
- (123) Suzer, S.; Sezen, H.; Ertas, G.; Dana, A. XPS measurements for probing dynamics of charging. *J. Electron Spectrosc. Relat. Phenom.* **2010**, *176*, 52–57.
- (124) Suzer, S.; Abelev, E.; Bernasek, S. L. Impedance-type measurements using XPS. *Appl. Surf. Sci.* **2009**, *256*, 1296–1298.
- (125) Sezen, H.; Suzer, S. Communication: Enhancement of dopant dependent x-ray photoelectron spectroscopy peak shifts of Si by surface photovoltaic. *J. Chem. Phys.* **2011**, *135*, 141102.
- (126) Papp, C.; Steinrück, H.-P. In situ high-resolution X-ray photoelectron spectroscopy—Fundamental insights in surface reactions. *Surf. Sci. Rep.* **2013**, *68*, 446–487.
- (127) Klyushin, A. Y.; Rocha, T. C. R.; Havecker, M.; Knop-Gericke, A.; Schlogl, R. A near ambient pressure XPS study of Au oxidation. *Phys. Chem. Chem. Phys.* **2014**, *16*, 7881–7886.
- (128) Wilson, K. R.; Rude, B. S.; Catalano, T.; Schaller, R. D.; Tobin, J. G.; Co, D. T.; Saykally, R. J. X-ray spectroscopy of liquid water microjets. *J. Phys. Chem. B* **2001**, *105*, 3346–3349.
- (129) Siefermann, K. R.; Liu, Y.; Lugovoy, E.; Link, O.; Faubel, M.; Buck, U.; Winter, B.; Abel, B. Binding energies, lifetimes and implications of bulk and interface solvated electrons in water. *Nat. Chem.* **2010**, *2*, 274–279.
- (130) Phillips, W. D. Laser cooling and trapping of neutral atoms. *Rev. Mod. Phys.* **1998**, *70*, 721–741.
- (131) Zhang, X.; Kuo, J. L.; Gu, M. X.; Fan, X. F.; Bai, P.; Song, Q. G.; Sun, C. Q. Local structure relaxation, quantum trap depression, and valence charge polarization induced by the shorter-and-stronger bonds

- between under-coordinated atoms in gold nanostructures. *Nanoscale* **2010**, *2*, 412–417.
- (132) Zhang, X.; Nie, Y. G.; Zheng, W. T.; Kuo, J. L.; Sun, C. Q. Discriminative generation and hydrogen modulation of the Dirac-Fermi polarons at graphene edges and atomic vacancies. *Carbon* **2011**, *49*, 3615–3621.
- (133) Sun, C. Q.; Zhang, X.; Zhou, J.; Huang, Y.; Zhou, Y.; Zheng, W. Density, elasticity, and stability anomalies of water molecules with fewer than four neighbors. *J. Phys. Chem. Lett.* **2013**, *4*, 2565–2570.
- (134) Bagus, P. S.; Ilton, E. S.; Nelin, C. J. The interpretation of XPS spectra: Insights into materials properties. *Surf. Sci. Rep.* **2013**, *68*, 273–304.
- (135) Johansson, B.; Martensson, N. Core-level binding-energy shifts for the metallic elements. *Phys. Rev. B* **1980**, *21*, 4427–4457.
- (136) Wertheim, G. K.; Guggenheim, H. J.; Buchanan, D. N. E. Size effect in ionic charge relaxation following Auger effect. *J. Chem. Phys.* **1969**, *51*, 1931–1934.
- (137) Williams, A. R.; Lang, N. D. Core-level binding-energy shifts in metals. *Phys. Rev. Lett.* **1978**, *40*, 954–957.
- (138) Pehlke, E.; Scheffler, M. Evidence for site-sensitive screening of core holes at the Si and Ge (001) surface. *Phys. Rev. Lett.* **1993**, *71*, 2338–2341.
- (139) Wang, Y.; Zhang, X.; Nie, Y. G.; Sun, C. Q. Under-coordinated atoms induced local strain, quantum trap depression and valence charge polarization at W stepped surfaces. *Physica B* **2012**, *407*, 49–53.
- (140) Vijayakrishnan, V.; Chainani, A.; Sarma, D. D.; Rao, C. N. R. Metal-insulator transitions in metal-clusters—a high-energy spectroscopy study of Pd and Ag clusters. *J. Phys. Chem.* **1992**, *96*, 8679–8682.
- (141) Citrin, P. H.; Wertheim, G. K. Photoemission from surface-atom core levels, surface densities of states, and metal-atom clusters: A unified picture. *Phys. Rev. B* **1983**, *27*, 3176–3200.
- (142) Mason, M. G. In *Cluster Models for Surface and Bulk Phenomena*; Plenum: New York, 1992.
- (143) Rao, C. N. R.; Kulkarni, G. U.; Thomas, P. J.; Edwards, P. P. Size-dependent chemistry: Properties of nanocrystals. *Chem.—Eur. J.* **2002**, *8*, 29–35.
- (144) Aiyer, H. N.; Vijayakrishnan, V.; Subbanna, G. N.; Rao, C. N. R. Investigations of Pd clusters by the combined use of HREM, STM, high-energy spectroscopies and tunneling conductance measurements. *Surf. Sci.* **1994**, *313*, 392–398.
- (145) Boyen, H.-G.; Herzog, T.; Kästle, G.; Weigl, F.; Ziemann, P.; Spatz, J.; Möller, M.; Wahrenberg, R.; Garnier, M.; Oelhafen, P. X-ray photoelectron spectroscopy study on gold nanoparticles supported on diamond. *Phys. Rev. B* **2002**, *65*, 075412.
- (146) Yang, D. Q.; Sacher, E. Platinum nanoparticle interaction with chemically modified highly oriented pyrolytic graphite surfaces. *Chem. Mater.* **2006**, *18*, 1811–1816.
- (147) Borgohain, K.; Singh, J. B.; Rao, M. V. R.; Shripathi, T.; Mahamuni, S. Quantum size effects in CuO nanoparticles. *Phys. Rev. B* **2000**, *61*, 11093–11096.
- (148) Schmeisser, D.; Bohme, O.; Yfantis, A.; Heller, T.; Batchelor, D. R.; Lundstrom, I.; Spetz, A. L. Dipole moment of nanoparticles at interfaces. *Phys. Rev. Lett.* **1999**, *83*, 380–383.
- (149) Yang, Z.; Wu, R. Origin of positive core-level shifts in Au clusters on oxides. *Phys. Rev. B* **2003**, *67*, 081403.
- (150) Nelin, C. J.; Uhl, F.; Staemmler, V.; Bagus, P. S.; Fujimori, Y.; Sterrer, M.; Kuhlenbeck, H.; Freund, H.-J. Surface core-level binding energy shifts for MgO (100). *Phys. Chem. Chem. Phys.* **2014**, *16*, 21953–21956.
- (151) Sun, C. Q.; Nie, Y.; Pan, J.; Zhang, X.; Ma, S. Z.; Wang, Y.; Zheng, W. Zone-selective photoelectronic measurements of the local bonding and electronic dynamics associated with the monolayer skin and point defects of graphite. *RSC Adv.* **2012**, *2*, 2377–2383.
- (152) Nie, Y.; Wang, Y.; Zhang, X.; Pan, J.; Zheng, W.; Sun, C. Q. Catalytic nature of under- and hetero-coordinated atoms resolved using zone-selective photoelectron spectroscopy (ZPS). *Vacuum* **2014**, *100*, 87–91.
- (153) Sun, C. Q.; Wang, Y.; Tay, B. K.; Li, S.; Huang, H.; Zhang, Y. B. Correlation between the melting point of a nanosolid and the cohesive energy of a surface atom. *J. Phys. Chem. B* **2002**, *106*, 10701–10705.
- (154) Egerton, R.; Li, P.; Malac, M. Radiation damage in the TEM and SEM. *Micron* **2004**, *35*, 399–409.
- (155) Lin, C.-Y.; Shiu, H. W.; Chang, L. Y.; Chen, C.-H.; Chang, C.-S.; Chien, F. S.-S. Core-Level Shift of Graphene with Number of Layers Studied by Microphotoelectron Spectroscopy and Electrostatic Force Microscopy. *J. Phys. Chem. C* **2014**, *118*, 24898–24904.
- (156) Sun, C. Q.; Shi, Y.; Li, C. M.; Li, S.; Yeung, T. C. A. Size-induced undercooling and overheating in phase transitions in bare and embedded clusters. *Phys. Rev. B* **2006**, *73*, 075408.
- (157) Sun, C. Q.; Chen, T. P.; Tay, B. K.; Li, S.; Huang, H.; Zhang, Y. B.; Pan, L. K.; Lau, S. P.; Sun, X. W. An extended ‘quantum confinement’ theory: surface-coordination imperfection modifies the entire band structure of a nanosolid. *J. Phys. D* **2001**, *34*, 3470–3479.
- (158) Zheng, W.-T.; Sun, C. Q. Underneath the fascinations of carbon nanotubes and graphene nanoribbons. *Energy Environ. Sci.* **2011**, *4*, 627–655.
- (159) Abrahams, E.; Anderson, P. W.; Licciardello, D. C.; Ramakrishnan, T. V. Scaling Theory of Localization: Absence of Quantum Diffusion in Two Dimensions. *Phys. Rev. Lett.* **1979**, *42*, 673–676.
- (160) Street, R. A. *Hydrogenated Amorphous Silicon*; Cambridge University Press: Cambridge, U.K., 1991.
- (161) Sun, C. Q.; Li, C. M.; Li, S.; Tay, B. K. Breaking limit of atomic distance in an impurity-free monatomic chain. *Phys. Rev. B* **2004**, *69*, 245402.
- (162) Reif, M.; Glaser, L.; Martins, M.; Wurth, W. Size-dependent properties of small deposited chromium clusters by x-ray absorption spectroscopy. *Phys. Rev. B* **2005**, *72*, 155405.
- (163) Sun, C. Q.; Sun, Y.; Nie, Y. G.; Wang, Y.; Pan, J. S.; Ouyang, G.; Pan, L. K.; Sun, Z. Coordination-Resolved C-C Bond Length and the C 1s Binding Energy of Carbon Allotropes and the Effective Atomic Coordination of the Few-Layer Graphene. *J. Phys. Chem. C* **2009**, *113*, 16464–16467.
- (164) Sun, Y.; Wang, Y.; Pan, J. S.; Wang, L. L.; Sun, C. Q. Elucidating the 4f Binding Energy of an Isolated Pt Atom and Its Bulk Shift from the Measured Surface- and Size-Induced Pt 4f Core Level Shift. *J. Phys. Chem. C* **2009**, *113*, 14696–14701.
- (165) Huang, Y.; Zhang, X.; Ma, Z.; Zhou, Y.; Zheng, W.; Zhou, J.; Sun, C. Q. Hydrogen-bond relaxation dynamics: resolving mysteries of water ice. *Coord. Chem. Rev.* **2015**, *285*, 109–165.
- (166) Pan, L. K.; Xu, S. Q.; Qin, W.; Liu, X. J.; Sun, Z.; Zheng, W. T.; Sun, C. Q. Skin dominance of the dielectric-electronic-phononic-photonic attribute of nanostructured silicon. *Surf. Sci. Rep.* **2013**, *68*, 418–455.
- (167) Pauling, L. Atomic radii and interatomic distances in metals. *J. Am. Chem. Soc.* **1947**, *69*, 542–553.
- (168) Johnston, H. S.; Parr, C. Activation energies from bond energies: 1. Hydrogen transfer reactions. *J. Am. Chem. Soc.* **1963**, *85*, 2544–2551.
- (169) Weinberg, W. H. The Bond-Energy Bond-Order (BEBO) Model of Chemisorption. *J. Vac. Sci. Technol.* **1973**, *10*, 89–94.
- (170) Shustorovich, E. Chemisorption phenomena: analytic modeling based perturbation theory and bond-order conservation. *Surf. Sci. Rep.* **1986**, *6*, 1–63.
- (171) Gross, H.; Campbell, C. T.; King, D. A. Metal-carbon bond energies for adsorbed hydrocarbons from calorimetric data. *Surf. Sci.* **2004**, *572*, 179–190.
- (172) Weinberg, W. H.; Merrill, R. P. Crystal-field surface orbital-bond-energy bond-order (CFSO-BEBO) model for chemisorption—application to hydrogen adsorption on a Platinum (111) surface. *Surf. Sci.* **1972**, *33*, 493–515.
- (173) Campbell, C. T.; Starr, D. E. Metal adsorption and adhesion energies on MgO(100). *J. Am. Chem. Soc.* **2002**, *124*, 9212–9218.
- (174) Bondzie, V. A.; Parker, S. C.; Campbell, C. T. The kinetics of CO oxidation by adsorbed oxygen on well-defined gold particles on TiO₂(110). *Catal. Lett.* **1999**, *63*, 143–151.

- (175) Popovic, Z. S.; Satpathy, S. Wedge-shaped potential and Airy-function electron localization in oxide superlattices. *Phys. Rev. Lett.* **2005**, *94*, 176805.
- (176) Nie, Y.; Wang, Y.; Sun, Y.; Pan, J. S.; Mehta, B. R.; Khanuja, M.; Shivaprasad, S. M.; Sun, C. Q. CuPd interface charge and energy quantum entrapment: A tight-binding and XPS investigation. *Appl. Surf. Sci.* **2010**, *257*, 727–730.
- (177) Sun, C. Q.; Wang, Y.; Nie, Y. G.; Sun, Y.; Pan, J. S.; Pan, L. K.; Sun, Z. Adatoms-Induced Local Bond Contraction, Quantum Trap Depression, and Charge Polarization at Pt and Rh Surfaces. *J. Phys. Chem. C* **2009**, *113*, 21889–21894.
- (178) Sun, C. Q. O-Cu(001): I. Binding the signatures of LEED, STM and PES in a bond-forming way. *Surf. Rev. Lett.* **2001**, *8*, 367–402.
- (179) Stipe, B. C.; Rezaei, M. A.; Ho, W. Single-Molecule Vibrational Spectroscopy and Microscopy. *Science* **1998**, *280*, 1732–1735.
- (180) Zheng, W. T.; Sun, C. Q.; Tay, B. K. Modulating the work function of carbon by N or O addition and nanotip fabrication. *Solid State Commun.* **2003**, *128*, 381–384.
- (181) Li, J. J.; Zheng, W. T.; Gu, C. Z.; Jin, Z. S.; Zhao, Y. N.; Mei, X. X.; Mu, Z. X.; Dong, C.; Sun, C. Q. Field emission enhancement of amorphous carbon films by nitrogen-implantation. *Carbon* **2004**, *42*, 2309–2314.
- (182) Zheng, W. T.; Li, J. J.; Wang, X.; Li, X. T.; Jin, Z. S.; Tay, B. K.; Sun, C. Q. Electron emission of carbon nitride films and mechanism for the nitrogen-lowered threshold in cold cathode. *J. Appl. Phys.* **2003**, *94*, 2741–2745.
- (183) Dingreville, R.; Qu, J.; Cherkaoui, M. Surface free energy and its effect on the elastic behavior of nano-sized particles, wires and films. *J. Mech. Phys. Solids* **2005**, *53*, 1827–1854.
- (184) Zhao, M. W.; Zhang, R. Q.; Xia, Y. Y.; Song, C.; Lee, S. T. Faceted silicon nanotubes: Structure, energetic, and passivation effects. *J. Phys. Chem. C* **2007**, *111*, 1234–1238.
- (185) Jacob, W.; Dose, V.; Goldmann, A. Atomic adsorption of oxygen on Cu (111) and Cu (110). *Appl. Phys. A: Mater. Sci. Process.* **1986**, *41*, 145–150.
- (186) Qin, W.; Wang, Y.; Huang, Y.; Zhou, Z.; Yang, C.; Sun, C. Q. Bond Order Resolved 3d(5/2) and Valence Band Chemical Shifts of Ag Surfaces and Nanoclusters. *J. Phys. Chem. A* **2012**, *116*, 7892–7897.
- (187) Sun, C. Q.; Pan, L. K.; Bai, H. L.; Li, Z. Q.; Wu, P.; Jiang, E. Y. Effects of surface passivation and interfacial reaction on the size-dependent 2p-level shift of supported copper nanosolids. *Acta Mater.* **2003**, *51*, 4631–4636.
- (188) Moretti, G. Auger parameter and Wagner plot in the characterization of chemical states by X-ray photoelectron spectroscopy: a review. *J. Electron Spectrosc. Relat. Phenom.* **1998**, *95*, 95–144.
- (189) Moretti, G. The Wagner plot and the Auger parameter as tools to separate initial-and final-state contributions in X-ray photoemission spectroscopy. *Surf. Sci.* **2013**, *618*, 3–11.
- (190) Satta, M.; Moretti, G. Auger parameters and Wagner plots. *J. Electron Spectrosc. Relat. Phenom.* **2010**, *178*, 123–127.
- (191) Practical Surface Analysis by Auger and X-Ray Photoelectron Spectroscopy, 2nd ed.; Wagner, C. D., Ed.; Wiley: Chichester, U.K., 1990.
- (192) McEleney, K.; Crudden, C. M.; Horton, J. H. X-ray Photoelectron Spectroscopy and the Auger Parameter As Tools for Characterization of Silica-Supported Pd Catalysts for the Suzuki-Miyaura Reaction. *J. Phys. Chem. C* **2009**, *113*, 1901–1907.
- (193) Sun, C. Q.; Pan, L. K.; Chen, T. P.; Sun, X. W.; Li, S.; Li, C. M. Distinguishing the effect of crystal-field screening from the effect of valence recharging on the 2P_{3/2} and 3d_{5/2} level energies of nanostructured copper. *Appl. Surf. Sci.* **2006**, *252*, 2101–2107.
- (194) Wallin, D.; Shorubalko, I.; Xu, H.; Cappy, A. Nonlinear electrical properties of three-terminal junctions. *Appl. Phys. Lett.* **2006**, *89*, 092124.
- (195) Hajati, S.; Coulter, S.; Blomfield, C.; Tougaard, S. XPS imaging of depth profiles and amount of substance based on Tougaard's algorithm. *Surf. Sci.* **2006**, *600*, 3015–3021.
- (196) Seah, M. P.; Gilmore, I. S.; Spencer, S. J. Background subtraction—II. General behaviour of REELS and the Tougaard universal cross section in the removal of backgrounds in AES and XPS. *Surf. Sci.* **2000**, *461*, 1–15.
- (197) Zhou, X. B.; Erskine, J. L. Surface core-level shifts at vicinal tungsten surfaces. *Phys. Rev. B* **2009**, *79*, 155422.
- (198) Riffe, D. M.; Wertheim, G. K. Ta(110) surface and subsurface core-level shifts and 4f^{7/2} line shapes. *Phys. Rev. B* **1993**, *47*, 6672–6679.
- (199) Cho, J. H.; Kim, K. S.; Lee, S. H.; Kang, M. H.; Zhang, Z. Y. Origin of contrasting surface core-level shifts at the Be(10–10) and Mg(10–10) surfaces. *Phys. Rev. B* **2000**, *61*, 9975–9978.
- (200) Fedorov, A. V.; Arenholz, E.; Starke, K.; Navas, E.; Baumgarten, L.; Laubschat, C.; Kaindl, G. Surface shifts of 4f electron-addition and electron-removal states on Gd(0001). *Phys. Rev. Lett.* **1994**, *73*, 601–604.
- (201) Lizzit, S.; Pohl, K.; Baraldi, A.; Comelli, G.; Fritzsche, V.; Plummer, E. W.; Stumpf, R.; Hofmann, P. Physics of the Be(10–10) surface core level spectrum. *Phys. Rev. Lett.* **1998**, *81*, 3271–3274.
- (202) Johansson, H. I. P.; Johansson, L. I.; Lundgren, E.; Andersen, J. N.; Nyholm, R. Core-level shifts on Be(10–10). *Phys. Rev. B* **1994**, *49*, 17460–17463.
- (203) Baraldi, A.; Lizzit, S.; Comelli, G.; Goldoni, A.; Hofmann, P.; Paolucci, G. Core-level subsurface shifted component in a 4d transition metal: Ru(1010). *Phys. Rev. B* **2000**, *61*, 4534–4537.
- (204) Lundgren, E.; Johansson, U.; Nyholm, R.; Andersen, J. N. Surface core-level shift of the Mo(110) surface. *Phys. Rev. B* **1993**, *48*, 5525–5529.
- (205) Riffe, D. M.; Kim, B.; Erskine, J. L. Surface core-level shifts and atomic coordination at a stepped W(110) surface. *Phys. Rev. B* **1994**, *50*, 14481–14488.
- (206) Cho, J. H.; Oh, D. H.; Kleinman, L. Core-level shifts of low coordination atoms at the W(320) stepped surface. *Phys. Rev. B* **2001**, *64*, 115404.
- (207) Slack, G. A.; Bartram, S. F. Thermal expansion of some diamond-like crystals. *J. Appl. Phys.* **1975**, *46*, 89–98.
- (208) Hart, T. R.; Aggarwal, R. L.; Lax, B. Temperature dependence of Raman scattering in silicon. *Phys. Rev. B* **1970**, *1*, 638–642.
- (209) Liu, M. S.; Bursill, L. A.; Prawer, S.; Beserman, R. Temperature dependence of the first-order Raman phonon line of diamond. *Phys. Rev. B* **2000**, *61*, 3391–3395.
- (210) Kuzmin, M.; Punkkinen, M. J. P.; Laukkonen, P.; Lång, J. J. K.; Dahl, J.; Tuominen, V.; Tuominen, M.; Perälä, R. E.; Balasubramanian, T.; Adell, J.; Johansson, B.; Vitos, L.; Kokko, K.; Väyrynen, I. J. Surface core-level shifts on Ge(111)c(2×8): Experiment and theory. *Phys. Rev. B* **2011**, *83*, 245319.
- (211) Lizzit, S.; Baraldi, A.; Groso, A.; Reuter, K.; Ganduglia-Pirovano, M. V.; Stampf, C.; Scheffler, M.; Stichler, M.; Keller, C.; Wurth, W.; Menzel, D. Surface core-level shifts of clean and oxygen-covered Ru(0001). *Phys. Rev. B* **2001**, *63*, 205419.
- (212) Cui, J. B.; Amtmann, K.; Ristein, J.; Ley, L. Noncontact temperature measurements of diamond by Raman scattering spectroscopy. *J. Appl. Phys.* **1998**, *83*, 7929–7933.
- (213) Wang, Y.; Nie, Y. G.; Pan, J. S.; Pan, L. K.; Sun, Z.; Wang, L. L.; Sun, C. Q. Orientation-resolved 3d(5/2) binding energy shift of Rh and Pd surfaces: anisotropy of the skin-depth lattice strain and quantum trapping. *Phys. Chem. Chem. Phys.* **2010**, *12*, 2177–2182.
- (214) Powell, C. J.; Jablonski, A. Progress in quantitative surface analysis by X-ray photoelectron spectroscopy: Current status and perspectives. *J. Electron Spectrosc. Relat. Phenom.* **2010**, *178–179*, 331–346.
- (215) Chawla, J.; Zhang, X.; Gall, D. Effective electron mean free path in TiN (001). *J. Appl. Phys.* **2013**, *113*, 063704.
- (216) Wang, Y.; Nie, Y. G.; Wang, L. L.; Sun, C. Q. Atomic-Layer- and Crystal-Orientation-Resolved 3d_{5/2} Binding Energy Shift of Ru(0001) and Ru(1010) Surfaces. *J. Phys. Chem. C* **2010**, *114*, 1226–1230.
- (217) Qi, W. H.; Huang, B. Y.; Wang, M. P. Bond-Length and -Energy Variation of Small Gold Nanoparticles. *J. Theor. Comput. Nanosci.* **2009**, *6*, 635–639.
- (218) Matsui, F.; Matsushita, T.; Kato, Y.; Hashimoto, M.; Inaji, K.; Guo, F. Z.; Daimon, H. Atomic-layer resolved magnetic and electronic

- structure analysis of Ni thin film on a Cu(001) surface by diffraction spectroscopy. *Phys. Rev. Lett.* **2008**, *100*, 207201.
- (219) Bianchi, M.; Cassese, D.; Cavallin, A.; Comin, R.; Orlando, F.; Postregna, L.; Galfetto, E.; Lizzit, S.; Baraldi, A. Surface core level shifts of clean and oxygen covered Ir(111). *New J. Phys.* **2009**, *11*, 063002.
- (220) Barrett, N.; Guillot, C.; Villette, B.; Treglia, G.; Legrand, B. Inversion of the core level shift between surface and subsurface atoms of the iridium (100)(1×1) and (100)(5×1) surfaces. *Surf. Sci.* **1991**, *251*, 717–721.
- (221) Borg, M.; Birgersson, M.; Smedh, M.; Mikkelsen, A.; Adams, D. L.; Nyholm, R.; Almbladh, C.-O.; Andersen, J. N. Experimental and theoretical surface core-level shifts of aluminum (100) and (111). *Phys. Rev. B* **2004**, *69*, 235418.
- (222) Bo, M.; Wang, Y.; Huang, Y.; Yang, X.; Yang, Y.; Li, C.; Sun, C. Q. Coordination-resolved local bond relaxation, electron binding-energy shift, and Debye temperature of Ir solid skins. *Appl. Surf. Sci.* **2014**, *320*, 509–513.
- (223) Heimann, P.; van der Veen, J. F.; Eastman, D. E. Structure-dependent surface core level shifts for the Au(111), (100), and (110) surfaces. *Solid State Commun.* **1981**, *38*, 595–598.
- (224) Yu, W.; Bo, M.; Huang, Y.; Wang, Y.; Li, C.; Sun, C. Q. Coordination-resolved bond and electron spectrometrics of Au atomic clusters, solid skins, and oxidized foils. *ChemPhysChem* **2015**, DOI: 10.1002/cphc.201500171.
- (225) Rocca, M.; Savio, L.; Vattuone, L.; Burghaus, U.; Palomba, V.; Novelli, N.; de Mongeot, F. B.; Valbusa, U.; Gunnella, R.; Comelli, G.; Baraldi, A.; Lizzit, S.; Paolucci, G. Phase transition of dissociatively adsorbed oxygen on Ag(001). *Phys. Rev. B* **2000**, *61*, 213–227.
- (226) Zhu, Y.; Qin, Q.; Xu, F.; Fan, F.; Ding, Y.; Zhang, T.; Wiley, B. J.; Wang, Z. L. Size effects on elasticity, yielding, and fracture of silver nanowires: In situ experiments. *Phys. Rev. B* **2012**, *85*, 045443.
- (227) Jupille, J.; Purcell, K. G.; King, D. A. W(100) clean surface phase transition studied by core-level-shift spectroscopy: Order-order or order-disorder transition. *Phys. Rev. B* **1989**, *39*, 6871–6879.
- (228) Purcell, K. G.; Jupille, J.; Derby, G. P.; King, D. A. Identification of underlayer components in the surface core-level spectra of W(111). *Phys. Rev. B* **1987**, *36*, 1288–1291.
- (229) Minni, E.; Werfel, F. Oxygen interaction with Mo (100) studied by XPS, AES and EELS. *Surf. Interface Anal.* **1988**, *12*, 385–390.
- (230) Zhou, W.; Bo, M.; Wang, Y.; Huang, Y.; Li, C.; Sun, C. Q. Local bond-electron-energy relaxation of Mo atomic clusters and solid skins. *RSC Adv.* **2015**, *5*, 29663–29668.
- (231) Himpel, F.; Heimann, P.; Chiang, T.; Eastman, D. Geometry-Dependent Si(2p) Surface Core-Level Excitations for Si(111) and Si(100) Surfaces. *Phys. Rev. Lett.* **1980**, *45*, 1112–1115.
- (232) Himpel, F.; Hollinger, G.; Pollak, R. Determination of the Fermi-level pinning position at Si(111) surfaces. *Phys. Rev. B* **1983**, *28*, 7014–7018.
- (233) Niikura, R.; Nakatsuji, K.; Komori, F. Local atomic and electronic structure of Au-adsorbed Ge (001) surfaces: Scanning tunneling microscopy and x-ray photoemission spectroscopy. *Phys. Rev. B* **2011**, *83*, 035311.
- (234) Bo, M.; Wang, Y.; Huang, Y.; Zhang, X.; Zhang, T.; Li, C.; Sun, C. Q. Coordination-resolved local bond contraction and electron binding-energy entrainment of Si atomic clusters and solid skins. *J. Appl. Phys.* **2014**, *115*, 144309.
- (235) Baraldi, A.; Lizzit, S.; Comelli, G.; Paolucci, G. Oxygen adsorption and ordering on Ru(1010). *Phys. Rev. B* **2001**, *63*, 115410.
- (236) Martensson, N.; Saalfeld, H. B.; Kuhlenbeck, H.; Neumann, M. Structural dependence of the 5d-metal surface energies as deduced from surface core-level shift measurements. *Phys. Rev. B* **1989**, *39*, 8181–8186.
- (237) Chan, A. S. Y.; Wertheim, G. K.; Wang, H.; Ulrich, M. D.; Rowe, J. E.; Madey, T. E. Surface atom core-level shifts of clean and oxygen-covered Re(1231). *Phys. Rev. B* **2005**, *72*, 035442.
- (238) Wang, Y.; Nie, Y. G.; Pan, J. S.; Pan, L. K.; Sun, Z.; Sun, C. Q. Layer and orientation resolved bond relaxation and quantum entrapment of charge and energy at Be surfaces. *Phys. Chem. Chem. Phys.* **2010**, *12*, 12753–12759.
- (239) Kittel, C. *Introduction to Solid State Physics*, 8th ed.; John Wiley & Sons, Inc.: New York, 2005.
- (240) Zhao, M.; Zheng, W. T.; Li, J. C.; Wen, Z.; Gu, M. X.; Sun, C. Q. Atomistic origin, temperature dependence, and responsibilities of surface energetics: An extended broken-bond rule. *Phys. Rev. B* **2007**, *75*, 085427.
- (241) Garitaonandia, J. S.; Insausti, M.; Goikolea, E.; Suzuki, M.; Cashion, J. D.; Kawamura, N.; Ohsawa, H.; Gil de Muro, I.; Suzuki, K.; Plazaola, F. Chemically induced permanent magnetism in Au, Ag, and Cu nanoparticles: localization of the magnetism by element selective techniques. *Nano Lett.* **2008**, *8*, 661–667.
- (242) Yamamoto, Y.; Miura, T.; Suzuki, M.; Kawamura, N.; Miyagawa, H.; Nakamura, T.; Kobayashi, K.; Teranishi, T.; Hori, H. Direct observation of ferromagnetic spin polarization in gold nanoparticles. *Phys. Rev. Lett.* **2004**, *93*, 116801.
- (243) Magyar, R.; Mujica, V.; Marquez, M.; Gonzalez, C. Density-functional study of magnetism in bare Au nanoclusters: Evidence of permanent size-dependent spin polarization without geometry relaxation. *Phys. Rev. B* **2007**, *75*, 144421.
- (244) Wang, B.; Xiao, X. D.; Huang, X. X.; Sheng, P.; Hou, J. G. Single-electron tunneling study of two-dimensional gold clusters. *Appl. Phys. Lett.* **2000**, *77*, 1179–1181.
- (245) Yeshchenko, O. A.; Dmitruk, I. M.; Alexeenko, A. A.; Losytskyy, M. Y.; Kotko, A. V.; Pinchuk, A. O. Size-dependent surface-plasmon-enhanced photoluminescence from silver nanoparticles embedded in silica. *Phys. Rev. B* **2009**, *79*, 235438.
- (246) Sancho-Parramon, J. Surface plasmon resonance broadening of metallic particles in the quasi-static approximation: a numerical study of size confinement and interparticle interaction effects. *Nanotechnology* **2009**, *20*, 235706.
- (247) Turner, M.; Golovko, V. B.; Vaughan, O. P.; Abdulkin, P.; Berenguer-Murcia, A.; Tikhov, M. S.; Johnson, B. F.; Lambert, R. M. Selective oxidation with dioxygen by gold nanoparticle catalysts derived from 55-atom clusters. *Nature* **2008**, *454*, 981–983.
- (248) Valden, M.; Lai, X.; Goodman, D. W. Onset of catalytic activity of gold clusters on titania with the appearance of nonmetallic properties. *Science* **1998**, *281*, 1647–1650.
- (249) Wittstock, A.; Neumann, B.; Schaefer, A.; Dumbuya, K.; Kübel, C.; Biener, M. M.; Zielasek, V.; Steinrück, H.-P.; Gottfried, J. M.; Biener, J.; Hamza, A.; Baümer, M. Nanoporous Au: an unsupported pure gold catalyst? *J. Phys. Chem. C* **2009**, *113*, 5593–5600.
- (250) Zheng, Y. B.; Jensen, L.; Yan, W.; Walker, T. R.; Juluri, B. K.; Jensen, L.; Huang, T. J. Chemically tuning the localized surface plasmon resonances of gold nanostructure arrays. *J. Phys. Chem. C* **2009**, *113*, 7019–7024.
- (251) Elbakry, A.; Zaky, A.; Liebl, R.; Rachel, R.; Goepferich, A.; Breunig, M. Layer-by-layer assembled gold nanoparticles for siRNA delivery. *Nano Lett.* **2009**, *9*, 2059–2064.
- (252) Pustovalov, V.; Babenko, V. Optical properties of gold nanoparticles at laser radiation wavelengths for laser applications in nanotechnology and medicine. *Laser Phys. Lett.* **2004**, *1*, 516–520.
- (253) Gu, M. X.; Sun, C. Q.; Tan, C. M.; Wang, S. Z. Local bond average for the size and temperature dependence of elastic and vibronic properties of nanostructures. *Int. J. Nanotechnol.* **2009**, *6*, 640–652.
- (254) McKenna, K. P. Gold nanoparticles under gas pressure. *Phys. Chem. Chem. Phys.* **2009**, *11*, 4145–4151.
- (255) Jadzinsky, P. D.; Calero, G.; Ackerson, C. J.; Bushnell, D. A.; Kornberg, R. D. Structure of a thiol monolayer-protected gold nanoparticle at 1.1 angstrom resolution. *Science* **2007**, *318*, 430–433.
- (256) Wang, B.; Wang, K. D.; Lu, W.; Yang, J. L.; Hou, J. G. Size-dependent tunneling differential conductance spectra of crystalline Pd nanoparticles. *Phys. Rev. B* **2004**, *70*, 205411.
- (257) Nilius, N.; Wallis, T. M.; Ho, W. Development of one-dimensional band structure in artificial gold chains. *Science* **2002**, *297*, 1853–1856.
- (258) Schouteden, K.; Lijnen, E.; Muzychko, D. A.; Ceulemans, A.; Chibotaru, L. F.; Lievens, P.; Haesendonck, C. V. A study of the electronic properties of Au nanowires and Au nanoislands on Au(111) surfaces. *Nanotechnology* **2009**, *20*, 395401.

- (259) Briner, B. G.; Hofmann, P.; Doering, M.; Rust, H. P.; Plummer, E. W.; Bradshaw, A. M. Charge-density oscillations on Be(10–10): Screening in a non-free two-dimensional electron gas. *Phys. Rev. B* **1998**, *58*, 13931–13943.
- (260) Bianchettin, L.; Baraldi, A.; de Gironcoli, S.; Vesselli, E.; Lizzit, S.; Petaccia, L.; Comelli, G.; Rosei, R. Core level shifts of under-coordinated Pt atoms. *J. Chem. Phys.* **2008**, *128*, 114706.
- (261) Gustafson, J.; Borg, M.; Mikkelsen, A.; Gorovikov, S.; Lundgren, E.; Andersen, J. N. Identification of Step Atoms by High Resolution Core Level Spectroscopy. *Phys. Rev. Lett.* **2003**, *91*, 056102.
- (262) Baraldi, A.; Lizzit, S.; Bondino, F.; Comelli, G.; Rosei, R.; Sbraccia, C.; Bonini, N.; Baroni, S.; Mikkelsen, A.; Andersen, J. N. Thermal stability of the Rh(110) missing-row reconstruction: Combination of real-time core-level spectroscopy and ab initio modeling. *Phys. Rev. B* **2005**, *72*, 075417.
- (263) Baraldi, A.; Vesselli, E.; Bianchettin, L.; Comelli, G.; Lizzit, S.; Petaccia, L.; de Gironcoli, S.; Locatelli, A.; Mentes, T. O.; Aballe, L.; Weissenrieder, J.; Andersen, J. N. The $(1 \times 1) \rightarrow$ hexagonal structural transition on Pt(100) studied by high-energy resolution core level photoemission. *J. Chem. Phys.* **2007**, *127*, 164702.
- (264) Cox, A. J.; Louderback, J. G.; Apsel, S. E.; Bloomfield, L. A. Magnetic in 4d-transition metal-clusters. *Phys. Rev. B* **1994**, *49*, 12295–12298.
- (265) Zheng, W. T.; Zhou, J.; Sun, C. Q. Purified rhodium edge states: undercoordination-induced quantum entrapment and polarization. *Phys. Chem. Chem. Phys.* **2010**, *12*, 12494–12498.
- (266) Nie, Y.; Zhang, X.; Ma, S.; Wang, Y.; Pan, J.; Sun, C. Q. XPS revelation of tungsten edges as a potential donor-type catalyst. *Phys. Chem. Chem. Phys.* **2011**, *13*, 12640–12645.
- (267) Asscher, M.; Carrazza, J.; Khan, M.; Lewis, K.; Somorjai, G. The ammonia synthesis over rhenium single-crystal catalysts: kinetics, structure sensitivity, and effect of potassium and oxygen. *J. Catal.* **1986**, *98*, 277–287.
- (268) Chan, A. S. Y.; Chen, W.; Wang, H.; Rowe, J. E.; Madey, T. E. Methanol Reactions over Oxygen-Modified Re Surfaces: Influence of Surface Structure and Oxidation. *J. Phys. Chem. B* **2004**, *108*, 14643–14651.
- (269) Ducros, R.; Fusy, J. Core level binding energy shifts of rhenium surface atoms for a clean and oxygenated surface. *J. Electron Spectrosc. Relat. Phenom.* **1987**, *42*, 305–312.
- (270) Spanjaard, D.; Guillot, C.; Desjonquères, M.-C.; Tréglia, G.; Lecante, J. Surface core level spectroscopy of transition metals: A new tool for the determination of their surface structure. *Surf. Sci. Rep.* **1985**, *5*, 1–85.
- (271) Bittencourt, C.; Felten, A.; Douhard, B.; Ghijsen, J.; Johnson, R. L.; Drube, W.; Pireaux, J. J. Photoemission studies of gold clusters thermally evaporated on multiwall carbon nanotubes. *Chem. Phys.* **2006**, *328*, 385–391.
- (272) Suprun, S. P.; Fedosenko, E. V. Low-temperature recrystallization of Ge nanolayers on ZnSe. *Semiconductors* **2007**, *41*, 590–595.
- (273) Tao, J. G.; Pan, J. S.; Huan, C. H. A.; Zhang, Z.; Chai, J. W.; Wang, S. J. Origin of XPS binding energy shifts in Ni clusters and atoms on rutile TiO₂ surfaces. *Surf. Sci.* **2008**, *602*, 2769–2773.
- (274) Balamurugan, B.; Maruyama, T. Size-modified d bands and associated interband absorption of Ag nanoparticles. *J. Appl. Phys.* **2007**, *102*, 034306.
- (275) Balamurugan, B.; Maruyama, T. Inhomogeneous effect of particle size on core-level and valence-band electrons: Size-dependent electronic structure of Cu₃N nanoparticles. *Appl. Phys. Lett.* **2006**, *89*, 033112.
- (276) Kim, S.; Kim, M. C.; Choi, S. H.; Kim, K. J.; Hwang, H. N.; Hwang, C. C. Size dependence of Si 2p core-level shift at Si nanocrystal/SiO₂ interfaces. *Appl. Phys. Lett.* **2007**, *91*, 103113.
- (277) Ahmadi, S.; Zhang, X.; Gong, Y.; Chia, C.-H.; Sun, C. Q. Skin-resolved local bond contraction, core electron entrapment, and valence charge polarization of Ag and Cu nanoclusters. *Phys. Chem. Chem. Phys.* **2014**, *16*, 8940–8948.
- (278) Ohgi, T.; Fujita, D. Consistent size dependency of core-level binding energy shifts and single-electron tunneling effects in supported gold nanoclusters. *Phys. Rev. B* **2002**, *66*, 115410.
- (279) Kara, A.; Rahman, T. S. Vibrational properties of metallic nanocrystals. *Phys. Rev. Lett.* **1998**, *81*, 1453–1456.
- (280) Feibelman, P. J. Relaxation of hcp(0001) surfaces: A chemical view. *Phys. Rev. B* **1996**, *53*, 13740–13746.
- (281) Nanda, J.; Sarma, D. D. Photoemission spectroscopy of size selected zinc sulfide nanocrystallites. *J. Appl. Phys.* **2001**, *90*, 2504–2510.
- (282) Grüneisen, E. Zustand des festen Körpers. In *Handbuch der Physik*; Geiger, H., Scheel, K., Eds.; Springer: Berlin, 1926; Vol. 10, pp 1–52. (*The state of a solid body (Engl. transl.)*); NASA Publ. RE 2-18-59W; National Aeronautics and Space Administration: Washington, DC, 1959.
- (283) Miller, J. T.; Kropf, A. J.; Zha, Y.; Regalbuto, J. R.; Delannoy, L.; Louis, C.; Bus, E.; van Bokhoven, J. A. The effect of gold particle size on Au-Au bond length and reactivity toward oxygen in supported catalysts. *J. Catal.* **2006**, *240*, 222–234.
- (284) Visikovskiy, A.; Matsumoto, H.; Mitsuhashi, K.; Nakada, T.; Akita, T.; Kido, Y. Electronic d-band properties of gold nanoclusters grown on amorphous carbon. *Phys. Rev. B* **2011**, *83*, 165428.
- (285) Zhang, P.; Sham, T. X-ray studies of the structure and electronic behavior of alkane-thiolate-capped gold nanoparticles: the interplay of size and surface effects. *Phys. Rev. Lett.* **2003**, *90*, 245502.
- (286) Howard, A.; Clark, D. N. S.; Mitchell, C. E. J.; Egdell, R. G.; Dhanak, V. R. Initial and final state effects in photoemission from Au nanoclusters on TiO₂(110). *Surf. Sci.* **2002**, *518*, 210–224.
- (287) Salmeron, M.; Ferrer, S.; Jazzaar, M.; Somorjai, G. A. Core-band and valence-band energy-level shifts in small two-dimensional islands of gold deposited on Pt(100)—The effect of step edge, surface, and bulk atoms. *Phys. Rev. B* **1983**, *28*, 1158–1160.
- (288) Felten, A.; Bittencourt, C.; Pireaux, J. J. Gold clusters on oxygen plasma functionalized carbon nanotubes: XPS and TEM studies. *Nanotechnology* **2006**, *17*, 1954–1959.
- (289) Tanaka, A.; Takeda, Y.; Nagasawa, T.; Takahashi, K. Chemical states of dodecanethiolate-passivated Au nanoparticles: synchrotron-radiation photoelectron spectroscopy. *Solid State Commun.* **2003**, *126*, 191–196.
- (290) Lim, D. C.; Dietsche, R.; Bubek, M.; Ketterer, T.; Gantefor, G.; Kim, Y. D. Chemistry of mass-selected Au clusters deposited on sputter-damaged HOPG surfaces: The unique properties of Au-8 clusters. *Chem. Phys. Lett.* **2007**, *439*, 364–368.
- (291) Boyen, H. G.; Ethirajan, A.; Kastle, G.; Weigl, F.; Ziemann, P.; Schmid, G.; Garnier, M. G.; Buttner, M.; Oelhafen, P. Alloy formation of supported gold nanoparticles at their transition from clusters to solids: Does size matter? *Phys. Rev. Lett.* **2005**, *94*, 016804.
- (292) DiCenzo, S. B.; Berry, S. D.; Hartford, E. H. Photoelectron spectroscopy of single-size Au clusters collected on a substrate. *Phys. Rev. B* **1988**, *38*, 8465.
- (293) Yasuda, H.; Mori, H. Spontaneous alloying of zinc atoms into gold clusters and formation of compound clusters. *Phys. Rev. Lett.* **1992**, *69*, 3747–3750.
- (294) Lim, D. C.; Lopez-Salido, I.; Dietsche, R.; Bubek, M.; Kim, Y. D. Electronic and chemical properties of supported Au nanoparticles. *Chem. Phys.* **2006**, *330*, 441–448.
- (295) Zou, C. W.; Sun, B.; Wang, G. D.; Zhang, W. H.; Xu, P. S.; Pan, H. B.; Xu, F. Q. Initial interface study of Au deposition on GaN(0001). *Physica B* **2005**, *370*, 287–293.
- (296) Barinov, A.; Casalis, L.; Gregoratti, L.; Kiskinova, M. Au/GaN interface: Initial stages of formation and temperature-induced effects. *Phys. Rev. B* **2001**, *63*, 085308.
- (297) Okazawa, T.; Fujiwara, M.; Nishimura, T.; Akita, T.; Kohyama, M.; Kido, Y. Growth mode and electronic structure of Au nano-clusters on NiO(001) and TiO₂(110). *Surf. Sci.* **2006**, *600*, 1331–1338.
- (298) Buffat, P.; Borel, J. P. Size effect on melting temperature of gold particles. *Phys. Rev. A* **1976**, *13*, 2287–2298.
- (299) Donnadieu, P.; Lazar, S.; Botton, G. A.; Pignot-Paintrand, I.; Reynolds, M.; Perez, S. Seeing structures and measuring properties with transmission electron microscopy images: A simple combination to

- study size effects in nanoparticle systems. *Appl. Phys. Lett.* **2009**, *94*, 263116–263113.
- (300) Sun, C. Q.; Bai, H. L.; Li, S.; Tay, B. K.; Li, C.; Chen, T. P.; Jiang, E. Y. Length, strength, extensibility, and thermal stability of a Au-Au bond in the gold monatomic chain. *J. Phys. Chem. B* **2004**, *108*, 2162–2167.
- (301) Sperl, A.; Kroger, J.; Neel, N.; Jensen, H.; Berndt, R.; Franke, A.; Pehlke, E. Unoccupied states of individual silver clusters and chains on Ag(111). *Phys. Rev. B* **2008**, *77*, 085422.
- (302) Roy, D.; Barber, Z.; Clyne, T. Ag nanoparticle induced surface enhanced Raman spectroscopy of chemical vapor deposition diamond thin films prepared by hot filament chemical vapor deposition. *J. Appl. Phys.* **2002**, *91*, 6085–6088.
- (303) Pal, S.; Tak, Y. K.; Song, J. M. Does the antibacterial activity of silver nanoparticles depend on the shape of the nanoparticle? A study of the gram-negative bacterium Escherichia coli. *Appl. Environ. Microbiol.* **2007**, *73*, 1712–1720.
- (304) Farmer, J. A.; Barciuato, J. H.; Campbell, C. T. Ag Adsorption on Reduced CeO₂ (111) Thin Films†. *J. Phys. Chem. C* **2010**, *114*, 17166–17172.
- (305) Branda, M. M.; Hernández, N. C.; Sanz, J. F.; Illas, F. Density Functional Theory Study of the Interaction of Cu, Ag, and Au Atoms with the Regular CeO₂ (111) Surface. *J. Phys. Chem. C* **2010**, *114*, 1934–1941.
- (306) Luches, P.; Pagliuca, F.; Valeri, S.; Illas, F.; Preda, G.; Pacchioni, G. Nature of Ag Islands and Nanoparticles on the CeO₂(111) Surface. *J. Phys. Chem. C* **2011**, *116*, 1122–1132.
- (307) Kong, D. D.; Wang, G. D.; Pan, Y. H.; Hu, S. W.; Hou, J. B.; Pan, H. B.; Campbell, C. T.; Zhu, J. F. Growth, Structure, and Stability of Ag on CeO₂(111): Synchrotron Radiation Photoemission Studies. *J. Phys. Chem. C* **2011**, *115*, 6715–6725.
- (308) Luo, K.; Lai, X.; Yi, C. W.; Davis, K. A.; Gath, K. K.; Goodman, D. W. The Growth of Silver on an Ordered Alumina Surface. *J. Phys. Chem. B* **2005**, *109*, 4064–4068.
- (309) Ohno, M. Many-electron effects in the Auger-photoelectron coincidence spectroscopy spectra of the late 3d-transition metals. *J. Electron Spectrosc. Relat. Phenom.* **2004**, *136*, 229–234.
- (310) Hernández, N. C.; Graciani, J.; Márquez, A.; Sanz, J. F. Cu, Ag and Au atoms deposited on the α-Al₂O₃(0001) surface: a comparative density functional study. *Surf. Sci.* **2005**, *575*, 189–196.
- (311) Lopez-Salido, I.; Lim, D. C.; Kim, Y. D. Ag nanoparticles on highly ordered pyrolytic graphite (HOPG) surfaces studied using STM and XPS. *Surf. Sci.* **2005**, *588*, 6–18.
- (312) Luo, K.; St. Clair, T. P.; Lai, X.; Goodman, D. W. Silver growth on TiO₂(110)(1 × 1) and (1 × 2). *J. Phys. Chem. B* **2000**, *104*, 3050–3057.
- (313) Cheshnovsky, O.; Taylor, K. J.; Conceicao, J.; Smalley, R. E. Ultraviolet photoelectron-spectra of mass-selected copper clusters—evolution of the 3d band. *Phys. Rev. Lett.* **1990**, *64*, 1785–1788.
- (314) Shin, D.-W.; Dong, C.; Mattesini, M.; Augustsson, A.; Mao, S.; Chang, C.; Persson, C.; Ahuja, R.; Nordgren, J.; Wang, S. X. Size dependence of the electronic structure of copper nanoclusters in SiC matrix. *Chem. Phys. Lett.* **2006**, *422*, 543–546.
- (315) Yang, D. Q.; Sacher, E. Initial- and final-state effects on metal cluster/substrate interactions, as determined by XPS: copper clusters on Dow Cyclotene and highly oriented pyrolytic graphite. *Appl. Surf. Sci.* **2002**, *195*, 187–195.
- (316) Yang, D. Q.; Martinu, L.; Sacher, E.; Sadough-Vanini, A. Nitrogen plasma treatment of the dow Cyclotene 3022 surface and its reaction with evaporated copper. *Appl. Surf. Sci.* **2001**, *177*, 85–95.
- (317) Yang, D. Q.; Sacher, E. Argon ion treatment of the Dow Cyclotene 3022 surface and its effect on the adhesion of evaporated copper. *Appl. Surf. Sci.* **2001**, *173*, 30–39.
- (318) Wu, Y. T.; Garfunkel, E.; Madey, T. E. Initial stages of Cu growth on ordered Al₂O₃ ultrathin films. *J. Vac. Sci. Technol., A* **1996**, *14*, 1662–1667.
- (319) Bearden, J.; Burr, A. Reevaluation of X-ray atomic energy levels. *Rev. Mod. Phys.* **1967**, *39*, 125.
- (320) DiDio, R.; Zehner, D.; Plummer, E. An angle-resolved UPS study of the oxygen-induced reconstruction of Cu (110). *J. Vac. Sci. Technol., A* **1984**, *2*, 852–855.
- (321) Egelhoff, W. F., Jr.; Tibbetts, G. G. Growth of copper, nickel, and palladium films on graphite and amorphous carbon. *Phys. Rev. B* **1979**, *19*, 5028.
- (322) Burkstrand, J. M. Substrate effects on the electronic structure of metal overlayers—an XPS study of polymer-metal interfaces. *Phys. Rev. B* **1979**, *20*, 4853.
- (323) Chtaib, M.; Ghijssen, J.; Pireaux, J.; Caudano, R.; Johnson, R.; Ortí, E.; Bredas, J. Photoemission study of the copper/poly (ethylene terephthalate) interface. *Phys. Rev. B* **1991**, *44*, 10815.
- (324) Sun, C. Q. A model of bonding and band-forming for oxides and nitrides. *Appl. Phys. Lett.* **1998**, *72*, 1706–1708.
- (325) Xu, M. L.; Tong, S. Y. The structure of overlayer adsorption on Ni(001) by high-resolution electron-energy loss spectroscopy. *J. Vac. Sci. Technol., A* **1986**, *4*, 1302–1303.
- (326) Nie, Y. G.; Pan, J. S.; Zhang, Z.; Chai, J. W.; Wang, S. J.; Yang, C. S.; Li, D.; Sun, C. Q. Size dependent 2p(3/2) binding-energy shift of Ni nanoclusters on SiO₂ support: Skin-depth local strain and quantum trapping. *Appl. Surf. Sci.* **2010**, *256*, 4667–4671.
- (327) Sun, Y.; Pan, J. S.; Tao, J. G.; Nie, Y. G.; Huan, C. H. A.; Zhang, Z.; Chai, J. W.; Li, D.; Wang, S. J.; Sun, C. Q. Size Dependence of the 2p(3/2) and 3d(5/2) Binding Energy Shift of Ni Nanostructures: Skin-Depth Charge and Energy Trapping. *J. Phys. Chem. C* **2009**, *113*, 10939–10946.
- (328) Woltersdorf, J.; Nepijko, A.; Pipel, E. Dependence of lattice parameters of small particles on the size of the nuclei. *Surf. Sci.* **1981**, *106*, 64–69.
- (329) Lamber, R.; Wetjen, S.; Jaeger, N. I. Size dependence of the lattice parameter of small palladium particles. *Phys. Rev. B* **1995**, *51*, 10968.
- (330) Zhao, M.; Zhou, X.; Jiang, Q. Comparison of different models for melting point change of metallic nanocrystals. *J. Mater. Res.* **2001**, *16*, 3304–3308.
- (331) Peredkov, S.; Öhrwall, G.; Schulz, J.; Lundwall, M.; Rander, T.; Lindblad, A.; Bergersen, H.; Rosso, A.; Pokapanich, W.; Mårtensson, N.; Svensson, S.; Sorensen, S.; Björneholm, O.; Tchaplyguine, M. Free nanoscale sodium clusters studied by core-level photoelectron spectroscopy. *Phys. Rev. B* **2007**, *75*, 235407.
- (332) Rosso, A.; Öhrwall, G.; Bradeanu, I. L.; Svensson, S.; Björneholm, O.; Tchaplyguine, M. Photoelectron spectroscopy study of free potassium clusters: Core-level lines and plasmon satellites. *Phys. Rev. A: At. Mol. Opt. Phys.* **2008**, *77*, 043202.
- (333) Bo, M.; Wang, Y.; Huang, Y.; Liu, Y.; Li, C.; Sun, C. Q. Atomistic spectrometrics of local bond-electron-energy pertaining to Na and K clusters. *Appl. Surf. Sci.* **2015**, *325*, 33–38.
- (334) Zhang, T.; Bo, M.; Guo, Y.; Huang, Y.; Chen, H.; Li, C.; Sun, C. Q. Coordination-resolved atomistic local bonding and 3p electronic energetics of K(110) skin and atomic clusters. *Appl. Surf. Sci.* **2015**, DOI: 10.1016/j.apsusc.2015.1005.1051.
- (335) Wertheim, G.; Riffe, D. M.; Smith, N.; Citrin, P. Electron mean free paths in the alkali metals. *Phys. Rev. B* **1992**, *46*, 1955.
- (336) Riffe, D. M.; Wertheim, G.; Citrin, P. Enhanced vibrational broadening of core-level photoemission from the surface of Na (110). *Phys. Rev. Lett.* **1991**, *67*, 116–119.
- (337) Wertheim, G.; Riffe, D. M. Evidence for crystal-field splitting in surface-atom photoemission from potassium. *Phys. Rev. B* **1995**, *S2*, 14906.
- (338) Mikkälä, M.-H.; Tchaplyguine, M.; Jänkälä, K.; Andersson, T.; Zhang, C.; Björneholm, O.; Huttula, M. Size-dependent study of Rb and K clusters using core and valence level photoelectron spectroscopy. *Eur. Phys. J. D: At., Mol., Opt. Plasma Phys.* **2011**, *64*, 347–352.
- (339) Bo, M.; Guo, Y.; Huang, Y.; Liu, Y.; Wang, Y.; Li, C.; Sun, C. Q. Coordination-resolved bonding and electronic dynamics of Na atomic clusters and solid skins. *RSC Adv.* **2015**, *5*, 35274–35281.
- (340) Vogel, M.; Kasigkeit, C.; Hirsch, K.; Langenberg, A.; Rittmann, J.; Zamudio-Bayer, V.; Kulesza, A.; Mitrić, R.; Möller, T.; v. Issendorff, B.; Lau, J. 2p core-level binding energies of size-selected free silicon

- clusters: Chemical shifts and cluster structure. *Phys. Rev. B* **2012**, *85*, 195454.
- (341) Pan, L. K.; Ee, Y. K.; Sun, C. Q.; Yu, G. Q.; Zhang, Q. Y.; Tay, B. K. Band-gap expansion, core-level shift, and dielectric suppression of porous silicon passivated by plasma fluorination. *J. Vac. Sci. Technol., B* **2004**, *22*, 583–587.
- (342) Dalmas, J.; Oughaddou, H.; Le Lay, G.; Aufray, B.; Tréglia, G.; Girardeaux, C.; Bernardini, J.; Fujii, J.; Panaccione, G. Photoelectron spectroscopy study of Pb/Ag (111) in the submonolayer range. *Surf. Sci.* **2006**, *600*, 1227–1230.
- (343) Le Lay, G.; Hricovini, K.; Bonnet, J. Ultraviolet photoemission study of the initial adsorption of Pb on Si (100) 2×1. *Phys. Rev. B* **1989**, *39*, 3927.
- (344) Peredkov, S.; Sorensen, S.; Rosso, A.; Öhrwall, G.; Lundwall, M.; Rander, T.; Lindblad, A.; Bergersen, H.; Pokapanich, W.; Svensson, S.; Björnholm, O.; Mårtensson, N.; Tchaplyguine, M. Size determination of free metal clusters by core-level photoemission from different initial charge states. *Phys. Rev. B* **2007**, *76*, 081402.
- (345) Bo, M.; Wang, Y.; Huang, Y.; Zhou, W.; Li, C.; Sun, C. Q. Coordination-resolved local bond relaxation and electron binding-energy shift of Pb solid skins and atomic clusters. *J. Mater. Chem. C* **2014**, *2*, 6090–6096.
- (346) Mironets, O.; Meyerheim, H. L.; Tusche, C.; Stepanyuk, V. S.; Soyka, E.; Hong, H.; Zschack, P.; Jeutter, N.; Felici, R.; Kirschner, J. Bond length contraction in cobalt nanoislands on Cu(001) analyzed by surface x-ray diffraction. *Phys. Rev. B* **2009**, *79*, 035406.
- (347) Mironets, O.; Meyerheim, H. L.; Tusche, C.; Stepanyuk, V. S.; Soyka, E.; Zschack, P.; Hong, H.; Jeutter, N.; Felici, R.; Kirschner, J. Direct evidence for mesoscopic relaxations in cobalt nanoislands on Cu(001). *Phys. Rev. Lett.* **2008**, *100*, 096103.
- (348) Rastei, M. V.; Heinrich, B.; Limot, L.; Ignatiev, P. A.; Stepanyuk, V. S.; Bruno, P.; Bucher, J. P. Size-Dependent Surface States of Strained Cobalt Nanoislands on Cu(111). *Phys. Rev. Lett.* **2007**, *99*, 246102.
- (349) Leontyev, I.; Kuriganova, A.; Leontyev, N.; Hennet, L.; Rakhmatullin, A.; Smirnova, N.; Dmitriev, V. Size dependence of the lattice parameters of carbon supported platinum nanoparticles: X-ray diffraction analysis and theoretical considerations. *RSC Adv.* **2014**, *4*, 35959–35965.
- (350) Ahmadi, S.; Zhang, X.; Gong, Y.; Sun, C. Q. Atomic under-coordination fascinated catalytic and magnetic behavior of Pt and Rh nanoclusters. *Phys. Chem. Chem. Phys.* **2014**, *16*, 20537–20547.
- (351) Ahmadi, S.; Zhang, X.; Gong, Y.; Chia, C. H.; Sun, C. Q. Skin-resolved local bond contraction, core electron entrapment, and valence charge polarization of Ag and Cu nanoclusters. *Phys. Chem. Chem. Phys.* **2014**, *16*, 8940–8948.
- (352) Marcus, P.; Hinnen, C. XPS study of the early stages of deposition of Ni, Cu and Pt on HOPG. *Surf. Sci.* **1997**, *392*, 134–142.
- (353) Yang, D. Q.; Sacher, E. Strongly enhanced interaction between evaporated Pt nanoparticles and functionalized multiwalled carbon nanotubes via plasma surface modifications: Effects of physical and chemical defects. *J. Phys. Chem. C* **2008**, *112*, 4075–4082.
- (354) Bittencourt, C.; Hecq, M.; Felten, A.; Pireaux, J. J.; Ghijssen, J.; Felicissimo, M. P.; Rudolf, P.; Drube, W.; Ke, X.; Van Tendeloo, G. Platinum-carbon nanotube interaction. *Chem. Phys. Lett.* **2008**, *462*, 260–264.
- (355) Yang, D.-Q.; Sacher, E. Characterization and oxidation of Fe nanoparticles deposited onto highly oriented pyrolytic graphite, using X-ray photoelectron spectroscopy. *J. Phys. Chem. C* **2009**, *113*, 6418–6425.
- (356) Di Castro, V.; Ciampi, S. XPS study of the growth and reactivity of FeMnO thin films. *Surf. Sci.* **1995**, *331*, 294–299.
- (357) Berkó, A.; Ulrych, I.; Prince, K. Encapsulation of Rh nanoparticles supported on TiO₂ (110)-(1×1) surface: XPS and STM studies. *J. Phys. Chem. B* **1998**, *102*, 3379–3386.
- (358) Sadeghi, H. R.; Henrich, V. E. Rh on TiO₂: Model catalyst studies of the strong metal-support interaction. *Appl. Surf. Sci.* **1984**, *19*, 330–340.
- (359) Óvári, L.; Kiss, J. Growth of Rh nanoclusters on TiO₂(110): XPS and LEIS studies. *Appl. Surf. Sci.* **2006**, *252*, 8624–8629.
- (360) Wang, Y.; Wang, L. L.; Sun, C. Q. The 2p_{3/2} binding energy shift of Fe surface and Fe nanoparticles. *Chem. Phys. Lett.* **2009**, *480*, 243–246.
- (361) Sun, C. Q. Atomic-coordination-imperfection-enhanced Pd-3d(5/2) crystal binding energy. *Surf. Rev. Lett.* **2003**, *10*, 1009–1013.
- (362) Novoselov, K. S.; Jiang, Z.; Zhang, Y.; Morozov, S. V.; Stormer, H. L.; Zeitler, U.; Maan, J. C.; Boebinger, G. S.; Kim, P.; Geim, A. K. Room-temperature quantum hall effect in graphene. *Science* **2007**, *315*, 1379–1379.
- (363) Novoselov, K. S.; Geim, A. K.; Morozov, S. V.; Jiang, D.; Zhang, Y.; Dubonos, S. V.; Grigorieva, I. V.; Firsov, A. A. Electric field effect in atomically thin carbon films. *Science* **2004**, *306*, 666–669.
- (364) Girit, C. O.; Meyer, J. C.; Erni, R.; Rossell, M. D.; Kisielowski, C.; Yang, L.; Park, C. H.; Crommie, M. F.; Cohen, M. L.; Louie, S. G.; Zettl, A. Graphene at the Edge: Stability and Dynamics. *Science* **2009**, *323*, 1705–1708.
- (365) Zhang, Y. B.; Tan, Y. W.; Stormer, H. L.; Kim, P. Experimental observation of the quantum Hall effect and Berry's phase in graphene. *Nature* **2005**, *438*, 201–204.
- (366) Ohta, T.; Bostwick, A.; Seyller, T.; Horn, K.; Rotenberg, E. Controlling the electronic structure of bilayer graphene. *Science* **2006**, *313*, 951–954.
- (367) Meyer, J. C.; Geim, A. K.; Katsnelson, M.; Novoselov, K.; Booth, T.; Roth, S. The structure of suspended graphene sheets. *Nature* **2007**, *446*, 60–63.
- (368) Caridad, J.; Rossella, F.; Bellani, V.; Grandi, M.; Diez, E. Automated detection and characterization of graphene and few-layer graphite via Raman spectroscopy. *J. Raman Spectrosc.* **2011**, *42*, 286–293.
- (369) Brey, L.; Fertig, H. Electronic states of graphene nanoribbons studied with the Dirac equation. *Phys. Rev. B* **2006**, *73*, 235411.
- (370) Lehtinen, P. O.; Foster, A. S.; Ma, Y.; Krasheninnikov, A. V.; Nieminen, R. M. Irradiation-Induced Magnetism in Graphite: A Density Functional Study. *Phys. Rev. Lett.* **2004**, *93*, 187202.
- (371) Palacios, J. J.; Fernandez-Rossier, J.; Brey, L. Vacancy-induced magnetism in graphene and graphene ribbons. *Phys. Rev. B* **2008**, *77*, 195428.
- (372) Červenka, J.; Katsnelson, M.; Flipse, C. Room-temperature ferromagnetism in graphite driven by two-dimensional networks of point defects. *Nat. Phys.* **2009**, *5*, 840–844.
- (373) Pereira, V. M.; Guinea, F.; Dos Santos, J. L.; Peres, N.; Neto, A. C. Disorder induced localized states in graphene. *Phys. Rev. Lett.* **2006**, *96*, 036801.
- (374) Soldano, C.; Mahmood, A.; Dujardin, E. Production, properties and potential of graphene. *Carbon* **2010**, *48*, 2127–2150.
- (375) Novoselov, K. S.; Geim, A. K.; Morozov, S. V.; Jiang, D.; Katsnelson, M. I.; Grigorieva, I. V.; Dubonos, S. V.; Firsov, A. A. Two-dimensional gas of massless Dirac fermions in graphene. *Nature* **2005**, *438*, 197–200.
- (376) Zhou, S. Y.; Gweon, G. H.; Graf, J.; Fedorov, A. V.; Spataru, C. D.; Diehl, R. D.; Kopelevich, Y.; Lee, D. H.; Louie, S. G.; Lanzara, A. First direct observation of Dirac fermions in graphite. *Nat. Phys.* **2006**, *2*, 595–599.
- (377) Acik, M.; Chabal, Y. J. Nature of Graphene Edges: A Review. *Jpn. J. Appl. Phys.* **2011**, *50*, 070101.
- (378) Yu, S. S.; Zheng, W. T. Effect of N/B doping on the electronic and field emission properties for carbon nanotubes, carbon nanocones, and graphene nanoribbons. *Nanoscale* **2010**, *2*, 1069–1082.
- (379) Matsui, T.; Kambara, H.; Niimi, Y.; Tagami, K.; Tsukada, M.; Fukuyama, H. STS Observations of Landau Levels at Graphite Surfaces. *Phys. Rev. Lett.* **2005**, *94*, 226403.
- (380) Li, G.; Andrei, E. Y. Observation of Landau levels of Dirac fermions in graphite. *Nat. Phys.* **2007**, *3*, 623–627.
- (381) Kondo, T.; Honma, Y.; Oh, J.; Machida, T.; Nakamura, J. Edge states propagating from a defect of graphite: Scanning tunneling spectroscopy measurements. *Phys. Rev. B* **2010**, *82*, 153414.
- (382) Niimi, Y.; Kambara, H.; Fukuyama, H. Localized Distributions of Quasi-Two-Dimensional Electronic States near Defects Artificially

- Created at Graphite Surfaces in Magnetic Fields. *Phys. Rev. Lett.* **2009**, *102*, 026803.
- (383) Kobayashi, Y.; Fukui, K.-i.; Enoki, T.; Kusakabe, K.; Kaburagi, Y. Observation of zigzag and armchair edges of graphite using scanning tunneling microscopy and spectroscopy. *Phys. Rev. B* **2005**, *71*, 193406.
- (384) Wang, Z. F.; Li, Q. X.; Zheng, H. X.; Ren, H.; Su, H. B.; Shi, Q. W.; Chen, J. Tuning the electronic structure of graphene nanoribbons through chemical edge modification: A theoretical study. *Phys. Rev. B* **2007**, *75*, 113406.
- (385) Zhang, X.; Kuo, J. L.; Gu, M. X.; Bai, P.; Sun, C. Q. Graphene nanoribbon band-gap expansion: Broken-bond-induced edge strain and quantum entrapment. *Nanoscale* **2010**, *2*, 2160–2163.
- (386) Gunlycke, D.; White, C. T. Tight-binding energy dispersions of armchair-edge graphene nanostrips. *Phys. Rev. B* **2008**, *77*, 115116.
- (387) Son, Y. W.; Cohen, M. L.; Louie, S. G. Energy gaps in graphene nanoribbons. *Phys. Rev. Lett.* **2006**, *97*, 216803.
- (388) Han, M. Y.; Ozyilmaz, B.; Zhang, Y. B.; Kim, P. Energy band-gap engineering of graphene nanoribbons. *Phys. Rev. Lett.* **2007**, *98*, 206805.
- (389) Yu, S. S.; Wen, Q. B.; Zheng, W. T.; Jiang, Q. Electronic properties of graphene nanoribbons with armchair-shaped edges. *Mol. Simul.* **2008**, *34*, 1085–1090.
- (390) Koskinen, P.; Malola, S.; Hakkinen, H. Evidence for graphene edges beyond zigzag and armchair. *Phys. Rev. B* **2009**, *80*, 073401.
- (391) Kim, K. J.; Lee, H.; Choi, J. H.; Youn, Y. S.; Choi, J.; Kang, T. H.; Jung, M. C.; Shin, H. J.; Lee, H. J.; Kim, S.; Kim, B. Scanning Photoemission Microscopy of Graphene Sheets on SiO₂. *Adv. Mater.* **2008**, *20*, 3589–3591.
- (392) Hibino, H.; Kageshima, H.; Kotsugi, M.; Maeda, F.; Guo, F.-Z.; Watanabe, Y. Dependence of electronic properties of epitaxial few-layer graphene on the number of layers investigated by photoelectron emission microscopy. *Phys. Rev. B* **2009**, *79*, 125431.
- (393) Starke, U.; Riedl, C. Epitaxial graphene on SiC(0001) and SiC(0001̄): from surface reconstructions to carbon electronics. *J. Phys.: Condens. Matter* **2009**, *21*, 134016.
- (394) Filleter, T.; Emtsev, K. V.; Seyller, T.; Bennewitz, R. Local work function measurements of epitaxial graphene. *Appl. Phys. Lett.* **2008**, *93*, 133117.
- (395) Emtsev, K. V.; Speck, F.; Seyller, T.; Ley, L.; Riley, J. D. Interaction, growth, and ordering of epitaxial graphene on SiC{0001} surfaces: A comparative photoelectron spectroscopy study. *Phys. Rev. B* **2008**, *77*, 155303.
- (396) Mao, H. Y.; Wang, R.; Huang, H.; Wang, Y. Z.; Gao, X. Y.; Bao, S. N.; Wee, A. T. S.; Chen, W. Tuning of C[sub 60] energy levels using orientation-controlled phthalocyanine films. *J. Appl. Phys.* **2010**, *108*, 053706.
- (397) Lizzit, S.; Zampieri, G.; Petaccia, L.; Larciprete, R.; Lacovig, P.; Rienks, E. D. L.; Bihlmayer, G.; Baraldi, A.; Hofmann, P. Band dispersion in the deep 1s core level of graphene. *Nat. Phys.* **2010**, *6*, 345–349.
- (398) Stacey, A.; Cowie, B. C. C.; Orwa, J.; Prawer, S.; Hoffman, A. Diamond C 1s core-level excitons: Surface sensitivity. *Phys. Rev. B* **2010**, *82*, 125427.
- (399) An, B.; Fukuyama, S.; Yokogawa, K.; Yoshimura, M. Surface Superstructure of Carbon Nanotubes on Highly Oriented Pyrolytic Graphite Annealed at Elevated Temperatures. *Jpn. J. Appl. Phys.* **1998**, *37*, 3809–3811.
- (400) Sun, C. Q.; Bai, H. L.; Tay, B. K.; Li, S.; Jiang, E. Y. Dimension, strength, and chemical and thermal stability of a single C-C bond in carbon nanotubes. *J. Phys. Chem. B* **2003**, *107*, 7544–7546.
- (401) Ostrikov, K. Colloquium: Reactive plasmas as a versatile nanofabrication tool. *Rev. Mod. Phys.* **2005**, *77*, 489–511.
- (402) Yang, D. Q.; Sacher, E. s-p hybridization in highly oriented pyrolytic graphite and its change on surface modification, as studied by X-ray photoelectron and Raman spectroscopies. *Surf. Sci.* **2002**, *504*, 125–137.
- (403) Wang, Y.; Yang, X. X.; Li, J. W.; Zhou, Z. F.; Zheng, W. T.; Sun, C. Q. Number-of-layer discriminated graphene phonon softening and stiffening. *Appl. Phys. Lett.* **2011**, *99*, 163109.
- (404) Yang, X. X.; Li, J. W.; Zhou, Z. F.; Wang, Y.; Yang, L. W.; Zheng, W. T.; Sun, C. Q. Raman spectroscopic determination of the length, strength, compressibility, Debye temperature, elasticity, and force constant of the C-C bond in graphene. *Nanoscale* **2012**, *4*, 502–510.
- (405) Shulga, Y. M.; Tien, T. C.; Huang, C. C.; Lo, S. C.; Muradyan, V.; Polyakova, N. V.; Ling, Y. C.; Loutfy, R. O.; Moravsky, A. P. XPS study of fluorinated carbon multi-walled nanotubes. *J. Electron Spectrosc. Relat. Phenom.* **2007**, *160*, 22–28.
- (406) Goldoni, A.; Larciprete, R.; Gregoratti, L.; Kaulich, B.; Kiskinova, M.; Zhang, Y.; Dai, H.; Sangaletti, L.; Parmigiani, F. X-ray photoelectron microscopy of the C 1s core level of free-standing single-wall carbon nanotube bundles. *Appl. Phys. Lett.* **2002**, *80*, 2165–2167.
- (407) Bennich, P.; Puglia, C.; Bruhwiler, P. A.; Nilsson, A.; Maxwell, A. J.; Sandell, A.; Martensson, N.; Rudolf, P. Photoemission study of K on graphite. *Phys. Rev. B* **1999**, *59*, 8292–8304.
- (408) Yannoni, C. S.; Bernier, P. P.; Bethune, D. S.; Meijer, G.; Salem, J. R. NMR determination of the bond lengths in C₆₀. *J. Am. Chem. Soc.* **1991**, *113*, 3190–3192.
- (409) Speranza, G.; Laidani, N. Measurement of the relative abundance of sp(2) and sp(3) hybridised atoms in carbon based materials by XPS: a critical approach. Part I. *Diamond Relat. Mater.* **2004**, *13*, 445–450.
- (410) Takabayashi, S.; Motomitsu, K.; Takahagi, T.; Terayama, A.; Okamoto, K.; Nakatani, T. Qualitative analysis of a diamondlike carbon film by angle-resolved x-ray photoelectron spectroscopy. *J. Appl. Phys.* **2007**, *101*, 103542.
- (411) Saw, K. G.; du Plessis, J. The X-ray photoelectron spectroscopy C 1s diamond peak of chemical vapour deposition diamond from a sharp interfacial structure. *Mater. Lett.* **2004**, *58*, 1344–1348.
- (412) Padture, N. P.; Gell, M.; Jordan, E. H. Thermal barrier coatings for gas-turbine engine applications. *Science* **2002**, *296*, 280–284.
- (413) Veprek, S.; Argon, A. S. Towards the understanding of mechanical properties of super- and ultrahard nanocomposites. *J. Vac. Sci. Technol., B* **2002**, *20*, 650–664.
- (414) Gabriel, N. T.; Talghader, J. J. Optical coatings in microscale channels by atomic layer deposition. *Appl. Opt.* **2010**, *49*, 1242–1248.
- (415) Tung, C. H.; Pey, K. L.; Tang, L. J.; Radhakrishnan, M.; Lin, W. H.; Palumbo, F.; Lombardo, S. Percolation path and dielectric-breakdown-induced-epitaxy evolution during ultrathin gate dielectric breakdown transient. *Appl. Phys. Lett.* **2003**, *83*, 2223–2225.
- (416) Allouche, A.; Wiltner, A.; Linsmeier, C. Quantum modeling (DFT) and experimental investigation of beryllium–tungsten alloy formation. *J. Phys.: Condens. Matter* **2009**, *21*, 355011.
- (417) Doerner, R. P.; Baldwin, M. J.; Causey, R. A. Beryllium-tungsten mixed-material interactions. *J. Nucl. Mater.* **2005**, *342*, 63–67.
- (418) Venezia, A. M.; Liotta, L. F.; Deganello, G.; Schay, Z.; Horvath, D.; Guczi, L. Catalytic CO oxidation over pumice supported Pd-Ag catalysts. *Appl. Catal., A* **2001**, *211*, 167–174.
- (419) Lee, C. L.; Tseng, C. M.; Wu, R. B.; Wu, C. C.; Syu, S. C. Catalytic characterization of hollow silver/palladium nanoparticles synthesized by a displacement reaction. *Electrochim. Acta* **2009**, *54*, 5544–5547.
- (420) Choi, I. S.; Whang, C. N.; Hwang, C. Y. Surface-induced phase separation in Pd-Ag alloy: the case opposite to surface alloying. *J. Phys.: Condens. Matter* **2003**, *15*, L415–L422.
- (421) Reilly, J. P.; Barnes, C. J.; Price, N. J.; Bennett, R. A.; Pouston, S.; Stone, P.; Bowker, M. The growth mechanism, thermal stability, and reactivity of palladium mono- and multilayers on Cu(110). *J. Phys. Chem. B* **1999**, *103*, 6521–6532.
- (422) Efremenko, I.; Matatov-Meytal, U.; Sheintuch, M. Hydrodenitrification with PdCu catalysts: Catalyst optimization by experimental and quantum chemical approaches. *Isr. J. Chem.* **2006**, *46*, 1–15.
- (423) Matensson, N.; Nyholm, R.; Cale, H.; Hedman, J.; Johansson, B. Electron-spectroscopic studies of the Cu_xPd_{1-x} alloy system: Chemical-shift effects and valence-electron spectra. *Phys. Rev. B* **1981**, *24*, 1725.
- (424) Rochefort, A.; Abon, M.; Delichere, P.; Bertolini, J. C. Alloying effect on the adsorption properties of Pd₅₀Cu₅₀{111} single crystal surface. *Surf. Sci.* **1993**, *294*, 43–52.

- (425) Pope, T. D.; Griffiths, K.; Norton, P. R. Surface and interfacial alloys of Pd with Cu(100): structure, photoemission and CO chemisorption. *Surf. Sci.* **1994**, *306*, 294–312.
- (426) Barnes, C. J.; Gleeson, M.; Sahrakorpi, S.; Lindroos, M. Electronic structure of strained copper overlayers on Pd(110). *Surf. Sci.* **2000**, *447*, 165–179.
- (427) Sengar, S. K.; Mehta, B. Size and alloying induced changes in lattice constant, core, and valance band binding energy in Pd-Ag, Pd, and Ag nanoparticles: Effect of in-flight sintering temperature. *J. Appl. Phys.* **2012**, *112*, 014307.
- (428) Pu, X. D.; Chen, J.; Shen, W. Z.; Ogawa, H.; Guo, Q. X. Temperature dependence of Raman scattering in hexagonal indium nitride films. *J. Appl. Phys.* **2005**, *98*, 033527.
- (429) Du, H. B.; De Sarkar, A.; Li, H. S.; Sun, Q.; Jia, Y.; Zhang, R. Q. Size dependent catalytic effect of TiO₂ clusters in water dissociation. *J. Mol. Catal. A: Chem.* **2013**, *366*, 163–170.
- (430) Wiltner, A.; Linsmeier, C. Surface alloying of thin beryllium films on tungsten. *New J. Phys.* **2006**, *8*, 181.
- (431) Sun, C. Q.; Wang, Y.; Nie, Y. G.; Mehta, B. R.; Khanuja, M.; Shivaprasad, S. M.; Sun, Y.; Pan, J. S.; Pan, L. K.; Sun, Z. Interface charge polarization and quantum trapping in AgPd and CuPd bimetallic alloy catalysts. *Phys. Chem. Chem. Phys.* **2010**, *12*, 3131–3135.
- (432) Ma, Z. S.; Wang, Y.; Huang, Y. L.; Zhou, Z. F.; Zhou, Y. C.; Zheng, W. T.; Sun, C. Q. XPS quantification of the hetero-junction interface energy. *Appl. Surf. Sci.* **2013**, *265*, 71–77.
- (433) Coulthard, I.; Sham, T. K. Charge redistribution in Pd-Ag alloys from a local perspective. *Phys. Rev. Lett.* **1996**, *77*, 4824–4827.
- (434) Lipton-Duffin, J. A.; Macleod, J. M.; Vondracek, M.; Prince, K. C.; Rosei, R.; Rosei, F. Thermal evolution of the submonolayer near-surface alloy of ZnPd on Pd(111). *Phys. Chem. Chem. Phys.* **2014**, *16*, 4764–4770.
- (435) Schriver-Mazzuoli, L.; Schriver, A.; Hallou, A. IR reflection-absorption spectra of thin water ice films between 10 and 160 K at low pressure. *J. Mol. Struct.* **2000**, *554*, 289–300.
- (436) Cole, R. J.; Brooks, N. J.; Weightman, P.; Francis, S. M.; Bowker, M. The physical and electronic structure of the Cu85Pd15(110) surface; Clues from the study of bulk Cu_xPd_{1-x} alloys. *Surf. Rev. Lett.* **1996**, *3*, 1763–1772.
- (437) Vegard, L.; Schjelderup, H. Constitution of mixed crystals. *Phys. Z.* **1917**, *18*, 93–96.
- (438) Tamkögl, A.; Kratzer, M.; Killman, J.; Winkler, A. Adsorption/desorption of H₂ and CO on Zn-modified Pd (111). *J. Chem. Phys.* **2008**, *129*, 224706.
- (439) de Siervo, A.; Soares, E. A.; Landers, R.; Kleiman, G. G. Photoelectron diffraction studies of Cu on Pd(111) random surface alloys. *Phys. Rev. B* **2005**, *71*, 115417.
- (440) de Siervo, A.; Paniago, R.; Soares, E. A.; Pfannes, H. D.; Landers, R.; Kleiman, G. G. Growth study of Cu/Pd(111) by RHEED and XPS. *Surf. Sci.* **2005**, *575*, 217–222.
- (441) Martinez, U.; Hansen, J. Ø.; Lira, E.; Kristoffersen, H. H.; Huo, P.; Bechstein, R.; Lægsgaard, E.; Besenbacher, F.; Hammer, B.; Wendt, S. Reduced Step Edges on Rutile TiO₂ (110) as Competing Defects to Oxygen Vacancies on the Terraces and Reactive Sites for Ethanol Dissociation. *Phys. Rev. Lett.* **2012**, *109*, 155501.
- (442) Jin, S.; Li, Y.; Xie, H.; Chen, X.; Tian, T.; Zhao, X. Highly selective photocatalytic and sensing properties of 2D-ordered dome films of nano titania and nano Ag²⁺ doped titania. *J. Mater. Chem.* **2012**, *22*, 1469–1476.
- (443) Borodin, A.; Reichling, M. Characterizing TiO₂ (110) surface states by their work function. *Phys. Chem. Chem. Phys.* **2011**, *13*, 15442–15447.
- (444) Kong, M.; Li, Y.; Chen, X.; Tian, T.; Fang, P.; Zheng, F.; Zhao, X. Tuning the relative concentration ratio of bulk defects to surface defects in TiO₂ nanocrystals leads to high photocatalytic efficiency. *J. Am. Chem. Soc.* **2011**, *133*, 16414–16417.
- (445) Tao, J.; Batzill, M. Role of surface structure on the charge trapping in TiO₂ photocatalysts. *J. Phys. Chem. Lett.* **2010**, *1*, 3200–3206.
- (446) Yim, C. M.; Pang, C. L.; Thornton, G. Oxygen Vacancy Origin of the Surface Band-Gap State of TiO₂(110). *Phys. Rev. Lett.* **2010**, *104*, 036806.
- (447) Diebold, U. The surface science of titanium dioxide. *Surf. Sci. Rep.* **2003**, *48*, 53–229.
- (448) Daghrir, R.; Drogui, P.; Robert, D. Modified TiO₂ for environmental photocatalytic applications: a review. *Ind. Eng. Chem. Res.* **2013**, *52*, 3581–3599.
- (449) Kollbek, K.; Sikora, M.; Kapusta, C.; Szlachetko, J.; Zakrzewska, K.; Kowalski, K.; Radecka, M. X-ray spectroscopic methods in the studies of nonstoichiometric TiO_{2-x} thin films. *Appl. Surf. Sci.* **2013**, *281*, 100–104.
- (450) Zuo, F.; Wang, L.; Wu, T.; Zhang, Z.; Borchardt, D.; Feng, P. Self-doped Ti³⁺ enhanced photocatalyst for hydrogen production under visible light. *J. Am. Chem. Soc.* **2010**, *132*, 11856–11857.
- (451) Mitsuhashi, K.; Okumura, H.; Visikovskiy, A.; Takizawa, M.; Kido, Y. The source of the Ti 3d defect state in the band gap of rutile titania (110) surfaces. *J. Chem. Phys.* **2012**, *136*, 124707.
- (452) Chrétien, S.; Metiu, H. Electronic Structure of Partially Reduced Rutile TiO₂ (110) Surface: Where Are the Unpaired Electrons Located? *J. Phys. Chem. C* **2011**, *115*, 4696–4705.
- (453) Krüger, P.; Bourgeois, S.; Domenichini, B.; Magnan, H.; Chandresris, D.; Le Fèvre, P.; Flank, A. M.; Jupille, J.; Floreano, L.; Cossaro, A.; Verdini, A.; Morgante, A. Defect States at the TiO₂ Surface Probed by Resonant Photoelectron Diffraction. *Phys. Rev. Lett.* **2008**, *100*, 055501.
- (454) Zhang, Z.; Jeng, S.-P.; Henrich, V. E. Cation-ligand hybridization for stoichiometric and reduced TiO₂ (110) surfaces determined by resonant photoemission. *Phys. Rev. B* **1991**, *43*, 12004.
- (455) Chen, X.; Liu, L.; Peter, Y. Y.; Mao, S. S. Increasing solar absorption for photocatalysis with black hydrogenated titanium dioxide nanocrystals. *Science* **2011**, *331*, 746–750.
- (456) Zhang, Z.; Yates, J. T., Jr. Band bending in semiconductors: chemical and physical consequences at surfaces and interfaces. *Chem. Rev.* **2012**, *112*, 5520–5551.
- (457) Li, L.; Tian, H.-W.; Meng, F.-L.; Hu, X.-Y. H.; Zheng, W.-T.; Sun, C. Q. Defects improved photocatalytic ability of TiO₂. *Appl. Surf. Sci.* **2014**, *317*, 568–572.
- (458) Kuznetsov, M. V.; Tel'minov, A. V.; Shalaeva, E. V.; Ivanovskii, A. L. Study of adsorption of nitrogen monoxide on the Ti(0001) surface. *Phys. Met. Metallogr. (Transl. of Fiz. Met. Metalloved.)* **2000**, *89*, 569–580.
- (459) Schwegmann, S.; Seitsonen, A.; Dietrich, H.; Bludau, H.; Over, H.; Jacobi, K.; Ertl, G. The adsorption of atomic nitrogen on Ru (0001): geometry and energetics. *Chem. Phys. Lett.* **1997**, *264*, 680–686.
- (460) Schwegmann, S.; Seitsonen, A.; De Renzi, V.; Dietrich, H.; Bludau, H.; Gierer, M.; Over, H.; Jacobi, K.; Scheffler, M.; Ertl, G. Oxygen adsorption on the Ru (1010) surface: Anomalous coverage dependence. *Phys. Rev. B* **1998**, *57*, 15487.
- (461) Li, L.; Meng, F.; Tian, H.; Hu, X.; Zheng, W. T.; Sun, C. Q. Oxygenation mediating the valence density-of-states and work function of Ti (0001) skin. *Phys. Chem. Chem. Phys.* **2015**, *17*, 9867–9872.
- (462) Göpel, W.; Anderson, J.; Frankel, D.; Jaehnig, M.; Phillips, K.; Schäfer, J.; Rocker, G. Surface defects of TiO₂(110): A combined XPS, XAES AND ELS study. *Surf. Sci.* **1984**, *139*, 333–346.
- (463) Hanson, D. M.; Stockbauer, R.; Madey, T. E. Photon-stimulated desorption and other spectroscopic studies of the interaction of oxygen with a titanium (001) surface. *Phys. Rev. B* **1981**, *24*, 5513.
- (464) Liu, X. J.; Yang, L. W.; Zhou, Z. F.; Chu, P. K.; Sun, C. Q. Inverse Hall-Petch relationship of nanostructured TiO₂: Skin-depth energy pinning versus surface preferential melting. *J. Appl. Phys.* **2010**, *108*, 073503.
- (465) Liu, X. J.; Pan, L. K.; Sun, Z.; Chen, Y. M.; Yang, X. X.; Yang, L. W.; Zhou, Z. F.; Sun, C. Q. Strain engineering of the elasticity and the Raman shift of nanostructured TiO₂(110). *J. Appl. Phys.* **2011**, *110*, 044322.
- (466) Tay, Y. Y.; Li, S.; Sun, C. Q.; Chen, P. Size dependence of Zn 2p 3/2 binding energy in nanocrystalline ZnO. *Appl. Phys. Lett.* **2006**, *88*, 173118.

- (467) Tay, Y.; Tan, T.; Liang, M.; Boey, F.; Li, S. Specific defects, surface band bending and characteristic green emissions of ZnO. *Phys. Chem. Chem. Phys.* **2010**, *12*, 6008–6013.
- (468) Tay, Y. Y.; Tan, T.; Boey, F.; Liang, M. H.; Ye, J.; Zhao, Y.; Norby, T.; Li, S. Correlation between the characteristic green emissions and specific defects of ZnO. *Phys. Chem. Chem. Phys.* **2010**, *12*, 2373–2379.
- (469) Li, J. W.; Ma, S. Z.; Liu, X. J.; Zhou, Z. F.; Sun, C. Q. ZnO mesomechano-thermo physical chemistry. *Chem. Rev.* **2012**, *112*, 2833–2852.
- (470) Hasegawa, M.; Shimakura, T. Observation of electron trapping along scratches on SiO₂ surface in mirror electron microscope images under ultraviolet light irradiation. *J. Appl. Phys.* **2010**, *107*, 084107.
- (471) Paredes, J. I.; Martinez-Alonso, A.; Tascon, J. M. D. Multiscale Imaging and tip-scratch studies reveal insight into the plasma oxidation of graphite. *Langmuir* **2007**, *23*, 8932–8943.